UNIVERSITAT DE BARCELONA

Advanced seismic methods applied to the study of snow avalanche dynamics and avalanche formation

Cristina Pérez Guillén

Aquesta tesi doctoral està subjecta a la llicència ***Reconeixement- NoComercial – SenseObraDerivada 3.0. Espanya de Creative Commons***.

Esta tesis doctoral está sujeta a la licencia ***Reconocimiento - NoComercial – SinObraDerivada 3.0. España de Creative* Commons**.

This doctoral thesis is licensed under the ***Creative Commons Attribution-NonCommercial-NoDerivs 3.0. Spain License***.

Advanced seismic methods applied to the study of snow avalanche dynamics and avalanche formation

Cristina Pérez Guillén

PhD Thesis

UNIVERSITAT DE BARCELONA

UNIVERSITAT DE BARCELONA

RISKNAT- Natural Hazards Research Group
Geomodels Research Institute
Department of Earth and Ocean's Dynamics
Faculty of Geology, University of Barcelona

Advanced seismic methods applied to the study of snow avalanche dynamics and avalanche formation

Dissertation presented by Cristina Pérez Guillén
to apply for the degree of Doctor under the
Doctorate Programme of Earth Sciences
of the University of Barcelona
Supervised by Dr. Emma Suriñach Cornet

May 2016

"Even the largest avalanche is triggered by small things"

Vernor Vinge

Abstract

Snow avalanches are extended moving sources of infrasonic and seismic energy. The acoustic and seismic wave fields generated by a snow avalanche is a complex natural phenomenon produced by the interaction of the flow with its environment. Seismic waves are mainly generated by friction and the impacts of the flow on the snow cover, the terrain and the obstacles in the path of the avalanche; whereas the infrasound waves are generated by the interaction of the turbulent powder cloud with the air. Nowadays, avalanches are recorded using seismic and infrasound sensors that provide data that can be used to obtain information about the characteristics of the source (type of flow regime and dimension) and the basic processes that govern avalanche dynamics such as erosion and deposition. So far, the knowledge of how all these dynamical processes and the inherent characteristics of avalanches affect the signatures of the recorded signals is limited and thus more quantitative data are required. Additionally, seismic and infrasonic monitoring systems can provide information on the mechanisms that trigger snow avalanches. They can be triggered by many different mechanisms, including the shaking produced by an earthquake. The forces induced by an earthquake can cause an increase in the load down the slope and can also decrease the shear strength; either effect can lead to the release of an avalanche. Few earthquakes that triggered snow avalanches have been documented to date, all of them visually or statistically identified. Hence, a complete dataset of such events does not exist.

This study aims to enlarge the current applications of seismic methods, mainly for snow avalanche research, which in turn, is relevant to improve monitoring systems. A catalogue of thirty-three snow avalanches of different natures is analysed using the seismic signals recorded with a set of seismic sensors at the Vallée de la Sionne (VdlS) test site in Switzerland . Seismic sensors were configured linearly both inside and outside the avalanche path. A comparative analysis of the seismic measurements and data acquired with other instrumentation such as an infrasound sensor, several frequency-modulated continuous wave radars, and two weather stations, is presented in each case to complement and validate the results obtained in this work. Quantitative parameterizations of the seismic signals have been conducted to infer the characteristics of the source. In order to correctly interpret the seismic results, a seismic characterization of VdlS is presented. The local seismic site and path effects, according to the characteristics of the terrain and

the geology of the area, are evaluated using the analysis of several earthquakes recorded at the different seismic stations.

The results of this thesis have contributed to the study of earthquake-triggered avalanches. As a first step, the joint analysis of seismic and infrasound data, correlated with the observations of a frequency-modulated wave phased radar array, provides data related to the onset of a snow avalanche with the arrival of an earthquake that occurred on 6th December 2010. The integrated data analysis has been used to characterize the avalanche path and size, showing that the avalanche started after the arrival of the earthquake. Seismic data were used to quantify energy parameters and changes in the elastic stress field within the snowpack due to the earthquake. This event was compared with two stronger earthquakes that did not trigger any snow avalanche. The study was complemented by nivo-meteorological data and simulations of the snow cover using the one-dimensional model SNOWPACK. These data were compared and used to evaluate the snowpack stability and the consequent likelihood of avalanche activity. The snowpack stability is the primary factor that determines whether an avalanche may be triggered by minor earthquakes. I conclude that when the snowpack is only marginally stable, then the displacement caused by even a small earthquake could be enough to trigger an avalanche. In addition, the analysis of the other two, even stronger, earthquakes shows that in stable conditions no avalanche was triggered.

Furthermore, in order to better understand the connection between seismic signals and avalanche dynamics, I quantify the seismic signals in a set of defined seismic indices. For each seismic signal, the duration, peak ground velocity of the envelope, and both the intensity and the frequency content were compared with the avalanche flow regimes and the thicknesses of the snow cover measured using frequency-modulated continuous wave radar, as well as with the avalanche run-out distances obtained from photographs. I show that the frequency content of the seismic signal can be used to infer the avalanche flow regime and to distinguish between the internal parts of avalanches. The frequency parameters presented were defined to quantify the signatures generated by different type of avalanches in order to directly deduce the type of avalanche. Furthermore, the seismic signal duration of both wet and powder-snow avalanches can be correlated to avalanche run-out distances. If the snow cover at the seismic sensor location is less than approximately 2 m and energy absorption does not significantly weaken the intensity of the signal, the avalanche run-out distance can also be deduced from the

peak ground velocity and its intensity. These results suggest that the flow type characteristics and the run-out distances of avalanches can be feasibly inferred using only seismic data. Such analysis of seismic data can be usefully employed in avalanche monitoring and management.

In summary, this thesis presents novel contributions using seismic methods in the research field of avalanche formation, specifically in the field of avalanches induced by earthquakes, and in the field of avalanche dynamics. It provides interesting results to characterize avalanche dynamics and size, and to assess earthquake-generated snow avalanches.

Resumen

Las avalanchas de nieve son extensas fuentes móviles de energia sísmica e infrasónica. El campo de ondas acústicas y sísmicas generado por ellas es un fenómeno natural complejo producido por la interacción del flujo con su medio ambiente. Las ondas sísmicas se generan principalmente por la fricción y los impactos del flujo con el manto de nieve, el suelo y los posibles obstáculos dentro del camino de la avalancha; mientras que las ondas de infrasonido se generan por la interacción de la turbulenta nube de aerosol con el aire. Actualmente, las avalanchas son registradas mediante sensores sísmicos y de infrasonido que proporcionan datos que pueden ser utilizados para obtener carácteristicas de la fuente (tipo de régimen de flujo y dimensión de la avalancha) y de los procesos básicos que gobiernan la dinámica de la avalancha, tales como la erosión y la deposición de la nieve. Hasta ahora, el conocimiento de cómo estos procesos dinámicos y las características inherentes de las avalanchas afectan a las firmas de las señales es limitado y cualitativo, y por tanto, se requiere una cuantificación de los datos. Además, los sistemas de monitoreo sísmico y de infrasonido también pueden proporcionar información sobre el mecanismo de desdencadenamiento de las avalanchas. Éstas pueden ser desecadenadas de varias formas, tales como las vibraciones producidas por los terremotos. Pocos eventos de avalanchas inducidas por terremotos se han documentado hasta la fecha, todos ellos visualmente o estadísticamente identificados. Por tanto, un cojunto de datos completos de estos eventos es inexistente.

El objetivo de este trabajo es ampliar las aplicaciones actuales de los métodos sísmicos principalmente para investigar avalanchas de nieve, y que a su vez, éstas sean relevantes para mejorar los sistemas de monitoreo. En este trabajo se analiza un catalálogo de treinta y tres avalanchas de diferente naturaleza utilizando las señales sísmicas registradas con un conjunto de sensores sísmicos en el sitio de test de Vallée de la Sionne (VdlS, Suiza). Los sensores sísmicos fueron linealmente distribuidos tanto dentro como fuera del camino de la avalancha. Un análisis comparativo de los registros sísmicos y datos aquiridos con otra instrumentación tales como un sensor de infrasonido, dos radares de frecuencia modulada, y dos estaciones meteorológicas, se presenta en cada caso para complementar y validar los resultados obtenidos en este trabajo. Se ha realizado una parametrización cuantitativa de las señales sísmicas para inferir características de la fuente. Para interpretar correctamente los resultados del análisis de los datos sísmicos, se presenta una caracterización sísmica del sitio de test de VdlS. Los efectos sísmicos de

sitio y de camino son evaluados, de acuerdo con las características del terreno y la geología del área, mediante el análisis de varios registros de terremotos en las diferentes estaciones sísmicas.

Los resultados de esta tesis han contribuido con éxito al estudio de las avalanchas desencadenadas por terremotos. En primer lugar, el análisis conjunto de datos sísmicos y de infrasonido, correlacionados con observaciones de un sistema de radar de frecuencia modulada, proporciona datos de la coincidencia de una avalancha de nieve con la llegada de un terremoto ocurrido el 6 de diciembre de 2010. El análisis integrado de datos se ha utilizado para caracterizar el camino y tamaño de la avalancha, mostrando que la avalancha se desencadenó después de la llegada del terremoto. Los datos sísmicos se utilizaron para cuantificar unos parámetros de energía y los cambios en el campo elástico en el interior del manto de nieve debido al terremoto. Este evento fue comparado con otros dos terremotos mas fuertes que no desencadenaron ninguna avalanche de nieve. El estudio fue complementado mediante datos nivo-meteorológicos y simulaciones del manto de nieve utilizando el modelo unidimensonal SNOWPACK. Estos datos fueron comparados y utilizados para evaluar la estabilidad del manto de nieve y su consecuente probabilidad de actividad de avalanchas. Se concluye que la estabilidad del manto de nieve es el factor principal que determina si una avalancha puede ser desecandenada por un terremoto menor. Además, el analísis de los otros dos terremotos mas fuertes muestra que en condiciones estables no se desencadenó niguna avalancha.

Por otro lado, con el fin de conocer la conexión entre las señales sísmicas y la dinámica de las avalanchas, he cuantificado las señales mediante un conjunto de índices sísmicos. Para cada señal sísmica, la duración, el pico de la envolvente del movimiento del suelo, y la intensidad y contenido frecuencial, fueron comparados con los régimenes de flujo y la profundidad del manto de nieve medidos mediante radares de frecuencia modulada, además de con las distancias recorridas por las avalanchas obtenidas mediante fotografías. Se muestra que el contenido frecuencial de la señal sísmica puede utilizarse para inferir el régimen de flujo y distinguir las diferentes partes internas de la avalancha. Se definen unos parámetros de frecuencia para cuantificar las firmas generadas por las distintas avalanchas con el fin de deducir directamente el tipo de avalancha. Además, la duración de la señal sísmicas puede ser correlacionada con las distancia recorrida por las avalanchas. Si el manto de nieve en la localización de la estación sísmica es menor que aproximadamente dos metros, y la absorción de energía no debilita significativamente

la intensidad de la señal, la distancia de recorrido de la avalancha puede tambien ser deducida del pico de velocidad del suelo y de su intesidad. Estos resultados sugieren que las características del tipo de flujo y las distancias recorridas por las avalanchas pueden ser inferidas usando únicamente datos sísmicos. Tal análisis de los datos sísmicos puede ser empleado en sistemas de monitoreo de avalanchas.

En resumen, esta tesis presenta aportaciones novedosas de los métodos sísmicos en el campo de investigación de la formación de avalanchas, específicamente en el campo de avalanchas inducidas por terremotos, y en el campo de la dinámica de avalanchas. Los resultados obtenidos sirven para caracterizar la dinámica y el tamaño de una avalancha, y evaluar posibles eventos de avalanchas desencadenadas por terremotos.

Acknowledgements

Finally, I get to this awaiting long point, the end of my PhD! All the amazing past years of working, learning, adventures and personal growth, they would not have been possible without the help of numerous people.

First of all, I would like to express my sincere gratitude to my supervisor Dr. Emma Suriñach for give me the chance of doing this thesis and for her continuous guidance, and for her patience, motivation and immense knowledge. I would like to thank you for encouraging my research, for supporting all my ideas and for allowing me to grow as a research scientist. Thank you for be always here all these years.

I am also particularly grateful to Dr. Mar Tapia for all the support that she always gave me, for all the concepts from earthquakes and instrumentation that I learnt from her, for all the time dedicated to help me in the field and for your friendship. I will always remember our numerous adventures in the trips to VdlS to install the sensors, as well as all the good times at the university in Barcelona. I am also grateful to Dr. Ignasi Vilajosana for his support and his good ideas, and for be always ready to give me a hand. I could also not forget Dr. Gloria Furdada, for all the concepts from the snow and avalanches that I learnt from her. I would also like to thank the support and help of Dr. Gia Khazaradze and Dr. Nue Vilaplana and the rest of members of the RISKNAT group of the University of Barcelona. Thank you to all of them for give me the opportunity of being part to this research group.

My sincere thanks also goes to Dr. Betty Sovilla, who provided me an opportunity to join their team at the WSL Institute for Snow and Avalanche Research SLF during my stays at Davos; part of the work of this thesis has been done under her supervision. Thank you for sharing your time and data with me, for all the knowledge from snow avalanches that I learnt from you, for the constructive discussions and the nice moments in the office of Davos. I would like to thank to Dr. J.N. McElwaine, for his help and for sharing his data. My sincere thanks also goes to Dr. Michael Bründl and the whole research group of Avalanche Dynamics and Risk Management (Martina, Walter, Jochen, Cesar, Juan, Linda and many others) of the SLF institute of Davos for making my stays there so nice and easy. It was very encouraging for me to work with all of them at that international

research institute and to collaborate in the different snow avalanche experiments conducted by the team at Flüelapass in Davos and at VdlS in Sion.

I would also like to thank to all the people who help me with the installation of the seismic and infrasound sensors at VdlS test field in Sion. Thank you to Mar Tapia, Arnold Kogelnig, Pere Roig, Ignasi Vilajosana, Manuel Royán and Anna Echevarría for helping me to carry the heavy sensors up and down of the mountain, for the support to solve the different issues in the field, and for the good moments together in Sion. I am also particularly grateful to Martin Hiller, Francois Dufuor, and Anselm Köhler for their support at VdlS, for their help in the installation and maintenance of the instruments, and for helping me to resolve the different adversities with the electronics.

I would like to thank to all the professors and administrative staff (Ana, M. Jose y Monica) of the Department of Earth and Ocean's Dynamics of the University of Barcelona and to all the members of the academic commission of my thesis (David Serrat, Lluis Rivero, Eduard Roca and Carles Martin). I also thank to all my office mates and friends of the University of Barcelona (Anna, Diego, Manu, Marta F., Mar, Sara, Perla, Jaume, Gia, Eva, Pere, Marta G., Eloi, Xenia, Höel, Fabian, Lena and many others), for the unforgettable and funny moments lived together in and outside of the university.

I especially want to thank my friends who have accompanied me during the numerous ski touring trips through the mountains (Elena, Raquel, Martina, Chris, Lara, Mathias, Timi and many others). Thank you for all the unforgettable moments in the mountains of Pyrenees and Davos that made me increase my motivation for studying deeply snow avalanches. A especial thanks also goes to all my friends (Eva, Yasmina, Itxas, Gabi, Marta, and many others from Bilbao and Barcelona) for the good moments together and for motivating me always!

I am very much thankful to my family: mi mother, Cristina, my father, Luis, and my brother, David. They always have believed in me and supported me in all my life. Finally, I would like to express my deep gratitude to Gerard, for his love, for his patiente during the last months, and for encourage me always.

Contents

List of Figures

List of Tables

Chapter 1

Introduction

In this introductory chapter, I first present the motivation of this PhD study and an overview of the main seismic applications used to monitor natural hazards. Additionally, I give a detailed overview of the past and current applications of the seismic methods to study avalanche formation, its dynamics and avalanche monitoring. Finally, I describe the main objectives and contents of this thesis.

1.1 Motivation

Snow avalanches are major natural hazards in mountainous terrain. They are responsible for significant economic losses and numerous fatalities. In recent years, the potential costs and the number of accidents has incremented considerably due to the growth of mountain settlements and the increase of winter recreational activities. Mitigation measures to reduce avalanche risk have been implemented in Alpine countries, with regard to avalanche forecasting, structural protections, land-use planning, procedures for warnings and the closure of roads, artificial triggering of avalanches and avalanche education. These measures require knowledge of specific variables such as the frequency of occurrence, location, volume, run-out distance, and dynamical parameters such as velocity or impact pressure. Measuring these avalanche properties is a challenge for humanity due to the unpredictable nature and the destructive power of avalanches.

Snow avalanche characterization is generally based on manual methods with the risk involved in taking measurements in avalanche hazard areas or visual methods

with the inconvenience that avalanches are often released under poor conditions of visibility. Given the complexity of characterizing snow avalanches, an improvement of the techniques used to acquire data is indispensable to automate the process. Consequently, monitoring systems based on seismic sensors have recently been developed. The use of these conventional seismic instruments is occasionally accompanied with acoustic sensors to increase the effectiveness of avalanche detection and characterization. These non-invasive methods acquire data from remote mountainous areas with rather low economic costs. Besides the importance for providing avalanche activity data, these methods may potentially be used to get inherent information of snow avalanche properties. These data are indispensable for assessing avalanche risk in terms of a proper design of structural protection, the development and validation of dynamical models widely used in land-use planning and automatic detection of avalanches.

Snow avalanche formation is mainly driven by interrelationships between meteorological conditions and snow cover properties, together with external factors such as explosions, the passage of skiers, cornice collapse and earthquakes. Earthquake ground vibrations can have severe consequences through causing failure in one of the weakest and most brittle materials: snow. Furthermore, the abrupt mountain topographies characterized by a complex geology might amplify earthquake effects with regards to inducing failure. Earthquake-induced snow avalanches have been rarely measured before now. As a consequence, a deeper understanding of the behaviour of the snow under external vibrations is required to evaluate this triggering mechanism. Seismic monitoring systems installed in avalanche paths are ideal to record new events which would provide quantitative data of avalanches induced by earthquakes, which have an unknown frequency of occurrence. Considering these secondary hazards associated with earthquakes is fundamental to a complete seismic risk assessment in snow-covered mountain areas.

1.2 Overview of the applications of seismic methods to monitor natural hazards

The term seismology is derived from a Greek roots and means the study of shakes or vibrations (Udías, 1999). Natural sources such as earthquakes, volcanoes or mass movements, and artificial sources such as explosions, generate seismic waves

that propagate through a medium. The recorded ground motion contains information on the location and nature of the source, and the physical properties of the propagation medium. Seismology is mainly employed to study earthquakes and to explore the Earth for scientific purposes or resource extraction. Furthermore, local seismic networks are currently operated to monitor diverse natural hazards including volcanoes, floods, and mass movements. The analysis of the seismic data acquired with these monitoring systems provides valuable information to characterize them. The scheme in Figure 1.1 summarizes the current natural hazards monitored by seismic systems.

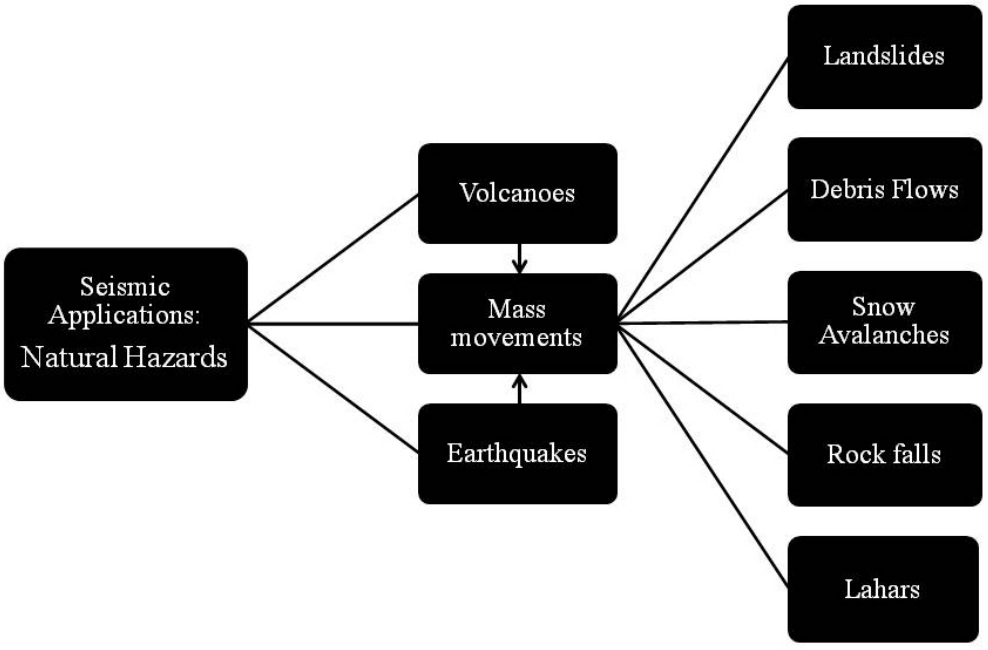

FIGURE 1.1: Scheme of the main natural hazards such as volcanoes, earthquakes and mass movements monitored by seismic systems.

Rapid mass movements such as landslides, debris flows, rock falls or snow avalanches are periodic phenomena with a daily occurrence in alpine regions. Mass movements can be triggered by climatic factors, different types of erosion, human activity, or inertial accelerations induced by earthquakes or volcanic eruptions. The ground shaking generated by earthquakes may lead to the temporary instability of slopes, releasing different types of mass movements. For example, one of the worst historical earthquake-induced rock and snow avalanche disasters occurred in the mountains of central Peru in 1970. The earthquake of M7.7 triggered 50-100 million m^3 of rock, ice and snow that travelled very fast downhill burying villages and

killing 30,000 people instantly (Plafker et al., 1971). Recently, on 25th April 2015, a large M7.8 earthquake shook the centre of Nepal and was followed by a series of M>6 aftershocks. The sequence of earthquakes caused more than 7,000 fatalities, and damaged or completely destroyed entire villages. Additionally, these earthquakes induced thousands of landslides (Collins and Jibson, 2015) in the extremely abrupt topography of Nepal which were responsible for hundreds of fatalities, and blocked numerous roads and trails that connected villages (Figure 1.2a). The first earthquake also triggered a huge snow avalanche that hit the Everest Base camp (Figure 1.2b and c) causing the deadliest day in Everest history with 24 deaths and more than 60 injuries (Aydan and Ulusay, 2015) .

At present, mass movements are monitored using local seismic arrays installed on numerous slopes worldwide. Seismic sensors are very well suited for remote detection of hazardous mass movements since each one generates a characteristic seismic and acoustic wavefield. The local seismic networks installed at volcanoes, in spite of be installed to detect the seismicity induced by volcanism, are also suitable for recording volcanic flow events such as lahars (e.g. Johnson and Palma, 2015; Vázquez et al., 2016) or pyroclastic flows (e.g. Uhira et al., 1994), as well as non-volcanic processes such as icequakes (e.g. Chaput et al., 2015), rockfalls (e.g. Hibert et al., 2011), rock-ice avalanches (e.g. Schneider et al., 2010) or landslides (e.g. Brodsky et al., 2003).

Landslides generate seismic waves by both shearing and loading the surface as the mass moves down in a slope (e.g. Brodsky et al., 2003). A review of several historical cases of seismic events associated with landslides is documented in Weichert et al. (1994). The amplitude of the seismic waves is proportional to the force dropped during the landslide. Hence, the seismic signals of landslides can be used to estimate and calibrate dynamical parameters used to characterize the flow (e.g. Brodsky et al., 2003; Favreau et al., 2010). In this regard, this result has significant importance as seismic recordings are usually the only dataset available of large landslides (Favreau et al., 2010).

Apart from landslides, the passage of a debris flow over seismic sensors can be clearly identified in the seismic recordings, as well as their internal surges (Arattano and Moia, 1999; Marchi et al., 2002; Arattano and Marchi, 2005; Kogelnig et al., 2011a). Debris flows also generate characteristic signals in the low-frequency infrasonic spectrum which are detectable thousands of kilometrers from the source. Kogelnig et al. (2011a) correlated infrasonic and seismic waves to characterize the

flow behaviour at the Illgraben torrent (Switzerland). At the same test-site, geophones were installed in the upper catchment to detect ground vibrations from the ongoing debris flow (Badoux et al., 2009). Then, an automatic alarm system is triggered if a predefined threshold value is exceeded (Sättele et al., 2013, 2015).

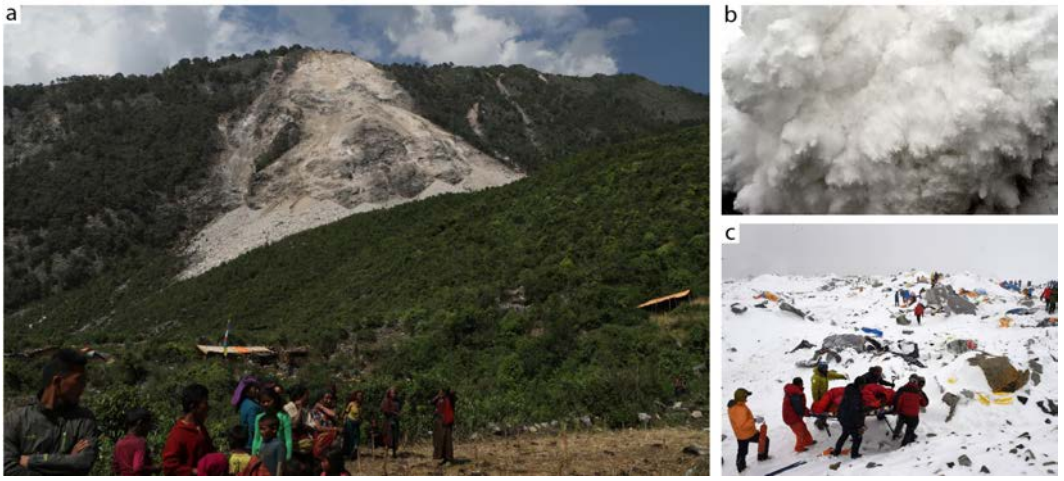

FIGURE 1.2: a) Landslide triggered by one of the aftershocks of the Nepal earthquake on 25th April 2015 (photo taken from Collins and Jibson (2015)). b) Picture of the powder cloud of the avalanche triggered by the M 7.8 earthquake in Nepal, moments before it hit the Everest Base Camp (photo taken from http://www.telegraph.co.uk/news/worldnews/asia/nepal/ (2016, March, 22)) c) Picture of the Everest Base Camp after the snow avalanche hit the site and destroyed the tents, killing 24 people and causing more than 60 injuries (photo taken from http://www.independent.co.uk/news/world/asia (2016, March, 22)).

Rockfalls are one of the most common consequences of slope instability in mountain areas. All the rockfall phases can be detected using seismic measurements providing valuable information on the characteristics of the source (Vilajosana et al., 2008; Deparis et al., 2008). Thus, seismic networks have been specifically installed to monitor and predict rockfall events (e.g. Spillmann, 2007; Lacroix and Helmstetter, 2011; Moore et al., 2011). Vilajosana et al. (2008) demonstrated that seismic measurements are very well suited to detect, localize and determine the size of rockfall events via estimating the seismic energy. Using the methodology proposed by Vilajosana et al. (2008), Hibert et al. (2011) estimated the volumes of hundreds of rockfalls seismically detected within a volcanic crater.

Additionally, in the recent decades, seismic methods have been employed in all the different branches of snow avalanche research as an indirect method to study or detect them. A review of the current applications of seismic methods to study

avalanche formation and dynamics, and to monitor and detect avalanches, are detailed in the following sections.

1.3 Using seismic methods to study avalanche formation

Snow avalanches are fast gravity-driven masses of snow flowing down mountain slopes. They are initiated when the snow cover becomes unstable and starts moving downwards. Favourable conditions for avalanche formation depend on the characteristics of the terrain, the meteorological conditions and the existence of large snow depths over weak layers. Common factors leading to natural avalanche release are loading by precipitation or snowdrift and warming (e.g. Schweizer et al., 2003). Generally, natural avalanche release occurs during or immediately after storms, when large accumulations of snow are the result of precipitation and wind transportation. In springtime conditions, solar radiation and temperature are the most important triggering factors. The snow cover stratigraphy, however, is the key contributing factor to avalanche formation (Schweizer et al., 2003). The existence of a weak layer, often consisting of a depth hoar and faceted crystals (Schweizer and Jamieson, 2001), beneath a cohesive slab is a prerequisite for slab avalanche release.

At present, it is impossible to predict exactly the location, in space and time, of an avalanche release (Van Herwijnen and Schweizer, 2011a). In an attempt to record signals preceding an avalanche release, different monitoring systems consisting in acoustic and seismic sensors have been used to date.

1.3.1 Seismic methods used to asses avalanche triggering mechanisms

Since the formation and propagation of cracks within a material is accompanied by the release of elastic energy generating acoustic signals (Lockner, 1993), recording these emissions from a natural snow cover can be used as a valuable aid in avalanche forecasting (St Lawrence and Williams, 1976; Sommerfeld and

Gubler, 1983; Van Herwijnen and Schweizer, 2011b). Acoustic signals in the ultrasonic range (> 10 kHz) are generally originated from micro-cracks, while large-scale cracking and crack propagation also generates low-frequency signals (< 100 Hz). Pioneering seismic arrays of sensors were installed at the starting zone of avalanches in order to detect acoustic precursory signals to spontaneous avalanche release (St Lawrence and Williams, 1976; Sommerfeld and Gubler, 1983). Seismic monitoring systems installed recently with the same purpose (Van Herwijnen and Schweizer, 2011b,a) show that the fracture propagation through the failure layer is recorded before spontaneous snow-slab avalanches. Identifying precursory acoustic signals, however, is not always possible due to the high background noise at low frequencies (Van Herwijnen and Schweizer, 2011b).

For avalanches triggered artificially, the external trigger induces localized deformations which are large enough to initiate a failure within the weak layer (Van Herwijnen and Jamieson, 2005). Typical external triggering mechanisms include skiers or provoked explosions, and less frequently, earthquakes. Earthquakes generate a high rate of oscillations in normal pressure, shear stress and tensile stress within the snow that may lead to avalanche release (Podolskiy et al., 2010b). The scheme of Figure 1.3 shows the principal changes in the elastic stress field of avalanches due to the vibrations of an earthquake. Experimental results of artificial snow samples subjected to vibrations on a shaking table showed that: i) the inertial forces induced by acceleration can produce fracture within a homogeneous or stratified samples; ii) the stress tensor has shear, tensile and compressive components; and iii) the shear strength of a weak layer is smaller under tensile stress (Podolskiy et al., 2010c). The properties of the snow cover and the magnitude of the stresses induced by the earthquake determine whether the weak layer to fail.

In the literature, only a few cases of earthquakes that induced snow avalanches have been reported to date (Podolskiy et al., 2010b). Most of them were statistically or visually identified, and data on the earthquake accelerations in the avalanche release area and the subsequent avalanche recordings are non-existent. For example, in the Khibiny Mountains (Russia), a statistical study showed that 225 snow avalanches occurred on the same days as mine explosions (Mokrov et al., 2000). Following these observations, the accelerations produced by these explosions were seismically recorded to assess the spatial distribution of the seismic effects on snow stability (Chernouss et al., 2006). Unfortunately, snow avalanches

induced by these explosions were not documented during the experiments. Recently, hundreds of snow avalanches occurred after an earthquake of M6.3 in Japan (Matsushita et al., 2013). In that case, an evaluation of the stability of the snowpack under earthquake vibrations was possible using snow-pit observations and real values of the maximum earthquake acceleration recorded about 4 km away from avalanche release areas.

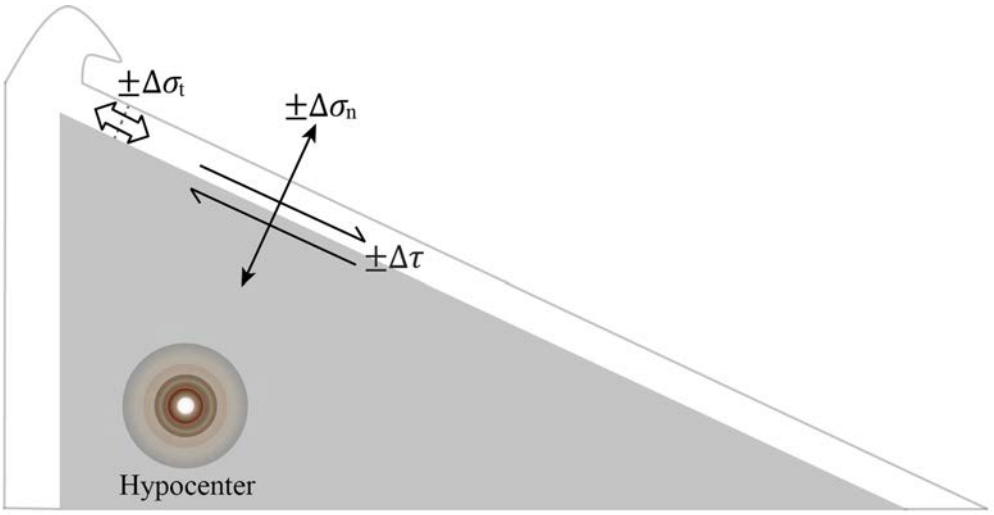

FIGURE 1.3: Scheme of the principal changes in the elastic stress field within the snow cover generated by an earthquake: normal stress (σ_n), tensile stress (σ_t) and shear stress (τ). Picture modified from Podolskiy et al. (2010b).

All the documented cases show the severe consequences of strong ground motions for the induction of failure on the snow-covered mountain slopes. None of previous studies, however, recorded the vibrations at the avalanche release zone, due to the scarcity of seismic sensors in these remote areas, where accelerations could also be amplified due to site effects. To evaluate these events, seismic sensors should be installed at or close to avalanche starting zones in seismically active zones. Quantifying the effectiveness of these types of triggering, by relating magnitude and snowpack stability, is required as part of earthquake risk assessment.

1.4 Using seismic methods to study avalanche dynamics

1.4.1 New insights into avalanche dynamics

Snow avalanches display a variety of sizes and forms. Flow depths range from 10^1 to 10^2 m, run-out distances from 10 to 10^4 m, flow velocities from 1 to 10^2 ms^{-1}, and masses from 1 to 10^6 t (Issler, 2003). Snow avalanche motion is mainly defined by three independent contributions: the amount of snow, the morphology of the avalanche path and the rheological properties of the snow (Naaim et al., 2013). The overall amount of snow inside an avalanche is the sum of the mass released and the snow entrained along the path. Larger avalanches involve more mass in movement and longer run-out distances, mainly controlled by the entrained mass (Steinkogler et al., 2014).

Depending on the snow temperature and moisture content, snow avalanches exhibit different behaviours, such as a sheared and fluid-like layer, plug flow or a dilute suspended powder cloud (Gauer et al., 2008). Specifically, moist or wet avalanches usually are formed by high-density shallow flows characterized by a slower-plug-like flow regime (Sovilla et al., 2008a; Kern et al., 2009). Experimental measurements have shown that different flow regimes can coexist together within the same avalanche (Sovilla et al., 2008a). For instance, the fast moving dilute front of a powder-snow avalanche evolves to a decelerating dense shear layer and finally, to a plug flow at the tail of the avalanche.

Powder-snow avalanches are often referred as dry-mixed avalanches because the cloud characterizing this kind of flow typically hides a dense flow region. The structure of powder avalanches is usually divided into three main layers (e.g. Turnbull and Bartelt, 2003; Gauer, 2014): the dense layer or avalanche core, the saltation layer and the powder cloud. In the literature, however, there is not currently a unified view of the structure of powder-snow avalanches, mainly because of the lack of experimental information (Hopfinger, 1983; Issler, 2003).

A review of experimental measurements of powder-snow avalanches by Sovilla et al. (2015) recently offered new insight into the structure of powder-snow avalanches. Sovilla et al. (2015) distinguish four regions with different dynamics (Figure 1.4). The avalanche front is a region characterized by its low density, as a result of the

rapid entrainment of a layer of light, cold snow lacking cohesion (#1, Figure 1.4). Maximum speeds are reached by the dilute front characterized by a mean density that is normally less than 10 kgm^{-3} and low maximum impact pressures (up to 100 kPa). A few metres behind the front, an energetic and turbulent stratified layer entrains deeper snow layers (#2, Figure 1.4). This region is characterized by an increase of the turbulence scale with higher average density and impact pressure. Large density and pressure fluctuations oscillate with maximum values up to 400 kgm^{-3} and 1000 kPa.

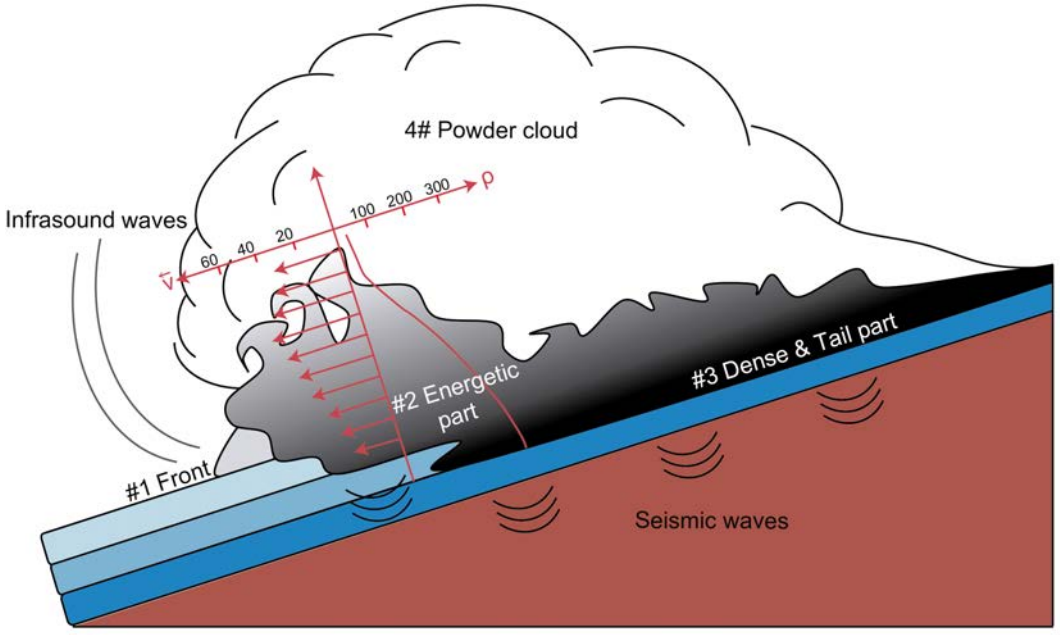

FIGURE 1.4: Structure of a powder-snow avalanche composed of four regions (diagram adapted from Sovilla et al. (2015) and Kogelnig et al. (2011b)): frontal part (#1), energetic part (#2), dense/tail part (#3) and the powder cloud (#4). The seismic waves generated by the avalanche propagate within the snowpack and the ground; the infrasound waves propagate through the air.

Following the faster head consisting of these two regions, the hidden basal layer is composed of a slower and denser layer (#3, Figure 1.4). In this region, density oscillates around a higher average value (typically of 250-400 kgm^{-3}) decreasing along the tail and superimposed with higher density peaks caused by well-formed granules. The pressure signal decrease and becomes steadier in the dense part (up to 400 kPa) superimposed with rapid pressure fluctuations that reveal the presence of larger granules (Sovilla et al., 2015). Finally, enveloping the whole avalanche, a powder cloud of small particles suspended by turbulent eddies of air can reach heights of hundred metres (#4, Figure 1.4).

The structure of wet-snow avalanches can be simplified from those of powder-snow avalanches to a granular dense layer. No turbulent cloud of suspended material is present during the motion of a wet avalanche. The topography strongly influences the movement of a wet flow, which normally spreads out laterally following small irregularities in the terrain (Sovilla et al., 2012).

1.4.2 Snow avalanches as sources of seismic and infrasonic waves

Snow avalanches are extended and moving sources of infrasonic and seismic waves. The complex wavefield is mainly generated by the interaction of the flow with its environment, i.e., the air, the snow cover and/or the ground when the avalanche slides directly over it, as well as, with terrain features and possible obstacles (Figure 1.4). Furthermore, the number of sources is variable, as avalanches entrain and deposit mass along their track.

Firstov et al. (1992) were some of the first researchers that studied the signals generated by avalanches. They postulated that the seismic signals are mainly generated by the dense and leading part of the avalanche; whereas the infrasound is generated by the turbulent snow-air flow (powder cloud) characteristic of dry avalanches. Moreover, earlier studies of seismic signals of avalanches provided strong evidence of internal surges within avalanches (Schaerer and Salway, 1980).

Subsequent studies of avalanche seismic signals have mainly been conducted by the snow avalanche group of the University of Barcelona (UB) since 1994, and since 2008, studies of avalanche infrasound signals have been also included. During the first stage, the studies focused on the characterization of seismic signals of avalanches triggered artificially in order to gain a better understanding of the seismic sources of avalanches. Synchronized recordings of the seismic signals and video images led to the conclusion that the sources of the seismic signals correspond to changes in the slope, interaction with obstacles and phenomena associated with the stopping phase (Sabot et al., 1998; Suriñach et al., 2000, 2001). At the same time, other studies carried out by Nishimura and Izumi (1997) suggested that the seismic signals are induced by the violent flow of the dense part of a snow avalanche, in agreement with Firstov et al. (1992).

Further comparisons of avalanche seismic signals with frequency modulated radar signals demonstrated that typically, the largest seismic amplitudes correspond to the breaking of the snow layers, i.e., the erosion of the snow cover and the entrainment of the snow layers (Biescas, 2003; Sovilla, 2004). The most energetic seismic peaks do not necessarily correspond to the largest avalanche depths and the highest intensities of the radar signals. Subsequent studies corroborated that the main sources of the seismic signals of avalanches corresponds to basal friction and ploughing at the avalanche front (Vilajosana et al., 2007b).

In recent years, the UB avalanche research group has recorded numerous infrasound and seismic signals emitted by avalanches of varying dimensions and flow regimes (Kogelnig et al., 2011b). The analysis of these signals has showed that the interaction of the external suspension and turbulent layers of the avalanche mainly generates the infrasound signal; whereas the main sources of the seismic energy are the basal friction produced by the dense body inside the flow in contact with the ground or snow cover.

1.4.3 Seismic methods and avalanche dynamics

One of the main goals of studying the seismic signals generated by avalanches is essentially to improve our understanding of avalanche dynamics. Firstly, seismic methods have been demonstrated to be valid for estimating dynamical parameters such as avalanche speed. The earliest studies of avalanche speed estimation based on seismic methods include works by Schaerer and Salway (1980) and Nishimura and Izumi (1997), who used basic picking techniques to obtain the arrival time of the avalanche over geophones along the avalanche path. More sophisticated methods for inferring avalanche speed were proposed by Vilajosana et al. (2007a), which used cross-correlation analysis of avalanche seismic signals, and by Lacroix et al. (2012), which applied a beam-forming seismic method.

Despite most of the kinetic energy of an avalanche being expended by internal processes, part of this kinetic energy is expended in overcoming the resistance exerted by the avalanche- sliding surface (Vilajosana, 2008). Part of this energy loss due to friction during avalanche motion is thus converted into seismic waves and heat. Vilajosana et al. (2007b) quantified the seismic energy transmitted into the ground. As this energy is proportional to the overall avalanche mass, the methodology presented may be used as an empirical method to classify avalanche size.

This method, however, requires a priori seismic characterization of the site and the knowledge of the avalanche location. Previous comparative studies between the seismic signals of avalanches of different sizes showed that the maximum amplitudes generated depend on the avalanche size (Suriñach et al., 2001; Biescas et al., 2003). These preliminary results showed the feasibility of using seismic methods to estimate avalanche size.

Seismic energy not only depends on the avalanche size, but also on the type of flow regime. Biescas et al. (2003) compared avalanches of the same run-out, i.e. same size, and showed that wet-snow avalanches generate seismic signals that are larger than those generated by powder-snow avalanches, probably due to the higher density of the mass involved. Vilajosana et al. (2007b) also showed that a large dry/dense avalanche dissipated slightly higher energy than a powder-snow avalanche of the same size. The differences were attributed to each flow regime, and also as a suggestion, to different snow cover depths along the path. However, an estimation of the avalanche seismic energy absorbed by the snow cover interface was not previously quantified. This is a requirement to obtain accurate energy estimations and thus to correlate with avalanche size and type.

Distinguishing between avalanche flow types can also be feasible not only because of the differences in the seismic amplitudes and thus, in the energy dissipated. The duration and shape of the seismograms are likely to depend on the avalanche type (Suriñach et al., 2001; Biescas et al., 2003). Wet-snow avalanches generate much longer seismic signals characterized by a long coda; whereas the signals of dry/mixed avalanches are much shorter (Biescas et al., 2003). The complementariness of seismic and infrasound signals also showed advantages in the distinction between flow regimes. Different types of flow have unique sensitivities in terms of the infrasound or seismic recordings. Kogelnig et al. (2011b) showed that powder-snow avalanches generate much larger infrasound amplitudes than wet avalanches. Avalanches can also change from a powder part in the upper part of the path to evolve to a wet flow as moist snow is entrained in the lower part of the path. This change in flow behaviour is observable in the infrasound signal as a strong decrease in the amplitudes (Kogelnig et al., 2011b) .

All the previous studies have qualitatively shown differences of the seismic signals depending on avalanche type and size. Quantifying these signatures is necessary to automatically recognize the type of avalanche flow or its size. Possible relationships between avalanche size and flow type might reflect the reproducibility of

the previous observations and be useful for characterizing avalanches. Such data is indispensable as seismic recordings are the only data available when avalanches are triggered in poor visibility conditions and they are not recorded by other instrumentation.

1.5 Seismic monitoring systems of avalanches

Over the last 20 years, seismic monitoring systems of snow avalanches have been deployed by several research groups. Although these monitoring systems were installed in most of the cases for research purposes, the results have proved adequate as automatic detection systems.

The first seismic systems to automatically detect avalanches were operative in the second half of the 1990s (Leprettre et al., 1996, 1998). Those systems also recorded a variety of seismic sources such as earthquakes, blasts, footsteps, helicopters or thunder bolts that could be mistaken for avalanches. Automatic recognition of avalanches from other sources based on signal features observed in the time-frequency domain and combined with fuzzy logic resulted in a average success rate of 90%. Subsequent automatic detection systems were based on a classification of events comparing a set of seismic parameters (Bessason et al., 2007). The size of the avalanches could also be estimated from one of these parameters, once the signal of the avalanche was correctly identified. However, the distinction between different types of mass movements in this automatic system was unsatisfactory. Suriñach et al. (2005) showed the reproducibility and similarity of the shape in the time-frequency evolution, i.e. the spectrograms of snow avalanches and other mass movements. These specific signatures of the spectrograms are currently applied to distinguish between common seismic sources on winter slopes (e.g. Biescas et al., 2003; Suriñach et al., 2005; Van Herwijnen and Schweizer, 2011a).

Seismic waves are rapid attenuated with distance, giving rise to a natural limit of detection of the signals generated. The range of detection of seismic systems varies depending on the characteristics of the avalanche path (length, terrain features and snow cover), the typical dimensions, the flow type and possible site effects, which may amplify or deamplify the seismic waves. The effective range of different seismic detection systems was about 3-6 km (Leprettre et al., 1998) or 2 km for small avalanches with a volume of about 10^3 m^3 (Biescas et al., 2003). Seismic

networks installed recently have shown the validity of these systems to detect avalanches as small as only a few metres of run-out distance up to a distant of 1 km (Van Herwijnen and Schweizer, 2011b).

Infrasonic waves travelling though the atmosphere are less affected by the travel path and the attenuation is practically negligible at local distances (Kogelnig et al., 2011b). Hence, infrasound monitoring systems have increased rapidly over recent years (e.g. Scott et al., 2007; Ulivieri et al., 2011; Kogelnig et al., 2011b; Thüring et al., 2015). Automatic identification of snow avalanches based on infrasonic waveform, however, can be extremely ambiguous and still requires further research (Marchetti et al., 2015).

Automatic seismic detection of avalanches would provide key information for a proper validation of avalanche forecast models. Inferring other parameters such as avalanche flow regime, volume, or run-out distance would improve future automatic systems in order to classify avalanche data without additional information.

1.6 Contents and goals of the study

The main goal of this study is to enlarge the current contributions of seismic methods to avalanche research, and to extend their applicability to avalanche monitoring systems. This study focuses on two main issues in the avalanche research field: 1) avalanche triggering mechanisms; and 2) inferring dynamic parameters and avalanche characteristics. In the research field of avalanche formation, only a few cases of earthquake-triggered snow avalanches have been documented to date. In this regard, real seismic recordings in order to quantify the effects of different earthquakes affecting different snowpack stability conditions were treated. In the research field of avalanche dynamics, a proper quantification of the seismic intensity of snow avalanches can be used to infer dynamic characteristics. This demands the identification of relevant seismic signatures for different types and sizes of avalanches. Consequently, avalanche seismic data were compared with other types of data to connect the avalanche flow regimes and the main dynamical processes with the seismic signals generated. The quantification of varying avalanche seismic signals is presented as a valuable tool for avalanche classification.

To achieve my goal, I tackle the following objectives:

1. Identification of the avalanche dynamic processes which generate the seismic wavefield and the sources of the seismic signals.

2. Parameterization of the seismic signals generated to infer avalanche flow regimes and avalanche size.

3. Assessment and quantification of the possibility of snow avalanches being induced by earthquakes.

4. Quantification of the effects of the snow cover in the detection of avalanche seismic signals.

These objectives were treated widely in two peer-reviewed journal articles. In this thesis, however, the content of these articles has been included with complementary information in a large volume of greater utility to the scientific community. Thereby, the characteristics of the test site and the instrumentation deployed to monitor snow avalanches are described in Chapter 2. In Chapter 3 a seismic characterization of the site is presented. This is a requirement previous to the quantification of the avalanche seismic signals. The procedure of analysis of the avalanche data (seismic signals, infrasound signals and radar data) are explained in the methodology in Chapter 4. The main results of the thesis are included separately in two chapters that corresponds to the applications of the seismic methods to the study of avalanche formation (Chapter 5) and the application of the methods to the study of avalanche dynamics (Chapter 6). In Chapter 5, an avalanche possibly triggered by an earthquake is compared with other non-avalanche-released earthquakes. The joint analysis of seismic, infrasound, radar, and weather data, as well as snow cover simulations, is used to characterize the avalanche flow and quantify the effects of the earthquake within the snow cover. A comprehensive analysis of these results has been published in the article *Evaluation of an avalanche possibly triggered by an earthquake at Vallée de la Sionne, Switzerland* (Pérez-Guillén et al., 2014). In Chapter 6, the results of a comparative study between the seismic signals and the signals acquired with two frequency-modulated radars of 32 avalanches is presented. As a contribution to the study of avalanche dynamics, a set of seismic indices was defined. Hence, the parameterization of the avalanche signals using these indices allows to infer avalanche characteristics. All these results have been published in the article *Deducing avalanche size and flow regimes from seismic measurements* (Pérez-Guillén et al., 2016). In both chapters, additional data are also included. The main conclusions of each chapter of results

are included at the end of the respective chapter, as each part has contributed to different branches of avalanche research. Finally, a discussion on the main results and conclusions of this PhD study, addressing the further needs and the possible future applications, is presented in two different chapters (Chapters 7 and 8).

Chapter 2

Vallée de la Sionne test site

All the data analyzed in this PhD study were acquired at the Vallée de la Sionne (VdlS) test site in Switzerland. In this chapter, I present the main characteristics of VdlS, the instrumentation deployed and the seismic and infrasound data treatment.

2.1 Introduction

The full-scale test site of Vallée de la Sionne (VdlS) in Switzerland was built in 1997 by the WSL Swiss Federal Institute for Snow and Avalanche Research SLF to investigate snow avalanche dynamics (Issler, 1999). VdlS is situated to the north of Sion (Switzerland) in the central Valais area (Figure 2.1). The test site was established to study physical processes in avalanches, to improve existing avalanche dynamic models, to develop new models and to determine the forces exerted by snow avalanches on different structures (Amman, 1999). Nowadays, a set of instruments installed along the main avalanche path provides extensive data on the internal velocity, flow height, and density of the flow at different heights of the avalanche profile, measurements of impact pressure on different obstacles, and volumes in the release and deposited areas (Sovilla et al., 2008b,a, 2013). Numerous international research groups from Switzerland, England, Spain, France and Austria collaborate at the site installing different test equipments which provide additional data for avalanche research.

The snow avalanche group of the University of Barcelona (UB) has been installing seismic stations at VdlS since the test site became operative in 1999. In the period from 1999 to 2003, two seismic stations were installed and more than 30 avalanches of different sizes and types were recorded (Biescas, 2003). During the subsequent winter seasons from 2004 to 2007, the UB snow avalanche group installed the seismic stations at the test site of Ryggfonn in Norway operated by the Norwegian Geotechnical Institute (NGI). In this period of time, a total of 11 avalanches were recorded and new methods of analysis were applied (Vilajosana, 2008). From 2008 until now, the stations were again installed at VdlS, increasing the number of seismic stations and adding infrasound sensors that complement the information extracted from the seismic measurements (Kogelnig, 2012). At present, four seismic stations and one infrasound sensor are installed both within and outside the avalanche path. The stations record in continuous mode. Hence, not only are snow avalanches recorded, but also other seismic and infrasound sources such as earthquakes, explosions, helicopters and airplanes.

In Section 2.2, a detailed description of the avalanche path characteristics at VdlS is presented. All the infrastructure and instruments deployed at VdlS are described in Section 2.3. The characteristics and technical details of the seismic and infrasound sensors installed by the UB snow avalanche group are described in Section 2.4. Finally, seismic and infrasound data treatment is detailed in Section 2.5.

2.2 Characteristics of the test site

Snow avalanches of different types and sizes can be released, naturally or artificially, in three main release areas at different elevations, ranging from 2200 to 2700 m a.s.l.: Pra Roua (PR), Crêta Besse 1 (CB1) and Crêta Besse 2 (CB2). The starting zone covers an extension of 30 ha (Figure 2.1) with mean slopes between 30° and 45° oriented towards easterly to south-easterly direction, which favours snow accumulating over the starting zone due to westerly and north-westerly winds. The total avalanche path length is approximately 2500 m with a vertical drop of 1400 m; the maximum altitude is 2700 m a.s.l. and the minimum is 1300 m a.s.l.

Snow avalanches follow three main paths (indicated with white arrows in Figure 2.1) depending on the release location. The avalanche track consists of two gullies

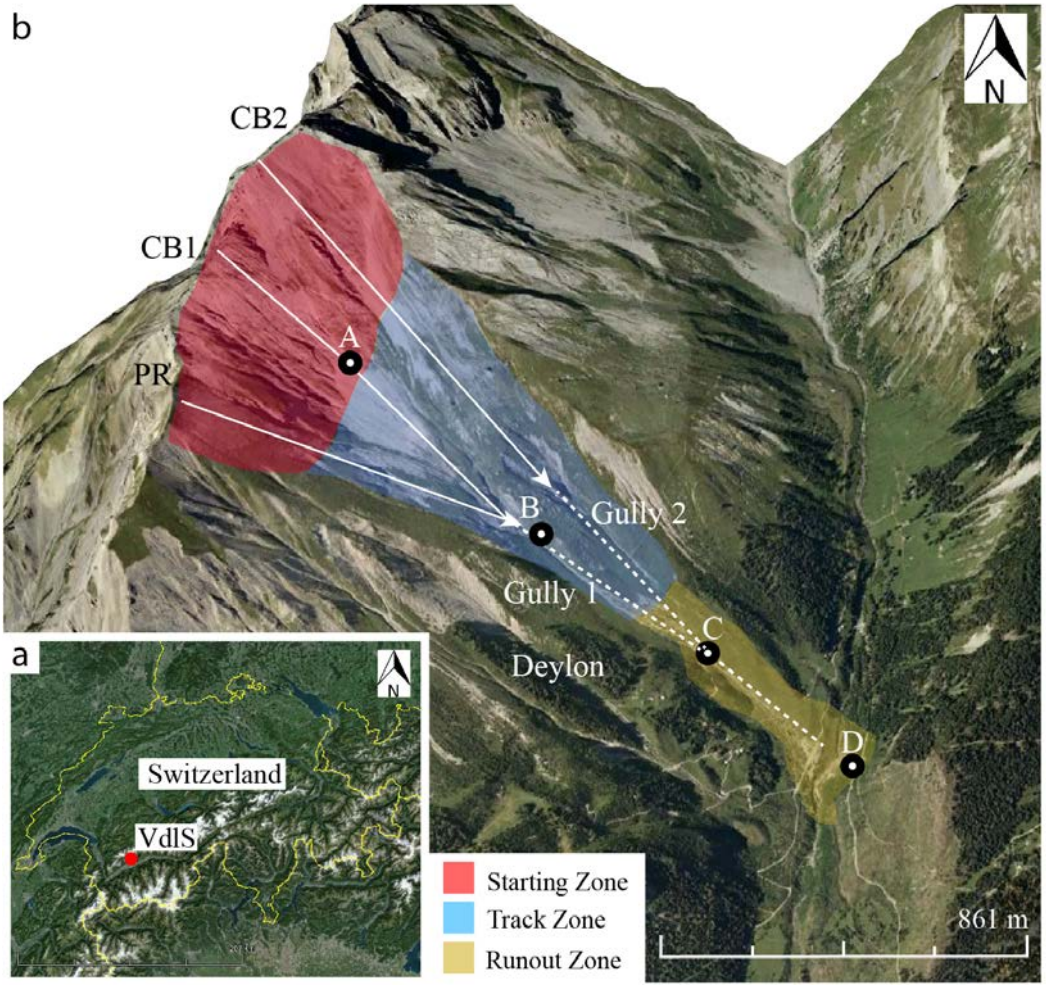

FIGURE 2.1: a) Map of Switzerland with the location of VdlS (source: Google Earth). b) Overview of VdlS (source: Google Earth). Different instrumentation is located at caverns A, B, C and D. Typical avalanche starting zones are indicated as Pra Roua (PR), Crêta Besse 1 (CB1) and Crêta Besse 2 (CB2). Black arrows show the main directions that avalanches initiated in the starting zone follow before reaching the channelled area, referred to as gully 1 and gully 2, in the track zone. Part of the mass of the avalanches released at PR can also flow along the channelled part of Deylon. The black dashed lines show the typical path of the flowing avalanche. VdlS data acquisition systems are located in a shelter near D on the opposite slope.

between 1700 and 1900 m a.s.l. (marked as gully 1 and gully 2 in Figure 2.1). In general, avalanches that start from PR and CB1 follow gully 1; while avalanches starting from CB2 may flow through either gully or both. The paths then converge in a common run-out zone characterized by an open slope with a mean inclination of 20° between 1300 and 1700 m a.s.l. The river *La Sionne* at the bottom of the Valley separates the long run-out zone and the opposite slope where a concrete shelter is situated at D (Figure 2.1) and operates as the instrumented control

centre. At the locations A, B, C and D, different instrumentation described in the following sections is installed inside of caverns (Figure 2.1).

2.3 Instrumentation

An extensive database of avalanches that occurred spontaneously or were triggered artificially in full-scale experiments, has been collected at VdlS since 1999. In order to measure impact pressures, speeds, flow depths and densities, several infrastructures with measurement equipment have been installed close to C in the run-out zone of VdlS at 1650 m a.s.l. (e.g. Schaer and Issler, 2001; Sovilla et al., 2008b; Kern et al., 2009; McElwaine and Turnbull, 2005; Louge et al., 1997) (Figure 2.2). A shelter construction, usually referred to as the bunker, is located on the slope opposite of the avalanche track, near D at 1500 m a.s.l. (Figure 2.1). It operates as the instrument control centre and serves as a data storage centre and protects the following instrumentation:

- Dual frequency pulsed Doppler radar system. This transmits short pulses of microwave energy and analyses the received echoes reflected from the dense and the powder part of an avalanche (Rammer et al., 2007).

- Frequency Modulated Continuous Wave Phased Array radar (henceforth referred to as the GEODAR radar) (Vriend et al., 2013; Ash et al., 2014). It can track the avalanche over the whole slope with a downslope spatial resolution of 0.75 m, and gives information on avalanche position, velocity and size. The technical specifications are described in Ash et al. (2010).

Along the main path of the avalanche, three pairs of FMCW radars (Gubler and Hiller, 1984) are buried in the track, the first at 2300 m a.s.l. (location A in Figure 2.1), the second at 1900 m a.s.l. (location B in Figure 2.1) and the third just above the instrumented area at 1650 m a.s.l. The radars provide local velocity profile measurements (Amman, 1999), and also serve to determine erosion (where and how much snow cover is eroded), flow depth distribution and mass deposition (Sovilla and Bartelt, 2002).

In order to determine the mass balance of an avalanche, air-borne laser scans (ALS) are usually performed to supplement the photogrammetric measurements

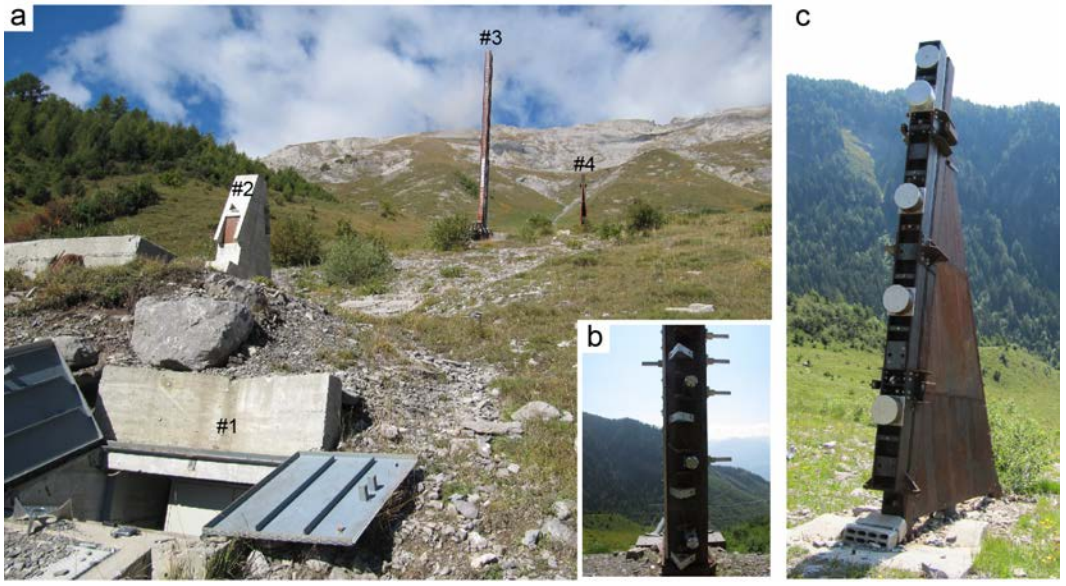

FIGURE 2.2: a) View of VdlS instrumented area near cavern C showing (from bottom to top): cavern C (#1), the small impact wall (#2), the pylon (#3) and the keil/narrow wedge (#4). b) Close up of the pressure and optical sensors mounted in the mast. c) Narrow wedge equipped with high-frequency load cells.

of snow depth in avalanche experiments (Sovilla et al., 2010). ALS measurements can be taken of the entire avalanche path with a horizontal spatial resolution of 500 mm and a vertical accuracy of 100 mm resulting in a high-resolution digital model of the snow (Sovilla et al., 2013).

Information on the snow conditions is obtained manually by digging snow pits in the avalanche path or from five automatic weather stations: three located close to the avalanche path and two at lower elevations (Sovilla et al., 2013). Data acquired from these weather stations serves as input data for snow cover models such as SNOWPACK and Alpine3D (Lehning and Fierz, 2008; Lehning et al., 2006) and allows reconstruction of the distribution of the snow cover and its properties at different locations along the avalanche path.

Three underground caverns have been built (a few metres from the FMCW radar locations) along the main avalanche path at A, B and C, and are provided with data acquisition computers (Figure 2.1). The local computers are linked, through a central backbone containing a fibre optic network, to the central data storage system located in the shelter. Different seismic stations have also been installed inside these caverns by the UB snow avalanche group. Details of the characteristics of these stations are given in the next section.

Numerous experiments consisting of snow avalanches triggered artificially by explosive charges have been performed by the SLF group and their partners from other European countries. In the case of spontaneously released avalanches, a special triggering system that uses seismic sensors positioned at points close to the release area initiate the whole data acquisition system. The system includes two seismic stations, MS2003 Syscom, of three-component seismometer located inside caverns A and B (Amman, 1999) (Figure 2.1). All the installed instrumentation is connected to the triggering system with a common time base, which allows all measurements to be synchronized with a time precision of ± 1 s. The system is triggered when the seismic signal exceeds the threshold of 50 ms^{-1}.

2.4 UB Seismic and infrasound equipment

The UB snow avalanche group has deployed several seismic and infrasound stations at VdlS. The data are used to measure the ground velocity and the air pressure generated by snow avalanches. These are non-invasive methods that detect the interaction of the different parts of the avalanche with the snow cover and terrain (erosion, impacts on the ground and changes of air pressure), and they are sensitive to the different flow regimes, types of snow and avalanche dimensions (Suriñach et al., 2000, 2001; Vilajosana et al., 2007b; Biescas et al., 2003; Kogelnig et al., 2011b).

VdlS is an ideal place to locate the stations in strategic locations of the avalanche path. The already existing VdlS infrastructure allowed the installation of the sensors inside several caverns (Figure 2.3) located at the avalanche starting zone (cavern A), the track zone (cavern B), the deposition area (cavern C) and on the slope opposite the avalanche path and close to the shelter (cavern D). All the caverns are provided with a power supply and connected to a computer network which facilitated the installation of the instruments and reduced equipment costs. The coordinates of the stations and the distances from each station to the top of CB1 are given in Table 2.1. The number of stations installed by the UB group has increased in over the years and the characteristics of them have improved since the first winter season. All the seismic and infrasound sensors are installed before the winter season and uninstalled for the summer. The characteristics of the seismic and infrasound stations deployed by the UB at the site for each winter season are given in Table 2.2.

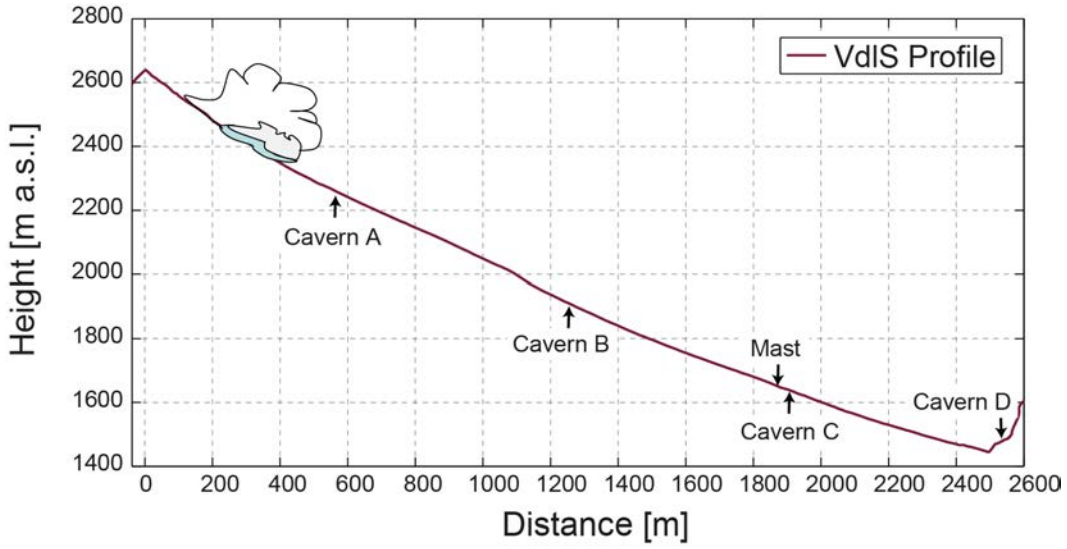

FIGURE 2.3: Main profile of the VdlS avalanche path (from CB1 release area, following gully 1 to cavern D). Several seismic stations are installed inside caverns A, B and C, and other seismic and infrasound sensors are installed in cavern D. The instrumented mast is located close to cavern C.

TABLE 2.1: Coordinates of the caverns where the seismic stations are installed and the linear distances from the top of CB1 to each station following the main profile of the avalanche path of Figure 2.3.

Cavern	Coordinates	Distance [m]
A	46.3007 ° N 7.3574 ° E 2250 m a.s.l.	581
B	46.2974 ° N 7.3637 ° E 1903 m a.s.l	1267
C	46.2948 ° N 7.3708 ° E 1640 m a.s.l	1901
D	46.2932 ° N 7.3770 ° E 1441 m a.s.l	2562

For the winter seasons from 1999 to 2003, two seismic stations were installed in caverns B and D (Figures 2.1 and 2.3) and a data logger with three channels PDAS (Teledyne-Geotech) or Orion (Nanometrics) and two different types of sensors (see Table 2.2 for details). The installation of these stations is reported in Biescas (2003). The current configuration of the seismic and infrasound sensors, from winter 2013 to now (winter 2015), follows a linear distribution of sensors located inside and outside of the usual avalanche path. The following sensors are installed inside the caverns:

- Cavern A (2300 m a.s.l.): data acquisition system SpiderNano (three channels) with a three-component seismometer, Miniseismonitor (eigenfrequency of 2 Hz sensitivity of 500/6 Vsm^{-1}) (Figure 2.4a).

- Cavern B (1900 m a.s.l.): data acquisition system REFTEK DAS-130-01 (six channels) with a three-component seismometer, Mark L-4C-3D (eigenfrequency of 1 Hz and sensitivity of 280 Vsm^{-1}) (Figure 2.4b).

- Cavern C (1640 m a.s.l.): data acquisition system REFTEK DAS-130-01 with a three-component seismometer, Mark L4-3D, and a three-component broad band seismometer, Lennartz 3D/20s (eigenfrequency of 0.05 Hz and sensitivity of 1000 Vsm^{-1}).

- Cavern D (1500 m a.s.l.): data acquisition system REFTEK DAS-130-01 with a three-component seismometer, Mark L4-3D, and an infrasound sensor, Chaparral Model 24 (eigenfrequency of 0.1 Hz and sensitivity of 2 VPa^{-1}; Figure 2.4c).

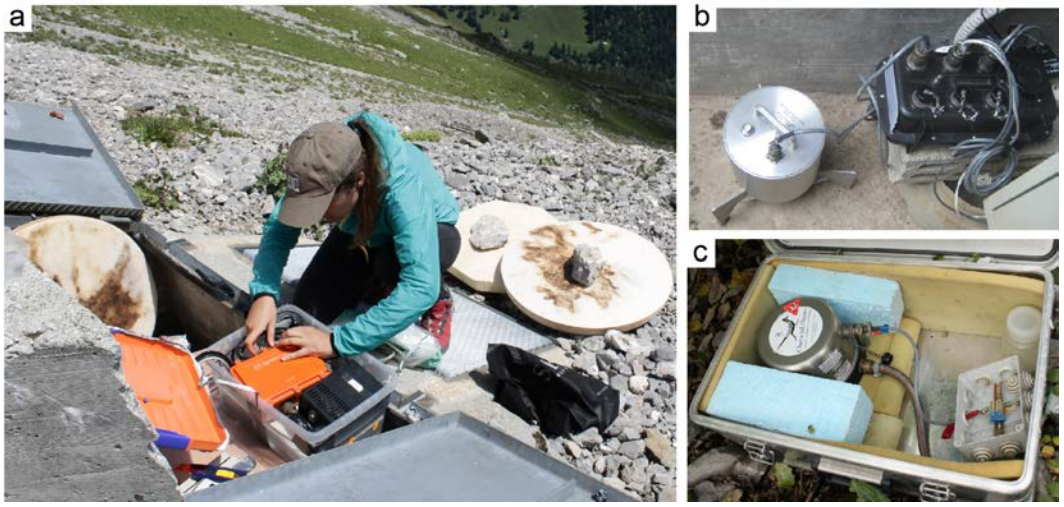

FIGURE 2.4: a) Image of the SpiderNano seismic station installation in the release area of the avalanche, inside cavern A. b) Image of the REFTEK DAS-130 data acquisition system and the Mark L-4C-3D seismometer at cavern B. c) Image of the Chaparral infrasound sensor installed inside a metallic box and connected to the garden hose near cavern D.

.

The sensors and the data acquisition systems in caverns A, B and C are installed together inside the cavern (Figure 2.4a and b); whereas the sensor in cavern D is located directly on the ground, and connected with the data acquisition system situated inside the shelter (Figure 2.5). All the seismometers were levelled and north-south oriented. They were positioned over specifically designed metallic platforms which provide good coupling with the ground (Figure 2.4b). The

TABLE 2.2: Type of station and sensor installed by the UB group in caverns A, B, C and D at VdlS from the first winter season up until the present. In the winter season 2014-2015, there were no data recorded by the Spider station.

Season	Location	Data Logger	Sensor
1998 - 1999	B D	PDAS	Lennartz 3D/5s
1999-2000	D	PDAS	Lennartz 3D-5s
2000-2001	D	Orion	Mark L-4C-3D
2001 - 2003	B D	Orion	Mark L-4C-3D
2008 - 2009	B D	REFTEK	Mark L-4C-3D
2009 - 2013	B C D	REFTEK	Mark L-4C-3D Mark L-4C-3D; Chaparral
2013 - 2016	A B C D	Spider REFTEK	Miniseismonitor Mark L-4C-3D Mark L-4C-3D; Lennartz 3D/20s Mark L-4C-3D; Chaparral

infrasound sensor was connected to a porous garden hose setup, which acted as a spatial wind noise reduction system (Kogelnig, 2012).

The data acquisition system (REFTEK DAS-130; Figure 2.4b) has two-channel input connectors on each of the three channels, a power connector, a net connector, a GPS connector and a control connector. All the acquisition systems are connected using fibre optic cables to the server and to the VdlS external triggering system. The data acquired by the stations are recorded in parallel in two different streams: a continuous stream with a sampling rate of 100 sps and an external triggering stream with a sampling rate of 200 sps that starts recording when the VdlS alarm system is triggered. The external triggering stream was programmed for a time window of 700 s with a pre-trigger window of 60 s. This time window is long enough to record the largest avalanches which have seismic signals with durations up to 600 s.

Most of the instrumentation at VdlS starts data acquisition when the VdlS seismic alarm system is triggered. This system is triggered when an avalanche is moving close to the triggering stations located at caverns A and B. Hence, the system starts recording with a time delay with regard to the beginning of the avalanche.

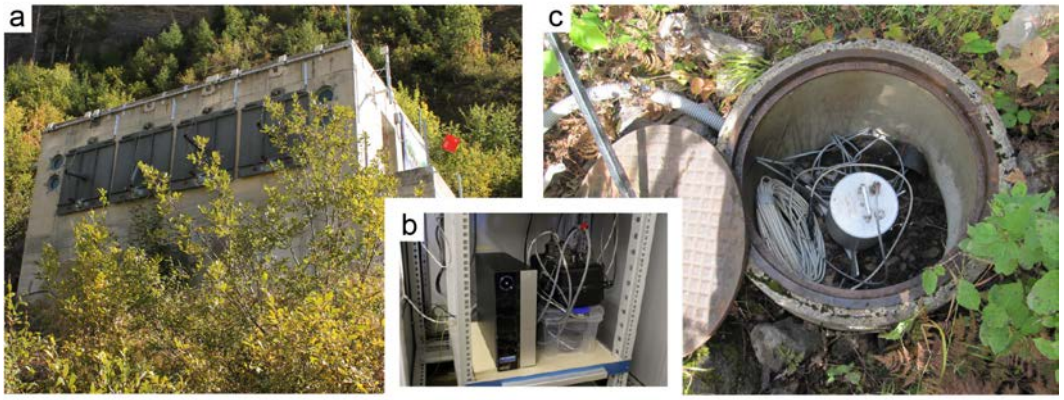

FIGURE 2.5: a) Shelter (bunker) that operates as the instrument control centre and serves as a data storage centre located on the slope opposite of the avalanche path. b) Server and data acquisition system (REFTEK DAS-130) installed inside the shelter. c) Mark L-4C-3D seismic sensor installed directly on the ground at cavern D and connected to the data acquisition inside the shelter.

.

This is not a problem for the UB stations as they record data continuously nor for any of the measurements acquired in lower parts of the avalanche track, i.e., in the instrumented area close to cavern C. Furthermore, the trigger recording mode of the UB stations is programmed with a pre-trigger window length of 60 s that is usually enough to capture the first movements of the avalanche. If the trigger system has a very long delay, the data acquired continuously warrants that the entire seismic signal generated by the avalanche is recorded. Additionally, other seismic and infrasound sources such as earthquakes or explosions, useful for this research, are also recorded in the continuous stream.

Access to the caverns during the winter is impossible because several meters of snow usually cover them and due to the risk involved in walking in an avalanche hazard area. To control the functioning of the stations and download the data, the stations are connected to the VdlS network. Each station with an assigned static IP is connected by TCP/IP communication protocol to the UB server located in the shelter (Figure 2.5b). Data are downloaded remotely from the UB via FTP connection to the server.

2.5 Seismic and infrasound data treatment

Data from different seasons have been acquired with different types of instrumentation. In order to compare all the data, the raw data are processed and converted into physical parameters (ground velocity, m/s; and air pressure, Pa) using the appropriate transfer functions. The data logger output signal is given in counts. The amplitude must be converted first to volts and then to ground motion (m/s). One count value is obtained from the ratio between the full scale (FS) of the data logger (10 V) and the maximum resolution (48 Mb), which in the case of the REFTEK data logger is:

$$1count = \frac{10}{6291456} Volts \tag{2.1}$$

The transfer functions for the first data loggers used in seasons before 2010 are detailed in Biescas (2003) and for the SpiderNano data logger:

$$1count = \frac{5}{2^{24}} Volts \tag{2.2}$$

The transfer function values are then corrected by the voltage output of the seismometers, e.g., 280 Vsm^{-1} for the Mark L-4C-3D; and the voltage output of the infrasound sensor, e.g., $2VPa^{-1}$ for the Chaparral. Subsequently, two signal preprocessing techniques are used to correct the trend and the offset of the signals. All the signals are filtered, with a 4th-order Butterworth band-pass filter, from 1 Hz (eigenfrequency) to a frequency below to the frequency of Nyquist (45 Hz for avalanches sampled at 100 sps; 90 Hz for avalanches sampled at 200 sps). Earlier works recorded the snow avalanche signals with a sample rate of 100 sps (Biescas, 2003; Kogelnig et al., 2011b). In this work, the sample rate of the trigger stream from the upper stations has been increased to 200 sps in order to capture a higher frequency spectrum. Maximum energies of the snow avalanches are usually concentrated below 40 Hz. However, depending on the type of snow avalanche, part of the seismic energy can be in the frequency spectrum over 40 Hz. This will be further analysed in the following chapters. All the data processing was carried out in MATLAB using different developed scripts.

Chapter 3

Seismic site characterization

In the present chapter, I deal with the main local site and path effects affecting on avalanche seismic data in order to facilitate correct interpretation of the avalanche seismic signals in later chapters. Additionally, I address several issues regarding to the time fit between the data from the stations and the background noise level analysis before an avalanche release.

3.1 Introduction

Previous to the analysis of the seismic signals generated by snow avalanches, different phenomena affecting the wave field propagation should be considered. The seismogram recorded at a given site is the convolution of the source (type and size of avalanche), path effect (attenuation of the waves) and site effect (local amplification or deamplification of the waves). Typically, a great variety of seismic sources are recorded at the UB seismic stations at VdlS. Besides snow avalanches, the most common sources of seismic waves are earthquakes, explosions, helicopters, planes and meteorological phenomena. Each type of source generates a characteristic wave field. The triggering of the VdlS alarm system, and a posteriori comparison of the data acquired with the different instrumentation, allows snow avalanche events to be easily recognized.

The generated seismic waves of an avalanche are attenuated with distance mainly due to geometrical spreading and the absorption of energy by the propagation

medium. So, at a given site, local geological conditions may modify the amplitude and frequency content of the seismic waves (Pedersen et al., 1994). Seismic wave amplification on mountain slopes is produced by a complex interaction of combined topographic and geological effects. Site effects on mountain slopes have previously been studied by several authors (Pedersen et al., 1994; Geli et al., 1988; Assimaki and Kausel, 2007; Bourdeau and Havenith, 2008). The analysis of different regional earthquakes allows us to evaluate possible seismic site effects at VdlS. Considering these effects is essential for proper interpretation of the seismograms generated by snow avalanches and then, further quantification of the energy recorded at each site; which is one of the objectives of this thesis. Additionally, for comparative analysis between the seismic recordings of the avalanches at the different sites along the path, accuracy of timing between the stations is required. Unfortunately, a time delay between the stations results from the characteristics of VdlS infrastructure. To resolve this issue, several earthquake recordings were used to establish the time between the seismic stations in spontaneous avalanche events. For artificially triggered avalanches, the seismic signals from the explosions are used to establish the time between the stations.

Firstly, a description of the geologic characteristics and the seismicity of the VdlS region is presented (Section 3.2). Considering the soil characteristics of the area, the total attenuation factor in function of the distance and frequency of the signals is calculated in Section 3.3. To evaluate possible local site effects, several earthquake recordings are analysed (Section 3.4.1) and interpreted in accordance with the topographic and geologic characteristics of VdlS (Section 3.4.2). Using the arrival of the P-waves from these earthquakes or the arrival of the air waves from explosions at each location, the time between the different stations is accurately established (Section 3.5). Finally, an analysis of the background noise before avalanche release events is performed to detect possible external noise sources that could overlap with the avalanche signal (Section 3.6).

3.2 Seismicity and geological setting in the VdlS region

3.2.1 Geological setting

The Vallée de la Sionne is drained by the Sionne River, which is a tributary of the Rôhne. The Rôhne valley is a sedimentary structure resulting from the combined action of tectonics and Quaternary glacier erosion, characterized by Quaternary deposits that reach a maximum depth of 900 m (Frischknecht and Wagner, 2004). The geological map of the VdlS area gives detailed information on the uppermost layers of the subsurface structure (Figure 3.1). The seismic stations in caverns A, B and C are located inside concrete caverns built in the middle of the path of the avalanche. According to the local geology, caverns A and C are built on a talus slope; the ground is mostly covered with loose material (gravel) at A, and with gravel and single boulders at C. Cavern B is located over a Wang Formation represented by dark grey marls and fine-grained calcarenites (Cardello and Mancktelow, 2014). The seismic sensor of D is buried in a hole approximately one metre deep and installed directly on ground characterized by Quaternary unconsolidated deposits (Figure 3.1).

3.2.2 Seismicity

Switzerland is located within an Alpine context with moderate seismic activity on average (Figure 3.2). Due to its high population density and vulnerable infrastructures, the risk in Switzerland is considered rather high in some areas, such as the canton of Valais (Giardini et al., 2004). Based on the earthquake catalogue of historical and instrumental seismic events in the zone, over 150 earthquakes with $M_L \geq 3.0$ and three major earthquakes of MSK intensity VIII-IX ($5.0 < M_L \geq 6.0$) have occurred over the past 250 years (Frischknecht, 2000).

VdlS belongs to the Valais region, one of the most seismically active zones in Switzerland. In the Valais region, earthquakes are the result of stress released along three major active fault zones: the Simplon fault, the Rhône fault and the faults of the Rawil depression (Maurer et al., 1997). In particular, the Wildhorn

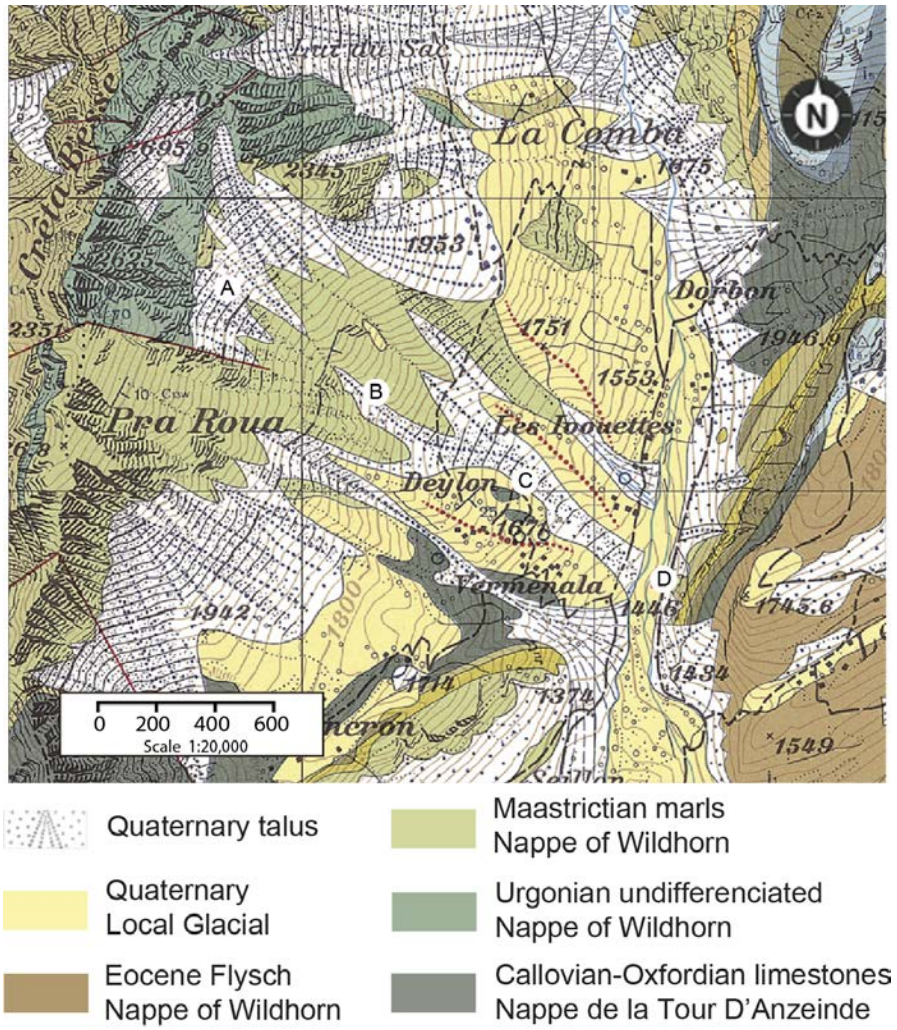

FIGURE 3.1: Geologic map of the Vallée de la Sionne (Geological Atlas of Switzerland (GA25), St-Lèonard, no. 35; http://map.geo.admin.ch/ (14th April 2016)) with detailed information on the uppermost layers of the subsurface and the location of the seismic stations A, B, C and D.

seismic zone in the Rawil depression, where VdlS is situated, is the most seismically active region in the Swiss Alps. The last major earthquake during the 20th century (magnitude M_w 6.1) occurred in 1946 in this zone causing about 150 million of Swiss francs of direct damages and triggering a number of landslides within the epicentral region (Fritsche and Fäh, 2009). Four months later, an M_w 6.0 aftershock triggered a large rock avalanche from the steep slopes of the Rawilhorn. The rock avalanche released 4-5 million m^3 of sedimentary rock from a ridge approximately 600 m high, and had a run-out distance of roughly 1.5 km (Moore et al., 2011). A topography effect might play an important role in the rock mass event as the release area was close to the ridge (Frischknecht, 2000). In this region, seismic soil amplification has also been previously observed inside this

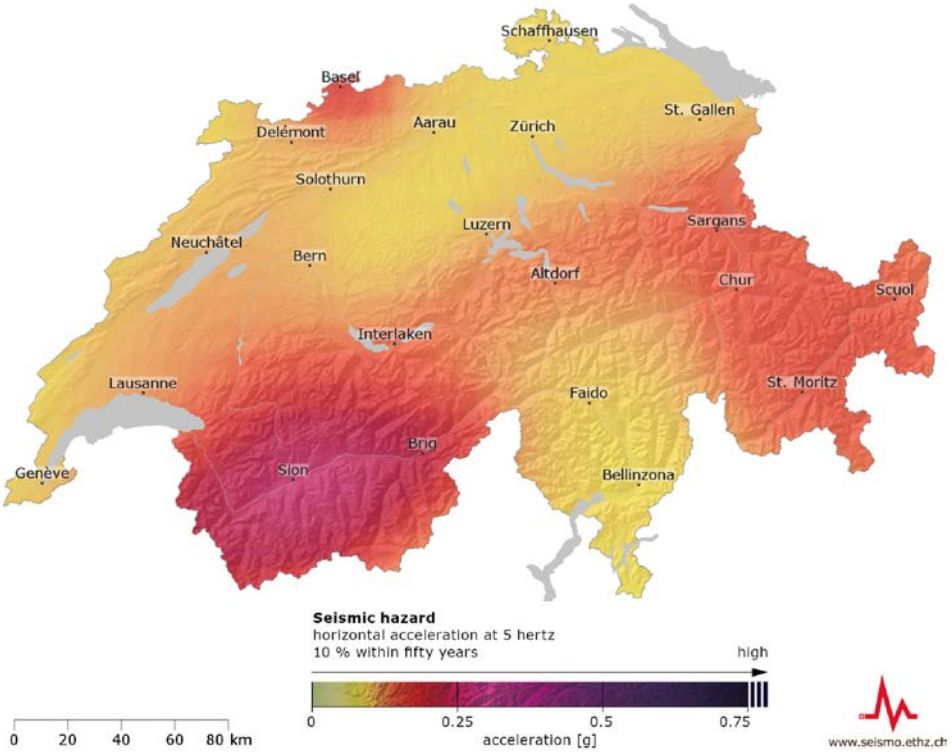

FIGURE 3.2: Seismic hazard map of Switzerland (from the Swiss Seismological Service (SED); www.seismo.ethz.ch) depicting the level of horizontal ground-motion in g (m/s2) (in units of 5% damped acceleration response spectrum at 5 Hz frequency) expected to be reached or exceeded in a period of 500 years (10% exceedance probability in 50 years). VdlS is situated 7.5 km north of Sion.

valley, characterized by unconsolidated deposits and a shallow water table (Roten et al., 2008).

3.3 Attenuation of waves

The two main types of seismic waves that a snow avalanche can generate, just as any other ground vibration source, are the surface waves and the body waves (P-waves and S-waves). The P-waves are the faster moving and are simply longitudinal waves. The S-waves are transverse waves that always travel slower than the P-waves. Surface waves are also typically generated by snow avalanches (Vilajosana et al., 2007b). The seismic waves generated by snow avalanches usually have a frequency spectrum below 100 Hz. Identifying the types of waves inside the seismograms of avalanches is no easy task, and often impossible due to an avalanche is a non-punctual, moving, multiple, and variable source of seismic waves. The

number and variation of the seismic sources, and the short distance between the sensor and avalanche, implies that different waves and phases may arrive simultaneously (Biescas, 2003). Additionally, the heterogeneities of the ground at near field may greatly modify the signals generated.

Infrasound waves are pressure fluctuations in the air, which occupy a relatively narrow band in the low-frequency acoustic spectrum (0.001 Hz to 20 Hz); too low to be perceived by the human ear (Johnson, 2003).

Attenuation of seismic waves

Different phenomena are responsible for the attenuation of seismic waves with distance, such as geometrical spreading, scattering, multipathing and anelasticity (e.g. Stein and Wysession, 2003). In general, the two processes that contribute to the decay of the seismic amplitudes generated by avalanches are geometrical spreading and anelastic attenuation. We can assume that, at local distances, the heterogeneities of the ground surface are much smaller than the wavelength of the seismic waves generated by avalanches (Vilajosana et al., 2007b). Hence, the scattering and multipathing processes can be neglected.

Geometrical spreading is defined as the variation of the energy per unit as a wavefront expands or contracts (e.g. Stein and Wysession, 2003). The initial energy released at the source is spread over an increasing area as the wavefront expands from the source producing a decrease of the intensity of the seismic wave with distance. A spherical wavefront moving away from the source is considered for body waves. The energy is conserved in the expanding spherical wavefront whose area is $4\pi r^2$, where r is the radius of the wavefront.

The anelastic, or also called, intrinsic attenuation involves the loss of energy due to the conversion of seismic energy to heat by permanent deformation of the medium. For travelling waves, the amplitude decays with distance due to anelastic attenuation as follows (e.g. Lay and Wallace, 1995):

$$A(r) = A_0 \, e^{-\frac{\pi \, r \, f}{Q(f) \cdot \, c(f)}} \tag{3.1}$$

where, A_0 is the amplitude at source, $A\,(r)$ the measured amplitude at a distance r from the source, f the frequency, $Q(f)$ the quality factor and $c(f)$ the phase velocity of the seismic waves. An important consequence of Eq.3.1 is that for a

constant value of Q and $c(f)$, a high-frequency wave will attenuate more rapidly than a low frequency wave. Large values of Q imply little attenuation. In general, Q increases with material density and velocity (e.g. Lay and Wallace, 1995).

Geophysical studies conducted in the Rhône valley (Frischknecht, 2000) showed that mean ground density varies between 1900 and 2200 kg/m^3 for the Quaternary unconsolidated sedimentary deposits and between 2400 and 2720 kg/m^3 for bedrock. Regarding the P-wave velocity, values range from 500 to 2800 m/s for the Quaternary deposits and from 4000 to 5000 m/s for bedrock (Frischknecht, 2000). The main value of the Q factor for unconsolidated deposits is usually chosen in the range 40-50 (Pedersen et al., 1994). Hence, considering a mean velocity of 2050 m/s and a mean Q value of 50, the total factor of attenuation for P-waves is:

$$F = \frac{1}{r} e^{-\frac{\pi \ r \ f}{50 \cdot \ 2050}} \tag{3.2}$$

where F is the total factor that includes the geometrical spreading term ($\sim \frac{1}{r}$) and the anelasticity term ($\sim e^{-\ r \ f}$).

The amplitude of the attenuation factor, F, in logarithmic scale (colour bar) against the distance and frequency is represented in Figure 3.3. The range of frequencies (1-100 Hz) and distances (1-3000 m) are selected according to the typical range of frequencies generated by avalanches and the distances travelled by the seismic waves in this study. The attenuation factor decreases as a function of distance and frequency. Due to anelasticity, higher frequencies are attenuated faster with distance than lower frequencies, as can be appreciated in Figure 3.3. Maximum distances recorded by the seismic waves propagating into the ground at VdlS are some 3000 m. (Figure 2.3). At a distance of 3000 m, 1 Hz waves are attenuated a factor of $3{\cdot}10^{-4}$, 40 Hz waves by a factor of $8{\cdot}10^{-6}$, and 100 Hz waves by a factor of $3{\cdot}10^{-8}$ (Figure 3.3b). Hence, the attenuation of waves is four orders of magnitudes higher for 100 Hz waves than for 1 Hz seismic waves.

Snow avalanches often slide over a snow cover that consists of different snow layers of varying height and physical properties. Thus, the seismic signals generated by an avalanche first propagate within the snow cover before reaching the snow-soil interface. Sidler (2015) has recently modelled the attenuation (as the inverse of the quality factor: $1/Q$) of compressional waves in light (high porosity) and dense snow (low porosity) using a porosity-based Biot model. His results show that the attenuation for the first compressional wave is lower in dense snow ($0 < 1/Q < 6^{-4}$)

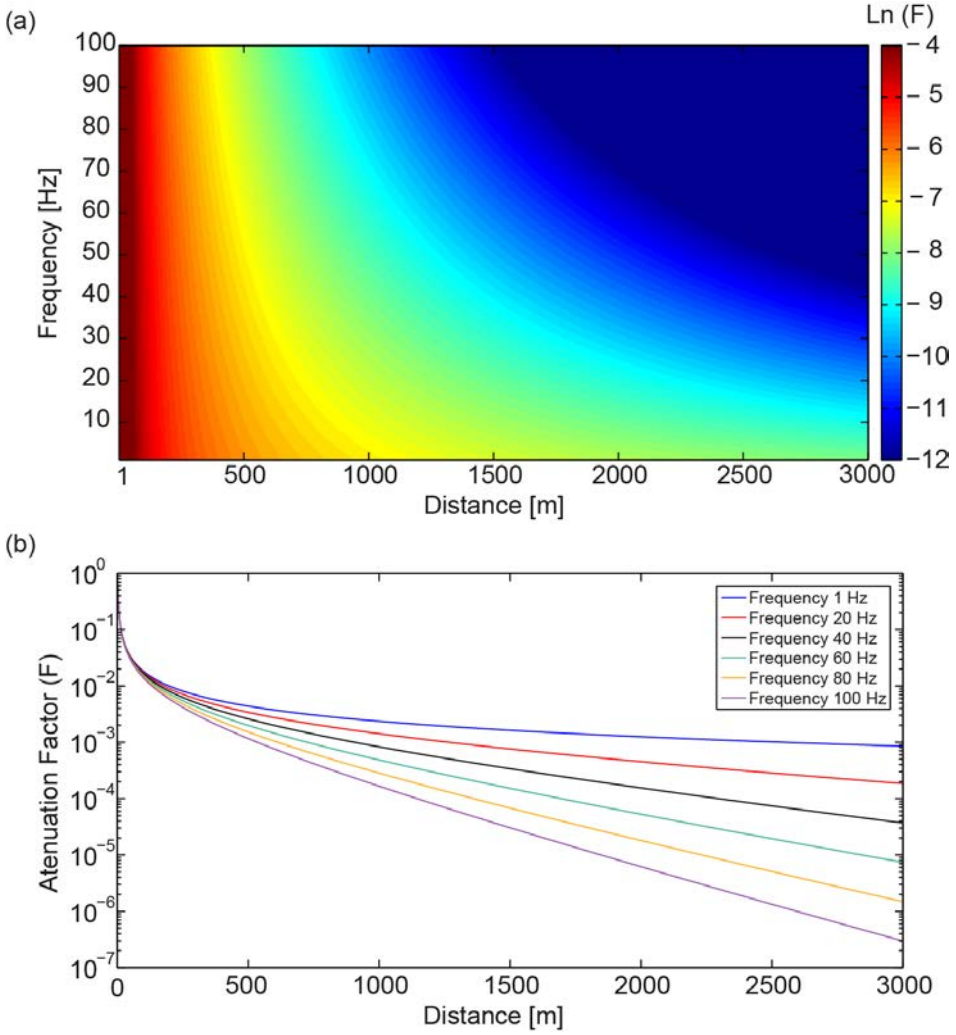

FIGURE 3.3: (a) Factor of attenuation, F (colours indicate logarithmic scale), displayed as a function of frequency and distance. (b) Factor of attenuation, F (in logarithmic scale), for six fixed frequencies displayed as functions of distance.

with a peak of attenuation at a high frequency ($f > 100$ Hz). In light snow, the attenuation is stronger ($0 < 1/Q < 0.1$) with a peak of attenuation at a lower frequency ($10 < f < 10^4$ Hz). Snow avalanches usually entrain the dry, low-density snow layers and slide over more resistant and older snow layers (Sovilla et al., 2006). Thus, less attenuation of the avalanche seismic waves should be expected over high-density layers. In addition, waves are similarly attenuated for frequencies below 100 Hz (the typical range of frequencies for avalanche signals).

Attenuation of infrasound waves

Infrasound can travel thousands of kilometres and still be detectable due to the frequency-dependency of atmospheric attenuation. The atmosphere absorbs high-frequency sound waves (audible and ultrasound) more than low-frequency waves (infrasound) (Pilger and Bittner, 2009). As for seismic waves, infrasound wave propagation is affected by different mechanisms that modify the amplitude and the frequency of the waves, such as geometrical spreading losses and absorption losses. Typical pressure perturbations for alpine mass movements such as snow avalanches are $\approx$ 3 Pa (Kogelnig et al., 2011a). The change in sound pressure level between two points at distances r_1 (near) and r_2 (far) from the source, due to geometrical spreading is:

$$\Delta dB_{SPL} = 20 \cdot log(\frac{r_2}{r_1}) \tag{3.3}$$

where ΔdB_{SPL} is the change in the sound pressure level. Hence, a change of a factor of, for example, 1000 in the distance leads to 60 dB attenuation, i.e., 0.02 Pa, which means two orders of magnitude less than typical pressure perturbations for alpine mass movements.

The dominant loss mechanism for infrasound is due to absorption processes in the atmosphere. Sound propagating from a source is subject to absorption by the atmosphere and absorption by the ground and ground cover, such as snow cover. In classic acoustic attenuation, amplitude decay due to transmission loss through the atmosphere is proportional to the square of the frequency (Johnson, 2003):

$$\Delta P = \Delta P_0 \cdot e^{-(\frac{\alpha_t f^2}{\rho_a})r} \tag{3.4}$$

where ΔP_0 is the original pressure fluctuation, α_t is the total attenuation coefficient, ρ_a is the density of the air, r is the distance from the source, and f is the frequency (Hz). According to Reed (1972) empirical values of α_t/ρ_a range from $1.3 \cdot 10^{-11}$ s^2/m to $3 \cdot 10^{-11} s^2$/m which translate to about $2 \cdot 10^{-5}$ dB/km for 10 Hz infrasound. These small values show that attenuation of infrasound is nearly insignificant in the lower atmosphere even at global distances (Johnson, 2003).

Therefore, seismic waves propagating into the ground are greatly attenuated with distance (up to several orders of magnitude depending on the distance and the

frequency content); whereas the attenuation of infrasound waves at this near field (less than 3 km) is practically negligible.

3.4 Evaluation of seismic site effects

3.4.1 Evaluation of ground shaking

In order to determine the local VdlS characteristics, several earthquakes are analysed in this work. As examples, the regional earthquake on 11th February 2012 of magnitude M_L 4.2 and epicenter in Zug (Switzerland; Figure 3.4); and the local earthquake on 21th March 2012 of magnitude M_L 2.1 and epicenter in St Leonartz (Switzerland; Figure 3.4) were analysed in this work. The information on the location of the earthquakes, the location of the stations, the epicenters and the hypocenters for each earthquake and station are given in Table 3.1. All the information on the earthquakes was extracted from the Swiss Seismological Service (SED; http://www.seismo.ethz.ch/) or from the European- Mediterranean Seismological Centre (EMSC;http://www.emsc-csem.org/#2).

TABLE 3.1: Information on the Zug (#1; 11/02/2012) and St Leonartz (#2; 21/03/2012) earthquakes (epicenter coordinates and depth; source SED), coordinates of VdlS stations, epicentral distance, hypocentral distance.

Earthquake	Stations		$\Delta[km]$	h [km]
#1: 47.15 N 8.55 E 32 km	B	46.29 N 7.36 E	131.0	134.9
	C	46.29 N 7.37 E	130.8	134.7
	D	46.29 N 7.38 E	130.7	134.5
#2: 46.32 N 7.34 E 0.1 km	B	46.29 N 7.36 E	3.1	3.1
	C	46.29 N 7.37 E	3.7	3.7
	D	46.29 N 7.38 E	4.1	4.1

The seismograms of the N-S component (more energetic) and the infrasound signals from these two earthquakes are shown in the Figure 3.4, where they are indicated the arrival of the P-waves and S-waves at the different sites. Maximum amplitudes correspond to the arrival of the S-waves. These earthquakes generated infrasound signals as a result of the coupling of the seismic waves to the air (Figure 3.4; e.g. Le Pichon, 2003).

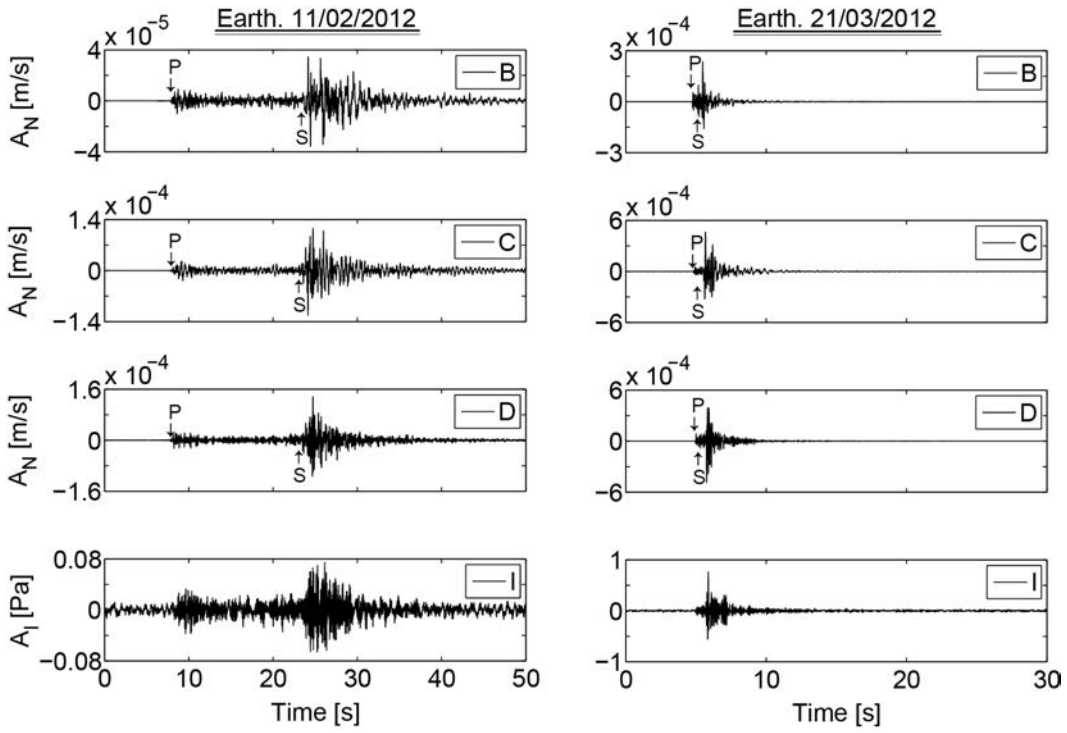

FIGURE 3.4: North-South component of the seismic signals recorded at B, C and D, and the infrasound signals of the earthquake with epicenter in Zug, Switzerland (left site), and in St Leonartz, Switzerland (right site). The origin of time is arbitrary.

Quantification indices of earthquakes

Six indices are usually employed in earthquake engineering to evaluate the effect of the ground shaking produced by an earthquake. In this thesis, the indices were used to quantify the energy of an earthquake at a given site in order to evaluate possible site effects at VdlS and the possibility of triggering avalanches. The indices take into account the amplitude, duration and frequency content of the time series. They are: the peak ground acceleration (PGA), the peak ground velocity (PGV), the peak ground displacement (PGD), the Arias intensity (I_a), the Trifunac duration (TD), and the pseudo-spectral acceleration (PSA). The PGA, PGV and PGD are the most simple indices and represent only punctual maximum values of the whole time series; whereas the TD and the I_a values are more related to the power of the shaking over the entire time series (Newmark, 1965). The PSA, in contrast, gives the maximum acceleration response of a structure for each period (T) (Newmark and Hall, 1982).

These indices are defined as follows:

- PGA (m/s^2): This index is obtained directly from the maximum value of the acceleration time history. The ground accelerations were obtained from the derivative of the ground velocity.

- PGV (m/s): This index is obtained directly from the maximum value of the velocity time history.

- PGD (m): This index is obtained directly from the maximum value of the displacement time history. The ground displacements were obtained from the integral of the ground velocity.

The PGA is the simplest index which is widely adopted in many worldwide structural design codes (e.g. Newmark and Hall, 1982). However, the complexity of the characteristics of an earthquake cannot be described fully by a single measure such as the PGA index (Housner and Jennings, 1977). The PGV and PGD indexes reflect the damage intensity level for a structure better than PGA values (Newmark, 1965).

- The Arias intensity, I_a (ms^{-1}), is a quantitative measure of the shaking intensity produced by the earthquake. It is calculated as (Arias, 1970):

$$I_a = \frac{\pi}{2g} \int_0^\infty a(t)^2 dt \tag{3.5}$$

  where I_a has units of velocity, $a(t)$ is the ground acceleration time series and g is acceleration due to gravity.

- Trifunac duration, TD (s), or the significant duration of the earthquake, is the time interval where the normalized Arias intensity of the ground motion is between 5% and 95 % (Trifunac and Brady, 1975), i.e., the time interval between 5% and 95 % of the Husid diagram (Husid, 1969). The Husid diagram is calculated as:

$$Husid(t) = \frac{\int_0^t a(t)^2}{\int_0^\infty a(t)^2} \tag{3.6}$$

- Pseudo-spectral accelerations, PSA (ms^{-2}), are commonly used to characterize the maximum response of a structure forced by an acceleration due to an earthquake. Resonance effects in a structure can appear owing to the frequency content of the ground motion, causing amplification of the vibration

(e.g. Newmark and Hall, 1982). PSA are calculated as:

$$PSA(\delta, w_0) = w_0^2 S_D(\delta, w_0) \tag{3.7}$$

where $S_D(\delta, w_0)$ are the maximum relative displacement spectrum values, w_0 is the undamped circular frequency and δ the sub-critical damping ratio, typically <1. In the field of earthquake engineering, the incorporation of a damping (viscous) reduction factor in the design of the structures is considered (Newmark and Hall, 1982). This factor depends on the characteristics of the structure. The typical three variable damping ratios of 1%, 5% or 8% were considered in this study to calculate the PSA. The values of the PSA for $T = 0$ s corresponds to the PGA values.

The previously defined indices are used in this work to evaluate possible local site effects (next Section 3.4.2), and to quantify the energy of several earthquakes that could induce a snow avalanche (Chapter 5). All these indices were calculated using different developed scripts in MATLAB.

3.4.2 Local VdlS site effects

Alpine valleys exhibit thick and young Quaternary unconsolidated deposits, steep slopes, rapid lateral variation of surficial deposits and a shallow water table due to the action of glaciers and rivers in the Quaternary period (Frischknecht and Wagner, 2004). The local geology and topography modify the characteristics of seismic waves (amplitude, frequency content and duration) resulting in an amplification or deamplification of the ground motion. These site effects could be considerable in mountain areas due to the complex topography, incoming wave field and geology beneath the mountain, the subsurface layering and three-dimensional effects. Previous studies of the site response carried out in the Rôhne Valley suggested that the 2-D structure of the basin would lead to amplification factors of up to 12 in the frequency band between 0.5 and 10 Hz (Roten et al., 2008).

Although the characterization of the local VdlS site effects is not the aim of this work, it needs to be considered when quantifying the seismic energy generated by avalanches or by earthquakes at the different sites. Due to the complexity of the terrain in mountain areas, seismic site characterization involves a long-term research with specific field campaigns and modelling the seismic response of

the valley. To quantify soil amplification, local earthquake recordings from both bedrock and soft soil sites are commonly used. However, none of our seismic stations are installed directly in bedrock or on non-inclined slopes. Hence, it is not possible to obtain the real amplification factors due to the lack of a reference station. However, the comparison between the recordings of an earthquake at the different stations shows relative amplifications between them.

Possible local site effects were evaluated by comparing the ground motion of eight earthquakes that occurred nearby to VdlS (Table 3.2). I have also incorporated data from the Swiss station in cavern A (Figure 2.1), although only data of three earthquakes were available. The ground motion recordings of the earthquakes were previously transformed to acceleration data and then the PGA and PSA values were calculated for comparison. The PGA values of the earthquakes recorded at each station are shown in Table 3.2. In general, comparison between them shows that the PGA values of stations A and D are up to one order of magnitude higher than the values recorded at stations B and C.

The acceleration response spectra of the soil, i.e. the PSA values, computed for four earthquakes recorded at A, B, C and D, using a typical damping ratio of 5%, are shown in Figure 3.5. Maximum PSA peaks were obtained at station A for periods below 0.2 s, i.e., for frequencies higher than 5 Hz. The PSA values at D were of similar magnitude than to those at A with maximum peaks which can overtake the values at A (Figure 3.5) and duplicate the values at C. The spectrum amplitudes at B do not show notable amplification peaks, with PSA values generally one order of magnitude lower than those obtained at A, C and D (Figure 3.5). The amplitudes of the maximum PSA at each seismic station and the corresponding periods differ for each earthquake due to the different nature of the incoming wave field. To summarize, station D shows values of PGA and PSA of the same order of magnitude as the values from A, and higher than those at B and C. The lowest values were obtained at station B. The relative amplifications observed at stations A and D may be the result of a combination of topographic and geologic effects.

The highest quantification values were obtained at station A, which is located close to the top of the mountain and the slope is characterized by the most abrupt topography. This result is in accordance with previous studies by Pedersen et al. (1994). In contrast, at station B (Table 3.2) where the slope inclination is greater than at C and D, the amplitudes and the quantification indices are lower than at

TABLE 3.2: Information on the earthquakes (epicenter location, date, magnitude; source SED), location of the seismic station (A, B, C and D; Figure 2.1), backazimuth, hypocentral distance and PGA values for all the components (V, N-S and E-W). No data are available for the vertical component at B in some recordings due to a malfunction of this component of the sensor.

Earthquake	Cavern	B [°]	H [m]	PGA [m/s^2] (V, N-S, E-O)
Col de Balme (France) 6/12/2010 M_L 3.1	A	229.2	42.6	$(2.3 \cdot 10^{-3}, 3.4 \cdot 10^{-3}, 2.7 \cdot 10^{-3})$
	B	230.0	42.8	(No data,$7.2 \cdot 10^{-4}, 7.9 \cdot 10^{-4}$)
	C	230.8	43.0	$(9.2 \cdot 10^{-4}, 1.7 \cdot 10^{-3}, 1.3 \cdot 10^{-3})$
	D	231.4	43.3	$(1.6 \cdot 10^{-3}, 3.4 \cdot 10^{-3}, 1.9 \cdot 10^{-3})$
Zug (Switzerland) 11/02/2012 M_L 4.2	A	316.5	134.9	$(3.6 \cdot 10^{-3}, 6.3 \cdot 10^{-3}, 4.2 \cdot 10^{-3})$
	B	316.8	134.9	(No data,$1.6 \cdot 10^{-3}, 1.3 \cdot 10^{-3}$)
	C	317.0	134.7	$(1.9 \cdot 10^{-3}, 5.2 \cdot 10^{-3}, 1.3 \cdot 10^{-3})$
	D	317.2	134.5	$(2.5 \cdot 10^{-3}, 6.7 \cdot 10^{-3}, 4.2 \cdot 10^{-3})$
Viadana (Italy) 25/01/2012 M_w 4.9	B	238.1	296.8	(No data,$1.8 \cdot 10^{-3}, 1.3 \cdot 10^{-3}$)
	C	238.1	296.2	$(1.9 \cdot 10^{-3}, 5.2 \cdot 10^{-3}, 1.3 \cdot 10^{-3})$
	D	238.0	295.7	$(1.5 \cdot 10^{-3}, 4.5 \cdot 10^{-3}, 3.0 \cdot 10^{-3})$
Corniglio (Italy) 27/01/2012 M_w 5	B	233.2	296.4	(No data,$2.0 \cdot 10^{-3}, 1.2 \cdot 10^{-3}$)
	C	233.1	268.8	$(4.6 \cdot 10^{-3}, 4.8 \cdot 10^{-3}, 5.1 \cdot 10^{-3})$
	D	233.1	268.3	$(3.0 \cdot 10^{-3}, 3.3 \cdot 10^{-3}, 3.3 \cdot 10^{-3})$
St Leonartz (Switzerland) 5/03/2012 M_L 1.1	B	352.4	4.8	(No data,$1.9 \cdot 10^{-3}, 2.1 \cdot 10^{-3}$)
	C	359.1	5.0	$(3.8 \cdot 10^{-3}, 2.2 \cdot 10^{-3}, 4.8 \cdot 10^{-3})$
	D	352.5	5.2	$(4.4 \cdot 10^{-3}, 3.5 \cdot 10^{-3}, 6.9 \cdot 10^{-3})$
St Leonartz (Switzerland) 21/03/2013 M_L 2.1	A	328.1	2.5	$(4.0 \cdot 10^{-2}, 3.8 \cdot 10^{-2}, 4.2 \cdot 10^{-2})$
	B	324.1	3.1	(No data,$1.2 \cdot 10^{-2}, 2.1 \cdot 10^{-2}$)
	C	319.9	3.7	$(1.3 \cdot 10^{-2}, 2.7 \cdot 10^{-2}, 3.0 \cdot 10^{-2})$
	D	316.4	4.1	$(1.4 \cdot 10^{-2}, 2.6 \cdot 10^{-2}, 3.8 \cdot 10^{-2})$
Zermatt (Switzerland) 2/02/2013 M_L 2.6	B	216.2	51.9	$(1.9 \cdot 10^{-4}, 2.6 \cdot 10^{-4}, 1.8 \cdot 10^{-4})$
	C	215.9	51.4	$(3.2 \cdot 10^{-4}, 5.4 \cdot 10^{-4}, 8.5 \cdot 10^{-4})$
	D	215.6	51.0	$(6.1 \cdot 10^{-4}, 1.0 \cdot 10^{-3}, 1.9 \cdot 10^{-3})$
Annecy (France) 6/04/2013 M_L 2.7	B	248.1	104.5	$(3.7 \cdot 10^{-5}, 4.8 \cdot 10^{-5}, 4.7 \cdot 10^{-5})$
	C	248.4	104.9	$(9.1 \cdot 10^{-6}, 1.6 \cdot 10^{-5}, 1.4 \cdot 10^{-5})$
	D	248.5	105.3	$(5.0 \cdot 10^{-5}, 8.6 \cdot 10^{-5}, 1.1 \cdot 10^{-4})$

those sites. The differences observed between stations B and the lower stations, where the topography is smoother, are an example that shows that the topographic amplification is not the only factor to be considered, in agreement with Bourdeau and Havenith (2008). Therefore, the possible site effects due to the local geological characteristics of the soil beneath each seismic site should be considered.

According to the local geology (Figure 3.1), no large site effects from surface soil are expected at B because the sensor is installed over well-consolidated marls. Hence,

we recorded minimum values of PGA at B and a response spectrum characterized by low amplifications (Table 3.2 and Figure 3.5). Low seismic amplifications should be expected in stations located over these types of rocks according to Frischknecht (2000). In contrast, we observed amplification of the ground motion at D relative to the recordings at B and C. This result was expected, as station D is installed directly over soft unconsolidated sediments. It is generally known that this type of deposits tends to amplify ground motions (e.g. Roten et al., 2008). Even larger amplifications were observed at A, the station close to the top of the mountain. At this site, the combination of a gravel soil and the topographic effect contributed to the amplification recorded.

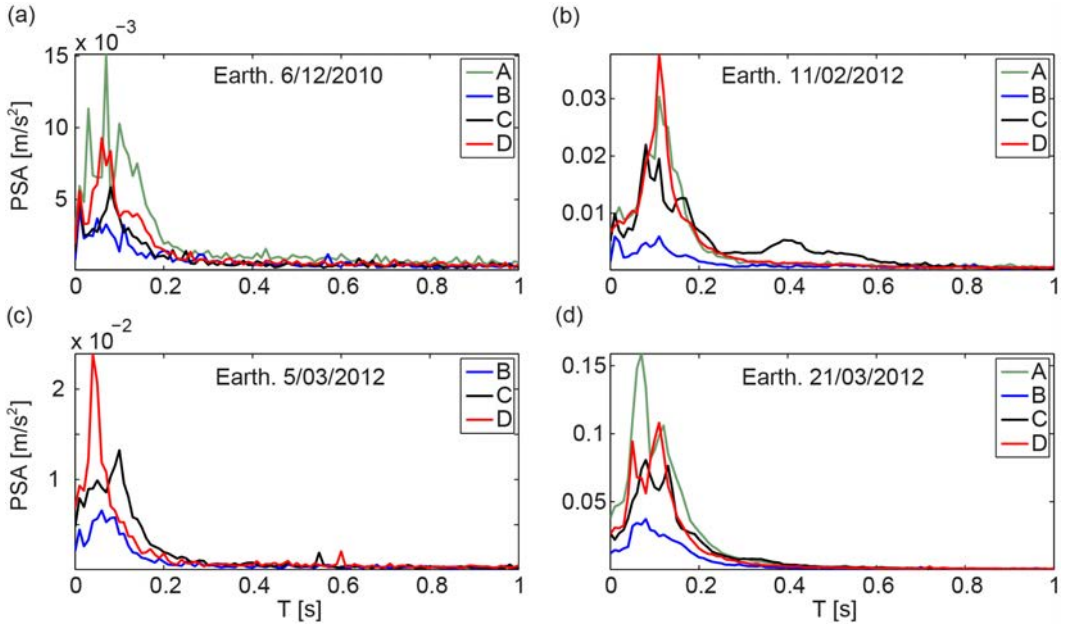

FIGURE 3.5: Response spectra computed with a damping ratio of 5% from the accelerograms of the earthquakes with epicenter in Col de Balme (a), Zug (b), and St Leonartz (c) and (d) at A, B, C and D.

3.5 Timing between seismic stations

Seismic waves generated by avalanches arrive practically simultaneously at the different stations due to the high velocity of propagation of seismic waves through the ground. All the seismograms generated by the avalanche at each location are compared in order to distinguish common seismic sources and characterize the flow. For example, the impacts of an avalanche on terrain features or other obstacles

generate narrow peaks with a different amplitude in each seismic recording. Hence, accurate timing between the stations is required.

Owing to the characteristics of the VdlS infrastructure, synchronizing signals between the different stations is a problem. Although during the installation the internal clock of each station is synchronized using a GPS antenna to UTM time, through the season a time shift appears between the stations. The infrastructure characteristics do not allow the GPS antenna to be connected with the station during the whole winter. This is due to the stations being installed in closed concrete caverns and buried several metres below the snow cover. The GPS antenna needs to be outside to receive a good signal and that implies the risk of being destroyed by an avalanche passing over it. Hence, the time shift is caused by the drift in the internal clocks of each station that cannot be corrected. Despite the good quality of the internal clock, a shift of several seconds may accumulate over the winter.

Avalanches usually trigger the alarm system of VdlS. The initial time of the trigger file can be considered as an approximation for establishing the time for the different stations. The initiation of the trigger file can have a delay between the stations of about $\pm$ 1 s caused by the VdlS alarm system characteristics. To obtain better timing accuracy and thus compare the signals generated by the avalanches in short time intervals, we established the timing between the stations using i) the records from the explosions for artificially triggered avalanches or ii) the records from earthquakes that occurred few days either before or after spontaneous avalanches. In addition, sometimes the trigger files were not provided by the stations and a method of timing between them was needed.

Timing using explosions

The detonation of an explosive charge in the snow causes a shockwave that develops into an air pressure wave (N-wave) that propagates through the air. The vibrations generated by the detonation also propagate within the snowpack and are transmitted to the ground with a velocity of one order of magnitude higher than the pressure waves in the air. The ground vibration caused by an explosion arrives almost immediately at all the seismic stations (velocity of propagation of about 4000 m/s; e.g. Suriñach et al. (2001)). The amplitude of the ground vibrations, however, is attenuated much faster with distance than the amplitude of

the acoustic wave. For example, at the farthest station (D) the amplitude of the waves from these explosions often has the same order of magnitude as that of the background noise (see example of Figure 3.6). Considering the difficulty in identifying the signal travelling through the ground, the signals were fitted using the arrival of the acoustic wave at the different stations, previously corrected for the time involved in traveling between the stations. The relative distances travelled by an acoustic wave through the air between the stations are:

$$\Delta d_{D-B} = 1272 \pm 1m$$

$$\Delta d_{D-C} = 631 \pm 1m$$

These distances were obtained from the GEODAR radar system located at the shelter. As an example, we used the explosion that triggered an avalanche (analysed in Chapter 5) in the experiment on 3rd February 2015. The velocity of propagation of the acoustic wave depends on the temperature of the air. The speed of sound was considered to be approximately 323 ±3 m/s for (-13 ±5)° (value from the weather station situated in CB2 and considering a variation of temperature due to the different altitude of the seismic stations). The time offset between the arrival of the acoustic wave at the different seismic stations is (no data available for cavern A):

$$\Delta t_{C-B} = 1.98 \pm 0.02s$$

$$\Delta t_{D-B} = 3.94 \pm 0.04s$$

The travel time plot in Figure 3.6 shows the corrected time signals for the explosion in the experiment recorded at the three seismic stations and for the infrasound recording. The corresponding offsets between the internal clocks of each station are given in Table 3.3. Station B has a high delay in comparison with C and D. During its installation, this station did not receive any GPS signal and could not be synchronized with the other stations. The infrasound sensor is always connected to the same data acquisition system as the seismic sensor in cavern D and thus they have a common timebase. The offsets of time relative to the station D are shown in Table 3.3.

TABLE 3.3: Values of the time offsets between the internal clocks at each station (B, C and D) calculated from the arrival times of the acoustic wave at each location on 3rd February 2015.

Station	$\Delta t(t_D - t_{station})$ [s]
B	203.09
C	54.63
D	0

Time fitting using earthquakes

In the last seasons, the number of avalanches spontaneously released exceeded those artificially released. To establish the time between the stations in these cases, I used the analysis of earthquakes. The arrival of the P-wave from an earthquake at each seismic station is usually easy to identify in the seismograms depending on the magnitude and epicentral distance of the earthquake. Ideally, teleseismic earthquakes should be used because the wavefront can be considered plane and arrives simultaneously at all the stations. Unfortunately, strong teleseismic earthquakes have a lower frequency of occurrence and thus I used the arrivals of P-waves from regional earthquakes that occurred at a time close to that of the avalanche release.

To estimate the arrival time of these waves at each station, a mean P-wave velocity of 5.5 km/s for the Earthś crust was considered (Stein and Wysession, 2003). The epicentral distance and the hypocentral distance are calculated by applying:

$$\Delta = cos^{-1}(cos(b) \cdot cos(c) + sin(b) \cdot sin(c) \cdot cos(A)) \tag{3.8}$$

$$h \approx \sqrt{\Delta^2 + z^2} \tag{3.9}$$

where Δ is the epicentral distance (in degrees), b and c are the colatitudes of the epicenter and the stations, A is the difference in the longitudes of the station and the epicenter, h is the hypocentral distance (in km) and z the depth of the earthquake (in km). Thus, the arrival time of the P-wave is approximately:

$$t_p \approx \frac{h}{v_p} \tag{3.10}$$

where v_p is the mean velocity of the P-waves in the crust (5.5 km/s). Two earthquakes, one of magnitude M_L 2.6 and epicenter in Zermatt (#1: Table 3.4), and

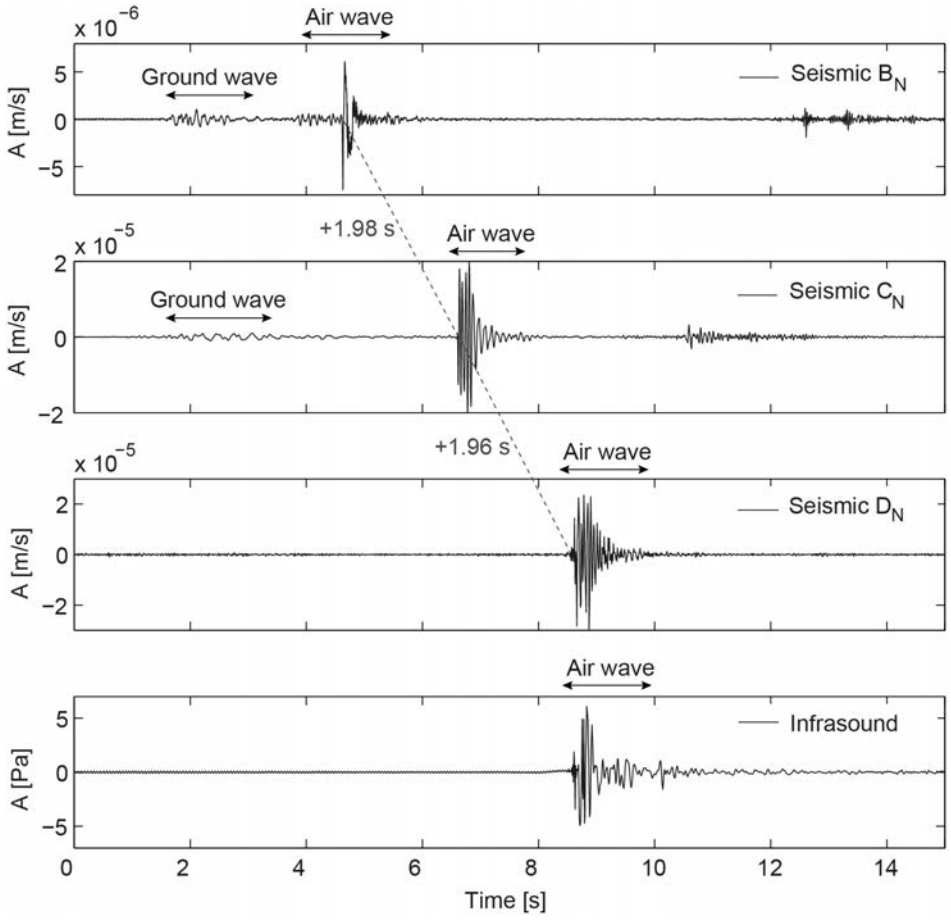

FIGURE 3.6: Travel time plot of the seismic signals (north-south component) generated by the detonation of an explosion that triggered an avalanche in VdlS, and recorded in B, C, and D (seismic and infrasound; Figure 2.1). The seismic waves propagating through the ground (ground waves) travel faster than the air pressure wave travelling through the air (air wave). The origin of the time is arbitrary and fitted considering the delay and arrival time of the air wave.

a second one of M_L 2.7 in Annecy (#2: Table 3.4), were used to establish the time between the stations of several avalanches released in the season 2012/2013. Considering a P-wave velocity variation of about ± 0.5 km/s, the corresponding errors of the P-wave arrivals (t_p) for the Zermatt earthquake is ± 0.8 s and ± 1 s for the earthquake of Annecy. The offset in the time for the arrival of the P-wave (Δt_{offset}) recorded between two stations is the sum of the time offset of the internal clocks of the stations (Δt) and the difference in the P-wave travel times (Δt_p):

$$\Delta t_{offset} = \Delta t + \Delta t_p \tag{3.11}$$

The offsets of time were calculated for both earthquakes using Eqs. 3.10 and 3.11. These time differences between the internal clocks of the stations increase during

TABLE 3.4: Information on the earthquakes: hypocenter location of the earthquakes (source SED), station recorded, epicentral distance (Δ), hypocentral distance (h), time of travel of the P-wave (t_p) and offset of time between the stations (Δt). Station B is used as the reference station.

Earthquake	Station	$\Delta[km]$	h [km]	t_p [s]	$\Delta t(t_B - t_{station})$ [s]
#1: 45.92 N 7.76 E 2 km 2/02/2013 (Zermatt)	B	51.9	51.9	9.1	0
	C	51.3	51.4	9.0	90.7
	D	50.9	51.0	8.9	79.3
#2: 45.94 N 6.11 E 3.2 km 6/04/2013 (Annecy)	B	104.5	104.5	19	0
	C	104.9	104.9	19	92
	D	105.3	105.3	19	80

the season (Table 3.4). In approximately 2 months, the time difference between stations B and C increased by 1.3 s; and that between B and D by 0.7 s. This observation reflects the need to use an earthquake that occurred close in time to the avalanche release.

The time offset values of the sample earthquakes in Table 3.4 were then used to establish the time between the seismograms of snow avalanches from the different stations. As an example, the seismograms of the earthquake in Zermatt are represented with the established time offset in Figure 3.7. The P-wave travel time (app. 8.9 s) from hypocenter to station D is shorter than that to stations C and B with a delay of 0.1 and 0.2 s, respectively (Figure 3.7).

3.6 Analysis of background noise

Before the interpretation of the seismic signals generated by avalanches, the seismic background noise at each location was analysed. The seismic background noise is primarily cultural at frequencies over 1 Hz and at continental sites such as VdlS, varying throughout the day (Peterson, 1993). Good locations for seismic sensors are those that present low levels of background noise. Choosing a good location was beyond the scope of this work because the sensors could only be installed inside the caverns built at VdlS. To characterize the background noise at a site, it is necessary to calculate the power spectral density (PSD) over different intervals of time throughout the year and at different times of night and day. Our stations were only operatives for some months during winter. Hence, the background noise

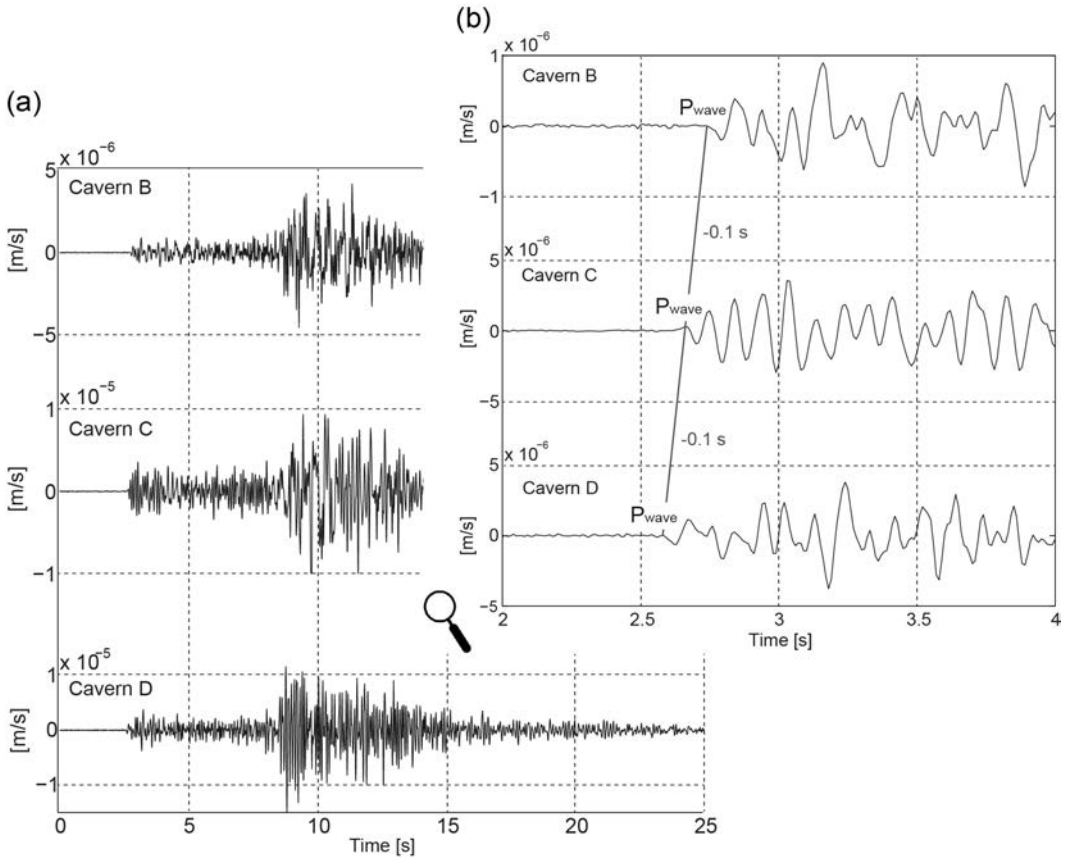

FIGURE 3.7: Seismograms of the north-south components of the earthquake in Zermatt recorded at the three stations of VdlS (B, C and D; Figure 2.1). b) Close up between 2 and 4s of the arrival of the P-wave at the different seismic stations of VdlS.

over some time intervals of interest was analysed in order to detect possible peaks of external noise that could overlap with the avalanche signal.

To analyse the seismic background noise, I calculated the PSD over selected time intervals in the pre-avalanche seismic signal. The noise spectra of each station are plotted together with the noisy and quiet models of Aki and Richards (1980), and the new low (NLNM) and high (NHNM) noise models of Peterson (1993). These new models are more accurate models of seismic background noise than the Aki and Richards models (Peterson, 1993). The Peterson models, however, are not available for frequencies over 10 Hz. I therefore used the Aki and Richard models as a reference for frequencies above this range. For examples of background noise signals analysed, see Figure 3.8. I selected 15 minutes of background noise just before the beginning of three avalanches released on 17/12/2011 , 2/02/2013 and 3/02/2015. The mean amplitude of the background noise usually shows similar

values for all the seismic stations, with values of the order of 10^{-7} m/s (Figure 3.8). The main differences are found for the avalanche experiment days, e.g. 3/02/2015, in which the noise is higher due to the presence of personnel involved in the experiments and the helicopter flying around VdlS.

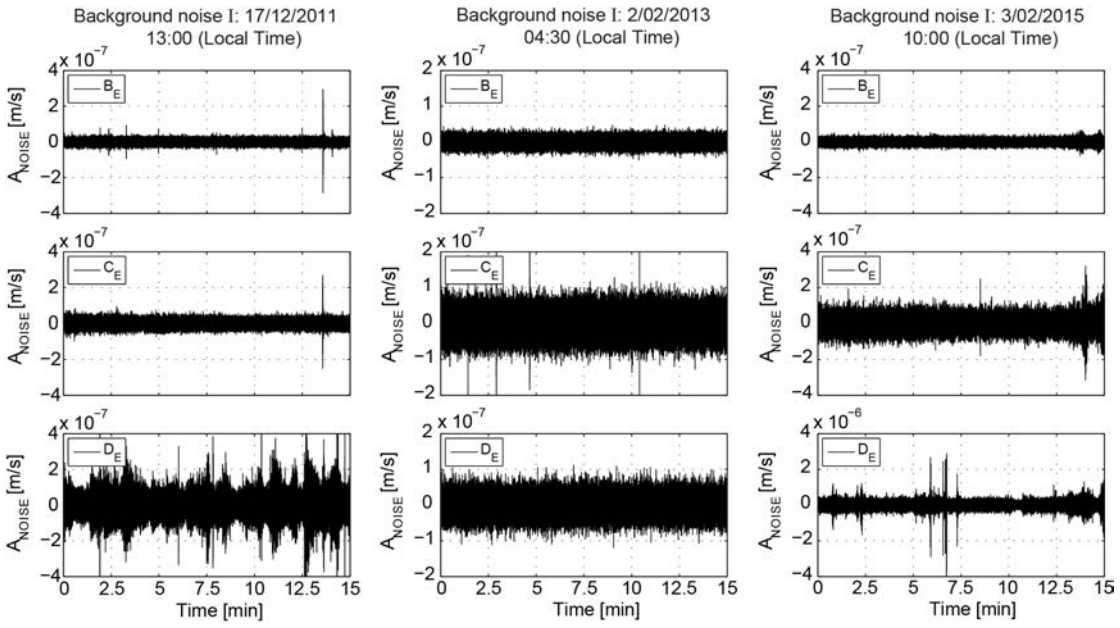

FIGURE 3.8: Seismic signals (east-west component) of the background noise for the 15 minutes before the three avalanches released on 17/12/2011, 2/02/2013 and 3/02/2015, and recorded at B (track zone), C (run-out zone) and D (opposite slope) stations.

The corresponding PSD of the selected time intervals recorded at each location and compared with the background noise models are shown in Figure 3.9. Before the calculation of the PSD, all the signals were filtered (1 Hz to 40 Hz) with a 4-th order Butterworth bandpass filter. The noisiest day was the experiment day 3/02/2015. The PSD on that day display various peaks that are notable at D station, located close to the shelter where the SLF team was working. On 17/12/2013, at the same location, the noise was also the highest with several peaks between 23 and 40 Hz exceeding the noisy curve (Figure 3.9). I attributed the noise on that day to the weather conditions, which were characterized by strong winds and storms. These phenomena could cause seismic noise at this location where the seismic sensor is less protected than in the other two caverns. A peak of noise at 20 Hz on 2/2/2013 is also notable at location C. An instrument near the seismic sensor may cause this peak. All the rest of the PSD values were between

the background noise models of Peterson (1993) for frequencies from 1 and 10 Hz, and of Aki and Richards (1980) models for frequencies between 10 and 40 Hz.

In general, the background noise level previous to an avalanche release is between the typical ranges of noise, meaning that the seismic signal generated by the avalanche is not overlapped with other seismic sources. For avalanches triggered artificially, however, the background noise level is higher, affecting the typical frequency ranges of avalanche seismic signals (f $>$ 10 Hz). This noise has to be considered for a proper interpretation of the avalanche seismograms.

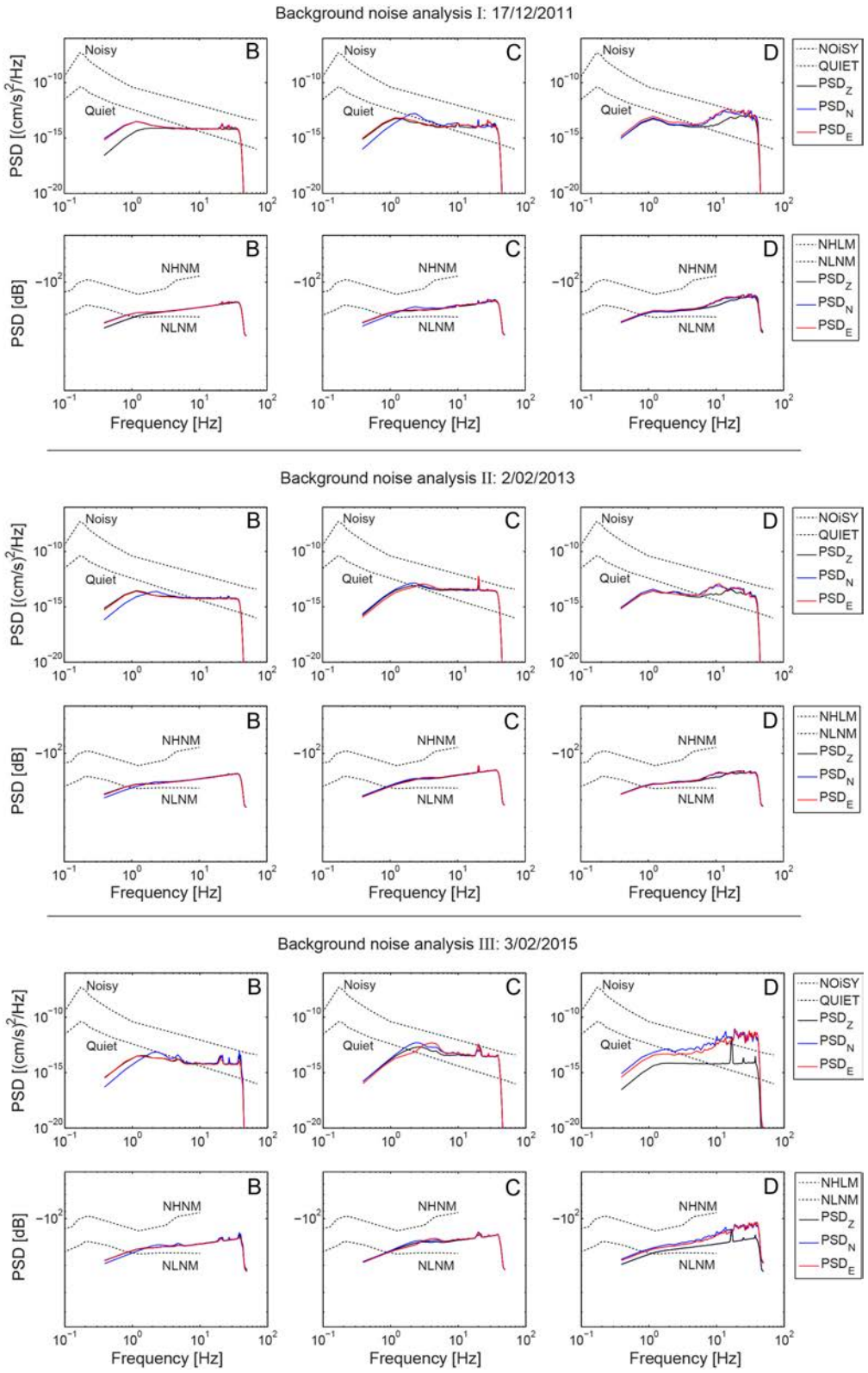

FIGURE 3.9: Power spectrum density (PSD) of the three seismic components calculated for three time intervals before the avalanches released on 17/12/2011 (top), 2/02/2013 (middle) and 3/02/2015 (bottom) recorded at three seismic stations B, C and D. The spectra are presented as a function of frequency in units of $(\mathrm{cm/s})^2/\mathrm{Hz}$ to compare with the noisy and quiet models of Aki and Richards (1980), and in decibels referred to 1 $(\mathrm{m/s^2})/\mathrm{Hz}$ to compare with the NHNM and NLNM models of Peterson (1993).

Chapter 4

Methodology

In the previous chapters, I introduced a description of the configuration of seismic and infrasound sensors installed by the UB group and the main effects that affect the wavefield and thus the analysis of the avalanche signals. In this chapter, I present a classification of the avalanches analysed in this work, and the methodology of analysis in the time and frequency domains of the avalanche seismic and infrasound signals.

4.1 Introduction

A collection of more than 50 snow avalanches has been recorded with the different instrumentation at VdlS since it became operative. In this work, I analyse a total of 33 snow avalanches mainly by using the seismic signals. Data acquired with other types of instrumentation are additionally used to compare with the avalanche seismic signals. For instance, to infer avalanche parameters, to characterize the flow and to quantify the absorption of the seismic intensity, seismic data are compared with data of two FMCW radars located at the same site of the avalanche path. To characterize earthquake-generated avalanches, the seismic data were compared with data acquired with the infrasound sensor, the GEODAR radar and two weather stations. The analysis of these data, and data from different earthquakes quantified using the set of seismic indices previously defined (Section 3.4), is detailed in Chapter 5 below.

In this chapter, I classify all the snow avalanches analysed in this work according to the type of flow, size and path characteristics (Section 4.2). A description of the methodology for the time and frequency analysis of the seismic and infrasound signals generated by avalanches, enabling the quantification of them in a set of seismic indices, is presented in Section 4.3. FMCW radar signals are compared in detail with seismic measurements acquired at the same location of the avalanche path (Section 4.4).

4.2 Snow avalanche classification

The nature of the avalanches analysed in this work varied as they were triggered by different mechanisms and they developed a variety of dimensions and flow regimes. According to the observable properties in the three parts characterizing a snow avalanche path (starting zone, track and run-out zone; Figure 2.1), a system to classify them was published by The International Commission on Snow and Ice (Unesco, 1981). The avalanches of our catalogue were classified depending on the following criteria: type of flow, triggering mechanism, avalanche path, and size. Table 4.1 shows for each avalanche the date, the number (the numbering of avalanches is according to the VdlS database) and the previously mentioned classification criteria.

Most of the snow avalanches occurred spontaneously (Table 4.1) due to the interplay of meteorological and snow cover properties. During full-scale experiments at VdlS, snow avalanches were artificially triggered by explosions. Snow avalanches often start at the PR and CB1 areas and follow the main channelled track of gully 1 (see Figure 2.1). Occasionally, part of the mass of an avalanche starting at PR flowed through the westerly gully (referred to as Deylon; Figure 2.1) to gully 1 (for example, the large powder avalanche of the picture in Figure 4.1), and outside VdlS. The avalanches released in the CB1-CB2 area usually flowed through both gullies (1 and 2, Figure 2.1). Snow avalanches flowing through only gully 2 did not trigger the VdlS alarm system because the seismic trigger system is situated along the main path (gully 1) and thus, the vibrations produced by avalanches flowing through annex zones are not energetic enough to trigger the system. However, the avalanche #3002 of 6th December 2010 only flowed along gully 2. This avalanche was released after the arrival of an earthquake that triggered the VdlS

seismic alarm system. Whether the earthquake triggered the avalanche or not will be evaluated in detail on the next chapter.

According to the type of snow and flow involved, snow avalanches were classified into three categories: powder-snow, wet-snow and transitional avalanches (when both powder and wet flows are present in the same avalanche). In winter, powder-snow avalanches which develop a dilute powder cloud are typical in VdlS (Figure 4.1). Wet-snow avalanches mostly occur at the beginning of the winter season or in spring, when the air and snowpack temperatures are higher. In transitional avalanches, both types of flow coexist when the avalanche is released from elevations where the snow is still dry, but later is transformed into a denser, granular flow through the entrainment of wet snow along its path (Steinkogler et al., 2014, 2015). These avalanches are also common at VdlS as they are initiated at high altitudes and can cover long run-out distances.

Snow avalanches are usually sized in terms of the distance travelled along the avalanche path (Greene et al., 2010). Following this criterion, the size of the avalanches of this work were classified according to the typical avalanche run-out distances observed, into five classes:

- Very small, with a path length shorter than 500 m. Such avalanches are normally too small to trigger the automatic system.
- Small, with a path length between 500 and 1000 m. These normally flow over sensor B and stop close by.
- Medium, with a path length between 1000 and 1500 m. These normally flow over sensor C and/or stop close to it.
- Large, with a path length between 1500 and 2500 m. These can reach the valley bottom and are usually deflected by the opposite slope. Sometimes the powder cloud can reach sensor D.
- Extreme, with a path length more than 2500 m. These run up the opposite slope and may cover the instrument control centre at D. Part of the mass is deflected by the slope and keeps flowing for several hundred metres along the valley bottom.

TABLE 4.1: Classification of the avalanches analysed: date, avalanche number, avalanche type (powder, wet or transitional), triggering mechanism (spontaneous, artificial), release area (CB1-PR, CB1-CB2), path (gully 1 (G1), gully 2 (G2) or both, and Deylon (Dl)), run-out distance and size (small, medium, large or extreme). The release location of some avalanches is unknown because the trigger started with a delay (see Section 2.4). The mechanisms involved in the release of avalanche #3002 are analysed and discussed in Chapter 5.

Date	Number	Type	Triggering	Release area	Path	Run-out distance	Size
30.01.99	301	Powder	Artificial	CB1-CB2	G1+G2	2500	Large
10.02.99	103	Powder	Artificial	PR-CB1	G1+G2	3000	Extreme
25.02.99	200	Powder	Artificial	CB1-CB2	G1+G2	3000	Extreme
13.02.02	4267	Wet	Spontaneous	PR	G1	1400	Medium
21.02.02	4270	Powder	Spontaneous	CB1	G1	1200	Medium
13.03.02	4288	Wet	Spontaneous	CB1-CB2	G1	1900	Large
20.03.02	4292	Wet	Spontaneous	PR-CB1	G1+G2	2200	Large
31.01.03	504	Powder	Artificial	PR-CB1	G1	2200	Large
	505	Powder	Artificial	CB1	G1	1000	Small
	506	Powder	Artificial	CB1-CB2	G1+G2	2500	Large
06.12.10	3002	Powder	Artificial	CB2	G2	1500	Medium
	3003	Transitional	Spontaneous	-	G1	1800	Large
07.12.10	3004	Transitional	Spontaneous	-	G1+G2	2000	Large
16.12.11	3006	Wet	Spontaneous	PR-CB1	G1	1400	Medium
17.12.11	3012	Powder	Spontaneous	-	G1	1300	Medium
30.12.11	3023	Powder	Spontaneous	PR-CB1	G1	1000	Small
29.02.12	3053	Wet	Spontaneous	-	G1	1000	Small
01.03.12	3054	Wet	Spontaneous	-	G1	600	Small
15.03.12	3060	Wet	Spontaneous	-	G1	1200	Medium
04.12.12	3003	Transitional	Spontaneous	PR-CB1	G1	1300	Medium
01.02.13	3018	Wet	Spontaneous	CB1	G1	1000	Small
	3019	Transitional	Spontaneous	CB1	G1	1900	Large
	3020	Wet	Spontaneous	CB1-CB2	G1+G2	2000	Large
02.02.13	3021	Transitional	Spontaneous	CB1-CB2	G1	1800	Large
05.02.13	3022	Wet	Spontaneous	PR	G1	800	Small
	3023_1	Powder	Spontaneous	PR	G1	800	Small
	3023_2	Powder	Spontaneous	PR	G1	900	Small
	3024	Powder	Spontaneous	CB1	G1	1800	Large
13.04.13	3049	Wet	Spontaneous	PR	G1	1100	Medium
14.04.13	3050	Wet	Spontaneous	CB1	G1	1200	Medium
	3053	Wet	Spontaneous	CB1	G1	1300	Medium
03.02.15	16	Powder	Artificial	PR	G1+Dl	2200	Large
	17	Powder	Artificial	CB1	G1	2000	Large

FIGURE 4.1: Image of a typical powder-snow avalanche at VdlS released in the experiment on 3rd February 2015. The avalanche was triggered by an explosion from the PR area and most of the mass flowed over gully 1 and the rest of the mass flowed through Deylon gully (see Figure 2.1). Photo courtesy of SLF.

The avalanche path profiles and run-out distances were deduced from video recordings and photogrammetry for the artificial avalanches or photographs of the deposits for the spontaneous avalanches. As an example, Figure 4.2 shows the delimited deposition areas of several consecutive avalanches released between 1st and 5th February 2013. Since 2010, the GEODAR radar has provided an additional method of establishing the run-out distance, as it tracks the whole avalanche path.

A total of 15 powder-snow avalanches, 13 wet-snow avalanches and 5 transitional snow avalanches were analysed in this work. The histogram of the classification of the avalanches in function of their size and type of flow is given in Figure 4.3. In our database, all the transitional avalanches have long path lengths, at least more than 1000 m, with large vertical drops where the snow conditions might change along the track.

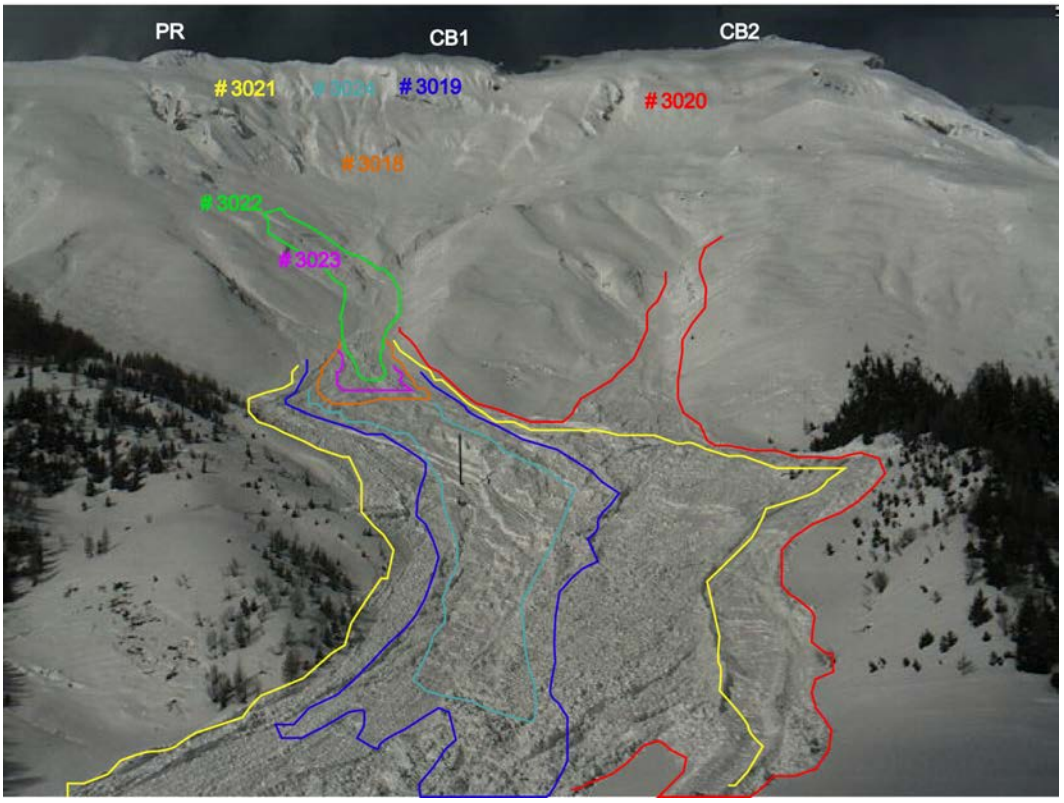

FIGURE 4.2: Deposits of the seven consecutive avalanches released in February 2013 (photo taken from location D). The number of each avalanche is located at the approximate height of the release area. The coloured lines delimit the run-out area.

4.3 Analysis of the avalanche signals

The seismic signals of the 33 snow avalanches are analysed in detail in both the time and frequency domains at different sites along the avalanche path. For some avalanches, the infrasound signal is also analysed following a similar procedure to that for seismic signals. The raw data are first transformed to ground velocity (m/s; seismic data) and to pressure (Pa; infrasound data) using the transfer functions indicated in Section 2.5. The seismic data are then analysed in detail in both the time (Section 4.3.1) and frequency (Section 4.3.2) domains, and divided into three sections related to the relative position of avalanche and sensor. Seismic signals contain information concerning avalanche size and type that can be extracted in the form the seismic indices defined in Section 4.3.3. In this study, all the seismic data of the avalanches analysed were acquired with the seismic stations B, C and D (Figure 2.1).

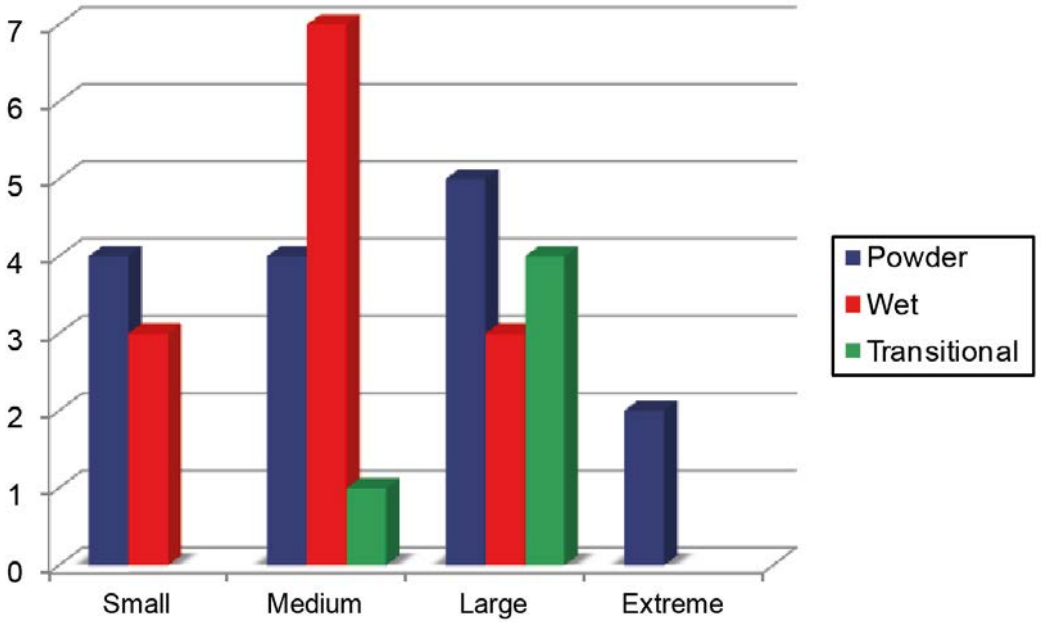

FIGURE 4.3: Histogram of the classification of the snow avalanches analysed in function of their size (small, medium, large, extreme) and type of flow (powder, wet and transitional).

4.3.1 Time domain analysis

Information on the evolution of a snow avalanche can be extracted from the analysis of the seismograms generated at different locations. The seismograms display a different shape at each location due to the geometrical characteristics of the distribution of the VdlS sensors. The sensors are located in a linear array with a separation of about 600 m between them (Table 2.1 and Figure 2.3). The assumption that seismic signals generated by the avalanche at any point of the path will be recorded at the same instant of time is reasonable, as the seismic waves propagate much faster (2000 - 3000 ms^{-1}) than the avalanche (maximum speeds of about 50 ms^{-1}). The differences in the amplitudes of the seismic recordings at the different locations are due to the attenuation of the seismic waves with distance and to local site effects. The maximum energy is thus recorded when the avalanche flows over or close to the sensor. Furthermore, the hypothesis of considering avalanches as a punctual seismic source is not valid at short distances or when the avalanche flows over the sensor (Vilajosana, 2008). The signatures of the seismic signals therefore change from one location to other because the avalanche approaches the sensors

at different instants of time and the distance between them is adequate to detect the evolution of the flow.

In contrast, infrasound signals are not influenced by the path (low attenuation at local distances) or site effects. The infrasound data also provide information on the evolution of avalanches as the signals are slightly attenuated with distance and they are sensitive to the type of flow regime of the avalanche. Avalanches usually develop a powder part in the upper section of their path which generates infrasound signals with high amplitudes; whereas the dense flow of the lower part of the avalanche path generates low infrasound amplitudes (Kogelnig et al., 2011b).

Rotation of the coordinate system

Snow avalanches tend to follow terrain features and the main down-slope direction. A coordinate system aligned with the local slope and with the main direction of the avalanche motion is more appropriate for determining correlations with the avalanche dynamic characteristics, which are also defined with the same coordinate system. Seismic data were acquired in the geographical coordinate system (zenithal, northsouth and eastwest). In this study, the data were rotated to a coordinate system aligned with the local slope and the main avalanche direction in which Z is the component normal to the slope (30° at B, 20° at C and 25° D), X is the component in the direction down the slope and Y is the cross-slope component, perpendicular to X and Z. These angles take into account the local slope of the seismic station locations (B, C and D of Figure 4.4). Figure 4.4 shows the main direction of the avalanche path at VdlS and the resulting three rotated components of the avalanche seismic signals. The main direction of the avalanche (X) forms an angle of 130° with the North direction (Figure 4.4).

For an example of the results of the rotation of the three components of the seismic signal, see Figure 4.5. The component X displays higher amplitudes than components Z and Y, as it represents the main direction of the avalanche motion (Figure 4.5).

Seismic signal duration and sections

In order to classify the different snow avalanches, I first determine seismically the duration of the avalanche. The total duration of the avalanche was estimated as

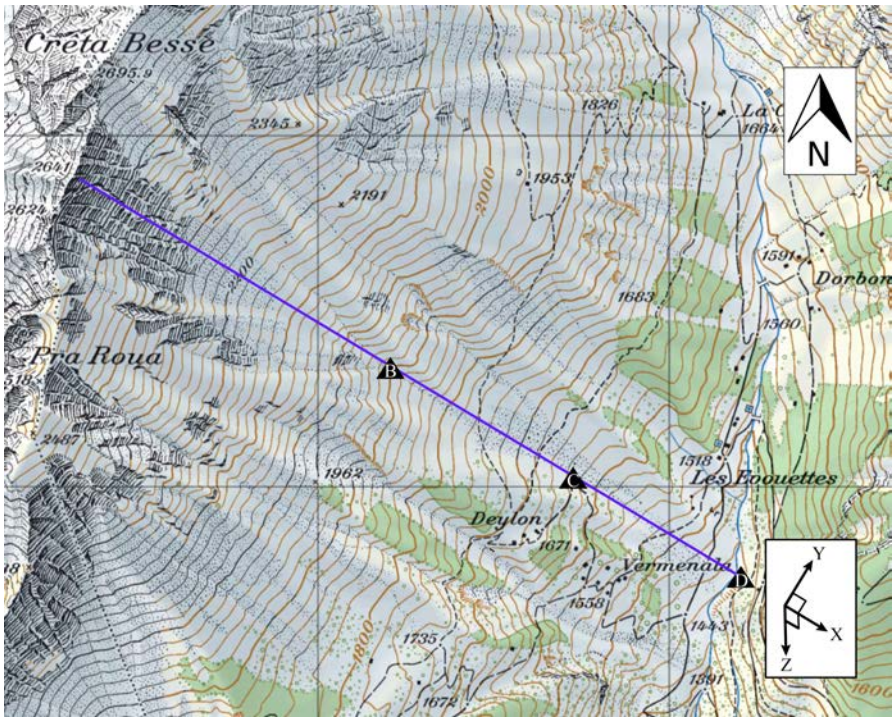

FIGURE 4.4: Fig. 1. Overview of VdlS. The blue line represents the main path usually followed by the avalanches. X, Y and Z represent the rotated coordinate system of the seismic components

the temporal length of the seismic signal generated from the first movements of the avalanche until the avalanche stopped.

To estimate the total duration, I previously calculated the mean amplitude of the envelope of the background noise using 20 s of the pre-avalanche seismic signal. The total envelope, A_t (t), is calculated as:

$$A_t = \sqrt{{A_z}^2 + {A_x}^2 + {A_y}^2} \tag{4.1}$$

where A_t (ms^{-1}) is the total amplitude smoothed each 0.5 s with a moving average, A_z (ms^{-1}) is the amplitude in the direction normal to the slope, A_x (ms^{-1}) is the amplitude in the direction down-slope, and A_y (ms^{-1}) is the amplitude in the cross-slope direction.

The initiation of the avalanche signal (t_i) was thus derived from the total envelope of the seismic signal at B and its end (t_f) from the total envelope of the seismic signal recorded at the station closest to the avalanche run-out zone (B or C). The

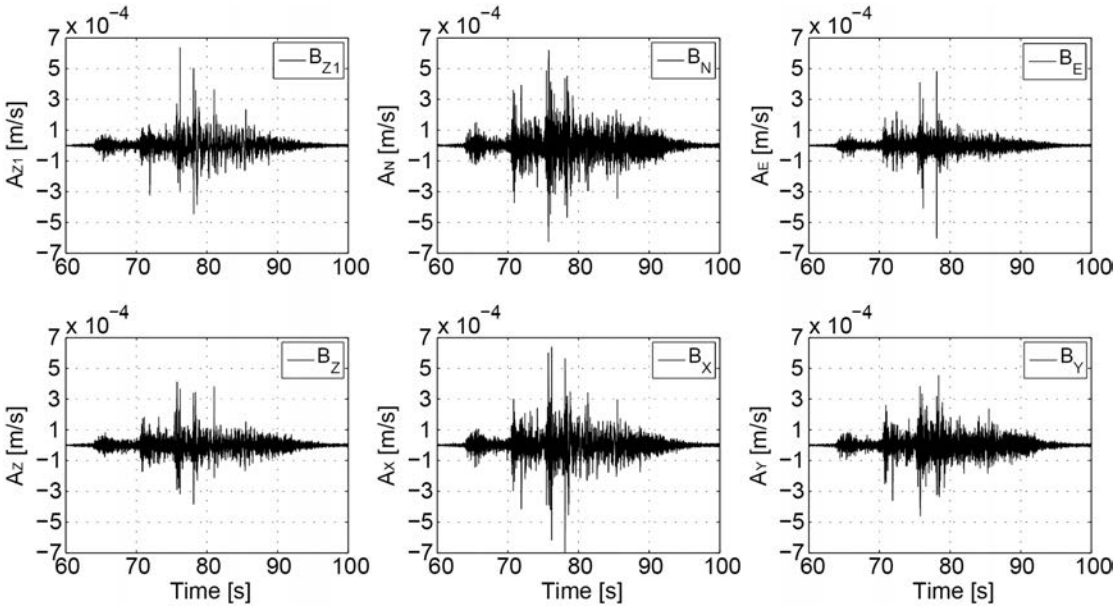

FIGURE 4.5: Seismic signals of the three components represented in the geographical coordinate system (top, zenithal (Z1), northsouth (N) and eastwest (E)) and the three coordinates rotated (bottom, Z, X and Y) of the avalanche #16 at B.

seismic signal duration, T_A (s), is defined as:

$$T_A = t_f - t_i \tag{4.2}$$

The initiation of the avalanche signal was defined as the instant when the mean amplitude of the total envelope, calculated in a sliding window of 1 s, exceeded twice the background noise. The same procedure was used to determine the end of the avalanche signal.

The total envelope of the seismic signal of the small wet-snow avalanche #3018 is shown in Figure 4.6 as an example. The initiation (t_i) and end (t_f) instants, which define the seismic signal duration of the avalanche, were determined by analysing the seismic signal at B.

Three different sections in the seismic signal have been distinguished that characterize the relative position of the avalanche with respect to the sensor (Vilajosana, 2008). This information provides the approximate location of the avalanche in space and time. These sections were previously defined in the frequency domain (Vilajosana, 2008). In this work, however, the definition of these sections has been modified and enlarged to the time domain. The division of the signal into these

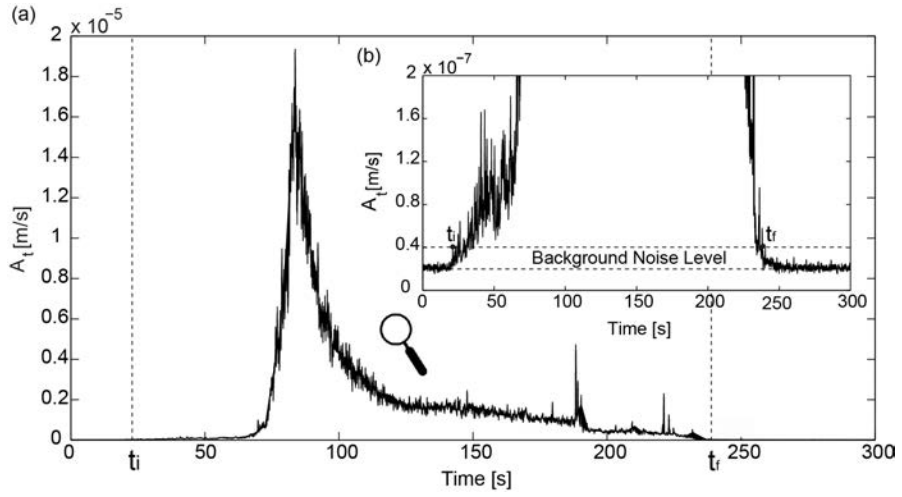

FIGURE 4.6: (a) Envelope of the seismic signal of the wet-snow avalanche #3018 at B. (b) Close-up of the envelope of the seismic signal at B.

sections was obtained by analysing the seismic time-frequency series and correlating it with the FMCW radar signal of the avalanche (see Section 4.4). At locations where the avalanche flows over the seismic sensor, the three sections in the time domain are defined as:

- The signal onset section (SON) characterizes the phase during which the avalanche is approaching the sensor. In this section, the amplitudes of the time series slowly increase.
- The signal over section (SOV) characterizes the phase during which the avalanche flows over the sensor. The maximum seismic energy due to the minimal attenuation of the seismic waves is recorded in this section. The avalanche temporal length, T_L, at the specific path location is defined as the duration of the SOV section.
- The signal end section (SEN) is the interval during which the avalanche is moving away from the sensor. This interval is characterized by a slow decrease in the seismic amplitudes until the avalanche completely stops. Higher amplitude peaks are superimposed on the decreasing time series signal.

Interpretation of the avalanche signals

I select two different flow type and size avalanches as examples to describe the methodology applied in this work. The first avalanche, #16, was released in the

experiment on 3rd February 2015 (Table 4.1). The avalanche was triggered by an explosion at PR at 10:20 am (Figure 4.1). The main part of the avalanche followed gully 1 and flowed over cavern B. The flow arrived at the run-out zone and flowed over cavern C before reaching the valley bottom. The second avalanche #3018 was a small wet avalanche, spontaneously released on 1st February 2013 at 2:54 pm (Table 4.1). The avalanche started at the bottom of CB1 (Figure 4.2) at the approximate height of cavern A. All the mass flowed over cavern B where part of the mass was deposited. The front stopped at the end of gully 1, some 300 m from cavern C (Figure 2.1).

The seismic and infrasound signals from avalanches #16 and #3018 recorded at the three sites (seismic: B, C and D; infrasound: I), and divided into the three sections previously defined, are shown in Figure 4.7. The seismograms of the large avalanche, #16, have maximum amplitudes of the order of 10^{-4} ms^{-1} exceeding the background noise at the three locations because the avalanche flowed over B and C, and the front stopped close to D. The signals from B and C are thus sectioned into three parts as the avalanche flowed over them. Maximum amplitudes are recorded in the SOV section, which represents the avalanche flowing over the sensor. A narrow amplitude peak stands out at the beginning of the signal from D and I, and after t_i. This peak, which is not visible at this scale of representation in the seismograms from sites B and C, is generated by the airwave of the explosion that triggered the snow avalanche (see Figure 3.6).

The seismograms of the small avalanche, #3018, have maximum amplitudes of the order of 10^{-5} ms^{-1} at B where the avalanche flowed over it (SOV section; Figure 4.7). The front of avalanche #3018 stopped 300 m before C and 960 m from D. The seismic amplitudes of this avalanche are strongly attenuated with distance. The amplitudes at C and D are thus small, with mean amplitudes of the order of the background noise at D. The shape of the seismograms at these sites is similar because the avalanche was always approaching them: not flowing over either of them. Comparing the avalanche signals of different size, it is noteworthy that the large avalanche, #16, has maximum amplitudes one (B) or several (C and D) orders of magnitude greater than the small avalanche, #3018.

The infrasound signal (e.g., I in Figure 4.7), however, displays a different shape from the seismograms as the amplitudes are practically non-attenuated at these distances (see Section 3.3). The maximum amplitudes, therefore, do not correlate

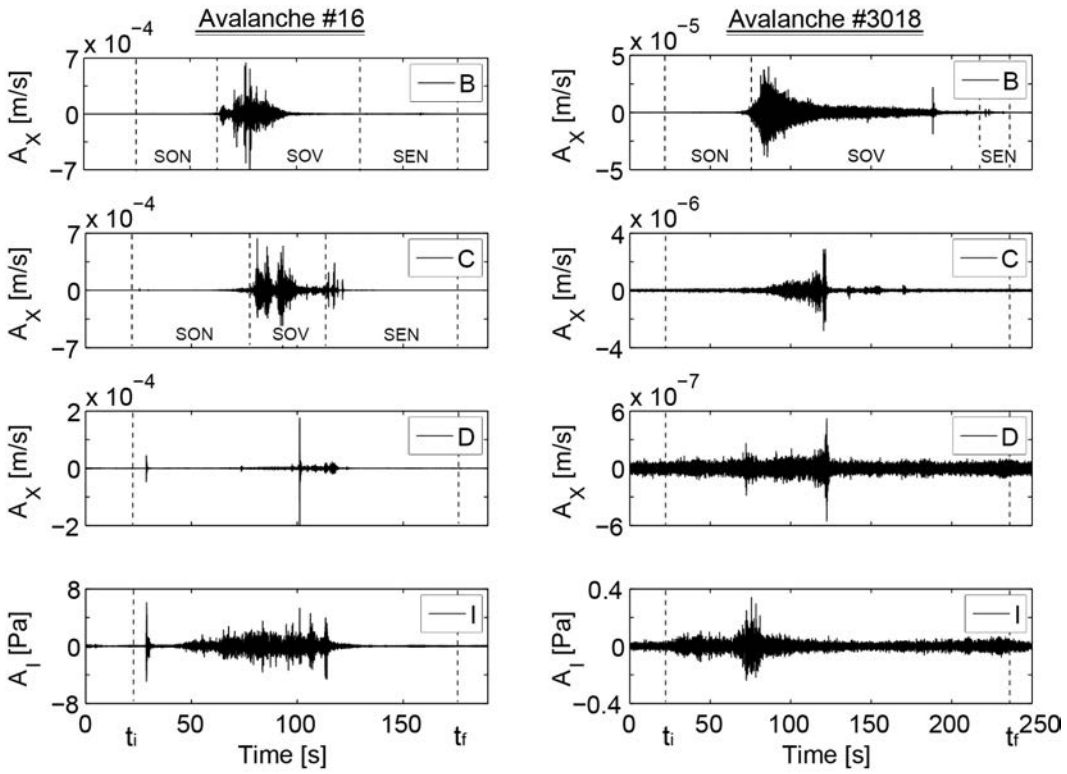

FIGURE 4.7: Down-slope component (X) of the seismic signals recorded at B, C and D, and the infrasound (I) signals of the large powder avalanche #16 (left) and the small wet avalanche #3018 (right). The signal is divided in three sections (SON, SOV and SEN) at the locations where the avalanche flowed over the sensor. The seismic signal duration is defined by the time interval [t_i, t_f].

well with the minimum relative distances between the avalanche and the sensor. The differences in the amplitude of the infrasound signals of avalanche #16 and #3018 are noteworthy. The former has a much greater amplitude than the latter, not only because of its larger size, but also because of the different flow types. Powder avalanches generate higher energetic infrasound signals as they propagate faster and they are characterized by the external powder cloud and turbulent part; the main sources of infrasound (Kogelnig et al., 2011b).

To analyse the individual sections of both example avalanches, the envelope time series are represented (Figures 4.8-4.10). For sites outside the avalanche path, such as, for example, C for the small avalanche, #3018, and D for both avalanches, none of these sections are defined (Figure 4.7). The SON sections of the powder-snow avalanche #16 correspond to the time intervals [25.0-63.6] s for B and [25.0-78.8] s for C (Figure 4.8 left). The first peak recorded in all the envelope signals, generated by the airwave from the explosion that arrived earlier at the upper location B (≈

25 s) and propagates to D ($\approx$ 29 s), is not considered in the interpretation of the time series. The envelope in B and C recordings shows how the amplitude increases slowly until the avalanche front is close to the sensor (instants t_b and t_c in Figure 4.8), characterized by a sudden and fast increase in the amplitudes. The envelope of D hardly increases the amplitude until the avalanche approaches C (t_c).

The SON section of the wet-snow avalanche, #3018, at B corresponds to the time interval [22.9-75.3] s (Figure 4.8 right). The envelope of the SON section of this avalanche displays similar characteristics to the SON sections of the powder-snow avalanche, #16. Due to the small size of the avalanche and the large distance of propagation of the seismic waves to C and D, the amplitudes of the envelope time series in this time interval are practically steady, with values of the order of the background noise.

The powder-snow avalanche, #16, flowed over B and C generating the SOV sections between 63.6 and 130.0 s; and 78.8 and 113.6 s, respectively (Figure 4.9). Both envelopes are characterized by a significant increase in amplitudes when the avalanche front arrives at the location of the seismic sensor (t_b and t_c). The subsequent parts of the avalanche flowing over the sensor generate consecutive high amplitude packets in the time-series (e.g. [64-89] s at B and [79-97] at C; Figure 4.9). A decrease in amplitudes, which generates the typical coda shape of the seismograms (Figure 4.7), is then recorded when the tail of the avalanche is flowing over the sensor (e.g. [89-130] s at B and [97-114] s at C). Several peaks along this coda are superimposed in the signal. It is noteworthy that the avalanche has different temporal lengths (length of the SOV section) at B and C, possibly due to the fact that not all the avalanche mass arrives at the lower part of the path, but is deposited along the way. The amplitude of the envelope at D (Figure 4.9 left) slowly increases over this time interval until the avalanche approaches the lower parts of the path. A strong peak is observed at about 110 s at D, possibly caused by the impact of the front of the avalanche on the bottom of the valley and the counterslope. When the avalanche is flowing over a sensor, the shapes of the envelope time series at different locations do not correlate between them. This reaffirms the hypothesis that the punctual source model is not valid at short distances (Vilajosana, 2008).

The wet-snow avalanche, #3018, only flowed over B generating a SOV section between 75.3 and 216.9 s (Figure 4.9 right). The shape of the envelope differs

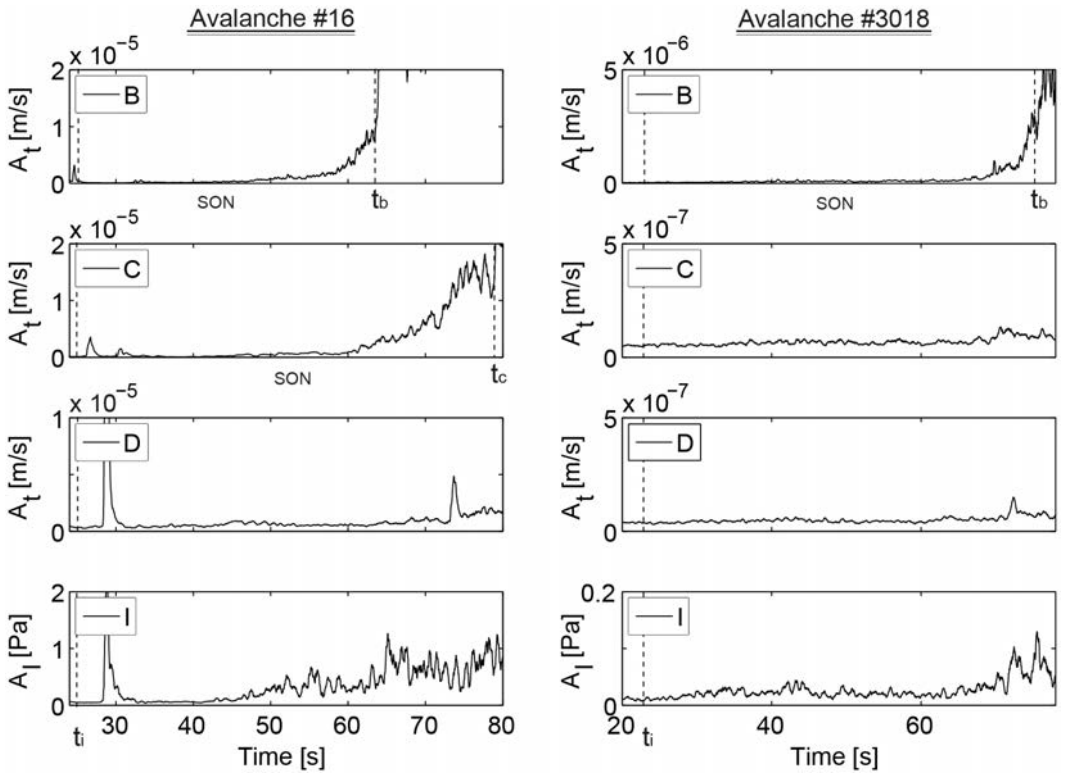

FIGURE 4.8: Total envelope of the SON sections of the seismic signals recorded at B, C and D, and the envelope of the infrasound signals of the large powder avalanche, #16 (left), and the small wet avalanche, #3018 (right). The avalanche front arrives at B at t_b and at C at t_c.

from that of the SOV sections of the powder-snow avalanche. A gradual increase in amplitudes until it reaches a maximum value characterizes this section. A decreasing in the amplitudes of the envelope, which produces a typical long seismic coda (Figure 4.7), characterizes the rest of the SOV section, with superimposed peaks at the end of the coda. At the lower sites (C and D), an increase in the amplitudes is observed over this time interval. The envelopes display a similar shape in the recordings from both sensors, owing to the fact that the avalanche is approaching them but it is still far from both. Hence, the hypothesis of a punctual source is more plausible in this case.

The SEN sections of the powder- snow avalanche, #16, correspond to the time intervals [130.0-177.0] s at B and [113.6-177.0] at C (Figure 4.10). The section at B is characterized by a slow decrease in the mean amplitude of the envelope with superimposed peaks of much higher amplitude. At C and D, the envelopes are characterized by high-amplitude peaks, possibly caused by the stopping of the main part of the avalanche, and followed by a strong amplitude decrease. The

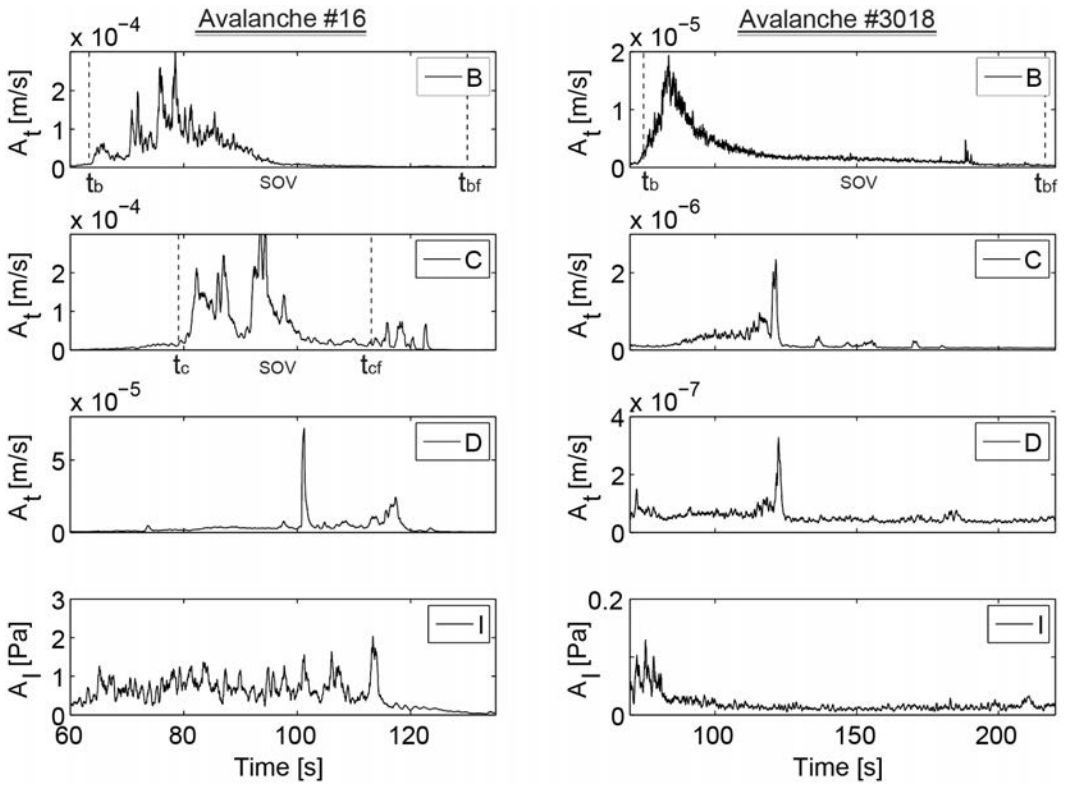

FIGURE 4.9: Total envelope of the SOV sections of the seismic signals recorded at B, C and D, and the envelope of the infrasound signals of the large powder avalanche, #16 (left) and the small wet avalanche, #3018 (right). The avalanche front arrives at B at t_b and at C at t_c and the end of the tail passes over B at t_{bf} and over C t_{cf}.

wet-snow avalanche, #3018 (Figure 4.10), shows similar characteristics to those of the powder-snow avalanche in the SEN section between 216.9 and 238.8 s.

All the characteristic peaks detected at the end of the SOV and SEN sections were also observed by previous researchers (Suriñach et al., 2000; Biescas, 2003; Kogelnig et al., 2011b) and correlate well with the deposition of the avalanche mass, as I will show in Chapter 6. Although here only two representative avalanches are examined in detail, similar signatures of the seismograms and the infrasound signals are observable for the rest of the avalanches. This fact enhances faith in the reproducibility of the avalanche signals mentioned previously by other authors (Suriñach et al., 2001; Biescas, 2003; Vilajosana, 2008; Kogelnig, 2012).

Regarding the infrasound envelopes, the powder-snow avalanche, #16, displays maximum amplitudes ($\approx$ 1 Pa) in the interval from when the avalanche reached B until it reached the bottom of the valley (Figure 4.9); whereas the wet-snow

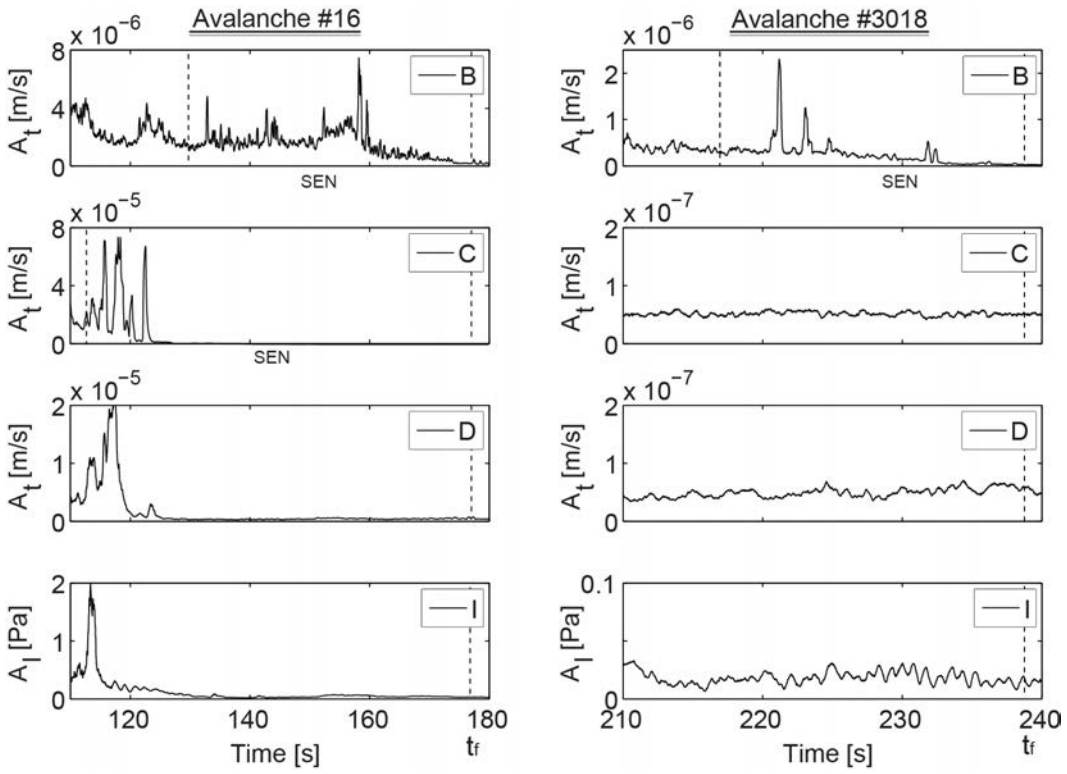

FIGURE 4.10: Total envelope of the SEN sections of the seismic signals recorded at B, C and D, and the envelope of the infrasound signals of the large powder avalanche, #16 (left), and the small wet avalanche, #3018 (right). The end of the avalanche is denoted by t_f.

avalanche, #3018, displays maximum amplitudes ($\approx$ 0.1 Pa) when the avalanche was flowing over B (Figure 4.9).

Cumulative energy quantification

The percentage of the seismic energy dissipated and recorded at a given site is represented in the cumulative energy (CE) diagram. This time-series diagram, similar to the Husid diagram for accelerograms (see Section 3.4 for the definition), shows the cumulative energy CE (t) ($(\mathrm{ms}^{-1})^2 \cdot \mathrm{s}$) dissipated through time:

$$CE(t) = \int_{t_i}^{t} A(t')^2 dt' \tag{4.3}$$

where, t_i is the initiation of the avalanche signal and $A(t')$ is the amplitude of the envelope of the ground velocity (ms^{-1}) at time t'.

The CE diagrams of each seismic component and the total envelope of the seismic signal of avalanches #16 and #3018 are shown in the Figure 4.11. The diagrams show that the down-slope component (X) of the ground motion is the most energetic, in agreement with the fact that this component corresponds to the main direction of the avalanche motion. The vertical ground motion, however, is in general the least energetic. The diagrams show a reproducible shape at the locations where the avalanche flows over the sensor (see avalanche #16 at B and C and avalanche #3018 at C in Figure 4.11). At locations the avalanche did not flow over, the shape of the diagram varies depending on the size of the avalanche and the type of flow.

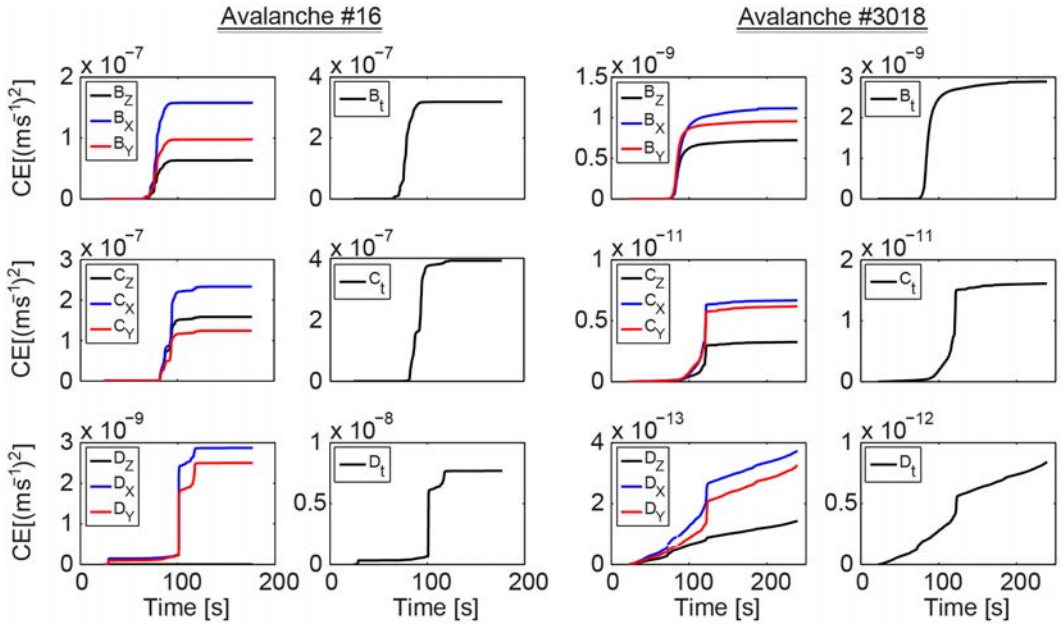

FIGURE 4.11: Cumulative energy diagrams calculated for each seismic component (Z, X and Y) and total envelope (t) of the seismic signals generated by the powder-snow avalanche #16 (left) and the wet-snow avalanche #3018 (right) at each seismic station (B, C and D).

In order to compare the diagrams for the different types of avalanche, the normalized cumulative energy in percentage, $CE(\%)$, is calculated as:

$$CE(\%) = \frac{CE}{max(CE)} \cdot 100\% \tag{4.4}$$

The $CE(\%)$ diagrams for each location are plotted together to compare the different shapes of the increase of the energy (Figure 4.12). At locations where the avalanche flowed over the seismic sensor (avalanche #16 at B and C and avalanche

#3018 at C in Figure 4.12), the increasing CE displays similar features. In the SON section (e.g. $[t_i,\ t_{b,c}]$ in Figure 4.12) the increase in the energy is very smooth, due to wave attenuation (see Section 3.3). The instant when the avalanche reaches the seismic sensor is characterized by a sudden increase in $CE(\%)$ (t_b and t_c in Figure 4.12). The SBO section (e.g. $[t_{b,c}\ ,\ t_{bf,cf}]$ of Figure 4.12) is characterized by a sharp increase of the $CE(\%)$ until a threshold (e.g. $\approx$ 92 s at B and $\approx$ 100 s at C for avalanche #16, and $\approx$ 107 s at B for avalanche #3018) where the slope of the $CE(\%)$ curve is practically constant for powder-snow avalanches and increases very slowly for wet-snow avalanches. The SEN section (e.g. $[t_{bf,cf}\ ,\ t_f]$ in Figure 4.12) is characterized by a negligible increase of $CE(\%)$. The slope of the $CE(\%)$ diagrams at the beginning of the SOV section for powder-snow avalanches is usually steeper than the slope of the $CE(\%)$ diagrams of wet-snow avalanches; probably because of the higher velocity of propagation of powder flows (Figure 4.12). The slope of the CE (%) diagrams of wet-snow avalanches is usually smoother; the slope of the curve starts increasing with a steep slope that is gradually reduced along the passing of the tail of the avalanche over the sensor (e.g. t $>$ 120 s for avalanche #3018 in Figure 4.12). The steepest part of the SOV section for both types of flows is often characterized by a stepwise increase of CE (e.g. time interval of [63-90] s for avalanche #16 at B) due to the arrival of the different internal surges of the avalanche, and the action of the dynamical processes of entrainment and deposition.

The shape of the $CE(\%)$ diagrams at locations the avalanche did not flow over the sensor (avalanche #16 at D; avalanche #3018 at C and D; Figure 4.12) is variable, depending on the relative distance between the stopping phase of the avalanche and the location of the sensor. If the avalanche stopped relatively close to the sensor (see the diagram at D for avalanche #16 and at C for avalanche #3018), the diagram is quite similar to those of the avalanche flowing over the sensor. A sudden increase in the energy is observed when the avalanche is close to the sensor (e.g. $\approx$ 100 s at D for avalanche #16 and $\approx$ 117 s at C for avalanche #3018). At locations far from the avalanche path, e.g. at D for avalanche #3018, the diagram is characterized by a gradual increase of $CE(\%)$ during the whole avalanche motion. A more accentuated increase of $CE(\%)$ correlates well with the increase of the amplitude of the diagram at C (t $\approx$ 117s), generated by the stopping phase of the head of the avalanche (Figure 4.9).

The $CE(\%)$ diagram for the infrasound of the powder-snow avalanche, #16, shows

a gradual increase of the curve in the time interval when the avalanche propagates faster until a threshold when the increase is practically negligible and correlates well with the avalanche stopping phase (Figure 4.12). The CE diagram of the infrasound of the small wet-snow avalanche, #3018, shows a significant increase of the amplitude between 60 and 80 s when the infrasound signal exceeded the background noise level (Figure 4.12).

The CE diagrams provide a novel representation of the avalanche seismic and infrasound signals in the time domain. When the avalanche flows over a specific location, these diagrams show reproducible characteristics (a smooth increase of the energy in the SON section, a sharp increase when the avalanche reaches the location and a slow increase in the last part of the SOV section and in the whole SEN section) that are useful to characterize the previously defined avalanche sections. When the avalanche does not flow over a specific location, in general the CE diagrams display a gradual increase of the energy throughout the whole avalanche duration.

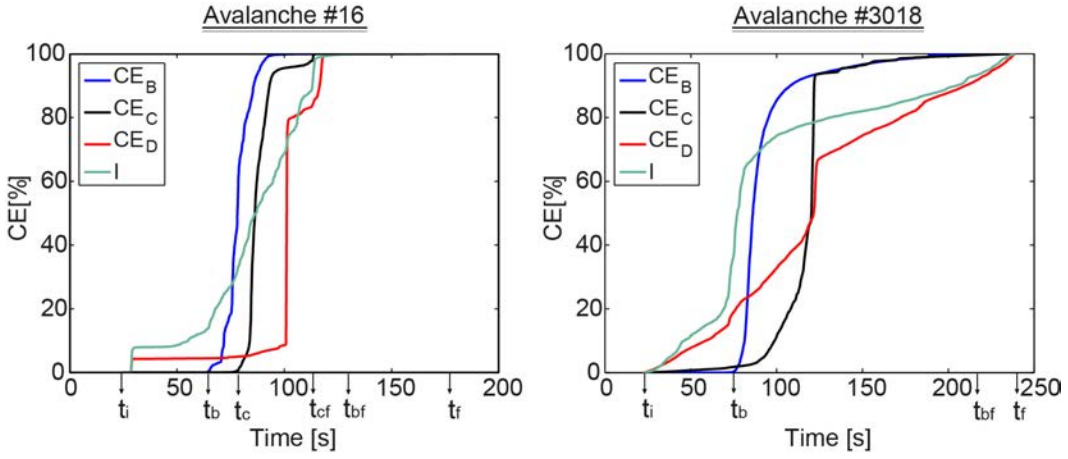

FIGURE 4.12: Cumulative energy diagrams in percentage calculated for the infrasound signals (I) and the total envelope of the seismic signal of the powder avalanche, #16 (left), and the wet-snow avalanche, #3018 (right), at each seismic station (B, C and D). The avalanche signal duration is denoted by the period between t_i and t_f. The arrival of the avalanche front at B and C is denoted by t_b and t_c, and the end of the tail passing over B and C by t_{bf} and t_{cf}.

4.3.2 Frequency domain analysis

The frequency analysis of the signals was conducted using the spectrograms, the power spectra of the signals and the cumulative diagrams of the signal filtered into frequency bands. Spectrograms show the time evolution of the frequency content of the seismic and infrasound signals. These diagrams were previously used to characterize snow avalanches and distinguish them from other seismic sources (Biescas et al., 2003; Van Herwijnen and Schweizer, 2011b,a). In this work, spectrograms are used to characterize the different sections of an avalanche. For a detailed inspection of the frequency content of each avalanche region flowing over the sensor, power spectra provide the total amount of information contained in the signal for a given frequency.

Spectrograms and Power spectra

The spectrograms of the snow avalanche signals were calculated using the short-time FFT (Fast Fourier Transform) with a Hanning Window (length 0.32 s) and 50% (0.16 s) overlap. Each spectrogram displays a different shape depending on the location of the seismic sensor and its position relative to the moving avalanche. The range of frequencies represented is from 1 Hz to the Nyquist frequency (50 Hz for data acquired at 100 Hz and 100 Hz for data acquired at 200 Hz). The spectrograms represent the evolution in time of the frequency content of the signal. The spectral amplitudes of the signals (in this study normalized in dB for better representation) are defined by the different colours of the colour bar: red corresponding to the highest, and blue to the lowest amplitudes. As examples, the spectrograms of the seismic signals in the down-slope direction, the most energetic, and the infrasound signals of avalanches #16 and #3018 are represented in Figure 4.13. The gradual appearance of the energy at the different frequencies in the seismic spectrogram is a characteristic of mass movements (Suriñach et al., 2005). The features of the spectrograms observed at each seismic section (similar sections were previously defined in Vilajosana (2008)) are:

- The SON section is characterized by an increase of the energy content of the higher frequencies while the avalanche is approaching the sensor. This is caused by the anelastic attenuation of the seismic waves (e.g. Figure 4.13).

- The SOV section displays the highest amplitudes for the entire frequency spectrum. The pass of the first parts of the avalanche over the sensor generates the highest energy in the spectrogram with a decrease in energy during the pass of the tail (e.g. Figure 4.13).
- The SEN section is characterized by a decrease of the amplitudes of the higher frequencies while the avalanche is moving away from the sensor until it finally stops (e.g. Figure 4.13).

High frequency peaks characterize the end of the SOV and SEN sections associated with the mass deposition process (e.g. Figure 4.13).

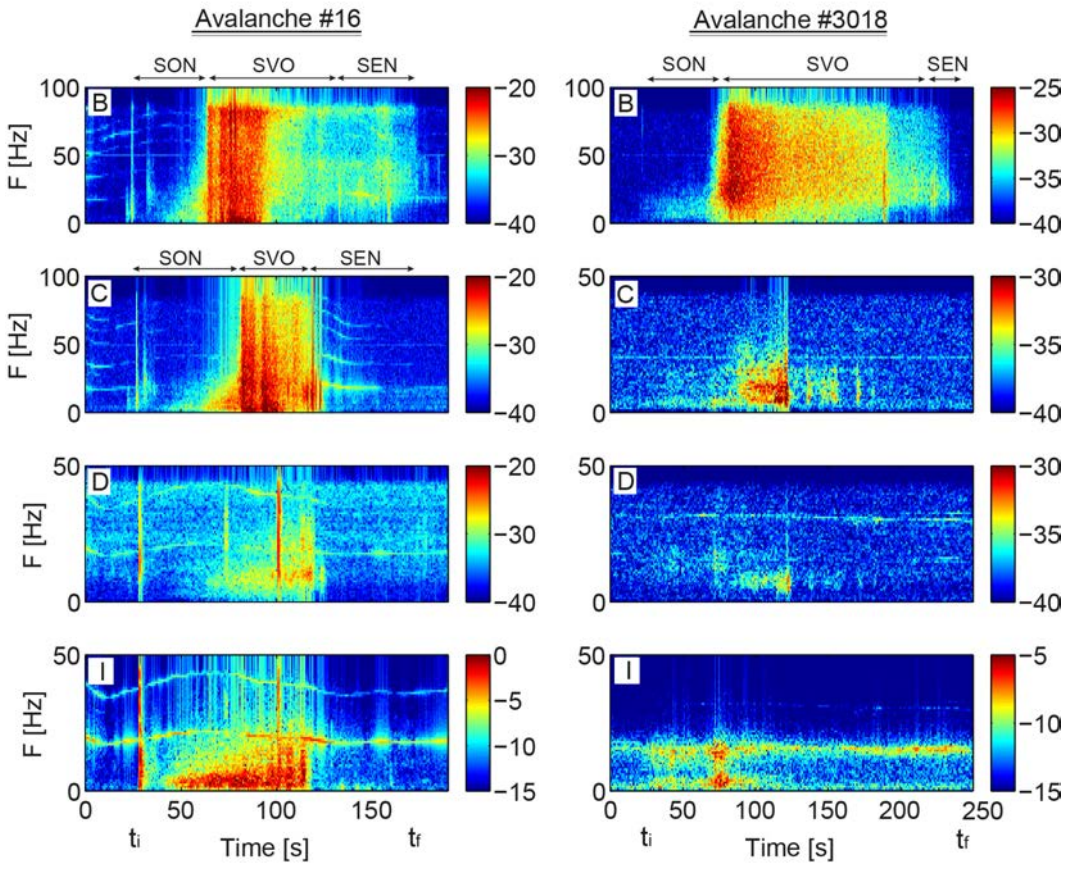

FIGURE 4.13: Spectrograms of the seismic signals of the down-slope component of the seismic and the infrasound signals (I) at the different locations (B, C and D) of the large powder-snow avalanche, #16, and the small wet-snow avalanche, #3018.

The spectrograms display the typical triangular shape when the avalanche is approaching the sensor, i.e., in the SON sections (Figure 4.13). The triangular shape also characterizes sites outside the avalanche path, until the arrival of the main

part of the avalanche at lower altitudes, e.g. at D for avalanche #16 and at C for avalanche #3018. The SOV section of the spectrogram at B can be subdivided into two subregions (Figure 4.13): the pass of the front and part of the body of the avalanche generates the energetic first part of the spectrogram (e.g. the time interval of [63.6- 89] s in avalanche #16 at B) followed by a less energetic part generated by the dense tail of the avalanche (e.g. the time interval of [89-130] s in avalanche #16 at B). The spectrograms of the infrasound signals are characterized by low frequencies (f $<$ 20 Hz). The maximum energies in the higher part of the spectrum (f $>$ 10 Hz) are recorded in the stopping phase of avalanche #16 ($>$ 100 s) and when the avalanche is flowing over B for avalanche #3018 (Figure 4.13).

Multiple bands of frequencies of approximately 15, 30, 50, 70 and 85 Hz are remarkable in the spectrograms of the artificial avalanche #16 caused by the helicopter flying around VdlS (Figure 4.13; left). This seismic energy is negligible comparing with the energy generated by the movement of the avalanche. However, it can be notable in some parts of the infrasound spectrum. Moreover, the signal of the explosion that triggered the avalanche #16 is also remarkable at the beginning of the SON section at B ($\approx$ 25 s), C ($\approx$ 27 s), and at D and I ($\approx$ 29). The echo of this explosion is also visible in the spectrograms of B ($\approx$ 32 s) and C ($\approx$ 30 s) (Figure 4.13; left).

A detailed analysis of the frequency content of each section is conducted using the normalized power spectra. These spectra were obtained using a FFT. The amplitudes of the spectra were normalized to define the width of the spectra using an unified criterion for all the signals. Hence, the width of the normalized power spectrum was considered in this work to be the range of frequencies with normalized amplitudes exceeding 0.2. The spectrum of each section of avalanches #16 and #3018 are shown in Figure 4.14. The energy generated by the explosion and its echo was not considered in the computation of the spectra of the avalanche #16.

The SON section is usually characterized by low frequency spectra (f $<$ 20 Hz). In this section the avalanche is approaching the sensor and the higher frequencies are attenuated due to the anelasticity (Figure 4.14). Maximum amplitudes for all the frequencies of the spectrum are recorded in the SOV section, as the attenuation is minimum when the avalanche flows over the sensor. The spectra of the SOV sections of the powder-snow avalanche, #16, are characterized by low-frequency content with maximum energies for frequencies below 5 Hz. The SOV spectrum

of the wet-snow avalanche, #3018, however, is characterized by high-frequency content with frequencies in the range of [16-80] Hz. Comparison of the avalanche spectra shows that the powder-snow avalanche generates a lower-frequency spectrum than the wet-snow avalanche (Figure 4.14). A further characterization of the spectrum of each avalanche type and region will show a connection between the flow regimen and the signal generated in the frequency domain (Chapter 6). The SEN section is characterized by high amplitude seismic peaks (previously observed in the time series and the spectrograms) caused by the mass deposition close to the sensor and thus by a high-frequency content spectra. Part of the mass of the tail may still be flowing close to the sensor, generating very high-frequency vibrations up to 85 Hz, e.g. the SEN section of avalanche #16 (Figure 4.14). Moreover, part of the high frequency peaks characteristics of the spectra SON and SEN sections for avalanche #16 can be also generated by the helicopter (Figure 4.14), as it is remarkable in the spectrograms (Figure 4.13). The last part of the SEN section is characterized by a decrease of the higher-frequency amplitudes due to fact that the mass is moving away from the sensor, as the spectrograms show (Figure 4.13).

Cumulative Energy quantification in the frequency domain

To quantify which part of the spectra of the avalanches is the most energetic, the CE of the signals separated into different frequency bands were calculated. After testing different frequency bands, a band of 10 Hz was selected to distinguish between different avalanche flow regimes. Hence, the seismic energy in the downslope direction, the most energetic, was divided into frequency bands of 10 Hz, from 1 Hz to 40 Hz for seismic recordings sampled at 100 sps and 90 Hz for recordings sampled at 200 sps. A 4th-order Butterworth bandpass filter was used to obtain the filtered bands. The normalized $CE(\%)$ curves for each band are represented in Figure 4.15.

The diagram of the powder-snow avalanche, #16, shows that the band of [1-10] Hz is the most energetic at sites the avalanche flowed over, B and C (Figure 4.15). The diagram of the wet-snow avalanche, #3018, shows that the band of [1-10] Hz is the least energetic at B, where the avalanche flowed over. At sites outside the avalanche path the most energetic band is usually the lowest frequency band of [1-10] Hz. However, the diagrams of large avalanches that suddenly stopped close to the sensor, e.g. the diagram at D for avalanche #16, which stopped in

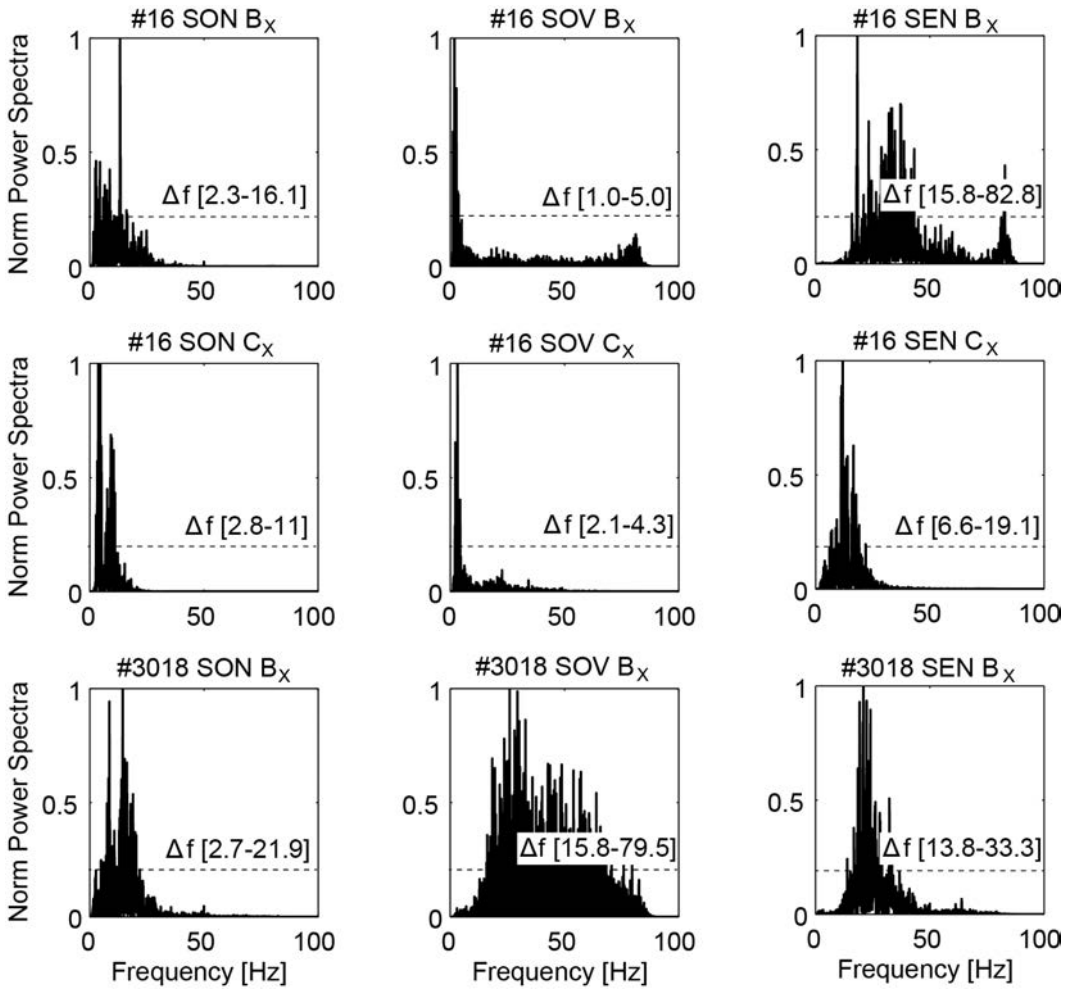

FIGURE 4.14: Normalized power spectra of the down-slope component calculated for the three sections of the seismic signals at recordings where the avalanche flowed over the sensor, at B and C for the powder-snow avalanche, #16, and at B for the wet-snow avalanche, #3018. The width of the spectra, Δf, for each region are considered the range of frequencies with amplitudes exceeding 0.2.

the valley bottom, shows that the most energetic band is the [10-20] Hz band. In each diagram, the relative position between the CE curves corresponding to the low-frequency bands and higher-frequency bands is dependent on the type of avalanche flowing over the sensor.

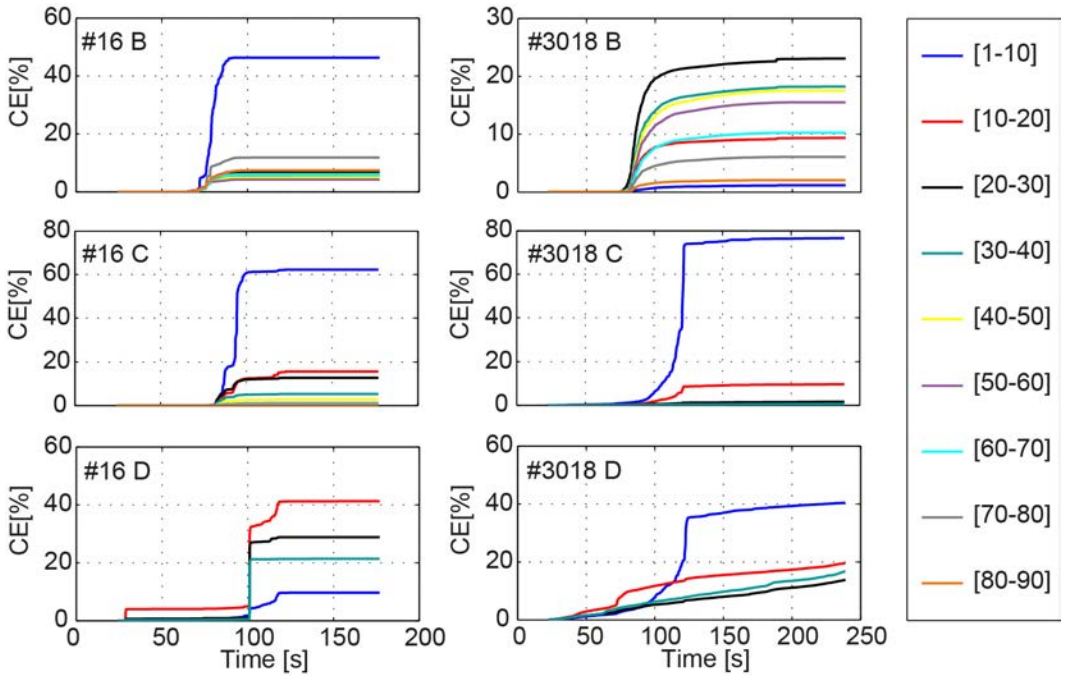

FIGURE 4.15: $CE(\%)$ diagrams of the seismic signals filtered in frequency bands of the powder-snow avalanche, #16 (left), and the wet-snow avalanche, #3018 (right), at each location (B, C and D).

4.3.3 Avalanche quantification indices

The seismic signals contain information concerning avalanche size and type that can be extracted in the form of a set of seismic indices. Following a similar procedure to that applied to evaluate the ground motion of earthquakes (see Section 3.4), the following parameters were calculated: the peak ground velocity of the total envelope ($PGVE$) of the seismic signal, the signal intensity (I) and the frequency parameters (P). Before calculate these indices, all the signals were filtered (1 Hz to 45 Hz) with a 4th-order Butterworth bandpass filter with the aim of homogenizing all the data acquired with different sample rates.

The Peak Ground Velocity of the Envelope (PGVE) (ms^{-1}) corresponds to the maximum value of the $A(t)$ time series:

$$PGVE = max(A(t)) \tag{4.5}$$

The avalanche intensity, $I(ms^{-1})^2 \cdot s$, is defined as a measure of the ground shaking intensity of the avalanche. The avalanche intensity is the maximum of the

cumulative energy ($CE(t)$):

$$I = max(CE(t)) \tag{4.6}$$

To quantify the distribution pattern of seismic energy observed, the frequency parameters, P_{1-n}, were defined as the ratio between the intensities of the lowest frequency band and those of the other bands:

$$P_{1-n} = \frac{\int_{t_i}^{t_f} A^2_{x[1,10]} dt}{\int_{ti}^{t_f} A^2_{x[10\cdot(n-1),10\cdot n]} dt} \quad for \;\; n = 2, ..., 4 \tag{4.7}$$

where n is a number between 2 and 4, depending on the frequency band; t_i and t_f represent the initial and end instants of the avalanche signal; and $A_{x[10\cdot(n-1),10\cdot n]}$ is the amplitude of the bandpass-filtered seismic signal component down-slope.

All the values of the seismic indices calculated for all the avalanches anlysed in this work are presented and compared in the chapter containing the results (Chapter 6).

4.4 Comparative analysis of the avalanche signals

In order to identify internal flow structures and flow regimes, data from two FMCW radars buried in the ground along the avalanche path were analysed. At VdlS, the FMCW radars are buried in the ground in the middle of the avalanche path and looking upward in a slope-normal orientation to monitor the avalanche flowing over them. Measuring the intensity of the received electromagnetic signal and its corresponding height provides information on the avalanche profile, and snow cover entrainment and deposition (Sovilla and Bartelt, 2002). The intensity of the reflected signal depends on the structure of the reflector. Higher intensities correspond to larger granules and to moister or denser snow. The reflected signal, however, can also be influenced by the subjacent layers near the ground (Gubler and Hiller, 1984). The duration and development of the flow regimes of the individual avalanche can be compared through the flow depth (y-direction) and in time (x-direction). A flow height spectrum every 0.025 s is evaluated with the result of a flow height resolution of 0.1 m.

Comparative analysis of the seismic signals of the snow avalanches and the FMCW radar signals at the same location was conducted in this work. Through this analysis, the signatures of the seismic signals generated by the different parts of an avalanche depending on the flow regime were determined. For examples of FMCW radar output signals from two different avalanches, see Figures 4.16 and 4.17, where the intensity of the radar signal was normalized for each signal. Seismic signals in the time-frequency domain were compared with the measurements of the FMCW radars located close to the seismic sensors to study the nature of the seismic signals generated by the different parts and flow regimes characteristic of an avalanche.

The beginning and end of the avalanche signal in the radar plot is the length of the SOV section, defined as the avalanche temporal length, T_L (Section 4.3.1). The SOV section can be partitioned into several regions with different dynamics characteristic of snow avalanches (Section 1.4.1). The radars can detect the three regions of an avalanche defined earlier: the front, the energetic and the dense regions (Figures 4.16 and 4.17). However, no information is obtained from the powder cloud as the particles are too small. The small particles reflect small amounts of energy and thus in the powder cloud, the signal is weak and the amount of energy returning to the detector is very small. The minimum particle size detectable by the radars is 1.4 -1.8 10^{-2} m which represents the physical minimum detection limit (Sovilla, 2004).

The FMCW radar signals at B and C of the powder avalanche #16 compared with the envelope of the seismic signal at the same location are shown in Figure 4.16. Two regions of the avalanche signal, the energetic (2#) and the dense/tail (3#) parts, are distinguishable in the radar signals from both locations. In this avalanche, the front region is too short or not distinguishable from the energetic part. Not all the regions described in Section 1.4.1 are always distinguishable in the radar signal. The energetic region (2#) at B lasted 25.2 s, measured from 63.6 to 88.8 s; its dense/tail part (3#) at B for 41.2 s, from 88.8 to 130 s; its energetic region (2#) at C for 18.2 s, from 78.8 to 97 s; its dense/tail (3#) part at C for 16.6 s, from 97 to 113.6 s (Figure 4.16). The seismic station at B is located at the same location of the avalanche path as the FMCW radar, so the arrival of the avalanche at the radar can be considered as the arrival of the avalanche to the seismic sensor. The seismic station at C, however, is located at a distance of 32 m from the FMCW radar location (mast location in Figure 2.3). Powder-snow

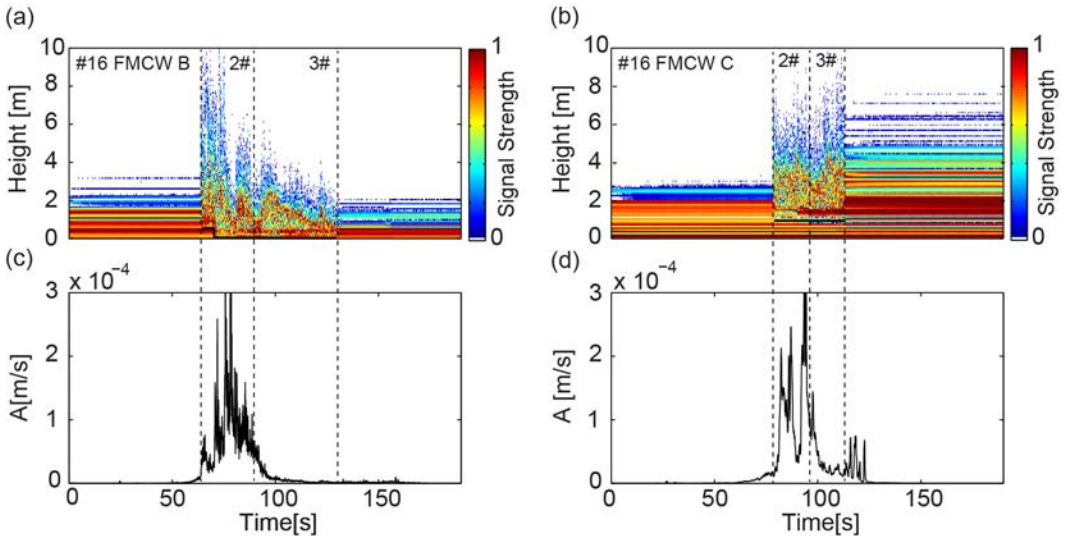

FIGURE 4.16: FMCW radar signals of the powder-snow avalanche detected at B (a) and C (b) compared with the envelope of the seismic signal recorded at B (c) and C (d). The dashed lines delimit the different parts of the avalanche in the SOV section. The solid black lines in the FMCW radar plot delimit the different bed surface levels of the avalanche.

avalanches propagating fast may take less than one second to travel this distance along the path, but wet dense avalanches may take up to several seconds. To determine the sections and the avalanche length at C, we calculated the shift in the arrival of the avalanche front at the two distinct positions. In the case of the powder avalanche #16, the front was moving at about 50 ms^{-1} and thus the time shift is only 0.6 s. In slower wet avalanches, the shift can be much higher (for example a wet avalanche propagating at 5 ms^{-1} takes 6.4 s).

The FMCW radar signals at B of the wet avalanche #3018 compared with the envelope of the seismic signal at the same location are shown in Figure 4.17. Two regions of the avalanche signal, the front and the dense/tail parts, are distinguishable in the radar signal. The front region (1#) lasted 2.5 s, measured from 75.3 to 77.8 s; its dense/tail part (3#) for 139.1 s, from 77.8 to 216.9 s (Figure 4.17).

Additionally, FMCW signals provide information on erosion (where and how much snow cover is eroded), flow depth distribution and mass deposition (Sovilla and Bartelt, 2002). This information is useful for characterizing each type of flow regime, which will be further associated with the seismic signal generated. Snow avalanches can flow directly over the ground or over a snow cover surface. The height of the avalanche sliding surface, i.e., the bed surface level, was extracted

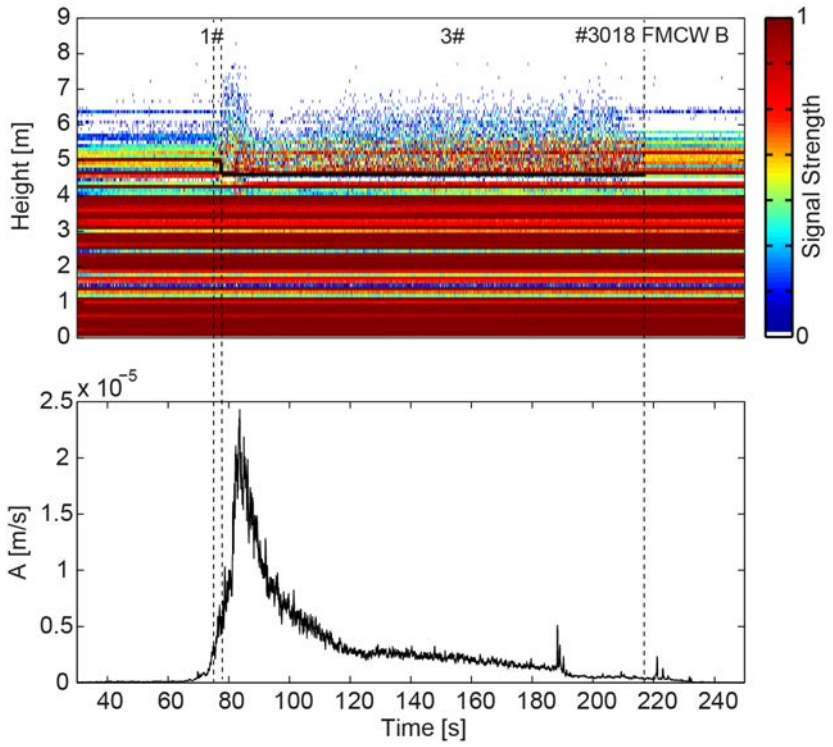

FIGURE 4.17: FMCW radar signal of the wet-snow avalanche detected at B (top) compared with the envelope of the seismic signal recorded at B (bottom). The dashed lines delimit the different parts of the avalanche in the SOV section: frontal region (#1) and dense/tail region (#3). The solid black lines in the FMCW radar plot delimit the different bed surface levels of the avalanche.

from the FMCW radar signals. The values of the thickness of the avalanche bed surface levels are compared in order to quantify the seismic intensity absorption due to the snow cover interface (Chapter 6).

The powder avalanche #16 entrains all the snow cover at B and slides directly over the ground (Figure 4.16a); whereas at C the avalanche entrains one meter of the snow and slides over a bed surface level of one meter (Figure 4.16b). The maximum amplitudes of the envelope time series correlate well with the energetic part flowing over the sensor (Figures 4.16c and d). Mass deposition occurs after the avalanche tail has passed over the radar. About 2 m of snow are deposited over cavern C, located in the run-out zone of avalanche #16 (Figure 4.16b). Maximum flow heights reach 8 m at B and 5 m at C. The wet avalanche #3018 entrains one meter of snow, mostly in the frontal region, and slides over a thick bed surface level of 5.5 m (Figure 4.17). The maximum amplitudes of the envelope correlate well with the pass of the first part of the dense region characterized by maximum flow heights of about 1.5 m.

All the information extracted from the comparative analysis of the FMCW radar signals and the seismic signals is used to determine the signatures of the signals generated by the different flow regimes. These signatures will then be useful to classify the avalanches using the seismic signals directly (Chapter 6).

Chapter 5

Evaluation of an avalanche possibly triggered by an earthquake

In the present chapter, results of the evaluation of an avalanche possible triggered by an earthquake, and the comparison with different earthquakes that did not trigger any snow avalanche, are presented. Seismic data are used to quantify energy parameters and changes in the elastic field within the snowpack due to the earthquake vibrations. The methodology of analysis of the seismic and infrasound signals is detailed in the previous Chapters 3 and 4. Furthermore, the study is complemented with nivo-meteorological data and snowpack stability evaluations. Most of the contents of this chapter has been published in Pérez-Guillén et al. (2014).

5.1 Introduction

The inertial forces induced by an earthquake can cause an increase in the load down the slope and can also decrease the shear strength. Both effects could lead to a destabilization of the snowpack and hence the release of an avalanche. Snow avalanches triggered by earthquakes have been poor investigated given the scarce occurrence and the lack of real monitored events (Podolskiy et al., 2010b). This phenomenon can be considered an important collateral hazard associated with earthquakes in snow-covered mountain areas with high seismicity.

An inventory of the few documented historic cases of earthquake-induced snow avalanches has been compiled in Podolskiy et al. (2010b). The relationship between an avalanche release and the seismic effect is related to the distance from the source (hypocentral distance), the local conditions (geology, topography, snowpack stability, etc.) and the characteristics of the seismic source: amplitude, frequency and duration of the vibrations (Suriñach et al., 2011). Large seismic wave amplifications effects can occur though focusing on mountain tops which can increase the probability of avalanche release (Geli et al., 1988; Pedersen et al., 1994; Massa et al., 2010).

Most of the avalanche fatalities in mountain areas are caused by dry snow slab avalanches triggered by the victims or their companions. These avalanches are initiated by a failure within a weak layer, resulting in the release of a rigid slab of variable dimensions produced by the propagation of fractures (McClung and Schaerer, 2006). These weak layers within the snowpack act as shear planes that facilitate an avalanche release. A necessary condition for failure is that the shear stress exceeds the shear strength at a point in the weak layer (Schweizer, 1999). Laboratory experiments carried out with artificial snowpacks containing a weak layer over a shaking table have revealed that vibration reduces the effective shear strength by increasing the peak shear loading (Chernouss et al., 2006; Podolsky et al., 2008; Podolskiy et al., 2010c). In cases of natural seismicity, a slab avalanche can be released by the loading due to the earthquake accelerations. This loading produces an amplification of the stress that can cause a fracture between the snow layers (Higashiura et al., 1979). The shear stress amplification is larger at higher accelerations which depend on the earthquake magnitude, the hypocentral distance and local conditions (site effect).

In this chapter, we asses whether an avalanche released after the arrival of an earthquake is triggered seismically or not. Firstly, the time-frequency joint analysis of seismic, infrasound and the GEODAR radar data provides information on the avalanche and earthquake characteristics (Sections 5.3, 5.2 and 5.4). Data from two local earthquakes that did not trigger any snow avalanche are used for comparison (Section 5.5). The intensity of shaking of these earthquakes is quantified using the six seismic indices defined on Section 3.4. In addition, we present an evaluation of the snowpack stability conditions comparing the nivo-meteorological

situation and the snow cover simulations of the days in which they occurred (Section 5.6). Finally, the coseismic displacement of the earthquake that possibly triggered the avalanche is calculated and compared with load-controlled experiments with layered snow samples (Section 5.7).

5.2 The event of 6th December 2010

On 6th December 2010, the snow avalanche alarm system of VdlS was triggered by a local earthquake (M_L 3.1; 6:41:24 UTC) with the hypocenter in Col de Balme, France (46.05° N; 6.94° E; depth 3 km; source SED) located at approx. 43 km from VdlS (Earthquake #1, Figure 5.1 and Table 5.1). The trigger in the avalanche warning system of VdlS caused by the earthquake was initially discarded because of the identification of the earthquake. However, a subsequent analysis of the infrasonic and seismic data of the UB stations (cavern B, C and D of Figure 5.1) showed that a signal generated by an avalanche appeared seconds after the arrival of the waves of the earthquake. Apart from these data, the only available data for this avalanche were acquired with the GEODAR radar and the seismic station Syscom of cavern A (Figure 5.1). This avalanche did not descend along the main gully 1 but along the secondary one (field observation). As a result, no data were recorded by the other monitoring instruments situated in the main gully. After the storm temporarily cleared, a small part of the deposit of this avalanche was visible in the secondary gully.

The earthquake and the snow avalanche were recorded at all the UB seismic stations at the experimental site. Figure 5.2 shows the correlation of the avalanche fronts detected by the radar with the time series of the seismic signals from the UB stations at caverns B, C and D. In cavern A only the record of the earthquake was obtained because of the short recording length of this station that only works in trigger mode. Only the E-W component is presented in Figure 5.2 for sake of space and because of the higher seismic energy of the horizontal components. The infrasound signal obtained at D is also presented. The joint analysis of both types of data (seismic and infrasound) yields information on the behaviour of avalanches (Kogelnig et al., 2011b). Figure 5.2 shows two differentiated packets of energy in the seismic time series, corresponding to the earthquake and subsequent avalanche. This is not the case of the infrasound time series that displays a spindle shape and will be discussed below. Figure 5.3 displays the corresponding spectrograms.

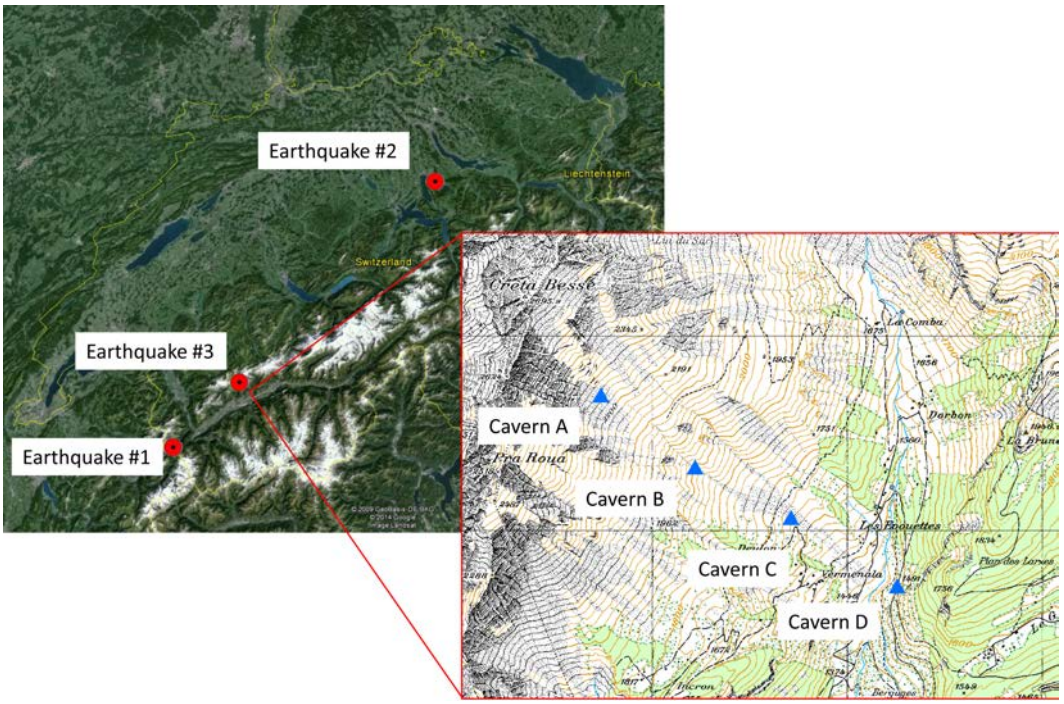

FIGURE 5.1: Map of the epicenters of the earthquake and zoom of the overview of Valle de la Sionne (VdlS) field site with the detailed position the four caverns where seismic stations are installed. The approximate avalanche path is delimited by the blue dotted line. The underlying grid has a size of 1 x 1 km.

The arrival of the earthquake is observed at all the seismic stations at approximate 16.5 s (arrival of P-wave in Figure 5.2. The origin of time is arbitrary). Note the clear and sudden appearance of energy at all frequencies in the seismic spectrograms (Figure 5.3). This is a characteristic of earthquakes. The arrival time of the S-wave is approx. at 22 s (Figure 5.2). The maximum amplitudes in the earthquake seismic time series were recorded at approximately 23 s.

The seismic spectrograms show that the signals of the earthquake and the avalanche overlapped (Figure 5.3). The coda of the earthquake overlaps the beginning of the seismic signal of the snow avalanche ($\approx$ 40 s). After the coda of the earthquake ($\approx$ 50 s) the increase in amplitude of the seismic signal produced by the snow avalanche is observed at different times in the different seismic records. This is a consequence of the evolution of the relative position of the avalanche and the sensors. The evolution of the frequency content in time allows us to estimate the relative position of the snow avalanche with respect to the seismic stations. None of the sections described in Section 4.3.1 were defined as the avalanche did not flow directly over the sensor.

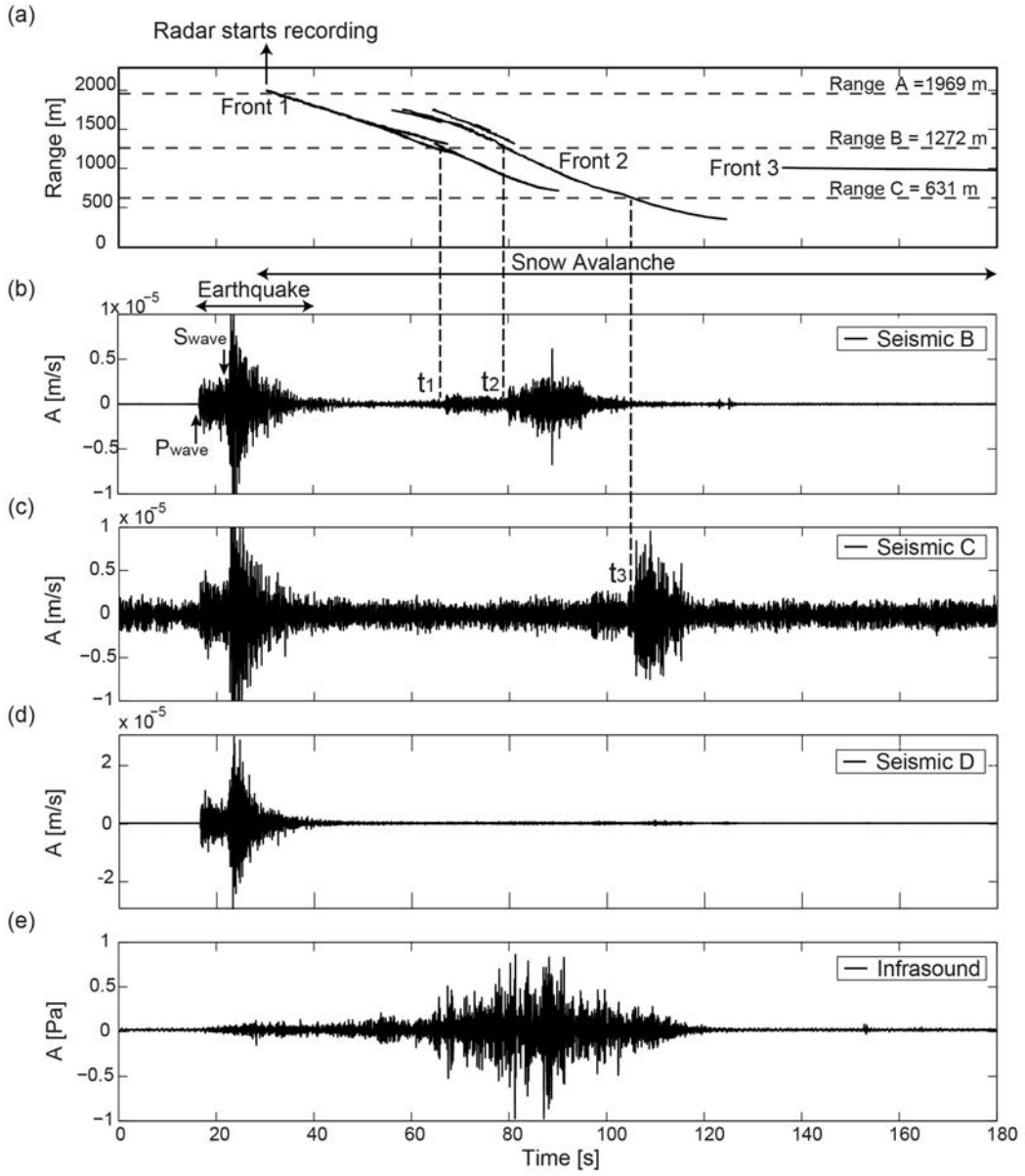

FIGURE 5.2: Correlation between the GEODAR radar (a), seismic (b-d; EW component) and infrasound (e) data of the event of 6th December 2010 (earthquake and avalanche). The radar provides the position (range, distance from bunker to the avalanche position) of the three avalanche fronts. The earthquake generates a similar seismic signal in the three different stations (B, C, D) followed by the avalanche seismic signal distinguishable in B and C. The P-wave arrives at approx. 16.5 s and the S-wave at 22 s. The instants t_1 = 66.4 s, t_2 = 79.8 s and t_3 = 105.4 s are the arrival of the fronts 1 and 2 to the range of seismic stations B and C. The data recorded in C were very noise possibly due to oscillations of the mast produced by the wind.

The approach of the snow avalanche to a sensor results in an increase of the energy content of the higher frequencies. Maximum amplitudes in the highest frequencies are recorded when the snow avalanche flows near or over the seismic sensor. The

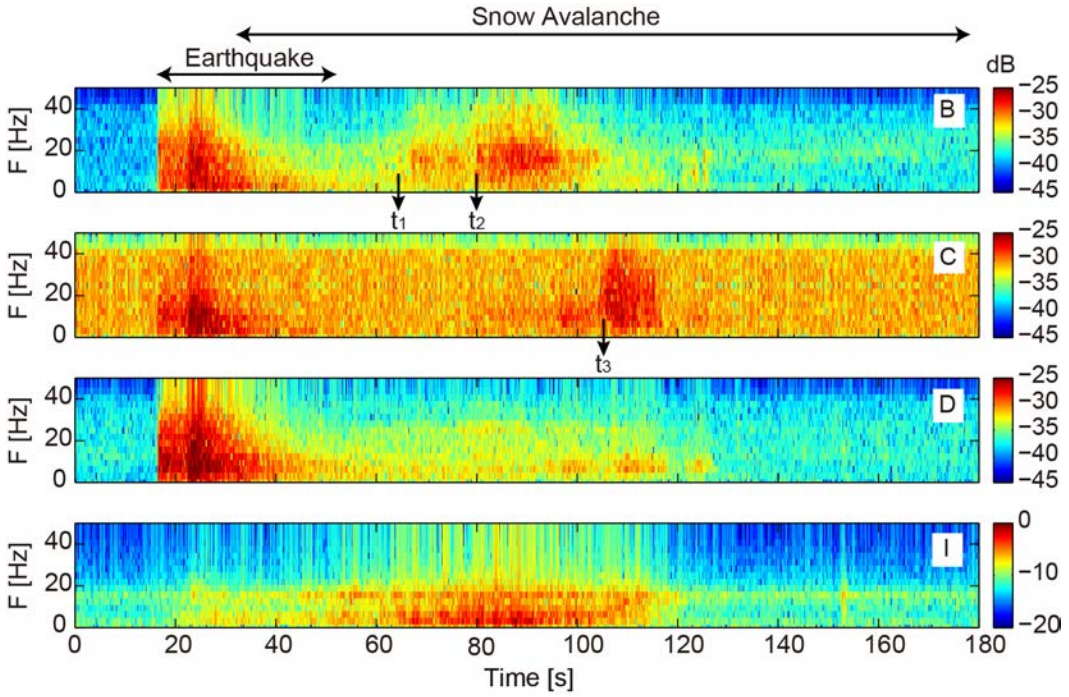

FIGURE 5.3: Spectrograms of the seismic (EW component) and infrasound signals at the different stations of VdlS of the event of 6th December 2010 (earthquake and avalanche). The instants $t_1 = 66.4$ s, $t_2 = 79.8$ s and $t_3 = 105.4$ s are the arrival of the fronts 1 and 2 to the range of seismic stations B and C. The colour scale represents the relative amplitude in dB.

maximum seismic energy is observed at different time intervals: [64-104] s at cavern B and [105-117] s at cavern C. No maximum values of amplitude are reached in the seismic spectrogram of cavern B for the higher frequencies (maximum amplitudes in the spectrogram are in the range of [1- 20] Hz) (Figure 5.3). This indicates that the avalanche did not flow over cavern B, in accordance with the field observation, which indicates that the avalanche descended along gully 2. The increase in the seismic amplitudes and frequency content indicates when the avalanche reached the minimum distance to B (Figures 5.2 and 5.3; $t_2 \approx 64$ s). The decrease in amplitudes of the seismic signal and in the frequency content observed in the records of B indicates that the avalanche moves away from cavern B. The same general characteristics are observed at cavern C despite a shift in the time interval, [105-120] s. However, the energy of the highest frequencies, [1- 40] Hz, in the spectrogram is higher than that of B, indicating that the avalanche passed very close to C. The snow avalanche stopped at short distance after cavern C at approx. 127 s. The low amplitude signals and frequency content recorded at cavern D are due to the avalanche stopped far from this station. The overlap of the signals of

the two sources (earthquake and avalanche) makes difficult the determination of the exact start of the snow avalanche. Moreover, the radar recorded movement at 30 s at a range of 2000 m (Figure 5.2). At this time interval, the returned radar signal is relatively weak, indicating the beginning of an avalanche at the approximate range of cavern A. Data before this time are unavailable because the VdlS alarm system was triggered after the arrival of the maximum amplitudes of the earthquake ($\approx$ 25 s) and the radar needs several seconds to record data.

5.3 Correlation of the seismic data with the infrasound and radar data

Data deduced from the radar are consistent with the previous analysis of the avalanche evolution obtained from the seismic signals. The analysis of the radar signal indicates that the avalanche was divided into three fronts descending with different velocities (Figure 5.2). Note that the radar range is the distance from the shelter to the avalanche position. The slope of the curves of the front positions against time is the instantaneous avalanche front velocities. The avalanche has three distinct velocity fronts. The first two fronts are traveling at a maximum velocity of 24 and 21 ms^{-1} (average from radar measurements). The first front (1, Figure 5.2) travelled from the starting zone and abruptly decelerated to zero within 3 seconds at range 722 m. At the range of cavern B (1272 m) it was divided into two parts which crossed the range of B at 64.2 and 66.4 s. The second front (2) which descended approx. at the same speed as front (1) from range 1756 m to the range of cavern C decelerated until it reached 359 m. It crossed the range of B at 79.8 s and the range of C at 105.4 s. The arrival of these fronts at the range in which seismic station B is placed corresponds to the peaks in the temporal seismic signals and to a maximum in the amplitudes of the highest frequencies in the spectrogram (t_1 and t_2 Figure 5.2 and 5.3). The arrival of front (2) at the range of cavern C corresponds to t_3 (Figure 5.2 and 5.3). The latter, third front (3), travels slowly at 13 ms^{-1} and expands far into the run-out zone. This front appears in the radar record at a range of 1020 m and still moves when the recording finishes after 3 minutes. Note that the maximum run-out distance has been reached by the front (2) (Figure 5.2). The seismic and infrasound energy generated by last slow moving front (3) is not detected because their amplitudes were very low with an order of magnitude similar to that of the background noise.

The infrasound time series displays a spindle shape with a maximum value in the time series amplitude of 1.1 Pa in the [65-110] s interval (Figure 5.2), which also corresponds to the maximum in the spectrograms (Figure 5.3). This shape was also observed in other avalanche infrasound signals (Kogelnig et al., 2011). The infrasound energy interval coincides with that of the seismic signals although the frequency content is lower, up to 20 Hz (Figure 5.3). However, the infrasound energy distribution is different. Very low amplitudes are observed in the earthquake interval (up to 50 s), whereas the highest amplitudes are present in the snow avalanche interval. The maximum amplitudes of the infrasound signal were recorded seconds after (infrasound time travel at sound speed) when the avalanche moved along the channelled path, reaching the maximum velocity. We can consider that the infrasound signal attenuation is negligible at local distances (d<3 km; Section 3.3). Note that the maximum energies in the infrasound (recorded at D) coincide when the avalanche is in between the range of B and C, in the channelled path before reaching C. The amplitudes and shape of the infrasound indicate that the avalanche developed a dilute faster part in this part of the path according to the analysis of other avalanches at the site (Kogelnig et al., 2011b).

TABLE 5.1: Hypocenter coordinates (source:SED), epicentral distance to station D of VdlS, *PGV* and maximum infrasound value recorded at station D for earthquakes #1, #2 and #3; M_L is the local earth- quake magnitude. The *PGV* values are the maximum values obtained from the velocity records of each component.

Earthquake	H [m]	Δ [km]	PGV $[ms^{-1}]$	A_I Pa
#1: M_L 3.1	46.05 N 6.94 E; 3km	43.2	$(2.5 \cdot 10^{-5}, 3.1 \cdot 10^{-5}, 2.9 \cdot 10^{-5})$	0.11
#2: M_L 4.2	47.15 N 8.55 E; 32km	132	$(4.8 \cdot 10^{-5}, 1.4 \cdot 10^{-4}, 6.8 \cdot 10^{-5})$	0.07
#3: M_L 2.1	46.32 N 7.34 E; 0.1 km	4.5	$(2.3 \cdot 10^{-4}, 4.5 \cdot 10^{-4}, 6.1 \cdot 10^{-4})$	0.76

The analysis of the evolution of the seismic signals allows us to determine first, that it was an avalanche and second, the approximate path that it followed. The velocities of the first fronts and the characteristics of the infrasound signal indicate that it was a dry avalanche. According to the length of the avalanche path (≈1500 m), we can classify it as a medium size avalanche (see classification criteria in Section 4.2).

5.4 Determination of the approximate start time of the avalanche

In order to determine whether the snow avalanche was triggered by the earthquake or not, first it is necessary to determine the arrival time of the earthquake at the site and the time when the snow avalanche was released. The determination of the arrival time of the earthquake does not present problems. The sudden appearance of the P-wave arrival in all the seismic stations is visible in the time series and spectrograms at 16.5 s (Figures 5.2 and 5.3). In addition, the snow avalanche had to be released after the arrival of the earthquake because no seismic energy of the avalanche is observed before the earthquake. However, the starting of the avalanche is not easy to detect due to the presence of the energy of the earthquake (Figures 5.2 and 5.3). The radar started recording at t $\approx$ 30 s (t_r in Figure 5.4) and the avalanche was at the range of cavern A but it did not flow directly over this cavern. The comparison of the seismic and infrasound signals of the 6th December 2010 event with that obtained for two local earthquakes recorded at the experimental site which did not trigger a snow avalanche are helpful.

On 11th February 2012 an earthquake occurred 132 km from VdlS (M_L 4.2; 22:45:26 UTC; earthquake #2 in Figure 5.4 and Table 5.1) with the hypocenter in Zug, Switzerland (Table 5.1). A second earthquake occurred on 21th March 2012, 4 km from VdlS (M_L 2.1; 11:01:57 UTC; earthquake #3 in Figure 5.4) with the hypocenter in St. Leonartz, Switzerland (Table 5.1). All these earthquakes generated (local) infrasound as a result of the coupling to air of the seismic waves to the air that travelled to the vicinity of the infrasound station (Burlacu et al., 2011). The amplitude of the infrasound signals depends on the magnitude of the earthquake and the distance of the station to the epicenter. The values of the maximum ground velocities (PGV) of the earthquakes at D are shown in Table 5.1. A comparison of these values shows that earthquake #3 generated higher infrasound amplitudes (A_{max} = 0.76 Pa) than the other two earthquakes which had a lower PGV and longer epicentral distances. However, earthquake #1 with lower PGV, but closer to the station, yields higher infrasound amplitudes (A_{max} = 0.11 Pa) than earthquake #2 (A_{max} = 0.07 Pa). In order to compare the different shapes of the seismic and infrasound signals of the three earthquakes, the envelopes of the complete seismic signals and those of the infrasound of these earthquakes recorded at cavern D were calculated. Figure 5.4 shows the envelopes

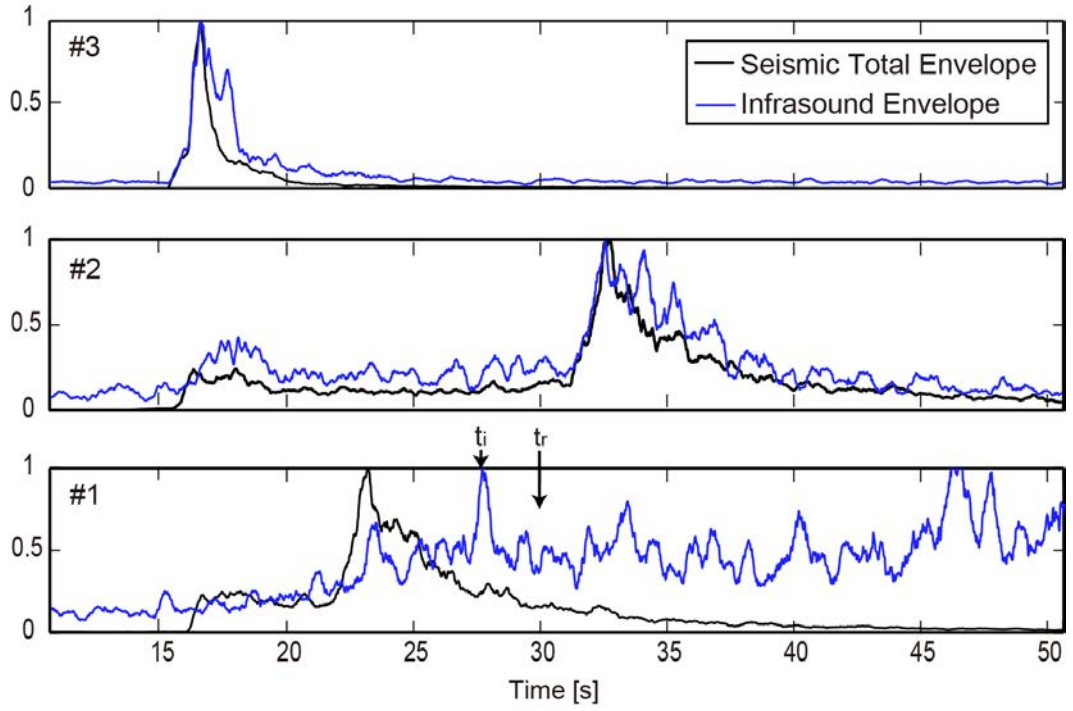

FIGURE 5.4: Comparison of the normalised envelopes of the seismic and infrasound signals of the event (earthquake and avalanche; #1) and the two earthquakes (#2 and #3). The origin of time is arbitrary. The infrasound generated by the snow avalanche is received at t_i and at t_r the radar started to record the movement of the snow avalanche.

normalized for comparison of the three earthquakes. In earthquakes #2 and #3, the infrasound amplitudes correlate well with the seismic signals although the distances from the epicentre were different and hence the shape of the seismograms, i.e. a) a sudden increase in the infrasound amplitude that corresponds to the P-wave arrival of the earthquake at the sensor, b) maximum infrasound amplitudes that correspond to the maximum seismic amplitudes and c) a decrease in the infrasound amplitude for the coda of the earthquake (Figure 5.4).

A different relative behaviour between the envelopes of the seismic and the infrasound signals is observed in the case of the event #1 in which the avalanche was triggered (Figure 5.4). The sudden increase in the infrasound signal at the moment of the arrival of the P-wave is not observed in the envelopes and in the time series. This is due to two factors: a low signal-to-noise ratio and the low seismic energy of the earthquake. The infrasound background noise of the given day had mean amplitude of 0.008 Pa (calculated 10 s before the earthquake). This value is similar to that of the day of earthquake #3 (0.007 Pa) and higher than that of earthquake #2 (0.003 Pa). The low signal-to-noise ratio of the amplitude

of the infrasound generated by the P-wave and the immediate phases that follow is not sufficient to distinguish the increase in the infrasound signal (Figure 5.4). The low energy of the seismic signal of these phases (maximum value below of $10^{-5}\, ms^{-1}$) did not generate enough infrasound energy to be distinguished at the beginning of the earthquake. However, at t = 23 s, a local maximum of the infrasound is observed on the arrival of the maximum energy of the earthquake. Note that the delay observed at this maximum is due to the travel time difference between the seismic and infrasound waves (Ichihara et al., 2012). The similar decrease in amplitudes of the coda section of the infrasound and seismic envelopes observed for earthquakes #2 and #3 (without avalanche) is not observed in the event. The fall in the seismic envelope amplitude does not correspond to a decrease in the infrasound envelope amplitudes. By contrast, the amplitude of the infrasound envelope increases, reaching a maximum at 28.01 s (t_i) that exceeds the local maximum at 23 s (Figure 5.4). A possible explanation for this increase that surpasses the local maximum is that the sensor was receiving the infrasound generated by the avalanche. We therefore infer that the avalanche was released a few seconds before this time and after the arrival of the earthquake. This assumes that the only sources of infrasound were the avalanche and the earthquake.

In our seismic recordings of the 6th December 2010 event the most energetic waves are the S-waves around 22 s (Figures 5.2 and 5.3). Therefore the inertial forces induced by the acceleration of these waves will be stronger and might cause more effects in the snow cover. Our data indicate that the avalanche was released shortly after the arrival of the waves of the earthquake, which strongly suggests that the avalanche was triggered by the earthquake. A quantification of the signals generated by the earthquakes could yield more information.

5.5 Earthquakes ground motion quantification

In order to evaluate the effect of ground shaking produced by the earthquake on 6th December 2010, we compared the seismic signals of this earthquake with those of the two earthquakes aforementioned (earthquakes #2 and #3). The seismograms obtained at cavern A were used because this cavern is situated at the release area (Figure 5.5). We assume that the earthquake shaking is similar over the entire release area.

Six indices are used to measure the effect of ground motion or shaking on a structure. We considered the snow slab using the same approach. The indices used were defined in Section 3.4. The PGD, PGV and PGA indexes consider the maximum values in the seismic time series, whereas the indices I_a and TD take into account their evolution in time and their duration over the seismic time series. The PSA gives the maximum acceleration response of a structure (in this case the snow slab) for each period (T). Resonance effects in the snow slab can appear if its natural frequency is close or equal to the resonant frequency of the soil, thus increasing the potentiality of damages. The damping factor depends on the structure characteristics, in our case on the characteristics of the snow slab, but the exact characteristics are unknown. Therefore we calculate the PSA using three different damping ratios in an appropriate range. The loss factor (two times the damping ratio) calculated in snow tests showed values in a range between [0.005 0.16] depending on the density and temperature of the snow (Mellor, 1975). Hence, to evaluate the different possibilities three variable damping ratios (1%, 5% or 8%) were considered in this study.

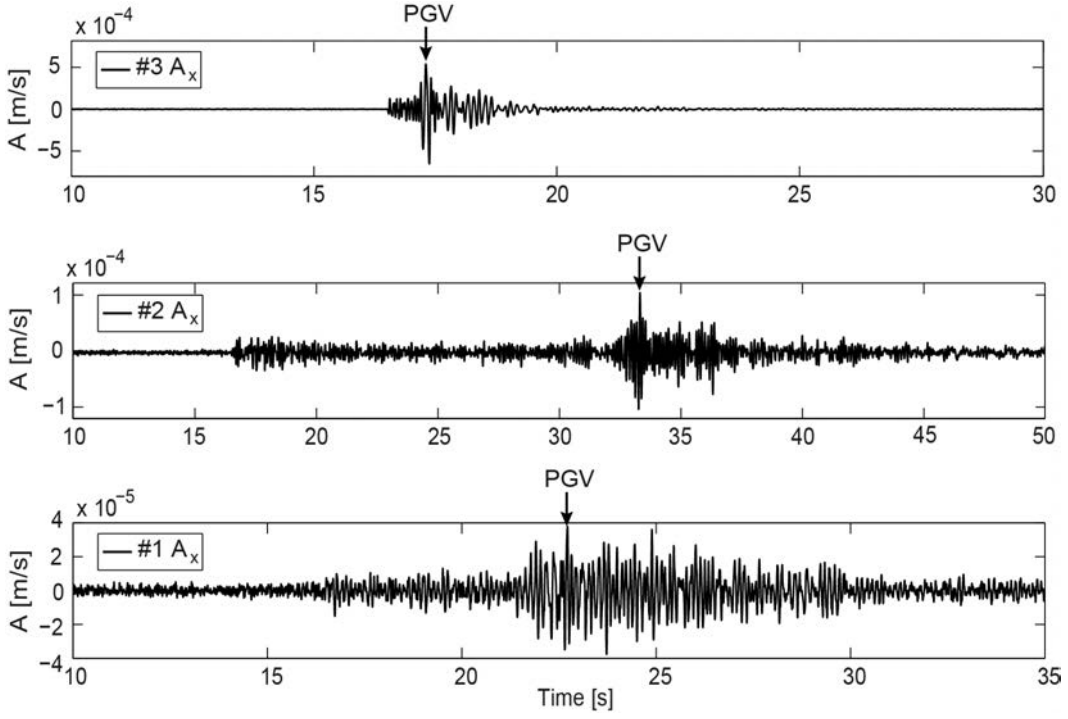

FIGURE 5.5: Down-slope components of the ground motion recorded at A of the three earthquakes occurred on 6th December 2010 (#1), on 11th February 2012 (#2) and on 21th March 2012 (#3). The arrows indicate the Peak Ground Velocity (PGV) values for each earthquake.

The parameters were calculated for all three seismic components. The ground accelerations were obtained from the derivative of the ground velocity time signals recorded at the station at cavern A, the cavern situated in the release area (Figure 5.1). The parameters were calculated in the rotated coordinate system and aligned with the local slope of 40° at A. The down-slope components of the ground velocity of each earthquake at A are shown in Figure 5.5.

Figure 5.6 shows the PSA values of the different components for earthquakes #1, #2 and #3, respectively, obtained at cavern A for different values of the damping ratio. The corresponding PGD, PGV, PGA, TD and I_a values are shown in Table 5.2. We compare the values of the six indices for all three earthquakes. The magnitude and epicentral distances of the different earthquakes are indicated with the symbol M_L and Δ with the corresponding subindex. The magnitude and epicentral distances of earthquake #1 accomplishes $M_{L2} > M_{L1} > M_{L3}$ and $\Delta_2 > \Delta_1 > \Delta_3$. The comparison of the quantification values shows that earthquake 3, the earthquake nearest to VdlS, has the maximum values of PGD, PGV, PGA, PSA and I_a (Table 5.2 and Figure 5.6). However, its duration, determined by TD, is the lowest of the three earthquakes. Earthquakes with longer duration of shaking i.e. higher TD, are more prone to cause a slab failure (Podolskiy et al., 2010b). These results are consistent with the physical conditions and the geographical situation of the earthquakes (Figure 5.1). Note that earthquake #3 is the closest to the VdlS site despite being the lowest in magnitude. Its highest PSA, PGD, PGV, PGA and I_a values, and the smallest TD value with respect to the other earthquakes are more attributable to the short epicentral distance than to its small size.

Earlier studies of artificial earthquakes caused by underground explosions in the Khibiny mountains in Russia (Fedorenko et al., 2002; Chernouss et al., 2006) have revealed a correlation between explosions with PGA in the order of 0.1- 8 ms^{-2} and avalanche release. These PGA values are much higher than those recorded in the earthquakes under study because of the proximity of the explosions to the release area. The explosions, however, usually have a TD much lower than the earthquakes.

The maximum PGD and PGV are obtained for the slope parallel plane components (X and Y) of the earthquake #3 (Table 5.2). The PGD and PGV values of earthquakes #1 and #2 are of the same order of magnitude, slightly higher for earthquake #2. Also in these earthquakes the values of the horizontal components

are higher than the vertical components. The effects of the PGV and PGD of the ground are even more important than PGA values because they lead to fissures in the ground surface (Newmark, 1965). The highest values are obtained for the earthquake #3 and the effect of this earthquake might produce more damage leading to a failure.

The maximum PSA values and the associated periods (or frequencies) are important factors to consider in the analysis of the shaking. Earthquake #1 and #3 present higher frequency content (lower period) of PSA than earthquake #2 because they were closer to the VdlS site: The periods for earthquakes #1 and #3 are in the range of [0.04 -0.15] s and earthquake #2 in [0.08-0.17] s (Figure 5.6). This is a consequence of the geometrical and anelastic attenuation of the seismic waves that produce, for the same magnitude earthquake, lower amplitude and frequency content for longer epicentral distances. The relationship between the frequency content of the seismic source and the slab failure has not been studied yet. All the documented cases of earthquakes-induced avalanches (Podolskiy et al., 2010b) were for earthquakes located at a distance relatively close to the source (in a range of 0.2-640 km). Teleseismic earthquakes do not usually trigger snow avalanches, although the peak ground acceleration recorded at the site could be higher than that of the studied local earthquakes. This suggests that the most effective accelerations that induced the slab failure are those of high frequencies (shorter epicentral distances). Note that snow avalanches are often triggered by explosions which are very high frequency seismic sources, though the analogy is only approximate.

The PSA values in the downwards direction to the slope (X) of earthquakes #1 and #2 are of the same order of magnitude, and earthquake #3 has the largest value, 0.25 ms^2 for a period of 0.07 s (f $\approx$ 14.3 Hz) for a damping ratio of 1% (Figure 5.6). In the discussion we use the lowest value of damping to consider the maximum values of PSA although the other values are represented in Figure 5.6. The value of earthquake #3 is one order of magnitude higher than those of earthquake #1 (0.029 m/s; f $\approx$ 16.7 Hz; 1%) and earthquake #2 (0.059 m/s; f $\approx$ 8.3 Hz; 1%). In summary, earthquake #1, which was followed by the avalanche, presents the minimum values of PGA and I_a, and the highest frequencies involved in the maximum PSA, although they are not the maxima. Nonetheless, only small differences between these values have been detected. The maximum values of the

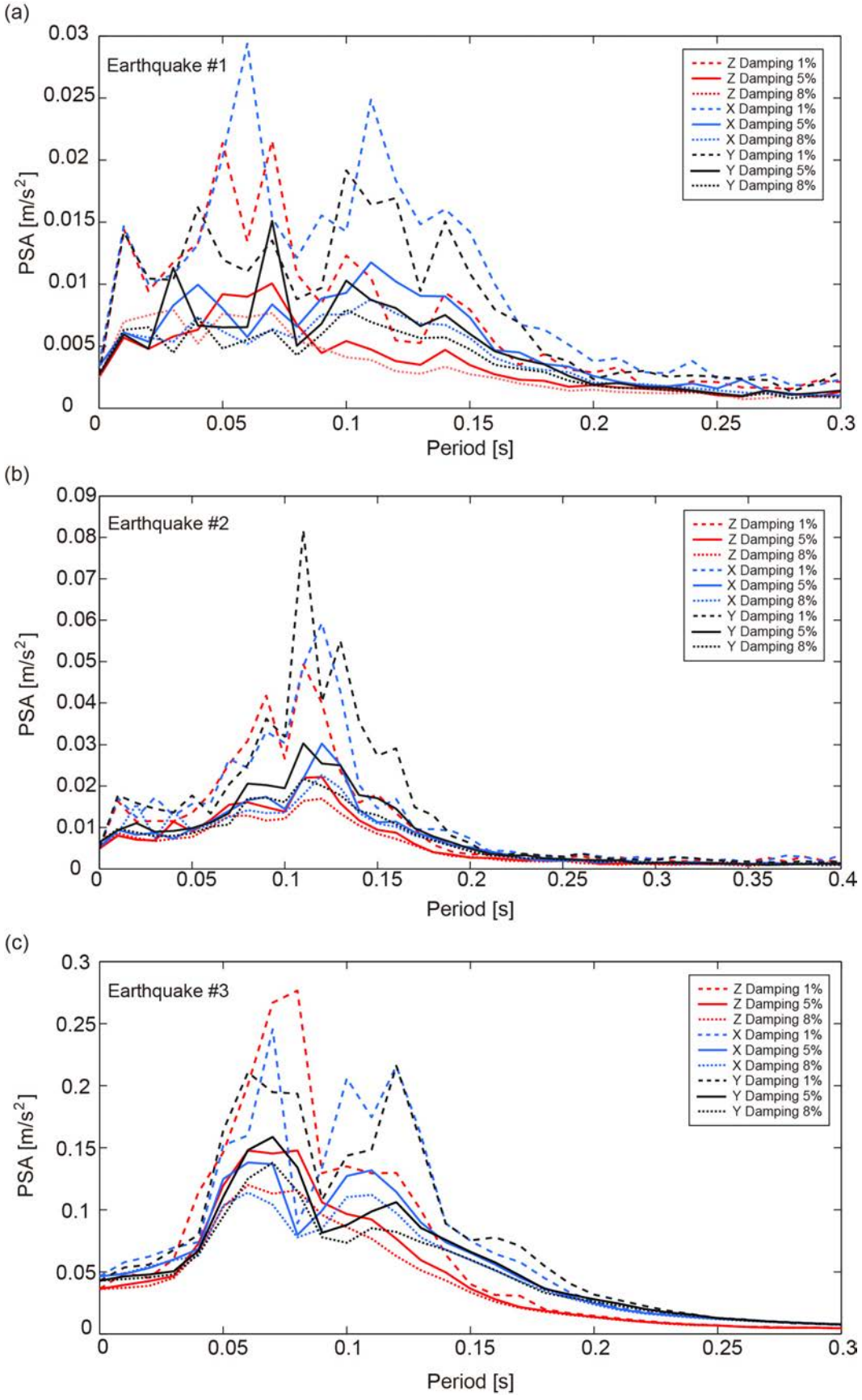

FIGURE 5.6: *PSA* values calculated for all the components of the seismic signal at A of the earthquake #1 on 6th December 2010 (a), earthquake #2 on 11th February 2012 (b) and earthquake #3 on 21th March 2012 (c) calculated with different damping factors 1%, 5%, 8%.

TABLE 5.2: Values of the PGD, PGV, PGA, TD and I_a calculated for the three components (Z, X, Y) in cavern A of all the earthquakes; M_L is the local earthquake magnitude.

Earthquake	Component	$PGD[m]$	$PGV[ms^{-1}]$	$PGA[ms^{2}]$	TD	$I_a[ms^{-1}]$
#1: M_{L1} 3.1	Z	$6.8 \cdot 10^{-7}$	$3.2 \cdot 10^{-5}$	$2.5 \cdot 10^{-3}$	16.4	$6.2 \cdot 10^{-7}$
	X	$1.2 \cdot 10^{-6}$	$3.7 \cdot 10^{-5}$	$3.4 \cdot 10^{-3}$	15.9	$9.8 \cdot 10^{-7}$
	Y	$1.2 \cdot 10^{-6}$	$3.7 \cdot 10^{-5}$	$3.4 \cdot 10^{-3}$	16.7	$9.8 \cdot 10^{-7}$
#2: M_{L2} 4.2	Z	$1.6 \cdot 10^{-6}$	$8.1 \cdot 10^{-5}$	$4.9 \cdot 10^{-3}$	30.3	$2.6 \cdot 10^{-6}$
	X	$1.8 \cdot 10^{-6}$	$1.1 \cdot 10^{-4}$	$5.3 \cdot 10^{-3}$	29.9	$3.5 \cdot 10^{-6}$
	Y	$2.1 \cdot 10^{-6}$	$9.5 \cdot 10^{-5}$	$6.4 \cdot 10^{-3}$	26.7	$4.5 \cdot 10^{-6}$
#3: M_{L3} 2.1	Z	$8.3 \cdot 10^{-6}$	$4.4 \cdot 10^{-4}$	$3.6 \cdot 10^{-2}$	1.5	$4.4 \cdot 10^{-5}$
	X	$8.6 \cdot 10^{-6}$	$5.4 \cdot 10^{-4}$	$4.6 \cdot 10^{-2}$	1.7	$4.0 \cdot 10^{-5}$
	Y	$1.2 \cdot 10^{-5}$	$6.1 \cdot 10^{-4}$	$4.3 \cdot 10^{-2}$	1.5	$3.5 \cdot 10^{-5}$

PSA represent the maximum acceleration loading to the slab when the slab had this frequency of resonance. Although the resonance frequency of a snow slab is unknown it must be related to the type of snow grain and the geometry of the slab as well as its stiffness. The values at cavern A presented here can be considered as an upper boundary of the accelerations obtained due to site effects (see Section 3.5). The earthquake accelerations at A, at the top of the mountain, are higher than those at caverns B, C and D (Table 3.2).

We compared the magnitude and epicentral distance of the event with previous reported cases of earthquake induced avalanches. Podolskiy et al. (2010b) suggested a limit for earthquake induced snow avalanches of M_w 1.9 earthquakes at zero source to site distance, that implies a PGA around $0.03g$ approx. This threshold is based on reported cases of avalanches triggered by underground explosions in the Khibiny Mountains in Russia (Chernouss et al., 2006). However, data derived from statistical analysis (Podolskiy et al., 2010a) showed an important reduction of that threshold. In particular, statistically identified earthquakes of magnitudes in the range M_w 3-3.9 induced snow avalanches at distances 100-199 km. The corresponding PGA is between $10^{-6}g$ and $10^{-4}g$. Our case study fits inside the limit of the reported statistical cases, although the reliability of these cases is questionable because most of them could be incorrectly identified or they correspond with an extremely unstable snowpack. Therefore it is difficult to estimate a threshold shaking intensity without knowledge of the local snowpack stability (Podolskiy et al., 2010b). Additional studies are needed to be more precise about the distance-magnitude threshold (Podolskiy et al., 2010a). In cases of landslides

triggered by earthquakes, recent works of Jibson and Harp (2012) have demonstrated a reduction of the maximum distance limit known until now with the addition of new reported cases.

In summary, we have shown that the characteristics of earthquake #1, which could trigger an avalanche, are similar to those of earthquakes #2 and #3, which did not trigger avalanches. The most likely explanation for the different effects of the earthquakes with respect to the avalanche release is the differences in the snowpack stability. The snowpack stability has a clear influence in the evaluation of the possibility that these earthquakes of minor magnitude can act as triggering mechanism for snow avalanches. The stability and the meteorological conditions of each day are thus evaluated in the next section.

5.6 Nivo-meteorological conditions and snow cover simulations

Avalanche release mechanisms can be more or less effective depending on the snowpack conditions. The snow cover stratigraphy is the key contributing factor for dry slab avalanche formation (Schweizer et al., 2003). The triggering of this type of avalanches can occur because of three factors (Schweizer et al., 2003): localized rapid loading (in this case the shaking of the earthquake), gradual uniform loading (for example, precipitation) or a non loading situation like surface warming causing changes in the effective shear strength. Thus, the snow cover structure is one of the most important factors, apart from earthquake magnitude and distance, to consider in the correlation of earthquakes and snow avalanches. Podolskiy et al. (2010b) using snow profiles from starting zones of avalanches triggered by earthquakes in Japan, showed the weakness of the snow strength to be stressed until failure by the inertial forces induced by the earthquake.

To obtain detailed information of the snow stratigraphy at the days of the earthquakes, we conducted simulations with the one-dimensional snow cover model SNOWPACK (Lehning and Fierz, 2008). The simulations were computed using data from the nearest automatic weather station Donin Du Jour (VDS2 at 2390 m a.s.l. and 2 km from the VdlS release area) that provide all the required data to run SNOWPACK. The result of simulations of the snow cover conditions of the three investigated days showed a significantly different stratigraphy and stability

(Figure 5.7). Additionally, data from the automatic weather station close to the release area (VDS1 station, 2696 m a.s.l.) and avalanche bulletins of the region have been used to complete the analysis (Figures 5.8, 5.9 and 5.10). Below, the detailed snow cover characteristics with the complementary meteorological information for each day are presented.

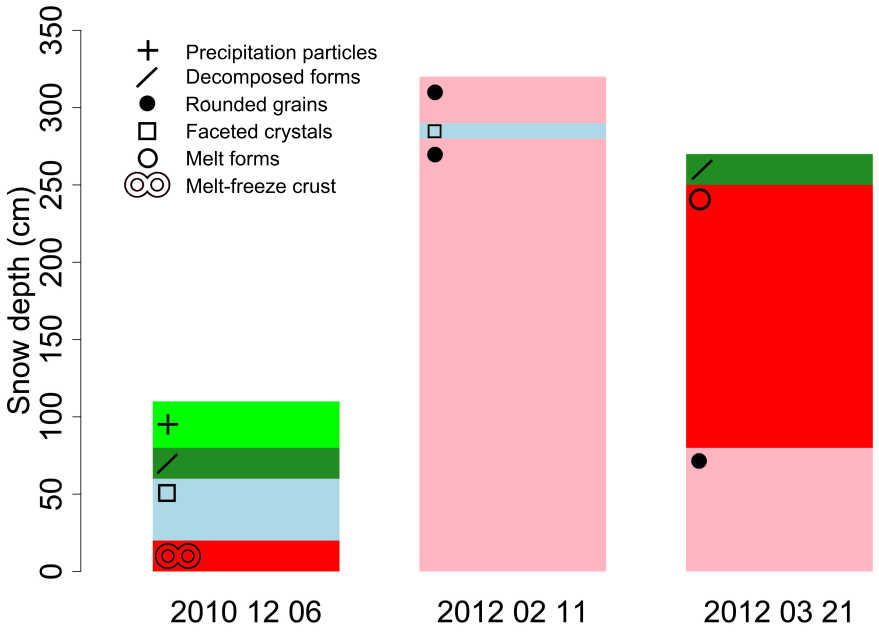

FIGURE 5.7: Modeled snow height and grain type (colours and symbols according to Fierz et al. (2009)) for the three days of the earthquakes using SNOWPACK.

6th December 2010

The avalanche on 6th December 2010 was released after a snow fall of 0.25 m in the preceding 8 hours on top of an existing snow cover of 0.8 m (VDS2 station; Figure 5.8c). The air temperature in the release zone (VDS1 station; Figure 5.8b) was −4°C at 07:41 (local time). The resulting snow cover simulation (Figure 5.7) of the day of the event, 6th December 2010, consists of a thick hard crust around 0.2 m. Above this crust a layer with a thickness of 0.4 m of faceted crystals was buried by decomposing forms and a fresh snow layer. This combination of a melt-freeze crust at the bottom, a well developed faceted layer and new snow on top (Figure 5.7) favors the release of slab avalanches according to McClung and Schaerer (2006). The weak snow cover structure at this time period was also

observed by SLF observers. They noted a weak, poorly cohesive layer of faceted crystals over a hard crust which was formed on 12 November (data from profiles made on 7 December 2010 at 14 km approx. away from VdlS).

The unstable snowpack described above, together with the adverse meteorological conditions of the day, led to a high avalanche danger (level 4 on a scale of $1-5$; Figure 5.8a). The national avalanche bulletin no. 28 for Monday, 6th December 2010 forecasted the possibility of dry avalanches on steep slopes in all exposures above approximately 1800 m a.s.l. An increase in air temperatures resulted in an ascending snowfall level. Therefore naturally triggered moist and wet avalanches were expected about 2400 m a.s.l. at early morning hours. Moreover, the bulletin also indicated that the south-westerly wind will be strong in this area, transporting fallen fresh snow and old snow. Therefore snowdrift accumulations were also possible in the release area.

A total of 11 avalanches (wet and dry snow avalanches) occurred around the VdlS test site on that day, confirming the forecast. A few hours later, two more avalanches were released at the VdlS test site (the first avalanche occurred at 17:00 of 6th December 2010 and the second at 03:00 of 7 December 2010) which did not correlate with the arrival of the earthquake, but they reflect the unstable conditions of the snowpack that day. The analysis of these avalanches is available in Kogelnig et al. (2011b) and Vriend et al. (2013). Several other avalanches were observed in the morning of 7 December 2010 around Anzère and Crans Montana ski areas, 2.5-8 km away from VdlS and farther from epicentre of the earthquake. None of these avalanches could be detected by the array of the VdlS due to the farther distance to the stations and their linear configuration.

11th February 2012

On 11th February 2012 the temperature of the air was $-17°C$ (VDS 1 station; Figure 5.9b) at 23:45 (local time) and there was no precipitation on the previous days. The VDS2 station recorded a snow depth of 3.07 m (Figure 5.9c). The resulting snow cover simulation of the day consisted (Figure 5.7) of a very homogeneous snow cover of a 3.00 m thick layer of rounded grains with a layer of faceted crystals between $2.80-3.00$ m. The snow cover consisted of well bonded crystals which were not very favorable for the formation of avalanches.

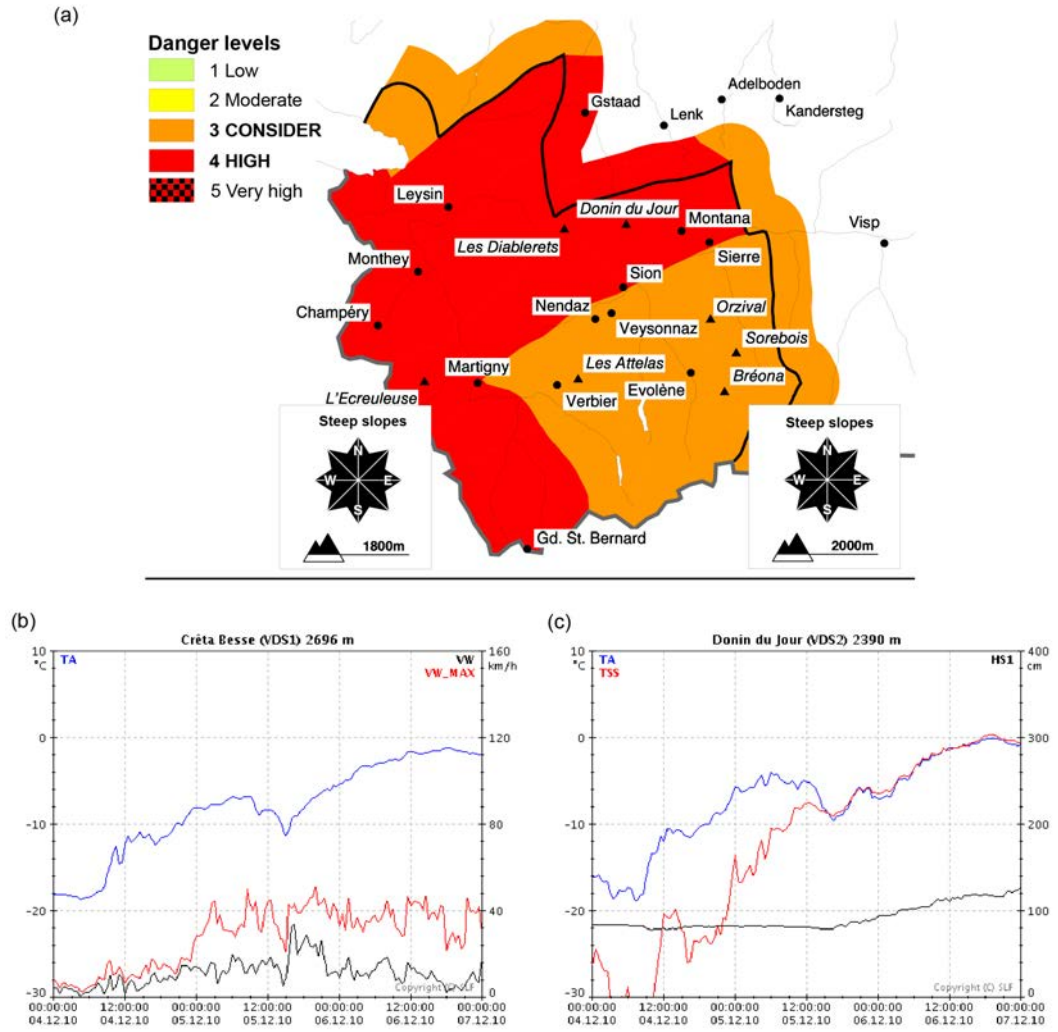

FIGURE 5.8: a) Regional avalanche danger map of Central Valais, lower Valais and Vaud Alps (avalanche bulletin no. 28 for Monday, 6th December 2010; www.slf.ch). b) Air temperature (TA), wind velocity (VW) and maximum wind velocity (VW_{MAX}) data measured during 4th to 6th December 2010 at Crêta Besse weather station (VDS1). c) Air temperature (TA), snow surface temperature (TSS), snow surface height (HS1) measured during 4th to to 6th December 2010 at Donin du Jour weather station (VDS2). Source: SLF (http://www.slf.ch)

The weekly report of the SLF indicated a moderate avalanche danger (level 2; Figure 5.9a) at Valais because of the stable snowpack and only low winds from the northeast in this part of the Alps. According to SLF data, there were no natural snow avalanches on the days before and after the earthquake because the snowpack was fairly stable.

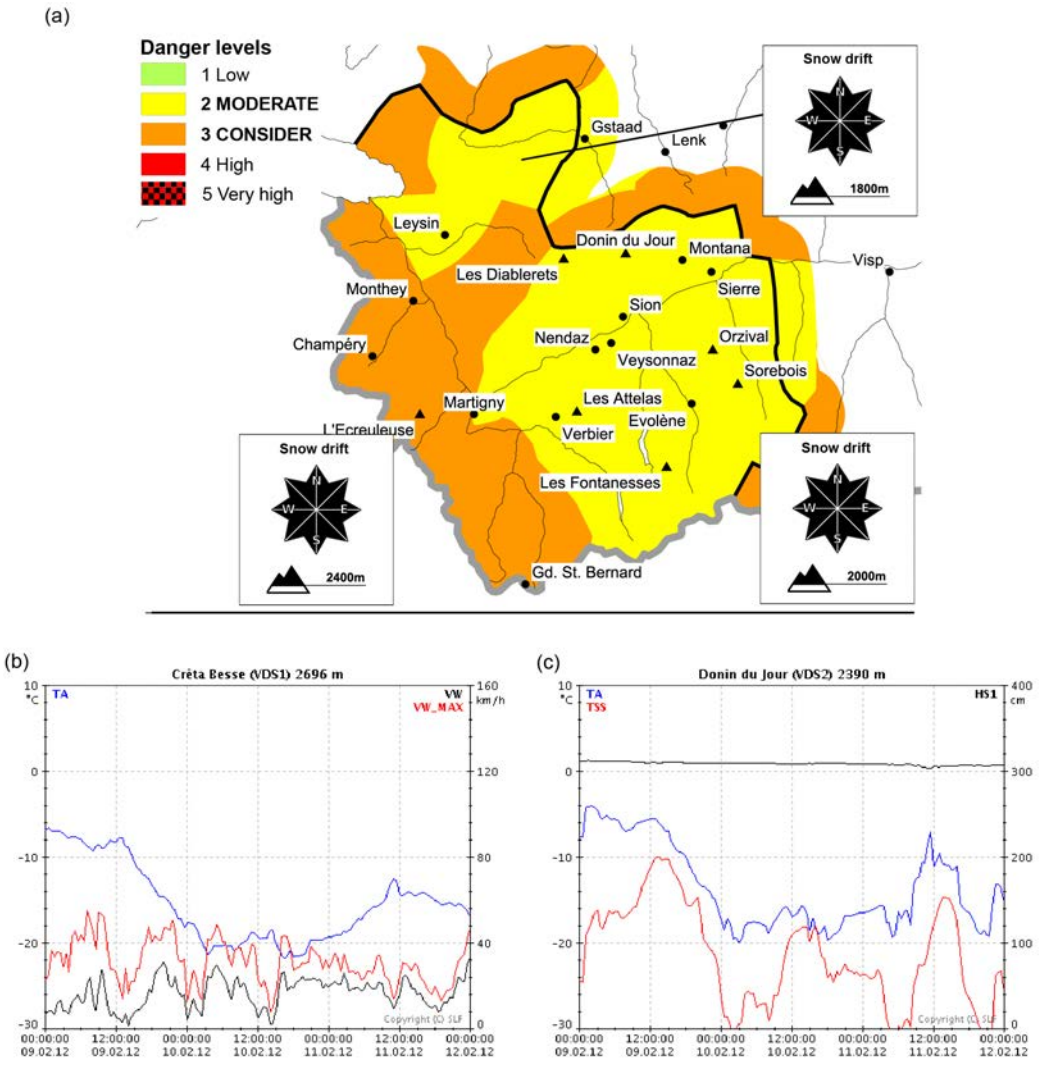

FIGURE 5.9: a) Regional avalanche danger map of Central Valais, lower Valais and Vaud Alps (avalanche bulletin for Saturday, 11th February 2012; www.slf.ch). b) Air temperature (TA), wind velocity (VW) and maximum wind velocity (VW_{MAX}) data measured during 9th to 11th February 2012 at Crêta Besse weather station (VDS1). c) Air temperature (TA), snow surface temperature (TSS), snow surface height (HS1) measured during 9th to 11th February 2012 at Donin du Jour weather station (VDS2). Source: SLF (http://www.slf.ch).

21th March 2012

On 21th March 2012 the temperature of the air was −3°C (VDS1 station; Figure 5.10b) at 11:01 (local time) and there was 0.1−0.2 m of snow precipitation during the night of 20 March 2012. There was a snow cover of 2.73 m at the VDL2 weather station (Figure 5.10c). The SNOWPACK simulation of this day (Figure 5.7) showed a snow cover that consisted of 0.7 m of rounded grains below 1.8 m of

melt forms. At the top a 0.2 m thick layer of decomposed forms was observed. The only possible weak layer was situated at the interface of the rounded grains and the decomposed forms at 2.5 m above the ground. The snow cover was mainly well bonded. Moreover, this day, the regional avalanche bulletin indicated a moderate avalanche danger (level 2; Figure 5.10a) for the area of VDLS. It was a spring situation with the possibility for spontaneous wet avalanche formation.

Comparing the snow cover conditions of the three days we can conclude that at the day of the earthquake followed by the avalanche, the conditions for an avalanche release were more favourable than for the days of the two other earthquakes. The snow profile this day showed a new snow layer on a very unfavourable old snow cover that consisted of a weak layer of faceted crystals over a crust. Therefore, the existence of this weak, non-cohesive layer in the snow cover, the loading produced by the snow precipitation during the previous hours and the rapid increase in the air temperature together with the rapid loading produced by the shaking of the earthquake were the factors that contributed to the avalanche release on 6th December 2010.

Another possible factor in the relationship between the snow cover conditions and the effectiveness of the shaking of the earthquakes should be taken into account. This is the position of the weak layer in the snow cover that could be fractured due to the shaking of the earthquake. Since the seismic waves propagate through the ground before reaching the snow cover and thus could be attenuated inside the different snow layers before reaching the weak layer. The amplitude of the shaking on the weak layer will depend on the distance travelled inside the snow cover. Field experiments carried out with explosives to release avalanches have shown that the effective range of an explosive depends on the position of the charge relative to the snow surface, the charge mass, the snow profile and the characteristics of the ground (Gubler, 1977). The snow cover simulations of the different days (Figure 5.7) showed that snow cover depths and position of the possible weak layers are much higher up in the snow cover of days of the earthquakes #2 and #3 than in the day of the event, which can also contribute to the attenuation of the seismic waves travelling through the snow cover.

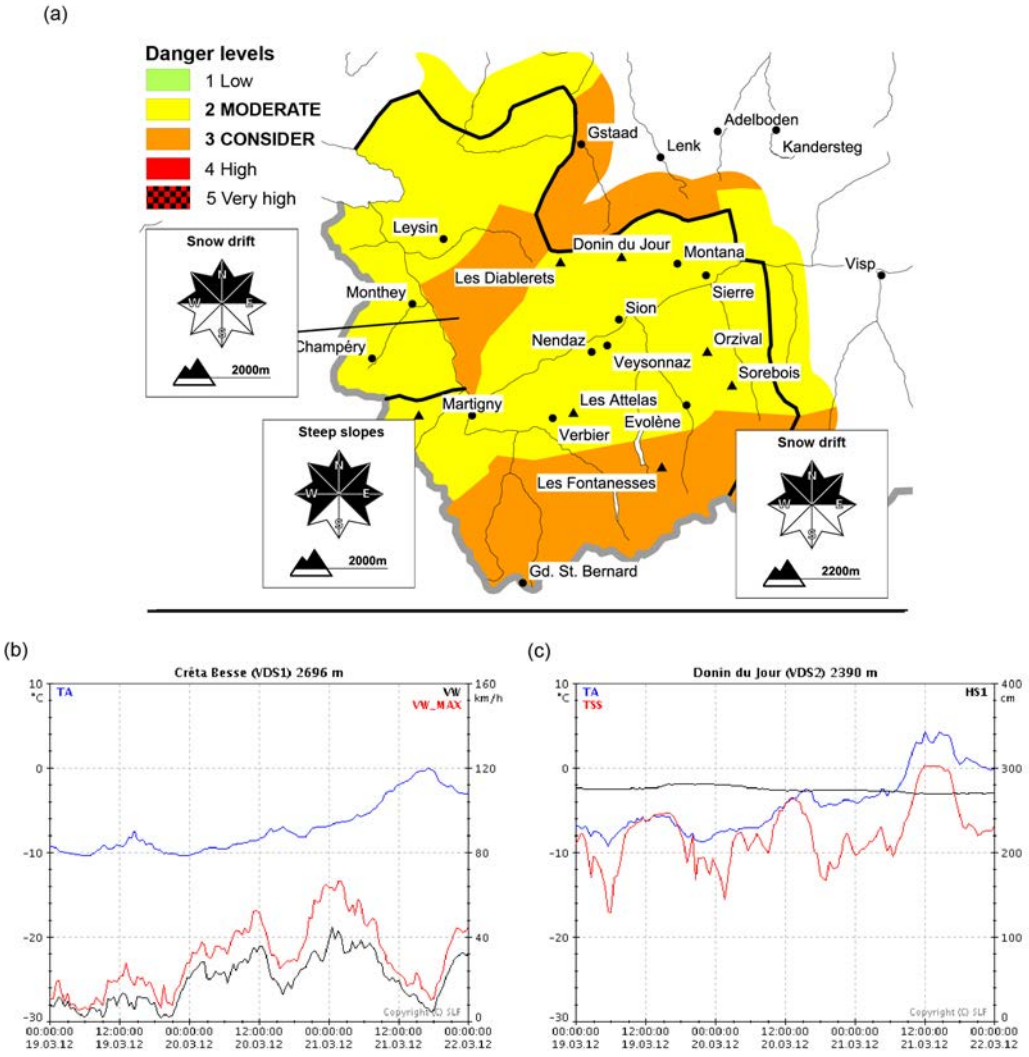

FIGURE 5.10: a) Regional avalanche danger map of Central Valais, lower Valais and Vaud Alps (avalanche bulletin for Wednesday, 21th March 2012; www.slf.ch). b) Air temperature (TA), wind velocity (VW) and maximum wind velocity (VW_{MAX}) data measured during 19th to 21th March 2012 at Crêta Besse weather station (VDS1). c) Air temperature (TA), snow surface temperature (TSS), snow surface height (HS1) measured during 19th to 22th March 2012 at Donin du Jour weather station (VDS2). Source: SLF (http://www.slf.ch)

5.7 Stability Factor and Newmark's method

The shaking of the earthquake produces inertial forces in the layered snow cover and in consequence a change in the elastic stress field within the snow. This loading of the snow induced a stress with shear, tensile and compressive components (Podolskiy et al., 2010c). Taking into account the snow conditions analyzed in the previous section, we calculate the stability factor of the slope in the presence of

ground vibration and the coseismic displacement produced by the earthquake #1 at A.

5.7.1 Stability Factor of the slab

The relationship between the retaining forces and shearing forces yields the stability factor of the slope S. For each layer boundary, the resulting stability index S is calculated as (Schweizer et al., 2003):

$$S = \frac{\tau_f}{\tau + \Delta\tau} \tag{5.1}$$

where τ_f is the shear strength, τ is the shear stress due to weight of the overlaying slab layers and $\Delta\tau$ is the additional shear stress due to the earthquake in this case. A failure occurs when the down-slope component of the force approaches the shear strength in the weak layer. However, it is possible to have a failure on snow without fracture propagation (McClung, 2009). The shear stress (denominator of Eq.5.1) of the snowpack in down-slope direction is described as the sum of the weight of the different layers and the loading produced by the acceleration of the earthquake in this direction:

$$\tau_x(t) = \sum_i \rho_i h_i \cdot (g \cdot sin(\alpha) + a_x(t)) \tag{5.2}$$

where τ_x is the shear stress, ρ_i and h_i are the density and height of each layer, and a_x (t) the acceleration due to the earthquake in the down-slope direction. In the presence of the earthquake, this shear stress is a function of time. In consequence, the maximum shear stress applied to the weak layer, during the time interval of the earthquake, is obtained at the instant when the earthquake reached the maximum acceleration (PGA):

$$\tau_{xmax}(t) = \sum_i \rho_i h_i \cdot (g \cdot sin(\alpha) + a_x(t_{PGA})) \tag{5.3}$$

Jamieson and Johnston (1998) obtained the following expressions for the shear strength of layers composed of decomposing forms (τ_I in Eq.5.4) or faceted crystals (τ_{II} in Eq.5.4):

$$\tau_I = 14.5 \cdot 10^3\, Pa\, (\frac{\rho}{\rho_{ice}})^{1.73} \qquad or \qquad \tau_{II} = 18.5 \cdot 10^3\, Pa\, (\frac{\rho}{\rho_{ice}})^{2.11} \tag{5.4}$$

where ρ is the density of the layer and ρ_{ice} is the density of ice. In our study ρ_{ice} is 917 kg/m^3 (McClung and Schweizer, 2006). We consider a range for the density of the decomposing forms layer of 150-200 kg/m^3 and of 200-250 kg/m^3 for the faceted layer (values obtained from the SNOWPACK simulations). Equations 5.4 give a range of values for the shear strength of [632.6-1040.5] Pa for a layer of decomposing forms and [744.3 1191.9] Pa for a layer of faceted crystals. According to the information on the snowpack conditions, two possibilities to calculate the stability factor were considered:

1. The avalanche released in the upper part of the snow cover. In this case only the two first layers of new snow and decomposing forms (100 kg/m^3 of fresh snow and 200 kg/m^3 of decomposing forms; mean values obtained from the simulations) are considered. The thicknesses of these layers are: 0.25 m which is the precipitation measured in VDS2 and 0.2 m the decomposing forms layer obtained from the simulation of the snow cover (Figure 5.7). The maximum value of the shear stress calculated in this evaluation (Eq.5.3) is 410.1 Pa.The stability index (Eq. 4.1) in this case is:

$$S = \frac{\tau_I}{\tau_{max}} \tag{5.5}$$

   The values obtained for S are in the range of [1.5-3.5] which correspond to stable conditions ($S > 1$).

2. The avalanche released in the old snow. In this case, we considered that the first layers (fresh snow and decomposing forms) and the second layer of 0.4 m of faceted crystals of a mean density of 225 kg/m^3 (mean value obtained from the simulation) are released. The maximum value of the shear stress calculated in this evaluation (Eq.5.3) is 977.92 Pa.The stability index in this case is:

$$S = \frac{\tau_{II}}{\tau_{max}} \tag{5.6}$$

   The values obtained for S are in the range of [0.7-1.2]. If the shear strength of the layer is below or equal to the shear stress we have unstable conditions ($S \leq 1$).

We consider that the earthquake could have more effectiveness if the avalanche broke in the interface of the crust and the faceted layer for two reasons: the shear

stress is larger (the stability index is bellow 1 in most of the cases) and the position of the weak layer is close to the ground.

5.7.2 Coseismic displacement

An evaluation of the whole effect of the earthquake was conducted applying Newmark's method (Newmark, 1965). This method has been previously applied to earthquake-induced landslides (Wilson and Keefer, 1983; Jibson, 1993, 2011) and snow avalanches triggered by artificial seismicity (Fedorenko et al., 2002; Chernouss et al., 2006). This method calculates the cumulative displacement (D) of one block, the Newmark displacement, owing to the effects of the earthquake acceleration time-history:

$$D = \int \int (a(t) - a_c)dt^2 \tag{5.7}$$

where a(t) is the acceleration of the earthquake and a_c is the critical acceleration. In this approach, displacement depends on the critical acceleration (Eq.5.7) which depends on the values of the shear strength and shear stress of the slab. The critical acceleration is (Jibson, 1993):

$$a_c = (S - 1) \cdot g \cdot sin(\alpha) \tag{5.8}$$

where α is the slope inclination (40°) and S is the stability factor calculated using Eq.5.1 without considering the earthquake.

The values of the critical acceleration calculated in the evaluation 2 give a range of values of critical acceleration that oscillates from negative values (the snow slab is unstable before the shaking of the earthquake) to values up to 1.2 m/s^2 (over the PGA of the earthquake). We assume that our snowpack is at or very close to the static equilibrium (the stability factor is 1) in the evaluation 2 and then we calculate the maximum cumulative displacement. In a situation very close to the static equilibrium the block experiences a very low critical acceleration (theoretically, $a_c = 0$) and thus should undergo higher inertial displacements (Jibson, 1993). Therefore, the maximum cumulative displacement (zero critical acceleration) produced by the earthquake in the down-slope direction from Eq.5.8 is 0.084 mm. In addition, the maximum cumulative displacement in the direction normal to the shear plane (the vertical component of the acceleration is used in Eq.5.8)

is 0.068 mm. Both shear and normal to the shear plane displacements are calculated because the initial failure could be in compression or in shear (Reiweger and Schweizer, 2010).

Ductile materials can accommodate more displacement without failure, while brittle materials can accommodate less (Jibson, 1993). Snow is one of the most rate dependent materials known (Kirchner et al., 2000). Laboratory experiments (Schweizer, 1998) showed that at high deformation rates snow behaves as a brittle material, but at at low deformation rates as a ductile material. What displacement causes a failure varies according to the material and the conditions. The strain necessary to reach the residual strength can be estimated from laboratory shear-strength tests. Reiweger et al. (2010) performed loading experiments to study the material behavior of snow samples containing a weak layer before fracture. They observed that in layered snow samples the global deformation is concentrated in the weak layer. They used layered snow samples consisting of small grains at the top and bottom and a weak layer of faceted crystals and some depth hoar in between. Comparing two photographs before fracture, they measured displacements between 0.06-0.08 mm within the weak layer. These values are of the same order of magnitude as the maximum cumulative displacement produced by the earthquake on 6th December 2010. Thus, the effects of a minor earthquake on a snow cover with a faceted weak layer, close to static equilibrium can produce enough displacement to cause failure.

5.8 Conclusions

We analysed a small earthquake that occurred on 6th December 2010, 43 km from the VdlS test-site and showed that it possibly triggered an avalanche. The main contribution of this study is the evaluation of the shaking produced by this earthquake to trigger an avalanche using for the first time acceleration data measured in the release area of an avalanche. The low magnitude of the earthquake and the existence of an unstable snowpack hinder the determination of the exact triggering mechanism. However, the evidence of a temporal coincidence of the two seismic sources, the earthquake and the avalanche, reinforces the idea that the earthquake could contribute to the triggering of the snow avalanche.

The study was carried out using seismic and infrasound data generated by three earthquakes and one avalanche obtained by instruments at different locations at the test site. The joint analysis of the infrasound and seismic data shows that the avalanche occurred after the arrival time of the earthquake, in agreement with the GEODAR radar data, suggesting that the earthquake was the triggering factor. The comparison of the radar with the seismic and infrasound data allows us to characterise the avalanche size and path. The avalanche was a dry medium size avalanche flowing down the secondary gully. The maximum infrasound signal was recorded when the avalanche descended in the channelled zone at a high velocity. The avalanche run-out below cavern C was determined by analyzing data from the GEODAR and seismic sensors.

The quantification of the ground motion of the earthquakes shows that the PGD, PGV, PGA, I_a, TD and PSA values of the 6th December 2010 earthquake are not particularly high with the result that we cannot be absolutely sure that the avalanche was triggered by the earthquake. Two other earthquakes with higher quantification parameters did not trigger any avalanches at the same site, because they occurred when the snowpack was much more stable. However, this small earthquake can be significant due to the instability conditions of the snowpack on 6th December 2010.

Despite the fact that possible resonance effects of a snow slab under vibration are unknown, the PSA values calculated for the earthquake of the event indicate that the snow slab could suffer amplifications of the acceleration being up to one order of magnitude higher (PSA maximum values are one order of magnitude higher than the PGA). Therefore in the case of resonance, higher increases of the stresses are produced due the acceleration of the earthquake. On the other hand, the accelerations used in our calculations recorded at the top of the mountain at the avalanche release area are higher than the values obtained at the stations situated at lower heights. The maximum acceleration values, PGA, at the top can be doubled. For a better evaluation and quantification of the earthquake-induced avalanches, it is necessary to know the acceleration time-history of the ground motion in the areas where the avalanches can be released. These data are not easy to obtain because only few seismic stations are situated in these areas where access and installation are complicated.

Owing to the uncertainty in the parameters involved in avalanche release, it is not easy to establish an area affected by snow avalanches triggered by an earthquake

taking into account only the earthquake magnitude and distance without considering the snowpack conditions on a given day. These conditions vary widely in mountain areas and are the key factors in limit cases. The SNOWPACK simulation computed for 6th December 2010 revealed an unstable snow cover with the presence of a weak layer of faceted crystals over a hard crust which was buried by the subsequent snowfall. In these unstable conditions, the maximum cumulative displacement that the earthquake can produce is in the order of magnitude of displacements measured before fracture in laboratory experiments for snow samples with faceted weak layers. Thus, this small displacement could be enough to produce failure when the snow is loaded at high loading rates, like in the case of an earthquake.

Further studies are warranted to evaluate the relationship between the seismic source (amplitude, duration and frequency content) and its effect on the snow, which is one of the most brittle and rate-depended materials that exist.

Note: A new event of an earthquake-generated avalanche has been documented (http://acnacat.weebly.com/notiacutecies.html; (2016, May, 11)) at the end of the writing of this thesis . The event has been visually recorded (https://www.youtube.com/watch?v=FlFEERMrHgY; (2016, May, 11)). This avalanche was triggered on 11th May 2016 in the *Circ de Gavarnie* and temporally coincided with the arrival of an earthquake of magnitude M_L 3.8 in the French Pyrenees (http://www.emsc-csem.org/Earthquake/earthquake.php?id=505942; (2016, May, 11)). The approximate distance of the earthquake epicenter to the avalanche release area was 50 km.

Chapter 6

Deducing avalanche size and flow regimes from seismic data

In the present chapter, the second part of the results of this PhD study are presented. The comparison of seismic signals with FMCW radar measurements generated by the different parts of an avalanche (front, energetic and dense/tail parts) allows determining specific signatures of each avalanche flow regime. In addition, the seismic signals of a catalogue of 32 avalanches of different type and size are quantified using a set of seismic indices defined on the previous Section 4.3.3. This quantification enables us to yield relationships between avalanche seismic signals and avalanche characteristics such as the type of flow and size. Most of the contents of this chapter has been published in Pérez-Guillén et al. (2016).

6.1 Introduction

Interest in the application of seismic methodology in the field of avalanche research has increased considerably in recent years as it enables data to be obtained from remote areas at a low economic cost. The methodology has been widely used to automatically detect or monitor avalanches (Section 1.5), to determine avalanche dynamic parameters (Section 1.4), and to record signals precursory to the avalanche release (Section 1.3).

While much progress has been made in the avalanche research field, the use of seismic sensors for real-time monitoring still requires further research. In remote

areas, real-time monitoring would ideally provide details such as the location of the release, the avalanche size, or the run-out distance. Vilajosana et al. (2007b) estimated the seismic energy dissipated by avalanches into the ground to be used for classifying avalanche size. Their method requires additional data, such as the location of the avalanche front at each instant of time. A beam-forming technique to locate avalanches using an array of seismic sensors was proposed by Lacroix et al. (2012). They estimated the front speed of avalanches and classified them as a function of the type of snow by correlating the data with meteorological data.

So far little research has been done on using seismic data to estimate the run-out distance of an avalanche. We therefore propose correlating the avalanche run-out distance with a set of seismic indices related to the duration and the intensity of the signals. As earlier seismic measurements of avalanches have shown, larger avalanches normally have longer signals and generate signals with higher amplitudes (Suriñach et al., 2001; Biescas et al., 2003; Kogelnig et al., 2011b). This analysis appears simple but it requires knowledge of such fundamental processes as the wave propagation, the effect of the different flow regimes on the features of the signals generated and the effect of the snow cover on the seismic signal attenuation (Reiweger et al., 2015).

Anelastic attenuation of seismic waves is affected by parameters such as anisotropy, fluid content and the porosity of the propagation medium (Toksöz and Johnston, 1981). A snowpack is a porous medium that very effectively absorbs energy (Gubler, 1977). It is stratified in layers with different physical properties (Schweizer et al., 2003) and acts as the interface between the sources of the seismic signals and the sensors buried in the ground. Little is known about the effects of the depth and properties of the snow cover on the seismic signals, but such information is essential for improving seismic methodology as a system for detecting or classifying avalanches. None of the seismic monitoring systems developed to date take snow cover characteristics along the avalanche path into account as an additional attenuation factor of the seismic signals.

Moreover, snow avalanches can display a variety of flow regimes as a function of the physical properties of the snow cover (Steinkogler et al., 2014). The ground motion generated by snow avalanches is directly connected to the flow regime that the avalanche develops. A deeper understanding of the sources of avalanche seismic signals is fundamental to elucidate their relation with avalanche dynamic processes.

In this chapter, we analysed the avalanches of Table 4.1 (excluding the avalanche #3002, previously analysed in Chapter 5) acquired with the seismic sensors positioned in and outside the avalanche path and compared them with Frequency Modulated Continuous Wave radar measurements (Section 4.4). This enabled us to characterize the avalanche flow regimes, deduce the snow cover thickness at the seismic locations and correlate a set of seismic indices with the avalanche run-out distance. The combined data analysis allowed us to relate the internal flow structures and the basic processes, such as erosion and deposition that govern the dynamics of the avalanche, with the signatures of the seismic signals (Section 6.2). Based on these results, we describe the nature of the seismic signals generated by the different avalanche typologies (Section 6.3) and the feasibility of using seismic measurements to distinguish avalanche flow regimes (Section 6.4). The basis of a method for avalanche classification based on a set of seismic indices is presented in Section 6.5, together with an evaluation of seismic absorption factors calculated for different snow cover thicknesses (Section 6.5.1). Finally, we discuss how the proposed method can be used to estimate the avalanche size (Section 6.6).

6.2 Comparison between FMCW radar data and seismic signals

We analysed a total of 32 snow avalanches recorded with the seismic sensors during the winters of 1999 to 2003 and 2010 to 2015. The classification of the snow avalanches in function of the triggering mechanism, avalanche path, type of flow and size are shown in Table 4.1. For each avalanche we calculated the following seismic indices (defined in Section 4.3.3) at each seismic station: the avalanche seismic signal duration (T_A), the peak ground velocity of the total envelope ($PGVE$) of the seismic signal and the signal intensity (I). All the seismic signals were filtered (1 Hz to 45 Hz) with a 4th-order Butterworth bandpass filter with the aim of homogenizing all the data acquired with different sample rates. Table 6.1 gives for each avalanche the number, the snow cover thickness (H) at locations where the avalanche flows over (B and/or C), and the seismic indices calculated at each site. Detailed characteristics of the instrumentation deployed at the site and the measurement procedures are described in Chapter 2 and Chapter 4, respectively.

TABLE 6.1: Characteristics of the avalanches analysed: avalanche number, recorded location, snow cover thickness, H (m), obtained from the FMCW radar of this site (B or C), and the values of the seismic indices ($T_A(s)$, $PGVE(ms^{-1})$ and $I(ms^{-1})^2 \cdot s$) determined at each seismic site (B, C and D). The date of each avalanche, the typology, the triggering mechanism, the avalanche path and the run-out distance are in Table 4.1.

$N°$	T_A	H_B	$PGVE_B$	I_B	H_C	$PGVE_C$	I_C	$PGVE_D$	I_D
301	217.8	[2.5-0.5]	$5.6 \cdot 10^{-4}$	$2.5 \cdot 10^{-6}$	-	-	-	-	-
103	304.0	[2.5-5]	$3.0 \cdot 10^{-2}$	$2.1 \cdot 10^{-4}$	-	-	-	-	-
200	290.0	[2-0]	$5.4 \cdot 10^{-3}$	$4.7 \cdot 10^{-5}$	-	-	-	-	-
4267	281.1	0.5	$1.0 \cdot 10^{-3}$	$4.9 \cdot 10^{-6}$	-	-	-	$1.1 \cdot 10^{-5}$	$1.1 \cdot 10^{-5}$
4270	80.9	1	$1.5 \cdot 10^{-4}$	$7.6 \cdot 10^{-8}$	-	-	-	$1.3 \cdot 10^{-6}$	$3.4 \cdot 10^{-11}$
4288	436.4	0.5	$2.2 \cdot 10^{-3}$	$2.2 \cdot 10^{-5}$	-	-	-	$1.6 \cdot 10^{-5}$	$4.3 \cdot 10^{-9}$
4292	542.2	[1.5-0.5]	$2.0 \cdot 10^{-3}$	$2.2 \cdot 10^{-5}$	-	-	-	$1.5 \cdot 10^{-4}$	$1.0 \cdot 10^{-7}$
504	148.8	[3-1.5]	$1.0 \cdot 10^{-3}$	$6.7 \cdot 10^{-6}$	-	-	-	$2.2 \cdot 10^{-3}$	$3.4 \cdot 10^{-6}$
505	76.1	2	$1.2 \cdot 10^{-4}$	$4.4 \cdot 10^{-8}$	-	-	-	-	-
506	190.1	[3-1]	$9.9 \cdot 10^{-4}$	$3.9 \cdot 10^{-6}$	-	-	-	$2.9 \cdot 10^{-4}$	$2.6 \cdot 10^{-5}$
3003(1)	404.3	[x-0]	$7.8 \cdot 10^{-4}$	$1.6 \cdot 10^{-6}$	[1.5-0]	$6.1 \cdot 10^{-5}$	$1.4 \cdot 10^{-7}$	$4.9 \cdot 10^{-6}$	$3.9 \cdot 10^{-10}$
3004	507.0	[1.5-0]	$3.8 \cdot 10^{-4}$	$2.1 \cdot 10^{-7}$	[1.5-1]	$6.4 \cdot 10^{-5}$	$1.4 \cdot 10^{-7}$	$3.5 \cdot 10^{-5}$	$7.6 \cdot 10^{-9}$
3006	291.8	[2-1]	$5.7 \cdot 10^{-4}$	$7.9 \cdot 10^{-7}$	1.5	$4.0 \cdot 10^{-5}$	$6.3 \cdot 10^{-9}$	$1.3 \cdot 10^{-6}$	$1.9 \cdot 10^{-11}$
3012	106.3	[3.5-1.5]	$1.8 \cdot 10^{-5}$	$1.1 \cdot 10^{-9}$	[3.5-2.5]	$4.6 \cdot 10^{-5}$	$5.4 \cdot 10^{-9}$	$3.2 \cdot 10^{-5}$	$1.1 \cdot 10^{-9}$
3023	74.5	[x-4.25]	$4.5 \cdot 10^{-5}$	$6.9 \cdot 10^{-9}$	-	$1.6 \cdot 10^{-6}$	$1.1 \cdot 10^{-11}$	$2.4 \cdot 10^{-7}$	$9.3 \cdot 10^{-13}$
3053(1)	202.0	3	$4.3 \cdot 10^{-5}$	$1.3 \cdot 10^{-8}$	-	$2.7 \cdot 10^{-6}$	$2.2 \cdot 10^{-11}$	$3.7 \cdot 10^{-7}$	$1.1 \cdot 10^{-12}$
3054	108.0	3	$1.0 \cdot 10^{-5}$	$1.2 \cdot 10^{-9}$	-	$1.1 \cdot 10^{-7}$	$5.0 \cdot 10^{-13}$	$7.5 \cdot 10^{-8}$	$1.6 \cdot 10^{-13}$
3060	236.6	0.75	$4.0 \cdot 10^{-5}$	$2.1 \cdot 10^{-8}$	-	$6.8 \cdot 10^{-6}$	$1.4 \cdot 10^{-10}$	$5.5 \cdot 10^{-7}$	$9.7 \cdot 10^{-12}$
3003(2)	320.7	[x-0]	$6.6 \cdot 10^{-5}$	$5.3 \cdot 10^{-9}$	[2-0.5]	$5.1 \cdot 10^{-5}$	$4.5 \cdot 10^{-9}$	-	-
3018	215.9	[5.5-4.6]	$1.9 \cdot 10^{-5}$	$2.9 \cdot 10^{-9}$	-	$2.3 \cdot 10^{-6}$	$1.6 \cdot 10^{-11}$	$3.3 \cdot 10^{-7}$	$8.4 \cdot 10^{-13}$
3019	412.8	[5.5-4]	$1.6 \cdot 10^{-4}$	$7.9 \cdot 10^{-8}$	[1.75-0.5]	$1.2 \cdot 10^{-4}$	$5.6 \cdot 10^{-7}$	$6.4 \cdot 10^{-6}$	$1.7 \cdot 10^{-10}$
3020	464.9	[4.5-4]	$2.7 \cdot 10^{-5}$	$1.2 \cdot 10^{-8}$	-	$6.7 \cdot 10^{-5}$	$9.2 \cdot 10^{-8}$	$1.1 \cdot 10^{-5}$	$6.0 \cdot 10^{-10}$
3021	380.5	[x-4]	$6.5 \cdot 10^{-5}$	$4.4 \cdot 10^{-8}$	[1.5-0.5]	$3.4 \cdot 10^{-4}$	$2.1 \cdot 10^{-6}$	$2.4 \cdot 10^{-5}$	$1.2 \cdot 10^{-8}$
3022	98.12	[x-3.75]	$3.4 \cdot 10^{-5}$	$1.1 \cdot 10^{-8}$	-	$5.8 \cdot 10^{-7}$	$2.8 \cdot 10^{-12}$	$1.3 \cdot 10^{-7}$	$2.5 \cdot 10^{-13}$
3023_1	48.4	[x-4.2]	$1.2 \cdot 10^{-5}$	$2.2 \cdot 10^{-10}$	-	$8.6 \cdot 10^{-8}$	$1.7 \cdot 10^{-13}$	$9.2 \cdot 10^{-8}$	$1.3 \cdot 10^{-13}$
3023_2	58.9	4.25	$1.2 \cdot 10^{-5}$	$1.8 \cdot 10^{-10}$	-	$6.3 \cdot 10^{-8}$	$1.7 \cdot 10^{-13}$	$9.5 \cdot 10^{-8}$	$1.5 \cdot 10^{-13}$
3024	148.4	4.2	$8.7 \cdot 10^{-5}$	$1.6 \cdot 10^{-8}$	-	$5.1 \cdot 10^{-5}$	$1.2 \cdot 10^{-8}$	$5.9 \cdot 10^{-6}$	$6.0 \cdot 10^{-11}$
3049	195.2	1.5	$6.4 \cdot 10^{-5}$	$2.7 \cdot 10^{-8}$	-	$5.2 \cdot 10^{-6}$	$6.6 \cdot 10^{-11}$	$5.6 \cdot 10^{-7}$	$1.6 \cdot 10^{-12}$
3050	202.1	1.5	$3.5 \cdot 10^{-5}$	$1.4 \cdot 10^{-8}$	-	$2.4 \cdot 10^{-6}$	$1.6 \cdot 10^{-11}$	$3.2 \cdot 10^{-7}$	$1.1 \cdot 10^{-12}$
3053(2)	208.5	2	$6.1 \cdot 10^{-5}$	$3.3 \cdot 10^{-8}$	-	$5.3 \cdot 10^{-6}$	$1.0 \cdot 10^{-10}$	$5.9 \cdot 10^{-7}$	$3.2 \cdot 10^{-12}$
16	152.0	[2-0]	$3.4 \cdot 10^{-4}$	$3.2 \cdot 10^{-7}$	[2-1]	$2.4 \cdot 10^{-4}$	$1.5 \cdot 10^{-7}$	$7.2 \cdot 10^{-5}$	$7.7 \cdot 10^{-9}$
17	123.2	[2-0]	$1.3 \cdot 10^{-3}$	$2.0 \cdot 10^{-6}$	[3.5-2.5]	$4.3 \cdot 10^{-4}$	$1.4 \cdot 10^{-7}$	$6.0 \cdot 10^{-5}$	$4.9 \cdot 10^{-9}$

Seismic signals in the time-frequency domain were compared with the FMCW radar measurements obtained from the nearest locations. The FMCW signals were used to qualitatively distinguish the internal flow regimes in the avalanche flow, and thus further dissect the SOV part of the signal into subregions, each one corresponding to a different flow regime, namely: the front, the energetic flow part and the dense/tail part (see Section 4.4). As examples, the FMCW radar signal generated by the powder-snow avalanche #504 is shown in Figure 6.1a and that generated by the wet-snow avalanche #3020 in Figure 6.2a, with the corresponding seismograms in Figure 6.1b and 6.2b, the CE diagrams in Figure 6.1c and 6.2c and the spectrograms of the seismic signals in Figure 6.1d and 6.2d.

Normally, the length of the SOV section, i.e. the avalanche temporal length, is deduced directly from the FMCW plots. After comparing all the avalanche data we observed that on average, the head of the avalanche is over the seismic sensor when the normalized $CE(\%)$ is 0.5%, with a standard deviation of 0.2% (Figures 6.1 and 6.2). The time when the end of the avalanche tail flows over the sensor is normally deduced from the FMCW plots and corresponds to an average normalized of $CE(\%)$ of 99.91%, with a standard deviation of 0.02% (Figures 6.1 and 6.2). We therefore defined the avalanche temporal length T_L (s) (Section 4.3.1) at a given site as the time interval in which the normalized $CE(\%)$, is between 0.5% and 99.91%. The avalanche temporal length can be calculated from the normalized $CE(\%)$ if the quality of the FMCW radar signal is poor.

6.2.1 Snow avalanche regions

Typically, a powder-snow avalanche is characterized by three parts (Figure 6.1a). For example, the front of avalanche #504 lasted for 5 s, measured from 40 to 45 s after t_i; its energetic part for 18 s, from 45 to 63 s; and the dense/tail part for 54.5 s, from 63 to 117.5 s. The frequency content of the seismic signal generated by each part of avalanche #504 is given in Figure 6.3 (a-c). In contrast, only one or two parts are distinguishable in the FMCW radar signal of a wet-snow avalanche. For example, the front of avalanche #3020 (Figure 6.2a) lasted for 5.2 s, from 72.6 to 77.8 s; and the dense/tail for 177.5 s, from 77.8 to 255.3 s (see Figure 6.3 (d-e) for the frequency content of the seismic signal generated).

Only a few avalanches had mixed characteristics, behaving like a powder-snow avalanche in the upper part of the track but like a wet flow in the lower part of the

track (see Figure 6.4 for an example). Avalanche #3019 was a large transitional avalanche characterized by a different flow regime between the upper part of the path (at B) and the lower part of the path (at C). At B, two characteristic parts of a powder-snow avalanche can be distinguished in the FMCW signal (Figure 6.4a): the energetic part (70.8-86 s; the front region was very short or not distinguishable from the energetic part) and the dense/tail part (86-234 s). At C, two parts are distinguishable, but with the characteristics of a wet flow (Figure 6.4e): the front (171.4-176.2 s) and the dense/tail part (176.2-290 s). The seismic signals at both locations and the corresponding power spectra of the different parts are shown in Figures 6.4 (b-d) and 6.4 (f-h).

Avalanches #504, #3020 and #3019 were taken as examples of the three different types of avalanche and the signals they produced in each distinguishable region were analysed in detail. Their duration (Section 4.3.1), maximum flow height (Section 4.4), CE (%) (Section 4.3.1) and frequency content (Section 4.3.2) are listed in Table 6.2 for each avalanche region and location.

Frontal Region

The frontal region of both powder-snow and wet-snow avalanches normally consists in a short time interval of a few seconds (up to 5 s). In this region, the FMCW radar signals are characterized by low-intensity signals and a small flow height (up to 2 m). A rapid entrainment of dry snow of low cohesion occurs in this region (Sovilla et al., 2006). For examples of this region with durations between 4.8 and 5.2 s, and flow heights between 0.5 and 2 m, see Figures 6.1a, 6.2a, 6.4e and Table 6.2.

The avalanche front passing over the seismic sensor generates a wave packet with low seismic amplitude (e.g. Figures 6.1b, 6.2b, 6.4f), low dissipation of CE (%) (less than 5%; Table 6.2) and a power spectrum in the range of [1-40] Hz (Table 6.2). The maximum CE (%) of 2.9% was dissipated by the passage of the front of the powder-snow avalanche #504; whereas the minimum of 0.7% was for the wet-snow avalanche #3020 (Table 6.2). The frequency content of the spectra of the signals of the wet flows are [16-27] Hz for avalanche #3020; and [14-40] Hz for avalanche #3019 (Figures 6.3d and 6.4g; Table 6.2). These values differ slightly from those of the spectrum of the powder-snow avalanche where the frequency range of [1-41] Hz is wider (Figure 6.3a; Table 6.2).

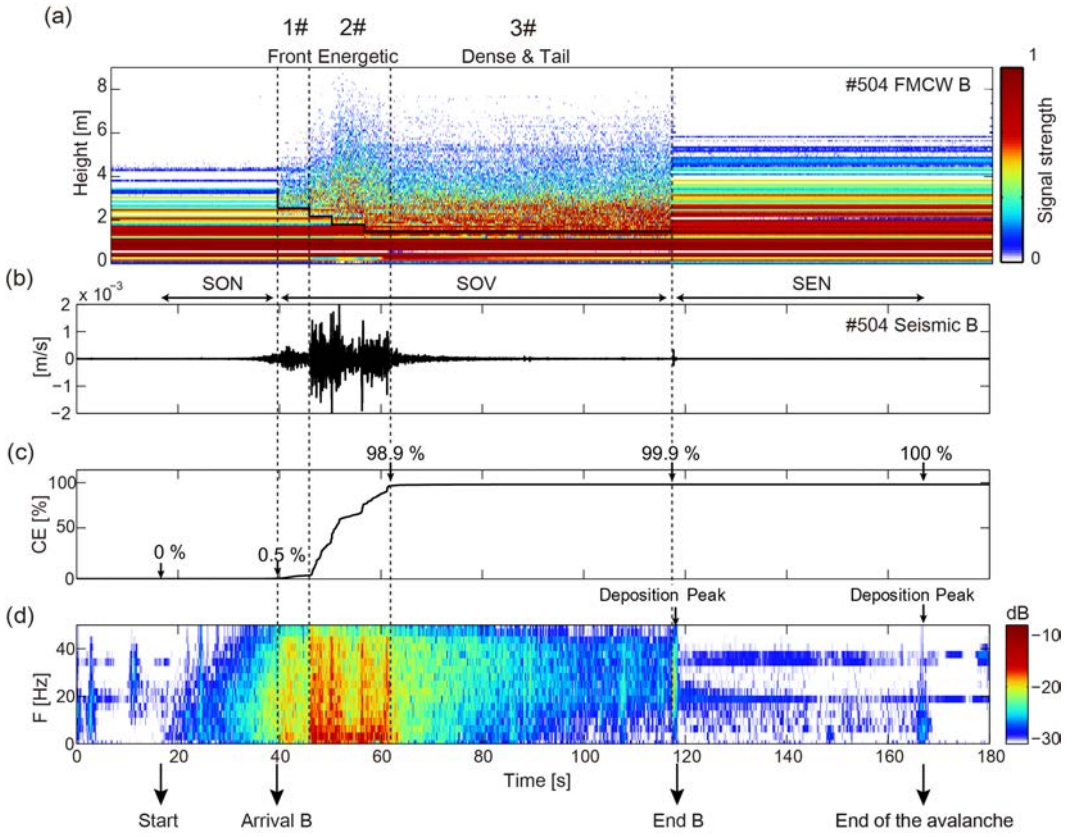

FIGURE 6.1: Comparison of the FMCW radar signal (a), the seismic signal (b), the CE diagram (c), and the spectrogram (d), of the powder avalanche #504 recorded at B. Three different sections can be distinguished in the seismic signal: SON, SOV and SEN. The dashed lines delimit the different parts of the avalanche in the SOV section: the front (#1), the energetic part (#2) and the dense/tail part (#3). The solid black lines of the FMCW radar signal delimit the bed surface levels of the avalanche at heights between 2.5 and 1.5 m.

Energetic Turbulent Region

The energetic region, which is only present in powder-snow avalanches, is characterized by density stratification, with a higher density close to the ground (Sovilla et al., 2015). This region is characterized by the highest entrainment rate and maximum flow heights (up to 8 m in our avalanche catalogue). The duration of the passing of this region in our dataset was up to 30 s. The energetic regions of the powder-snow avalanches #504 and #3019 at B are shown in Figures 6.1a and 6.4a, respectively. The maximum height of the avalanche flow was 4.5 m for 504 and 3 m for #3019 (Table 6.2).

The energetic flow passing over the seismic sensor generates the highest seismic amplitudes, and $CE(\%)$ rapidly reaches values over 50%. The seismic signals

of the examples indicate that, for avalanche #504, 95.6% of $CE(\%)$ is dissipated during the passage over the sensor of the energetic part (Figure 6.1b) and for #3019 (Figure 6.4b), 60.0% (Table 6.2). A narrow power spectrum with frequencies below 10 Hz characterizes the spectra of this region. For instance, the power spectra of the energetic parts of avalanches #504 (6.1b) and #3019 (6.4c) have maximum amplitudes for frequencies below 6 Hz (Table 6.2).

The seismic signals generated by the energetic region of larger powder-snow avalanches, e.g. avalanche #504 (Figure 6.1b), frequently contain different seismic wave packets. The breaking and entrainment of the subsequent deeper snow layers correlates well with the highest increases in seismic amplitude (Figure 6.1b), as a previous comparison between the FMCW and seismic signals of avalanches has shown (Biescas, 2003).

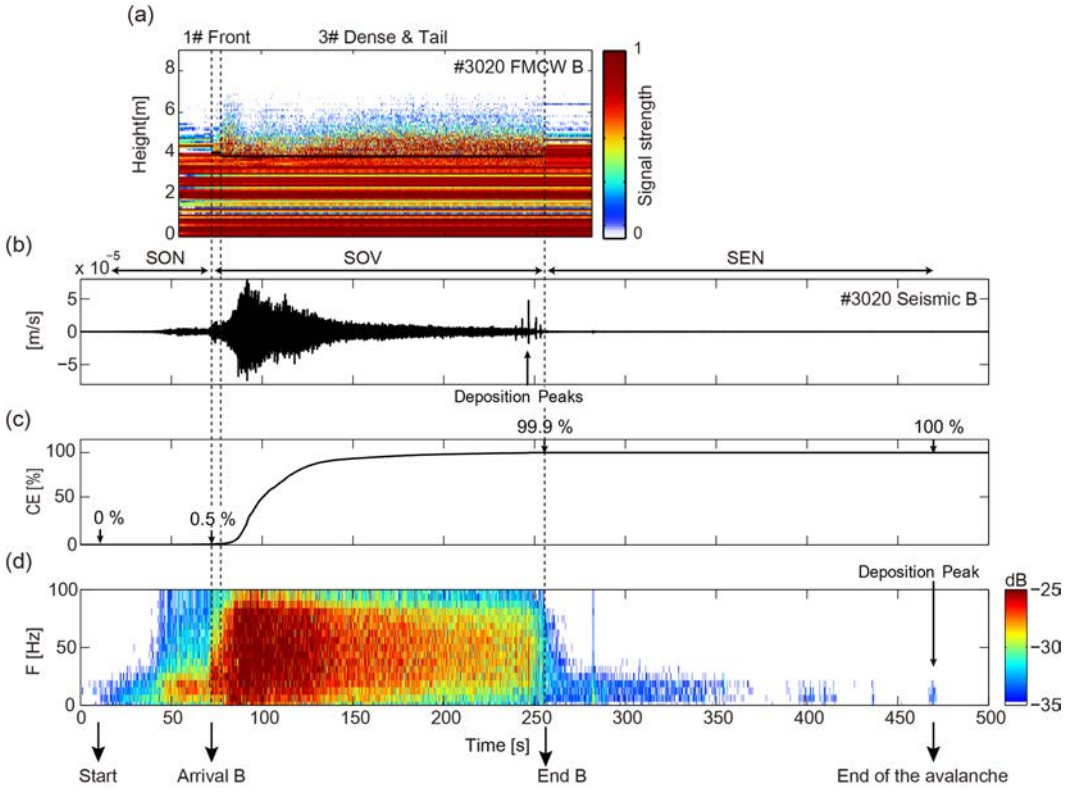

FIGURE 6.2: Comparison of the FMCW radar signal (a), the seismic signal (b), the CE diagram (c), and the spectrogram (d), of the wet-snow avalanche #3020 recorded at B. Three different sections can be distinguished in the seismic signal: SON, SOV and SEN. The dashed lines delimit the different parts of the avalanche in the SOV section: the front (#1), the energetic part (#2) and the dense/tail part (#3). The solid black lines of the FMCW radar signal delimit the different bed surface levels of the avalanche at heights between 4.1 and 4 m.

A ground particle motion analysis of the filtered signals was performed to identify specific waves. An explanation of the particle motion analysis is detailed, for example, in Vilajosana et al. (2008). A low pass filter with a cutoff frequency of 10 Hz is applied to the signals. We selected this cutoff frequency because the energetic part of an avalanche is mainly characterized by a low frequency spectrum with maximum amplitudes below 10 Hz (Figures 6.3b and 6.4c). The analysis of the diagram of the particle (Figure 6.5) allows us to identify pressure waves (P-waves) within the seismograms of the energetic part of powder-snow or transitional avalanches at B, where the flow is confined in a channeled terrain (Figure 6.6). The diagrams of the particle of the avalanches #504 and #3019 are shown in Figure 6.5. Least square regression lines are fitted to the amplitudes of the seismic signals to obtain the angles $[\alpha, \phi]$. The ϕ angle represents the impact direction of the avalanche in the XY plane (Figure 6.6a). The α angle represents the impact direction of the total vector R, composed by X and Y, and the vertical component Z.

We observed that the angle ϕ correlate well with the flowing direction of the avalanches before reaching B location (Figure 6.6). A change in the main avalanche flow direction occurs just at the height of the cavern B, where three sub-gullies are joined at this location. Snow avalanches released from PR-CB1 area have ϕ angles in the range between $35° - 45°$ and between $15° - 45°$ if they were released in CB1-CB2. At C, the avalanche spreads laterally after flowing through the channelled part of the path and thus, none explicit impact direction has been recorded.

Dense/Tail Region

The passing of the dense/tail region of both powder-snow and wet-snow avalanches over the sensors may take as long as 400 s. The FMCW radar signals of this region show a relatively constant flow height (0.5-2.5 m), while the bed surface remains at the same level (0 - 4.5 m above ground) until the avalanche stops (Figures 6.1a, 6.2a, 6.4a and 6.4e). No significant quantity of snow is entrained in this region because the avalanche slides over a high strength snow surface, usually formed from older avalanche deposits (e.g. avalanches #3019 and #3020) or melt-freeze crusts.

In this region, the seismic signal of a powder-snow avalanche is characterized by a large coda where the amplitudes decrease with time (e.g. Figure 6.1b and 6.4b)

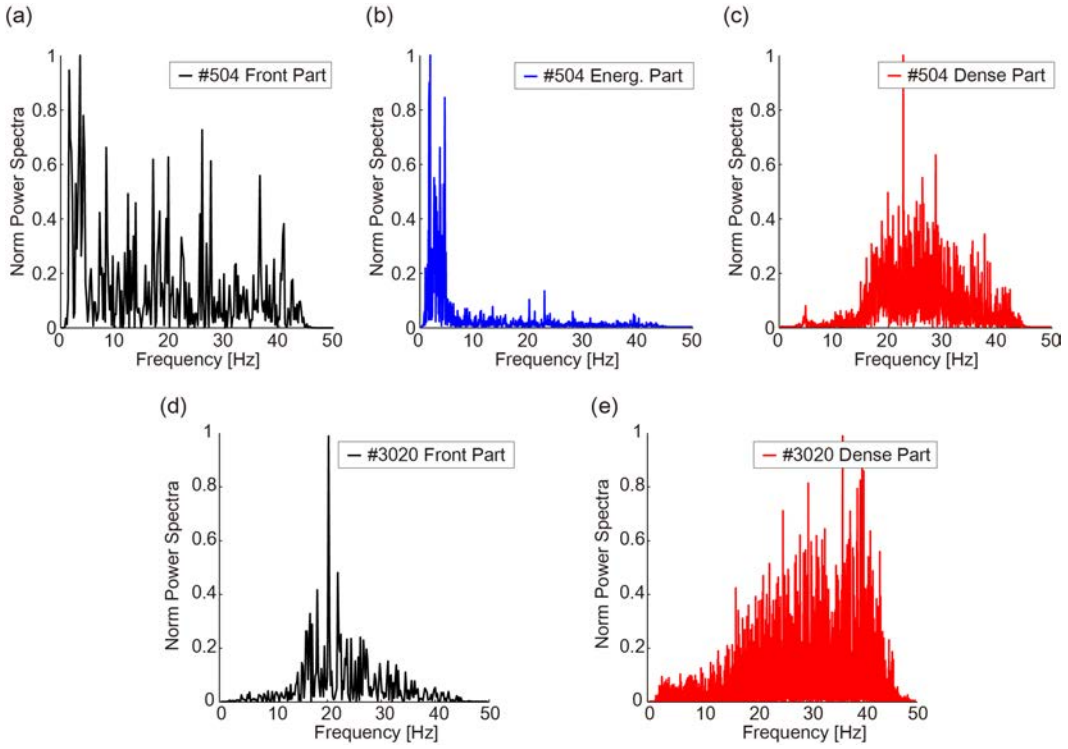

FIGURE 6.3: Normalized power spectra of the seismic signal at B of the different parts of the powder avalanche #504: front (a; black), energetic part (b; blue) and dense/tail part (c; red), and of the wet-snow avalanche #3020: front (d; black) and dense/tail part (e; red).

and generate the typical inverse triangular shape of the spectrograms of avalanches flowing over the seismic sensor with a higher amplitude in the high frequency part of the spectrum as in Figure 6.1d (Biescas et al., 2003). The dense region of wet-snow avalanches presents a typical spindle shape seismic signal with a large coda that also generates an inverse triangularly shaped spectrogram (e.g. Figure 6.2d).

In the powder-snow avalanche #504, the increase in the cumulative energy throughout this interval time is insignificant, according to the $CE(\%)$ diagram (Table 6.2; Figure 6.1c); whereas the cumulative energy of the wet-snow avalanche #3020 increases 98.6% (Table 6.2; Figure 6.2c). The high seismic amplitude peaks in the tail of the avalanche at the end of the FMCW radar signal indicate that the avalanche is depositing mass (e.g. at 118 s in Figure 6.1d and 246.7 in Figure 6.2b). The power spectra of the dense/tail part of all avalanches have a higher frequency content with maximum energies for frequencies over 9 Hz (Table 6.2 and Figures 6.3c, 6.3e, 6.4d and 6.4h).

TABLE 6.2: Detailed information of selected avalanches: avalanche number, recorded location, avalanche typology, type of region, seismic signal duration in the region, maximum flow height, normalized cumulative seismic energy and frequency content for each distinguishable region.

$N°$	Site	Type	Region	Durat. (s)	Max. Flow Height (m)	$CE[\%]$	$\Delta f[Hz]$
# 504	B	Powder	Front	5.0	1.5	2.9	[1.2 - 40.7]
			Energetic	18.0	4.5	95.6	[1.0 - 4.8]
			Dense/Tail	54.5	2.5	1.0	[16.1 - 38.7]
# 3020	B	Wet	Front	5.2	0.5	0.7	[16.0 - 26.7]
			Dense/Tail	177.5	1.5	98.6	[14.7 - 45.0]
# 3019	B	Trans./ Powder	Energetic	15.2	3.0	60.0	[1.2 - 2.5]
			Dense/Tail	148.0	1.5	39.5	[15.8 - 39.0]
	C	Trans./ Wet	Front	4.8	2.0	1.6	[14.1 - 37.2]
			Dense/Tail	169.9	1.5	97.1	[9.3 - 42.1]

6.3 Nature of avalanche seismic signals

At least 50% of the seismic energy dissipated by powder-snow avalanches appears to be generated by the energetic part of the flow with a low frequency content (f $<$ 10 Hz). By contrast, almost all the seismic energy generated by wet-snow avalanches is produced by the dense part of the flow with a higher frequency content (f $>$ 10 Hz).

The maximum seismic energies of powder-snow avalanches are recorded when the energetic part of the avalanche passes over the sensor. This part has a high velocity with large density fluctuations and large energetic impacts with the terrain (Sovilla et al., 2015). Snow is rapidly entrained in the form of abrupt eruptions, increasing the scale of the turbulence. Furthermore, a frontal impact between the avalanche and the snow cover occurs if the avalanche changes the sliding surface (Sovilla et al., 2006). This impact could be correlated with the large seismic peaks recorded after the entrainment of deeper layers. This correlation has been also observed in previous comparisons of FMCW radar and seismic signals of avalanches at VdlS (Biescas, 2003). At the channelled part of the path, as for example at B, these impacts are characterized by pressure waves (P-waves) indicating the direction of the impact of the flow with the sliding surface.

Powder-snow avalanches typically also have a long dense tail. However, the passage of this dense tail over the seismic sensor produces less seismic energy than the

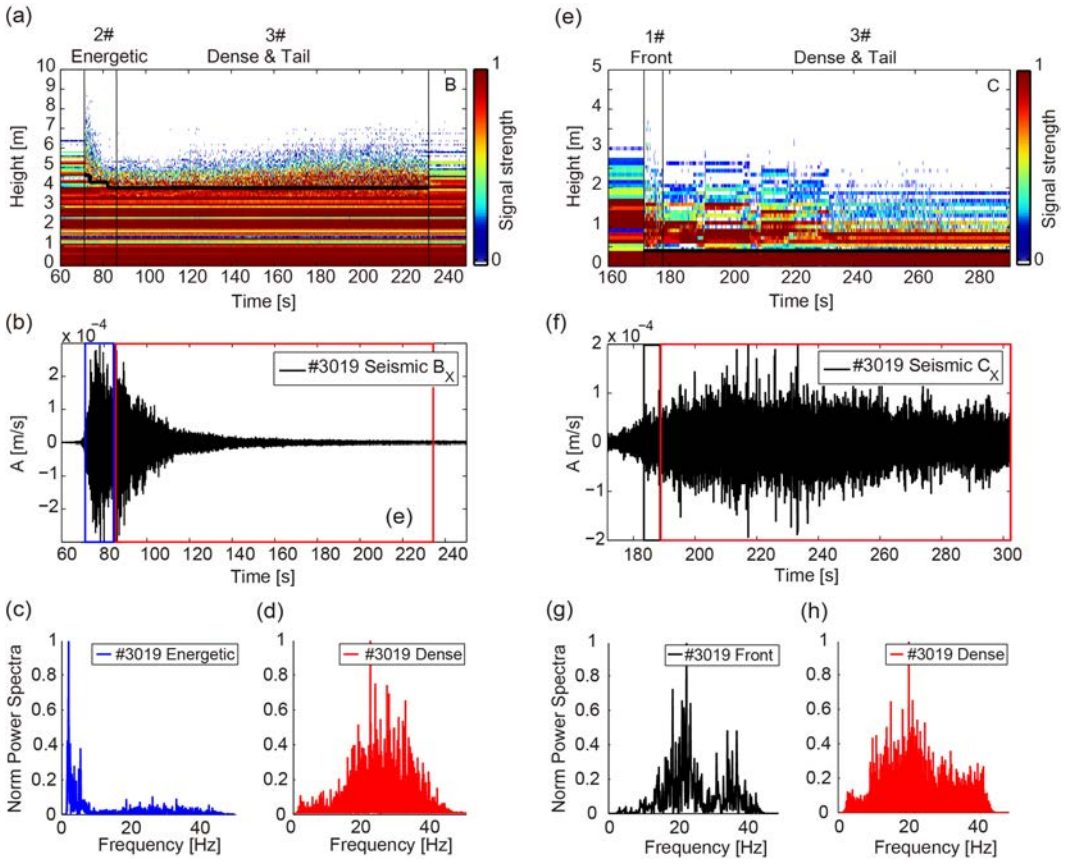

FIGURE 6.4: FMCW radar signals and seismic signals at B (a-d) and C (e-h) of the transitional avalanche #3019 compared: (a) FMCW radar signal divided into the energetic part (#2) and dense/tail part (3); (b) Seismic signal generated by the avalanche; (c) Normalised power spectra of the energetic part and (d) the dense/tail part; (e) FMCW radar signal divided into the front (1) and dense/tail part (3); (f) Seismic signal generated by the avalanche; (g) Normalized power spectra of the front part and (h) the dense/tail part. Note that there is a shift in the arrival time of the avalanche at the FMCW radar equipment and the seismic station at C due to their different positions. No radar data are available for t > 290 s, but the seismic signal of the dense part extends until 346.1 s. The horizontal black lines of the FMCW radar signals delimit the different bed surfaces levels of the avalanche at B and C.

energetic part, possibly because it propagates with a velocity close to zero at the bed surface (Sovilla et al., 2008a; Kern et al., 2009), with no observable erosion processes. Furthermore, the pressure gradually decreases along the dense/tail region, and rapid pressure fluctuations are superimposed on the steadier pressure signal (Sovilla et al., 2015). These fluctuations could generate the high-frequency vibrations characteristic of the tail of the avalanche, thereby producing the typical inverse shape of the spectrograms of the seismic signals.

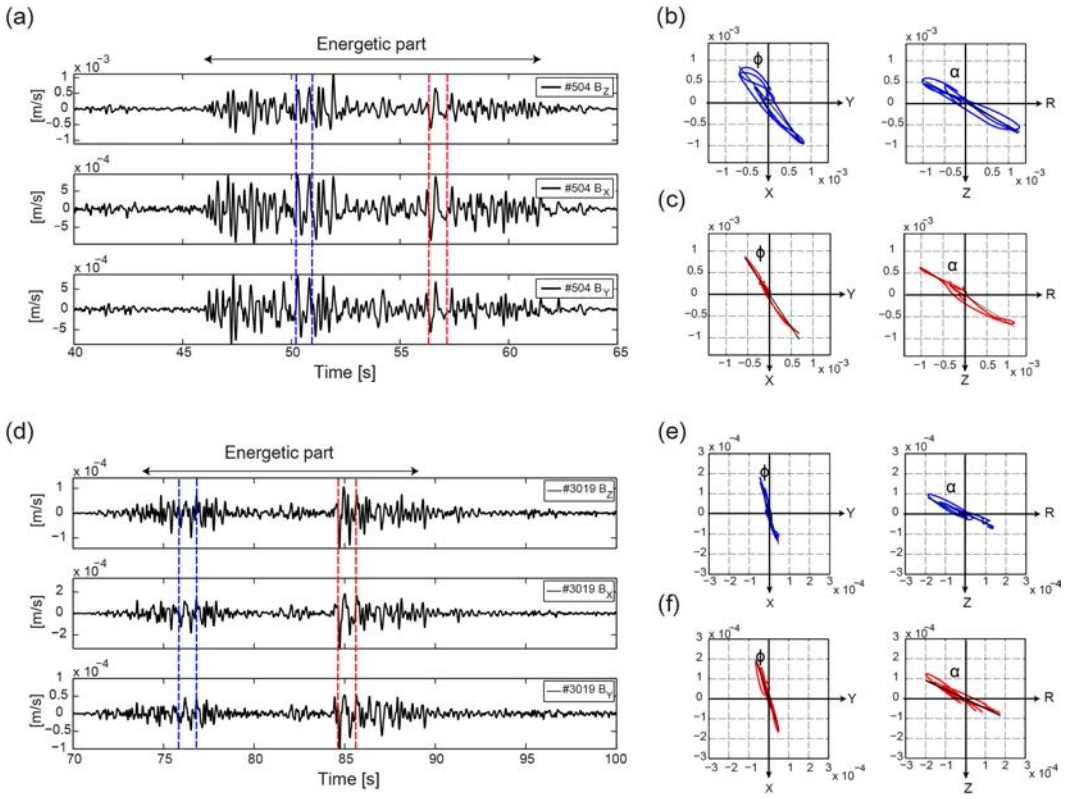

FIGURE 6.5: (a) Filtered (between 1 to 10 Hz) seismograms generated by the energetic part of the powder-snow avalanche #504. The dashed lines represent time intervals where the ground particle analysis was performed. (b) Ground particle diagrams of the first time interval (blue dashed lines). The angles $[\phi, \alpha]$ represent the impact direction of the avalanche with the terrain. (c) Ground particle diagrams of the second time interval (red dashed lines). (d) Filtered (between 1 to 10 Hz) seismograms generated by the energetic part of the transitional avalanche #3019. (e) Ground particle diagrams of the first time interval (blue dashed lines). (f) Ground particle diagrams of the second time interval (red dashed lines). The values for the angles $[\phi, \alpha]$ at the different locations are: $[40°, 62°]$ (b), $[33°, 58°]$ (c), $[20°, 65°]$ (e) and $[16°, 67°]$ (f).

Wet-snow avalanches adopt completely different flow regimes that are characterized by plugs, several metres high, sliding over a thin, sheared basal layer (Sovilla et al., 2008a; Kern et al., 2009). The movement of wet-snow avalanches is strongly influenced by the roughness of the local terrain (Sovilla et al., 2012). In these flows, the largest pressure and fluctuations are found near the sliding surface, which indicates that the contact between the snow granules and terrain is permanent and frictional (Sovilla et al., 2008a). Wet-snow avalanches which may also usually drag along denser material, such as rocks, contribute to the higher seismic energy observed.

In summary, the origin of the high frequency vibrations generated by wet-snow

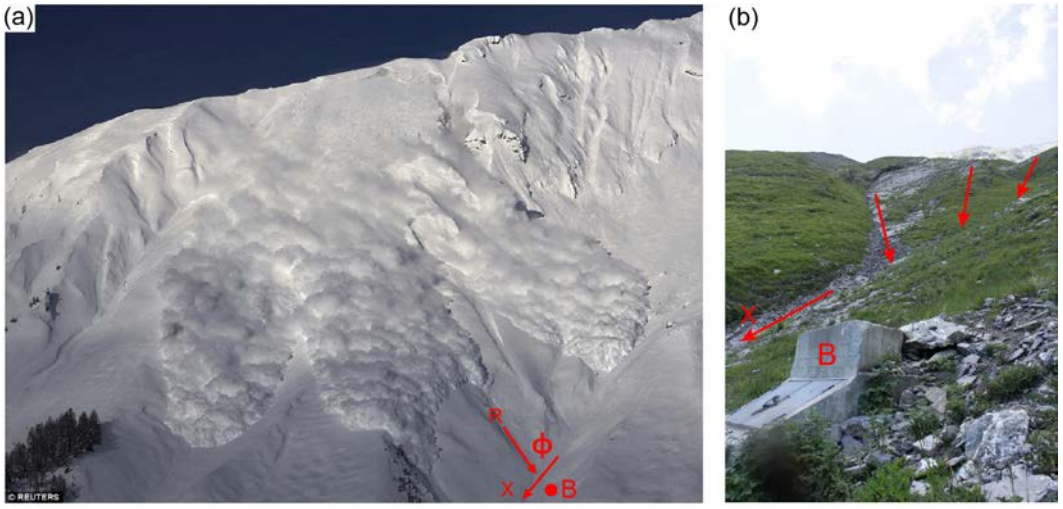

FIGURE 6.6: (a) Picture of the powder-snow avalanche #16 released on the experiment of 3 February 2015 (from http://in.reuters.com/news/picture/creating-an-avalanche?articleId=INRTR4O22L. The avalanche flow splits in different fronts that follow different path. At B, the flow impact with an angle of ϕ relative to the main avalanche direction X. (b) Picture of cavern B. The red arrows indicate the main avalanche direction (X) and the possible direction of the flow before reaching the location of cavern B.

avalanches may thus be attributed to the rapid density and pressure fluctuations observed in the bottom part of the avalanche (Sovilla et al., 2015). In contrast, the low frequency seismic signals characteristic of the fast core of powder-snow avalanches are probably due to the large fluctuations in the energetic part of the flow, and thus probably depend on the scale of the turbulence present in this region. Large seismic amplitude peaks are recorded in the tail of both types of avalanche. In the tail, the avalanche mass stops suddenly once the velocity of the flow drops below a critical value (Sovilla et al., 2006). Such abrupt mass deposition is probably the origin of these characteristic seismic peaks also detected in previous research (e.g. Suriñach et al., 2000; Biescas, 2003; Kogelnig et al., 2011b).

6.4 Distinction of snow avalanche flow regimes

In the previous sections, we showed that the distribution of the seismic energy in the frequency domain (Figures 6.3, 6.4c-d and 6.4g-h) is different for each avalanche type. The seismic signals of each type exhibit a distinctive pattern which is visible in the cumulative energy diagrams partitioned in four frequency-filtered bands (see

Section 4.3.2). Thus the avalanche flow regimes can be distinguished by analysing seismic signals.

Figure 6.7 shows the CE(%) diagrams for the four frequency-filtered bands for powder-snow, wet-snow and transitional avalanches. The distribution of the seismic energy of the powder-snow and transitional avalanches flowing over B (Figure 6.7a and 6.7c) is such that the lowest frequency band of [1-10] Hz is the most energetic. For the wet-snow (Figure 6.7b) and the transitional avalanches flowing over C (these avalanches transform to wet dense flows close to C; Figure 6.7d), this band is the least energetic. These results are in accordance with the observation that the highest seismic energy dissipated by powder-snow avalanches is mainly generated by low frequency content signals (< 10 Hz), whereas for wet-snow avalanches is mainly generated by high frequency content signals (> 10 Hz).

The frequency parameters described by Eq.4.7 can be used to quantify the differences observed in Figure 6.7. The frequency parameters calculated using the relative intensities between the [1-10] Hz and the three subsequent frequency bands ([10-20] Hz, [20-30] Hz and [30-40] Hz) of all the avalanches that flowed over B and C are shown in Figure 6.8. Only these bands are considered to homogenize all the data acquired with different sample rates. The results, however, are independent of considering the whole spectra for avalanches acquired at 200 Hz (see Figure 4.15). In general, the frequency parameters of powder-snow avalanches satisfy $P_{1-n} > 1$ for $n = 2, .., 4$. This means that the maximum seismic energy is dissipated in the low energy band: [1-10] Hz. In contrast, the frequency parameters calculated for wet-snow avalanches satisfy $P_{1-n} < 1$ for $n = 2, .., 4$, i.e. the maximum seismic energy is dissipated in the energy bands above 10 Hz.

An exception of this rule occurred for the frequency parameter P_{1-2} of some powder-snow avalanches flowing over B and C (Figure 6.8). Hence, a shift in the distribution of the frequency bands is recorded and the second [10-20] Hz band is the most energetic one. The frequency parameters satisfy $P_{1-n} > 1$ for $n = 3, .., 4$ and $P_{1-2} < 1$. In theses cases, field observations and data from other instrumentation indicate that the flow is decelerating and depositing the mass over these locations. As a possible explanation, this change in the observed pattern is likely produced by a change in the main flow regime characteristic of the avalanche at this part of the path. When an avalanche decelerates, the flow changes between a sheared flow regime to a plug regime (Sovilla et al., 2008a) that may produce a

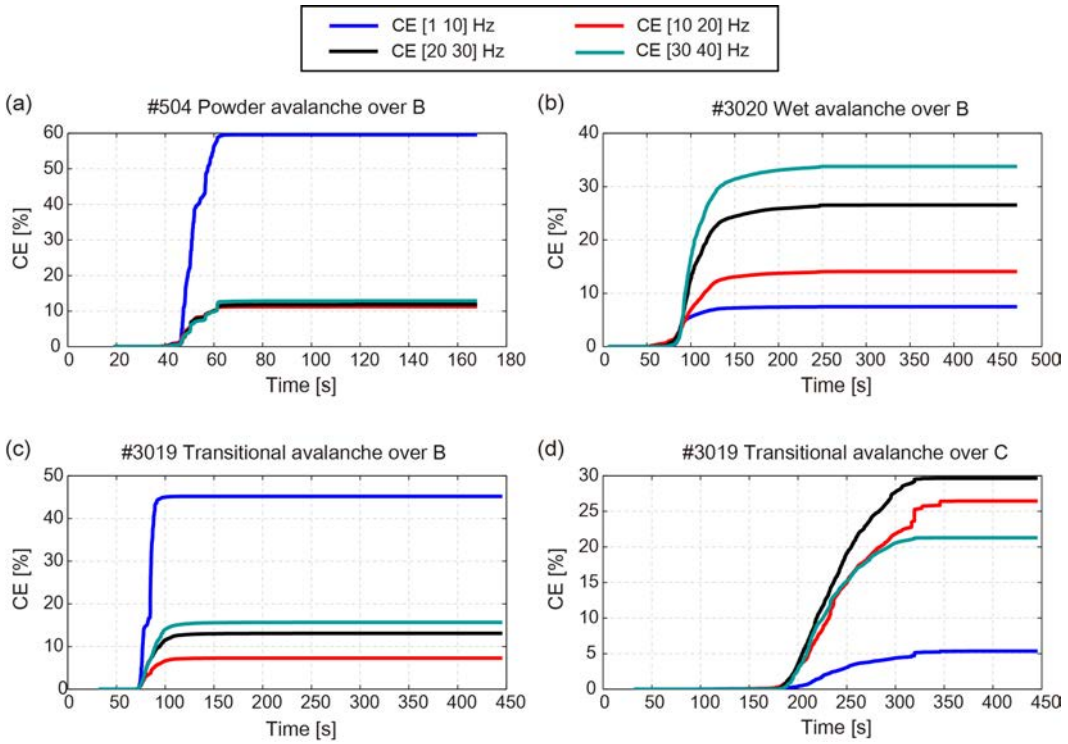

FIGURE 6.7: CE[%] diagrams divided into four filtered- frequency bands for three avalanches flowing over B (#504 (a); #3020 (b); and #3019 (c)); and C (#3019 (d)).

shift in the distribution of the energies across the spectra of the signals of these avalanches at the end of their path.

None of the above characteristics are observed in the data from seismic station D on the opposite slope, which is normally outside the avalanche path, because the anelastic attenuation strong reduces the high-frequency content of the signals. As a result, all the seismic signals generated by the different types of avalanches at D have a similar low-frequency content (f $<$ 20 Hz). Thus, it is not possible to determine the type of avalanche using the frequency parameter values if the avalanche does not flow directly over the sensor.

6.5 Correlation between avalanche size and seismic signals

The values of T_A, $PGVE$ and I (see Section 4.3.3) calculated for the 32 avalanches are given in Table 6.1. Powder-snow avalanches have seismic signal durations

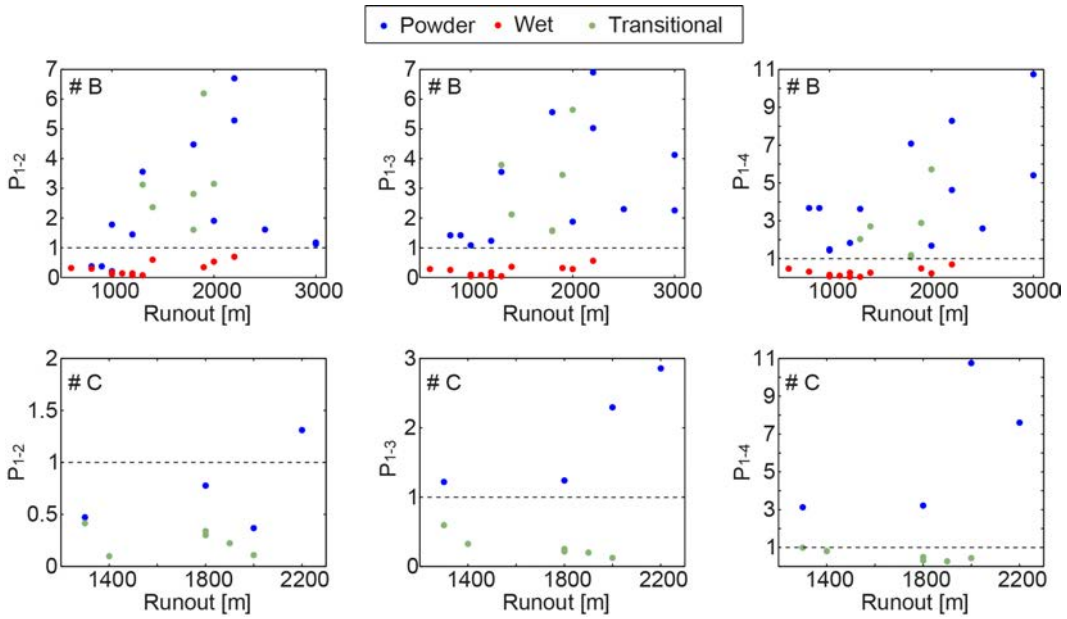

FIGURE 6.8: Frequency parameters values plotted against the run-out distance of the avalanche flowing over B (top) and C (bottom).

ranging from 48 s (small) to 304 s (extreme), while wet dense flows have durations of between 98 s (small) and 542 s (large), and transitional avalanches of 320 s (medium) to 507 s (large). The values for transitional avalanches and wet dense flows are similar, as along most of their path they propagate with a low velocity, generating long signals.

The relationship between the seismic signal duration and the avalanche run-out distance follows a linear regression in the form, if the intercept is set to zero, of:

$$D = A \cdot T_A \tag{6.1}$$

where D (m) is the run-out distance, T_A(s) is the seismic signal duration of the avalanche, and A(ms^{-1}) is the coefficient of the regression fitted to the data.

The analysis of the correlations between seismic signal duration and run-out distance for the different flow regimes reveals two main groups (Figure 6.9): powder-snow avalanches (blue dots), on the one hand, and wet-snow and transitional avalanches (red and green dots) on the other. Powder-snow avalanches can be fitted using the coefficient $A = 13 \pm 1$ ($R^2 = 0.90$); while wet/transitional avalanches require the coefficient $A = 4.5 \pm 0.3$ ($R^2 = 0.83$).

The size of the avalanche can thus be estimated using Eq.6.1 if the type of avalanche is known. Hence it is possible to classify the size of avalanches using either their run-out distance (see Section 4.2) or the seismic signal duration T_A. We can thus define small powder-snow avalanches as those where the signal lasts from 37 to 75 s; medium ones for durations between 75 and 113 s; and large from 113 to 188 s. Extreme powder-snow avalanches have durations $>$ 188 s. Wet/transitional avalanches are small for durations from 111 to 222 s; medium for durations from 222 to 333 s; and large from 333 to 556 s (Figure 6.9).

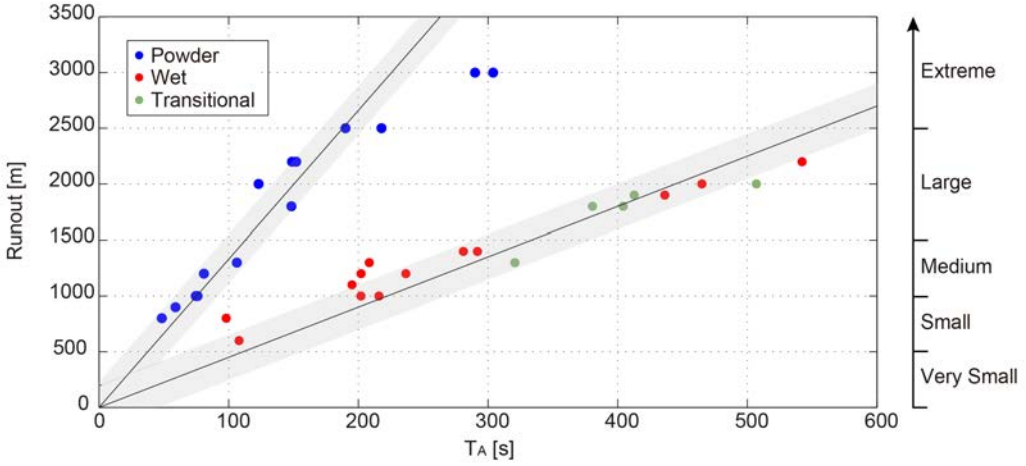

FIGURE 6.9: Correlations between the seismic signal duration (T_A) and the run-out distance of all the avalanches analysed, forming two distinct clusters: 1) wet-snow and transitional avalanches (red and green points); and 2) powder-snow avalanches (blue points). The grey area delimits the standard RMS error. Extreme powder avalanches are not considered when calculating the linear fit because they flowed down to the valley and the corresponding run-out distance is approximate.

$PGVE$ or I and T_A parameters are likely to be exponentially related. Thus, the best fits for both powder-snow and wet/transitional avalanches are expressed in the form:

$$PGVE = C_1 \cdot e^{C_2 \cdot T_A} \tag{6.2}$$

$$I = C_3 \cdot e^{C_4 \cdot T_A} \tag{6.3}$$

where C_i for $i = 1, , 4$ are the coefficients of the regressions. The logarithm of the $PGVE$ and I values are fitted with two least squares linear regressions for each avalanche typology.

Correlations between the seismic signal duration T_A of avalanches of different sizes (small, medium, large and extreme) recorded at the three different locations (B, C and D) and, $PGVE$ and I (on a logarithmic scale) are shown in Figure 6.10. At each recording station they cluster mainly into two groups: either powder-snow avalanches (blue dots) or wet-snow and transitional avalanches (red and green dots). The grey dashed lines in Figure 6.10 indicate the standard RMS error for each regression. The R^2 coefficients in Table 6.3 are between 0.56 and 0.93. Data from station C are available for only a few powder-snow avalanches, which decreases the reliability of the results, but the data show a clear trend.

In general, $PGVE$ and I increase with the size of the avalanche, depending on the type of flow regime (Figure 6.10). Eq.6.1 provides an ideal fit to describe the correlation between run-out distance and seismic signal duration, but poorer correlations are obtained for Eq.6.2 and 6.3, especially for wet and transitional flows at B (Figure 6.10a-b). This suggests that the seismic parameters $PGVE$ and I are influenced not only by the avalanche characteristics (duration), but also by additional factors such as: absorption of the seismic wave intensity by the snow cover lying above the seismic station and the seismic site effects.

All the avalanches flowing over B and C are characterized by a $PGVE$ greater than 10^{-5} ms^{-1} and intensity values higher than 10^{-10} $((ms^{-1})^2 \cdot s)$ (Figures 6.10a-d). Avalanches with a $PGVE$ and I below these thresholds represent flows that stopped before reaching the location of the sensor (i.e. the blue area in Figures 6.10c-d). The absolute values of $PGVE$ and I at the different stations cannot however be compared directly. At D, the threshold values listed above are easily reached by avalanches that stop before they reach the sensor (Figures 6.10e-f) due to the seismic amplification effect recorded there.

Seismic site effects are considerable, especially for seismic station D, which is situated close to the bottom of the valley on quaternary sediments (Figure 3.1). These may, according to Pedersen et al. (1994), amplify the seismic waves. The seismic recordings of earthquakes at the VdlS test site reveal that the Peak Ground Acceleration (PGA) at D is up to one order of magnitude greater than it is at B and C (Table 3.2).

The grey areas in Figures 6.10c-f indicate the avalanches detected at B, but not at C or D due to the low avalanche signal to background noise ratio. Theses avalanches (#3022, #3023_1 and #3023_2; Table 6.1) were the smallest avalanches

detected by station B. They stopped at least 300 m away from the sensor at C and flowed over a bed surface of 4 m.

TABLE 6.3: Values of the R^2 coefficients of the regression fits calculated with the $PGVE$ and T_A and, I and T_A indices for the different types of avalanches (powder or wet/transitional in Figure 6.10).

Location	Typology	R^2 ($PGVE$ Fit)	R^2 (I Fit)
B	Powder	0.77	0.74
	Transitional/Wet	0.56	0.62
C	Powder	0.83	0.88
	Transitional/Wet	0.78	0.90
D	Powder	0.82	0.80
	Transitional/Wet	0.93	0.91

6.5.1 Absorption of the seismic intensity by the snow cover

To quantify the absorption of the seismic signal by the snow cover, we plotted the bed surface level measured at B and C against the run-out distance and the seismic intensity (I) (Figure 6.11). The bed surface level at B varied between 0 (when the avalanche slid directly over the ground) and 4.5 m above ground (Figure 6.11a). The bed surface was thickest where small avalanches stopping near B during winter 2012/13 had created an avalanche deposit (Table 6.1). At C, the thickness varies between 0.5 m and 2.5 m (Figure 6.11b).

In general, the intensity of the seismic signals increases with the size of the avalanche and decreases with the bed surface level (Figure 6.11). Different types of avalanche also vary in intensity (see Figure 6.11, where the circles represent powder-snow avalanches and the squares wet ones; transitional avalanches were considered as powder avalanches at B and as wet avalanches at C). The intensities of wet-snow avalanches with a similar run-out distance and flowing over a bed surface at a similar level are greater than those of comparable powder-snow avalanches.

The snow cover interface between the bed surface level and the ground absorbs some of the intensity of the seismic signal generated at the bottom of the avalanche. To quantify this effect, the absorption factor (F_{AS}), i.e., the amount of seismic

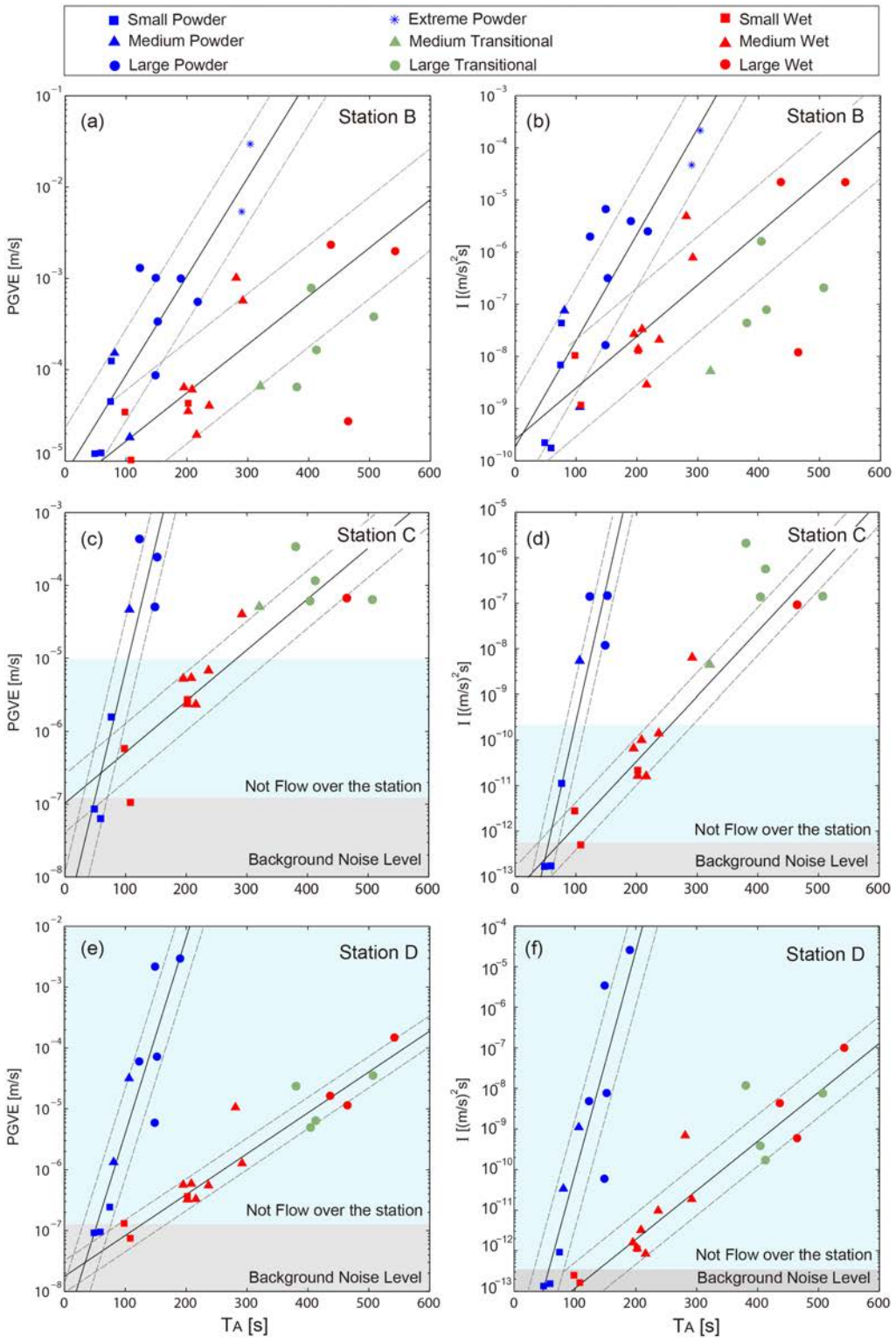

FIGURE 6.10: $PGVE$ and I parameters plotted against avalanche seismic signal duration T_A for all avalanche sizes (small, medium, large and extreme) calculated at the three different seismic stations (B, C and D). The black lines show the regression fits calculated for the powder-snow avalanches and the wet/transitional avalanches. The grey dashed lines show the standard RMS error. The grey areas delimit the undetected avalanches and the blue areas the avalanches that did not flow over the seismic station at C or D.

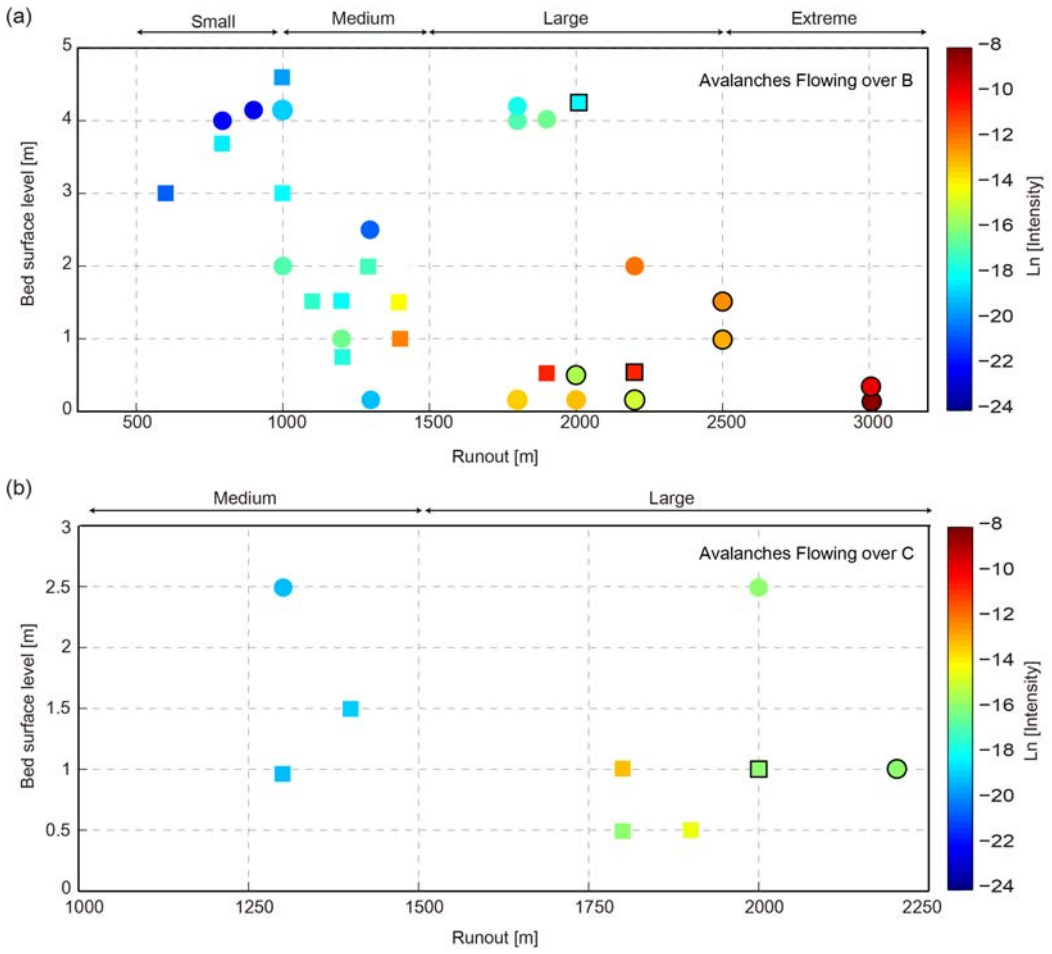

FIGURE 6.11: Bed surface level plotted against run-out distance and seismic intensity (logarithmic scale) for powder-snow (round dots) and wet-snow (square dots) avalanches flowing over B (a) and C (b). Black outlines indicate avalanches that descended through both gullies.

intensity absorbed by the snow cover, is defined as:

$$F_{AS} = \frac{I_H}{I_{H+\Delta H}} \tag{6.4}$$

where I_H is the intensity of the avalanche (Eq.4.7) that slides over a H(m) thick snow cover and $I_{H+\Delta H}$ is the intensity of another avalanche of the same size (run-out distance) but sliding over a $H + \Delta H$ (m) thick snow cover, where H is the difference in the bed surface levels between the two avalanches. F_{AS} increases exponentially with increasing difference in the bed surface level, ΔH, between two avalanches (Figure 6.12).

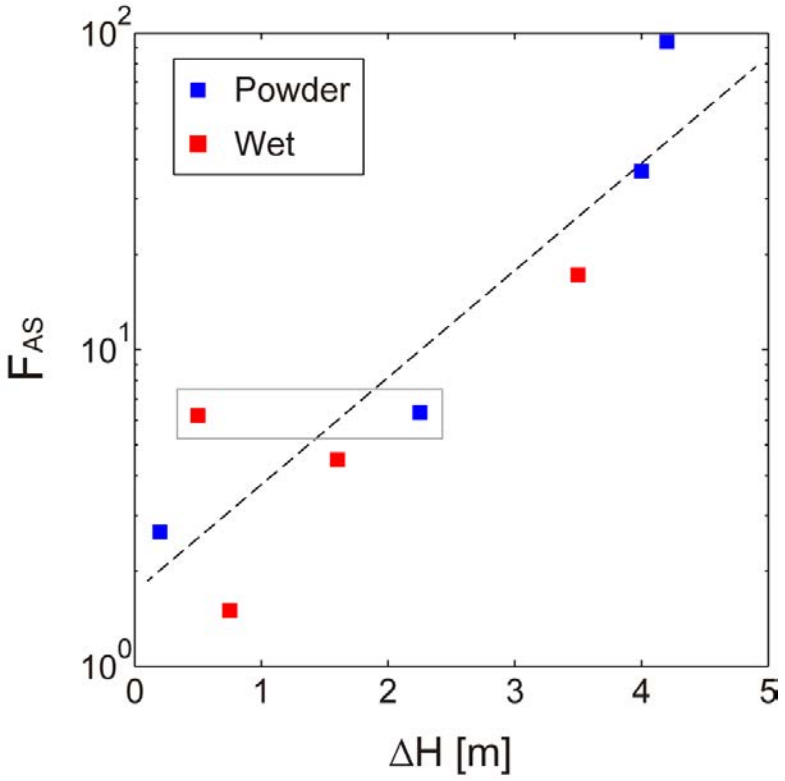

FIGURE 6.12: Snow cover absorption factors of the intensity (F_{AS} on a logarithmic scale) plotted against the difference in the bed surface level (ΔH) between two powder-snow avalanches (blue) and two wet-snow avalanches (red). The black dashed line shows the regression fit calculated for the data.

Some of the avalanches split in two with part of the mass flowing along the secondary gully (squares or circles highlighted with black outlines in Figure 6.11). In this case, the energy generated by this secondary surge suffers much higher attenuation due to the distance than the energy produced by the mass flowing over the sensor. To calculate F_{AS}, we therefore only considered avalanches of the same flow type that took a similar path, i.e. avalanches flowing through both gullies were not compared with avalanches flowing through only one gully.

The factors F_{AS} were calculated by comparing the intensity values of two powder-snow avalanches (blue dots) and two wet-snow avalanches (red dots). The maximum F_{AS} is 97.4 for a value of ΔH of 4.2 m. The box in Figure 6.12 highlights similar factors (6.2 and 6.4) for two wet snow avalanches ($\Delta H = 0.5$ m) and two powder-snow avalanches ($\Delta H = 2$ m). In this case, more seismic intensity is absorbed by the wet snow cover. However, we also observed a minimum F_{AS} of 1.5 in wet snow cover 0.75 m thick. In general, the seismic intensity of the signals is absorbed in a similar way in both types of snow cover (Figure 6.12). The linear

fitting of the logarithm of F_{AS} and ΔH ($ln(F_{AS}) = 0.8 \cdot \Delta H + 0.5$) had an R^2 value of 0.82 (see dashed black line in Figure 6.12).

The signal absorption of the snow cover is not as significant at the lower locations, C and D, due to the less snow accumulating at lower elevations of the avalanche path (Table 6.1). At C, avalanches flow over a maximum bed surface level of 2.5 m (Figure 6.11b) and the correlations between T_A and both $PGVE$ and I are good, with R^2 coefficients closer to 1 (Table 6.3, Figure 6.11c-d).

6.6 Estimating the avalanche size using seismic measurements

Avalanche size can be estimated as a function of the run-out distances using the duration (T_A) of the seismic measurements if the main avalanche flow regime is known (Figure 6.9). The main avalanche flow regime can be inferred from the values of the frequency parameters as described in Section 6.4.

Avalanches can change the flow regime along their path, which goes against the assumption that the avalanche flow regime is uniquely defined. Large avalanches, in particular, which have a long path and a large vertical drop, are prone to change their flow regime if the snow conditions along their path change. The flow type estimation of these transitional avalanches can thus differ depending on the part of the avalanche path where seismic sensor is installed. This problem can be resolved by optimizing the sensor configuration, and thus installing several seismic sensors in a linear array inside the path.

Avalanche size can also be estimated from the values of $PGVE$ and I (Eqs. 6.2 and 6.3). However, this method is less reliable since the $PGVE$ and I values are greatly affected by the energy absorption caused by the snow cover lying on the sensor. The underestimation of the size caused by this energy absorption can be particularly important for snow deposits more than 2 m deep on the sensors ($F_{AS} > 10$ for $\Delta H > 2.3$ m; Figure 6.12). In our case study, the station most affected by the seismic energy absorption is B, where deposits from previous small avalanches could lead to deep snow cover accumulating there (up to 4 m).

The seismic waves generated by avalanches propagating within the layers of the snow cover suffer attenuation depending on the depth of the snow layers and the

physical properties of the snow. Seismic reflection experiments in glacial ice (Peters et al., 2012) showed that the anelastic attenuation of the seismic waves is higher at higher temperatures, especially close to T $\approx 0°$ C. Experiments with detonations on the snow showed (Gubler, 1977) that the amplitude of the oscillations of the snow cover depend on the density and type of snow with less attenuation with dry snow cover that is denser. Thus, less absorption of seismic waves should be expected in a snow cover composed of dry, higher-density layers than in wet-snow avalanche deposits. We found, however, no significant differences between the effects of a dry or wet snow cover. In both cases, the intensity of the seismic signals decreases exponentially with the thickness of the snow cover interface (Figure 6.12). The thickness of the snow cover should, therefore, be included as an additional parameter to obtain accurate estimations of the avalanche size from the $PGVE$ and I indices.

Stations C and D are more appropriate for estimating avalanche size using relationships 6.2 and 6.3 as they are installed at lower elevations where less snow accumulates than at B. Part of the problem could be solved by estimating the snow cover thickness over the seismic station using data from weather stations. However, the effect of avalanche activity on the path could change the snow cover thickness considerably due to the avalanche erosion and deposition processes along the path.

If the fits of Eqs. 6.1, 6.2 and 6.3 are combined with the ranges of seismic indices values in Table 6.4, it may be possible to develop a classification system to detect automatically avalanche size and type.

6.7 Conclusions

The flow regimes and size of snow avalanches can be identified, as we have shown, using seismic measurements. The signatures of the seismic signals were found to depend on the type of flow regime, and reveal characteristics of the dynamic processes governing avalanche movement. The two main flow regimes that generate seismic signals are:

1. The energetic flow of powder-snow avalanches. This region generates short wave packets with high seismic amplitudes, characterized by a low-frequency

TABLE 6.4: Ranges of values of T_A, $PGVE$ and I at VdlS for each site, type of avalanche (powder and wet/transitional) and size (small, medium, large and extreme).

Size	Type	T_A (s)	Site	$PGVE$ (ms^{-1})	I ($(ms^{-1})^2 \cdot s$)
Small	Powder	[38 -75]	B	$[2 \cdot 10^{-5} - 5 \cdot 10^{-5}]$	$[1 \cdot 10^{-9} - 6 \cdot 10^{-9}]$
			C	$[5 \cdot 10^{-8} - 9 \cdot 10^{-7}]$	$[5 \cdot 10^{-14} - 9 \cdot 10^{-12}]$
			D	$[4 \cdot 10^{-8} - 6 \cdot 10^{-7}]$	$[3 \cdot 10^{-14} - 3 \cdot 10^{-12}]$
	Wet/Trans.	[111 - 222]	B	$[2 \cdot 10^{-5} - 7 \cdot 10^{-5}]$	$[3 \cdot 10^{-9} - 4 \cdot 10^{-8}]$
			C	$[6 \cdot 10^{-7} - 4 \cdot 10^{-6}]$	$[2 \cdot 10^{-12} - 7 \cdot 10^{-11}]$
			D	$[1 \cdot 10^{-7} - 6 \cdot 10^{-7}]$	$[2 \cdot 10^{-13} - 4 \cdot 10^{-12}]$
Medium	Powder	[75 - 113]	B	$[5 \cdot 10^{-5} - 1 \cdot 10^{-4}]$	$[6 \cdot 10^{-9} - 4 \cdot 10^{-8}]$
			C	$[9 \cdot 10^{-7} - 2 \cdot 10^{-5}]$	$[9 \cdot 10^{-12} - 1 \cdot 10^{-9}]$
			D	$[6 \cdot 10^{-7} - 1 \cdot 10^{-5}]$	$[3 \cdot 10^{-12} - 4 \cdot 10^{-10}]$
	Wet/Trans.	[222 - 333]	B	$[7 \cdot 10^{-5} - 3 \cdot 10^{-4}]$	$[4 \cdot 10^{-8} - 5 \cdot 10^{-7}]$
			C	$[4 \cdot 10^{-6} - 2 \cdot 10^{-5}]$	$[7 \cdot 10^{-11} - 3 \cdot 10^{-9}]$
			D	$[6 \cdot 10^{-7} - 3 \cdot 10^{-6}]$	$[4 \cdot 10^{-12} - 8 \cdot 10^{-11}]$
Large	Powder	[113 188]	B	$[1 \cdot 10^{-4} - 8 \cdot 10^{-4}]$	$[4 \cdot 10^{-8} - 1 \cdot 10^{-6}]$
			C	$[2 \cdot 10^{-5} - 8 \cdot 10^{-3}]$	$[1 \cdot 10^{-9} - 4 \cdot 10^{-5}]$
			D	$[1 \cdot 10^{-5} - 3 \cdot 10^{-3}]$	$[4 \cdot 10^{-10} - 5 \cdot 10^{-6}]$
	Wet/Trans.	[333 556]	B	$[3 \cdot 10^{-4} - 4 \cdot 10^{-3}]$	$[5 \cdot 10^{-7} - 8 \cdot 10^{-5}]$
			C	$[2 \cdot 10^{-5} - 8 \cdot 10^{-4}]$	$[3 \cdot 10^{-9} - 4 \cdot 10^{-6}]$
			D	$[3 \cdot 10^{-6} - 1 \cdot 10^{-4}]$	$[8 \cdot 10^{-11} - 4 \cdot 10^{-8}]$
Extreme	Powder	> 188	B	$> 8 \cdot 10^{-4}$	$> 1 \cdot 10^{-6}$
			C	$> 8 \cdot 10^{-3}$	$> 4 \cdot 10^{-5}$
			D	$> 3 \cdot 10^{-3}$	$> 5 \cdot 10^{-6}$

content (f<10 Hz). In this highly turbulent part, frontal and step entrainment processes are dominant. Turbulent impacts between the avalanche and the sliding surface, together with erosion processes, contribute to the generation of the seismic waves. The movement of the ground (P-waves) indicates the direction of the impact of a turbulent flow in a confined path with the bed surface.

2. The dense part of wet-snow avalanches. This region generates long energetic wave packets with a high-frequency content (f >10 Hz). The generation of the seismic waves is chiefly produced by friction and dissipation processes dominant in this type of flow regime.

The dense tail of powder-snow avalanches presents similar characteristics to those of dense wet flows; but generates less seismic energy than the energetic part and thus its contribution is of secondary importance when characterizing the signal. The location of the seismic sensors is crucial to distinguish avalanche flow regimes. Snow avalanches need to flow over the seismic sensors to reveal the internal flow regimes coexisting inside them.

The seismic signals generated by avalanches can be used to estimate the avalanche size, and thus the run-out distance, by determining the seismic signal duration and inferring the avalanche flow regime from the frequency parameters. Avalanche size can also be deduced from $PGVE$ and I values when the avalanche bed surface level is close to the ground and seismic energy absorption therefore not significant. Large accumulations of snow (>2 m approx.) can absorb seismic intensity (F_{AS}) at more than one order of magnitude. To calculate the attenuation factors of the seismic waves propagating within the snow cover and how they vary according to stratigraphy of the snow layers and the physical properties of each layer, specially designed experiments will be necessary. Our results, combined with further field-work, can be used to develop an automatic system for classifying avalanches. The methodology presented here can also be applied in monitoring avalanche activity and thus provides a valuable tool for risk management.

Chapter 7

Discussion

In this chapter, a general discussion of the results of this thesis are presented. The main contributions from seismic methods to the avalanche research are discussed separately.

7.1 Contribution of seismic methods to the study of avalanche formation

In the research field of avalanche formation, this PhD study has focused in the analysis of one snow avalanche possibly induced by an earthquake on 6th December 2010. This event constitutes a unique and well-documented dataset of the seismic records of the earthquake response in the avalanche starting zone with detailed information on the snow cover stratigraphy and the evolution of the avalanche flow. The earthquake recordings at different sites show the importance of measuring the vibrations produced by the earthquake in the avalanche starting zone. These zones are generally characterized by an abrupt topography and loose materials that might amplify the effects of the earthquake greatly (Pedersen et al., 1994). In our case study, the PGA values on the avalanche starting zone (cavern A) can be up to one order of magnitude more than at lower elevation sites (Table 3.2) Furthermore, the data from the stations located at lower elevations of the avalanche path were very useful to characterize the avalanche flow. The correlation with the infrasound data was also essential in this study to determine the time interval when the snow avalanche was released. The estimation of this time interval

was very difficult to establish from the seismic recordings due to the overlapping of the signals generated by both seismic sources (the earthquake and the snow avalanche). Thus, the combination of several seismic sensors along the avalanche path and an infrasound sensor is very well suited to detecting and characterizing earthquake-triggered snow avalanches.

Additionally, different local and regional earthquakes of different magnitude and epicentral distance were analysed to assess the possibility of avalanches triggered by them. In general, all the recorded earthquakes had epicentral distances less than 300 km and magnitudes smaller than M_w 5 (Table 3.2). From all of them, only the analysed earthquake on 6th December 2010 coincided temporally with a snow avalanche. Podolskiy et al. (2010b) suggested a limit for earthquake-induced snow avalanches of M_W 1.9 at zero source to site distance, which implies a PGA of around $0.03g$ approx. This limit was based on data from snow avalanches induced by mine explosions in the Khibiny mountains (Chernouss et al., 2006). My case study, with an earthquake of M_w 3.1 and an epicentral distance of about 40 km, which generated a maximum PGA of $3.5{\cdot}10^{-4}g$ (Table 5.2), is outside of the suggested limit of $0.03g$. However, this case fits with in the previously reported statistical cases where snow avalanches were triggered by earthquakes of M_w 3 - 3.9 that occurred at distances of 100-199 km (Podolskiy et al., 2010b).

Furthermore, none of the earlier reported events included details of the snow cover properties and the stability conditions in order to establish a proper limit for earthquake-induced snow avalanches. Snow cover properties play a major role in avalanche release (Schweizer et al., 2003). In this regard, the snow cover simulations conducted (Figure 5.7) and the analysis of the meteorological data (Figures 5.8-5.10) provided details of the snow cover stratigraphy on the day of the event and the days of occurrence of the earthquakes that did not trigger snow avalanches. Additionally, to quantify the total effect of the earthquake, I applied the Newmark's method, which was previously used for snow avalanches triggered by artificial seismicity (Fedorenko et al., 2002; Chernouss et al., 2006) and also widely used for landslides (e.g. Jibson, 1993). In the snowpack, close to instability conditions, on 6th December 2010, the maximum cumulative displacements obtained were of the order of magnitude of displacements measured before failure in laboratory tests with similar snow layers (Reiweger and Schweizer, 2010). Hence, the temporal coincidence of the phenomena and the calculated effects of

the earthquake under these snowpack conditions shows the feasibility of this snow avalanche of being triggered by such a small earthquake.

7.2 Contribution of seismic methods to the study of avalanche dynamics

7.2.1 Identification of the sources of the seismic signals

Snow avalanches are characterized by different regions with different dynamics. In order to improve our understanding of snow avalanches as moving seismic sources, I performed detailed analysis of the seismic signals in the different sections defined (SON, SOV and SEN). The characteristics of the SON and SEN sections are dependent of the relative distance of the avalanche flow and the sensor due to the attenuation phenomena that affect to the seismic waves propagating into the ground. In addition, the SOV section was then sectioned taking into account the internal parts of the avalanche flow (front, energetic and dense/tail regions) passing over the seismic sensors. This section is slightly affected by the attenuation of the waves. The observed signatures in the time and frequency domains of the signals generated by each avalanche region have enabled me to characterize them as follows:

- Frontal Region. The pass of the frontal region is characterized by low seismic energy dissipation with a wide frequency spectrum of [1, 40] Hz. In this region, the characteristic dynamical process of frontal entrainment or ploughing of the first snow layer does not usually make a major contribution to the generation of seismic energy ($CE[\%] < 5\%$). This may be due to the properties of the entrained layer, characterized by a low density and cohesionless snow, and the short duration of the process (up to 5 s; Table 6.2). Furthermore, the absorption of seismic energy by these types of layers (dry snow characterized by low density and high porosity) is expected to be larger than by high density layers, according to Gubler (1977) and Sidler (2015).

- Energetic turbulent Region. The pass of the energetic region (only present in powder-snow avalanches) is characterized by high seismic energy dissipation with a low frequency spectrum (f < 10 Hz). In correlation with this observation, in this region, higher density layers are entrained by the impact of the avalanche on the snow cover (Sovilla et al., 2006). This mechanical process, also known as impact erosion (Gauer and Issler, 2004), is the main mechanism of generation of seismic energy in powder-snow avalanches.

- Dense/Tail Region. The pass of the dense/tail region is characterized by high seismic energy dissipation in wet-snow avalanches and by low seismic energy dissipation in powder-snow avalanches. Both types of flows present a high frequency spectrum (f > 10 Hz) in this region. Typically, the seismic signal of the last part of this region is characterized by a large seismic coda with superimposed narrow peaks. Previous works correlated these peaks with the stopping phase of the avalanche (Suriñach et al., 2000; Kogelnig et al., 2011b). Detailed comparison of the data of this thesis shows that these peaks are generated either by the deposition of the avalanche mass in the run-out zone or by the deposition of the mass of the tail along all the avalanche path (e.g. Figures 6.1 and 6.2).

In general, the main generation of the seismic energy was previously attributed to the dynamical processes of ploughing at the avalanche front (front erosion) and basal friction (Vilajosana et al., 2007b). These mechanisms, however, do not always make the highest contribution in the generation of seismic energy in powder-snow avalanches. In these avalanches, the highest dissipation of energy is generated by the energetic turbulent part which travels just behind the front. At times, the front part is too short (and indistinguishable from the energetic part) and the first layers, including higher density layers, are rapidly entrained into the flow (e.g. Figures 4.16 and 6.4). When this occurs, the front erosion makes a major contribution to the generation of the seismic energy. Furthermore, the basal friction plays the most important role in the generation of seismic energy for wet-snow avalanches; while it is less significant for powder-snow avalanches.

An explanation of the observed signatures in the frequency domain characterizing each avalanche region can be derived from the different type of interaction of the avalanche with the snow cover/terrain. By comparison with impact pressure measurements recorded at VdlS (Sovilla et al., 2008b), wet-snow avalanches and

slower parts of powder-snow avalanches are characterized by a fairly stationary base pressure with rapid fluctuations. The origin of the high frequency content of the seismic signals generated could be attributed to these rapid fluctuations recorded in the bottom of the avalanche. By contrast, the fast moving core of powder-snow avalanches is characterized by slow fluctuations of pressure that could thus generate low frequency signals.

7.2.2 Inferring avalanche properties from the seismic parameterization

A set of seismic indices connected to the type of flow and the size of snow avalanches is defined in this work. I also derive several novel relationships between them in order to deduce avalanche size.

The avalanche flow type can be inferred from the frequency parameters, P_{1-n}, defined by Eq. 4.7. These parameters are defined for first time in this study in order to quantify the observed frequency domain signatures. Data recorded in the station situated in the track zone of the snow avalanche (Figure 2.1), station B, show that powder-snow avalanches satisfy $P_{1-n} > 1$ for $n = 2, .., 4$, and wet-snow avalanches $P_{1-n} < 1$ for $n = 2, .., 4$. Data recorded in the station situated in the run-out zone of avalanches (Figure 2.1), station B for small avalanches or C for medium and large avalanches, show that $P_{1-n} > 1$ for $n = 3, .., 4$ for powder-snow avalanches and $P_{1-n} < 1$ for $n = 2, .., 4$ for wet-snow avalanches (Figure 6.8). The differences between the recordings from the track and the run-out zone for powder-snow avalanches may be justified by changes in the flow behaviour of the avalanches when they decelerate in the run-out zone (Sovilla et al., 2008b). These parameters are also useful to detect changes in the avalanche typology. Transitional avalanches present $P_{1-n} > 1$ for $n = 2, .., 4$, values that are equal to those of powder-snow avalanches in the upper part of the path where the snow is still dry, and $P_{1-n} < 1$ for $n = 2, .., 4$ in the lower part of the path, equal to values of wet-snow avalanches (Figure 6.8). In both cases (powder and transitional avalanches), the frequency spectra of the avalanches change from the track zone (low-frequency spectra) to the run-out zone (high-frequency spectra) due to changes in the flow regime.

In order to estimate avalanche size, I derived different relationships from the analysis of the data. The first, Eq. 6.1, relates avalanche run-out distance (size) with

the seismic signal duration (T_A). This simple approach shows that the duration strongly depends on the type of flow regime (i.e. on the velocity of propagation) more than on the size of the avalanche (Figure 6.9). Wet/transitional avalanches have much longer durations than powder-snow avalanches; as expected. Furthermore, the defined duration of the seismic signal generated by an avalanche can be used as a good approximation of the real duration of the avalanche motion. To an accurate estimation of the duration, the seismic signals recorded at the different stations have been compared. In this regard, I used the closest station to the avalanche initiation (B) and end parts (B or C) to determine the whole duration. The durations obtained at sites far from the avalanche path (e.g. at D) are usually shorter due to a weaker signal-to-noise ratio. This could imply an underestimation of avalanche size. Hence, several stations located along the avalanche path are necessary for a better determination of the avalanche properties such as flow type, changes in the flow regime, and avalanche duration.

To quantify the intensity of the seismic signals, and thus also connect to the avalanche size, I defined the indices: $PGVE$ and I. These parameters were adapted in this study from the parameters defined in the field of earthquake engineering. To calculate them, the three components of the ground motion are considered to account for all the recorded energy. Previous analysis of avalanche seismic signals has roughly related the avalanche size with the maximum amplitudes of the signals generated (Biescas, 2003; Kogelnig et al., 2011b). Maximum values of the velocity time series, PGV values, are often used as a seismic quantification parameter in earthquake engineering. In this work, however, I considered it more appropriate to use instead the $PGVE$ values, i.e. the PGV of the total envelope, because the punctual peaks are smoothed in the envelope time series and thus it is a more representative parameter of the intensity of the signal. My results shows that both quantification indices ($PGVE$ and I) can also be used to estimate avalanche size when the snow cover interface is not too thick. For large snow cover thicknesses, a correction factor proportional to the absorption of seismic energy by the snow cover should be included in the relationships obtained.

Additionally, I obtained a set of threshold values of $PGVE$ and I for detection or not of avalanches (grey areas in Figures 6.10c-d), and for avalanches that flowed over the station or not (blue areas in Figures 6.10c-d). All the avalanches analysed in this work were detected by the station B, located in the upper part of the avalanche path; whereas the snow avalanches with run-out distances of 900 m, that

slid over a mean bed surface level of about 4 m, were not detected at a minimum distance of avalanche sensor of about 300 m. However, the smallest avalanche recorded with a run-out distance of 600 m was detected at a minimum avalanche-sensor distance of about 600 m, because it flowed over a lower bed surface level of about 3 m. This result reflects the importance of considering the snow cover energy absorption in order to establish an accurate limit for avalanche detection with a seismic array of sensors. I also obtained limit thresholds of the values of $PGVE$ and I for avalanches flowing over the location of a seismic station, such as B or C (see Section 6.5). These thresholds, however, are not valid for station D where the local seismic site effects are more important.

The range of values in Table 6.4 can be used as a reference for VdlS for future avalanche size classification using seismic signals. However, I should point out that these values cannot be directly extrapolated to other sites. The range of values is unique for each site and depends on the avalanche type, size, distance from the avalanche to the seismic sensor, snow cover thickness at the site and local site effects. In the small VdlS area, these ranges vary strongly from one site to another due to local effects, as reflected in the Table 6.4 values.

7.2.3 Quantification of the effects of the snow cover on avalanche seismic signals

In order to quantify the absorption of seismic energy due to the snow cover interface, I compared snow avalanches of the same type and size sliding over different snow cover depths. Earlier experiments of detonations within the snow showed that the snow cover is a high absorption medium of the waves generated by the explosions (Gubler, 1977; Albert and Hole, 2001; Simioni et al., 2015). Those results cannot be directly extrapolated to the avalanche seismic signals, because of the different nature of the sources. Unlike explosions, snow avalanches are multiple and moving sources of seismic waves. The passing of an avalanche over snow cover is characterized by different erosion processes such as ploughing, impact erosion or abrasion, which produce a densification of the snow cover. Snow cover is thus partly compacted by the pass of the avalanche and partly loosened due to the entrainment of snow (Gauer and Issler, 2004). Both effects may reduce the absorption of the seismic energy due to a reduction of snow cover depth and a

densification of the subjacent layers. Recent models of seismic waves propagating into the snow have shown that the attenuation is lower for high-density and low-porosity snow layers (Sidler, 2015). Thus, a reduction of the seismic energy absorption may be resulted from the compactation of the layers subjacent to the avalanche bed surface. Our estimations show that the factor of absorbtion of the avalanche intensity, F_{AS}, increases exponentially ($\propto e^{0.8 \cdot \Delta H}$) with the thickness of the snow cover interface (Figure 6.12).

It is also known that high-frequency seismic waves are also attenuated faster within the snow than low-frequency waves, as in other types of material. However, similar attenuation factors are expected for seismic waves characterized by frequencies below 100 Hz propagating within high-density layers, according to Sidler (2015). In addition, no large differences are expected between the attenuation factors of the low- and high-frequency waves due to the short distances travelled by the waves from the bed surface to the ground (maximum snow cover thicknesses of 5.5 metres; Table 6.1). As analogy, the attenuation factor of seismic waves propagating through the ground shows similar values for waves of low- or high-frequency for distances below 100 m (Figure 3.3). The differences in the values of the attenuation factor for low- and high-frequency waves are remarkable at long distances ($>$ 500 m). For instance, powder-snow avalanches sliding directly over the ground (e.g. avalanche #16 in Figure 4.16) generated the same low frequency content (Figure 4.14) as snow avalanches sliding over a snow cover depth of about 2 m (e.g. avalanche #504 in Figure 6.1). Wet-snow avalanches (e.g. the avalanches #3018 and #3020) that slid over a large snow cover thickness (Figures 4.17 and 6.2) generated seismic energy characterized by a high-frequency spectrum (section SOV of Figure 4.15 and Figure 6.3d and e).

Chapter 8

Conclusions

8.1 Conclusions

In this thesis, I present novel applications of the seismic methods for avalanche research. These methods can be applied to implement current avalanche monitoring systems and further develop avalanche warning systems. First, seismic methods (such as time-frequency analysis of the evolution of the avalanche flow, quantification of the earthquake ground motion and Newmark's method) are successfully applied to study snow avalanche formation; in particular, to detect and study the possibility of avalanches triggered by earthquakes. Furthermore, I show the feasibility of using seismic methods (such as parameterization of the signals in the time and frequency domains) to characterize avalanche dynamics and to infer inherent properties of the flow without any other type of measurements. A catalogue of 33 snow avalanches analysed mainly using seismic measurements at different VdlS locations is presented. All the data are compared in each case with other available and proper measurements such us infrasound data, two different types of radar data and weather data. All the results obtained by the seismic methods are in agreement with the results from other acquiring techniques, entrenching and validating the findings of this thesis.

In the field of avalanche formation research, our avalanche seismic monitoring system (consisting of four seismic sensors and an infrasound sensor) is applied, for first time, to detect and evaluate a snow avalanche possibly triggered by an earthquake. The joint analysis of seismic and infrasound data enable us to characterize the whole event, determining the trigger time interval and locating the avalanche

path. This analysis is in agreement with the observations obtained from the GEODAR radar installed at the site. Additionally, earthquake seismic recordings are used to quantify energy parameters and changes in the elastic stress field within the snowpack due to the earthquake vibrations. The study is complemented by nivo-meteorological data and snowpack stability evaluations. I showed that in a snowpack close to instability, the consequences of a minor magnitude earthquake can be favourable to trigger a snow avalanche. The methodology presented can be used to quantify the effects of an earthquake on avalanche starting zones, to determine whether an avalanche may be triggered or not, and to characterize the avalanche path and size. Thus, this methodology can be applied to assess similar future events.

In the field of avalanche dynamics research, this PhD study provides deeper knowledge of the sources of the seismic signals generated by the different parts of an avalanche, connected with avalanche flow regimes. Thereby the results enable us to infer the avalanche flow regimes by means of the analysis of the signatures of the seismic signals. The interaction of the energetic turbulent part of powder-snow avalanches with the snow cover/terrain mainly generates low-frequency seismic waves through impacts with the sliding surface; whereas the basal friction between the dense part of the avalanches and the snow cover/terrain mainly generates high-frequency seismic waves. The deposition of the mass along the avalanche path generates characteristic high amplitude peaks in the seismograms of both types of snow avalanches. Therefore, impact erosion, basal friction and mass deposition are the three main mechanisms of generation of the seismic waves of snow avalanches.

The parameterization of snow avalanche seismic signals in a set of seismic indices defined in this thesis allows avalanche characteristics such as the type of flow and avalanche size to be inferred. The frequency parameters quantify the distribution of seismic energy across the spectra and can be used to deduce the main type of avalanche flowing over a seismic location. In this regard, changes in the flow regime characteristics of transitional avalanches or those occurring in the stopping phase of snow avalanches are also detectable if several sensors are installed along the avalanche path. Hence, as demonstrated, at least two seismic sensors located at strategic sites along the avalanche path are adequate to characterize the avalanche flow and detect possible flow regime changes. An estimation of the size of snow avalanches flowing over a specific avalanche path is feasible using the relationships between the set of seismic indices presented in this thesis.

8.2 Outlook

Snow avalanches induced by earthquakes have rarely been studied to date due to the scarcity of documented cases. In addition, all the earlier events correspond to strong ground motions which produced high stresses within the snowpack and thus led the possibility of triggering snow avalanches. The dataset presented in this study is unique and not directly comparable with the previous documented cases due to its small magnitude. New reported cases of earthquake-triggered snow avalanches are needed in order to establish a proper limit of the earthquake magnitude to trigger snow avalanches in nearby areas. Additionally, this limit should be calibrated with different snowpack stability conditions. As the snow cover properties vary strongly in space and time in mountain areas (Schweizer et al., 2008), snow cover modelling could be a solution for cross correlation between the snow cover properties and earthquake occurrences close to mountain areas. For instance, the one-dimensional model SNOWPACK (Lehning and Fierz, 2008) used in this work for a specific location, or the three dimensional model Alpine 3-D (Lehning et al., 2006), could be applied for this purpose.

The array of sensors located at VdlS is very suitable to detect these events. However, on average, ten earthquakes of magnitude 2.5 or higher are expected each year in Switzerland; whereas a destructive earthquake with magnitude of 6 or higher is expected each 50 to 150 years (source: SED). This low probability of occurrence of stronger ground motions may significantly reduce the detection of future events in this area. The temporal coincidence of an earthquake with enough magnitude, the proper epicentral distance to the avalanche starting zone and the snowpack stability prone to avalanche release are the three major factors to determine future probability events.

Even though this PhD study was intended for research purposes, the results have provided suitable indications for further implementations of seismic monitoring systems of snow avalanches. The features of the seismic signals are parameterized in the set of seismic indices presented here. The calculation of these indices involves an easy computation, making it simple and feasible to include in detection algorithms. Hence, an algorithm developed in the future would be trained to automatically infer avalanche properties and classify them. To that end, additional data would complete this dataset to be further divided into training, testing and validation datasets. In addition, the range of thresholds of $PGVE$ and I obtained

to determine whether an avalanche flowed over a specific location or not could be also very useful in real-time monitoring systems. In this regard, knowledge of an avalanche flowing directly over a specific location or not can be used to close or re-open a traffic route, mountain path or other location of interest. We should be conscious that the values obtained in this thesis are unique for the locations studied at VdlS. The methods, however, can be applied at other locations. Earlier works demonstrated the reproducibility of the avalanche seismic characteristics in other sites such as the Pyrenees in Spain (Suriñach et al., 2000, 2001) and Ryggfonn test site in Norway (Vilajosana, 2008).

A collaboration between the snow avalanche group of the UB and a Japanese avalanche research group is envisaged. This collaboration opens up the possibility of applying the results of this thesis at other experimental sites, providing new insights into the field. Japan is also an ideal field test site to record new events of avalanches induced seismically and thus deepen our understanding of this triggering mechanism.

Bibliography

Aki, K. and Richards, P. G. (1980). *Quantitive Seismology. Theory and Methods.* Freeman, San Francisco.

Albert, D. G. and Hole, L. R. (2001). Blast noise propagation above a snow cover. *The Journal of the Acoustical Society of America*, 109(6):2675–2681.

Amman, J. (1999). A new Swiss test site for avalanche experiments in the Vallée de la Sionne/Valais. *Cold Regions Science and Technology*, (30):3–11.

Arattano, M. and Marchi, L. (2005). Measurements of debris flow velocity through cross-correlation of instrumentation data. *Natural Hazards and Earth System Sciences*, 5:137–142.

Arattano, M. and Moia, F. (1999). Monitoring the propagation of a debris flow along a torrent. *Hydrological Sciences Journal*, 44(5):811–823.

Arias, A. (1970). *A measure of earthquake intensity*, pages 438–483. Seismic Design for Nuclear Power Plants. MIT Press, Cambridge, Massachusetts.

Ash, M., Brennan, P. V., Keylock, C. J., Vriend, N. M., McElwaine, J. N., and Sovilla, B. (2014). Two-dimensional radar imaging of flowing avalanches. *Cold Regions Science and Technology*, 102(2):41–51.

Ash, M., Chetty, K., Brennan, P., McElwaine, J., and Keylock, C. (2010). FMCW radar imaging of avalanche-like snow movements. *2010 IEEE Radar Conference*, pages 102–107.

Assimaki, D. and Kausel, E. (2007). Modified topographic amplification factors for a single-faced slope due to kinematic soilstructure interaction. *Journal of Geotechnical and Geoenvironmental Engineering*, 133(11):1414–1431.

Aydan, Ö. and Ulusay, R. (2015). A quick report on the 2015 Gorkha (Nepal) earthquake and its geo-engineering aspects. pages 1–26.

Badoux, A., Graf, C., Rhyner, J., Kuntner, R., and McArdell, B. W. (2009). A debris-flow alarm system for the Alpine Illgraben catchment: Design and performance. *Natural Hazards*, 49(3):517–539.

Bessason, B., Eiríksson, G., Thórarinsson, Ó., Thórarinsson, A., and Einarsson, S. (2007). Automatic detection of avalanches and debris flows by seismic methods. *Journal of Glaciology*, 53(182):461–472.

Biescas, B. (2003). *Aplicación de la sismología al estudio y detección de aludes de nieve*. PhD thesis, Universidad de Barcelona.

Biescas, B., Dufour, F., Furdada, G., Khazaradze, G., and Suriñach, E. (2003). Frequency content evolution of snow avalanche seismic signals. *Surveys in geophysics*, 24(5):447–464.

Bourdeau, C. and Havenith, H. (2008). Site effects modelling applied to the slope affected by the Suusamyr earthquake (Kyrgyzstan, 1992). *Engineering Geology*, (97):126–145.

Brodsky, E. E., Gordeev, E., and Kanamori, H. (2003). Landslide basal friction as measured by seismic waves. *Geophysical Research Letters*, 30(24):1–5.

Burlacu, R., Arrowsmith, S., Hayward, C., and Stump, B. (2011). Infrasonic observations from the February 21, 2008 Wells earthquake. *Nevada Bureau of Mine and Geology. Special Publication*, 36:173–180.

Cardello, G. L. and Mancktelow, N. S. (2014). Cretaceous syn-sedimentary faulting in the Wildhorn Nappe (SW Switzerland). *Swiss Journal of Geosciences*, 107(2-3):223–250.

Chaput, J., Campillo, M., Aster, R. C., Roux, P., Kyle, P. R., Knox, H., and Czoski, P. (2015). Multiple scattering from icequakes at Erebus volcano, Antarctica: Implications for imaging at glaciated volcanoes. *Journal of Geophysical Research: Solid Earth*, 120(2):1129–1141. 2014JB011278.

Chernouss, P., Fedorenko, Y., Mokrov, E., and Barashev, N. (2006). Studies of seismic effects on snow stability on mountain slopes. *Polar meteorology and glaciology*, 20:62–73.

Collins, B. D. and Jibson, R. W. (2015). Assessment of existing and potential landslide hazards resulting from the April 25, 2015 Gorkha, Nepal earthquake sequence. Technical report, US Geological Survey.

Deparis, J., Jongmans, D., Cotton, F., Baillet, L., Thouvenot, F., and Hantz, D. (2008). Analysis of rock-fall and rock-fall avalanche seismograms in the French Alps. *Bulletin of the Seismological Society of America*, 98(4):1781–1796.

Favreau, P., Mangeney, A., Lucas, A., Crosta, G., and Bouchut, F. (2010). Numerical modeling of landquakes. *Geophysical Research Letters*, 37(15):1–5.

Fedorenko, Y., Chernouss, P., Mokrov, E., Husebye, E., and Beketova, E. (2002). Dynamic avalanche modeling including seismic loading in the Khibiny Mountains. In *International Congress INTERPRAEVENT 2002 in the Pacific Rim–Matsumoto, Japan, Congress publication*, volume 2, pages 702–714.

Fierz, C., Armstrong, R., Durand, Y., Etchevers, P., Greene, E., McClung, D., Nishimura, K., Satyawali, P., and Sokratov, S. (2009). The international classification for seasonal snow on the ground. *Hydrology*, 83(1):90.

Firstov, P., Sukhanov, L., Pergament, V., and Rodionovskiy, M. (1992). Acoustic and seismic signal from snow avalanches. In *Transactions (Doklady) of the USSR Academy of Sciences: Earth science sections*, volume 312, pages 12–15.

Frischknecht, C. (2000). *Seismic soil amplification in alpine valleys: a case study: the Rhône valley, Valais, Switzerland*. PhD thesis, University of Geneva.

Frischknecht, C. and Wagner, J.-J. (2004). Seismic Soil Effect in an Embanked Deep Alpine Valley: A Numerical Investigation of Two-Dimensional Resonance. *Bulletin of the Seismological Society of America*, 94(1):171–186.

Fritsche, S. and Fäh, D. (2009). The 1946 magnitude 6.1 earthquake in the Valais: site effects as a contributor to the damage. *Swiss Journal of Geosciences*, 102:423–439.

Gauer, P. (2014). Comparison of avalanche front velocity measurements and implications for avalanche models. *Cold Regions Science and Technology*, 97:132–150.

Gauer, P. and Issler, D. (2004). Possible erosion mechanisms in snow avalanches. *Annals of Glaciology*, 38(1):384–392.

Gauer, P., Issler, D., Lied, K., Kristensen, K., and Sandersen, F. (2008). On snow avalanche flow regimes: Inferences from observations and measurements. In *Proceedings Whistler 2008 International Snow Science Workshop September 21-27, 2008*, page 717.

Geli, L., Bard, P.-Y., and Jullien, B. (1988). The effect of topography on earthquake ground motion: a review and new results. *Bulletin of the Seismological Society of America*, 78(1):42–63.

Giardini, D., Wiemer, S., Fäh, D., and Deichmann, N. (2004). Seismic Hazard Assessment of Switzerland, 2004. *Swiss Seismological Service, ETH Zurich.*

Greene, E., Atkins, D., Birkeland, K., Elder, K., Landry, C., Lazar, B., McCammon, I., Moore, M., Sharaf, D., Sterbenz, C., Tremper, B., and Williams, K. (2010). Snow, Weather and Avalanches: Observational Guidelines for Avalanche Programs in the United States. *American Avalanche Association (AAA), Pagosa Springs CO, U.S.A. (152 pp.).*

Gubler, H. (1977). Artificial Release of Avalanches by Explosives. *Journal of Glaciology*, 19(81).

Gubler, H. and Hiller, M. (1984). The use of microwave FMCW radar in snow and avalanche research. *Cold Regions Science and Technology*, (9):109–119.

Hibert, C., Mangeney, a., Grandjean, G., and Shapiro, N. M. (2011). Slope instabilities in Dolomieu crater, Réunion Island: From seismic signals to rockfall characteristics. *Journal of Geophysical Research*, 116(F4):F04032.

Higashiura, M., Nakamura, T., Nakamura, H., and Abe, O. (1979). An avalanche caused by an earthquake. *Rep. Nat. Res. Cent. Disaster Prev*, 21:103–112.

Hopfinger, E. (1983). Snow avalanche motion and related phenomena. *Annual review of fluid mechanics*, 15(1):47–76.

Housner, G. and Jennings, P. (1977). The capacity of extreme earthquake motions to damage structures. *Structural and Geotechnical Mechanics, A volume honoring NM Newmark, Prentice Hall: 102-126.*

Husid, R. (1969). Analisis de terremoros: analisis general. *Revista del IDIEM*, 8:21–42.

Ichihara, M., Takeo, M., Yokoo, A., Oikawa, J., and Ohminato, T. (2012). Monitoring volcanic activity using correlation patterns between infrasound and ground motion. *Geophysical Research Letters*, 39(4).

Issler, D. (1999). Vallé de la Sionne (Switzerland) en European avalanche test sites. *In:Mitteilungen, Nr (Ed.), Overview and analysis in viewof coordinated*

experimentsDavos. 59. Swiss Federal Institute of Snow and Avalanche research, page 122.

Issler, D. (2003). Experimental information on the dynamics of dry-snow avalanches. In *Dynamic Response of granular and porous materials under large and catastrophic deformations*, pages 109–160. Springer.

Jamieson, J. B. and Johnston, C. D. (1998). Refinements to the stability index for skier-triggered slab avalanches. *Annals of Glaciology*, 26:296–302.

Jibson, R. W. (1993). Predicting earthquake-induced landslide displacements using Newmark's sliding block analysis. *Transportation research record*, pages 9–17.

Jibson, R. W. (2011). Methods for assessing the stability of slopes during earthquakes. A retrospective. *Engineering Geology*, 122(1-2):43–50.

Jibson, R. W. and Harp, E. L. (2012). Extraordinary Distance Limits of Landslides Triggered by the 2011 Mineral, Virginia, Earthquake. *Bulletin of the Seismological Society of America*, 102(6):2368–2377.

Johnson, J. B. (2003). Generation and propagation of infrasonic airwaves from volcanic explosions. *Journal of Volcanology and Geothermal Research*, 121(1-2):1–14.

Johnson, J. B. and Palma, J. L. (2015). Lahar infrasound associated with Volcán Villarrica's 3 March 2015 eruption. *Geophysical Research Letters*, 42(15):6324–6331.

Kern, M. A., Bartelt, P., Sovilla, B., and Buser, O. (2009). Measured shear rates in large dry and wet snow avalanches. *Journal of Glaciology*, 55(190):327–338.

Kirchner, H., Michot, G., and Suzuki, T. (2000). Fracture toughness of snow in tension. *Philosophical Magazine A*, 80(5):1265–1272.

Kogelnig, A. (2012). *Development of acoustic monitoring for alpine mass movements*. PhD thesis, University of Natural Resources and Life Sciences, Vienna.

Kogelnig, A., Hübl, J., Suriñach, E., Vilajosana, I., and McArdell, B. W. (2011a). Infrasound produced by debris flow: propagation and frequency content evolution. *Natural Hazards*, 70(3):1713–1733.

Kogelnig, A., Suriñach, E., Vilajosana, I., Hübl, J., Sovilla, B., Hiller, M., and Dufour, F. (2011b). On the complementariness of infrasound and seismic sensors for monitoring snow avalanches. *Natural Hazards and Earth System Science*, 11(8):2355–2370.

Lacroix, P., Grasso, J.-R., Roulle, J., Giraud, G., Goetz, D., Morin, S., and Helmstetter, a. (2012). Monitoring of snow avalanches using a seismic array: Location, speed estimation, and relationships to meteorological variables. *Journal of Geophysical Research*, 117(F1):F01034.

Lacroix, P. and Helmstetter, A. (2011). Location of seismic signals associated with microearthquakes and rockfalls on the Séchilienne landslide, French Alps. *Bulletin of the Seismological Society of America*, 101(1):341–353.

Lay, T. and Wallace, T. (1995). *Modern global seismology*, volume 58. Academic Press.

Le Pichon, A. (2003). Infrasonic imaging of the Kunlun Mountains for the great 2001 China earthquake. *Geophysical Research Letters*, 30(15):1814.

Lehning, M. and Fierz, C. (2008). Assessment of snow transport in avalanche terrain. *Cold Regions Science and Technology*, 51(2-3):240–252.

Lehning, M., Völksch, I., Gustafsson, D., Nguyen, T. A., Stähli, M., and Zappa, M. (2006). ALPINE3D: a detailed model of mountain surface processes and its application to snow hydrology. *Hydrological Processes*, 20(10):2111–2128.

Leprettre, B., Martin, N., Glangeaud, F., and Navarre, J.-P. (1998). Three-component signal recognition using time, time-frequency, and polarization information-application to seismic detection of avalanches. *Signal Processing, IEEE Transactions on*, 46(1):83–102.

Leprettre, B. J., Navarre, J.-P., and Taillefer, A. (1996). First results from a pre-operational system for automatic detection and recognition of seismic signals associated with avalanches. *Journal of Glaciology*, 42(141):352–363.

Lockner, D. (1993). The role of acoustic emission in the study of rock fracture. In *International Journal of Rock Mechanics and Mining Sciences & Geomechanics Abstracts*, volume 30, pages 883–899. Elsevier.

Louge, M., Steiner, R., Keast, K., Decker, R., Dent, J., and Schneebeli, M. (1997). Application of capacitance instrumentation to the measurement of density and velocity of flowing snow. *Cold Regions Science and Technology*, 25(1):47–63.

Marchetti, E., Ripepe, M., Ulivieri, G., and Kogelnig, A. (2015). Infrasound array criteria for automatic detection and front velocity estimation of snow avalanches: towards a real-time early-warning system. *Natural Hazards and Earth System Sciences*, 15(11):2545–2555.

Marchi, L., Arattano, M., and Deganutti, A. M. (2002). Ten years of debris-flow monitoring in the Moscardo Torrent (Italian Alps). *Geomorphology*, 46(1-2):1–17.

Massa, M., Lovati, S., D'Alema, E., Ferretti, G., and Bakavoli, M. (2010). An Experimental Approach for Estimating Seismic Amplification Effects at the Top of a Ridge, and the Implication for Ground-Motion Predictions: The Case of Narni, Central Italy. *Bulletin of the Seismological Society of America*, 100(6):3020–3034.

Matsushita, H., Ikeda, S., Ito, Y., Matsuzawa, M., and Nakamura, H. (2013). Avalanches induced by earthquake in North Tochigi prefecture on 25 February 2013. pages 1122–1129, Grenoble (France). Proceedings of the 2013 International Snow Science Workshop.

Maurer, H., M., B., N., D., and Green, A. (1997). Active tectonism in the central Alps: contrasting regimes north and south of the Rôhne Valley. *Terra Nova*, 9(2):91–94.

McClung, D. and Schaerer, P. (2006). *The avalanche handbook*. The Mountaineers Books.

McClung, D. M. (2009). Dry snow slab quasi-brittle fracture initiation and verification from field tests. *Journal of Geophysical Research*, 114(F1):F01022.

McElwaine, J. N. and Turnbull, B. (2005). Air pressure data from the Vallée de la Sionne avalanches of 2004. *Journal of Geophysical Research: Earth Surface*, 110(F3). F03010.

Mellor, M. (1975). A review of basic snow mechanics. volume 114, pages 251–291. In: Rodda, J., Kisby, P. (Eds), Snow Mechanics-Sysmposium at Grindelwald.

Mokrov, E., Chernouss, P., Fedorenko, Y., and Husebye, E. (2000). The influence of seismic effect on avalanche release. pages 338–341, Big Sky, Montana (USA). Proceedings of the 2000 International Snow Science Workshop.

Moore, J. R., Gischig, V., Burjanek, J., Loew, S., and Fäh, D. (2011). Site effects in unstable rock slopes: Dynamic behavior of the Randa instability (Switzerland). *Bulletin of the Seismological Society of America*, 101(6):3110–3116.

Naaim, M., Durand, Y., Eckert, N., and Chambon, G. (2013). Dense avalanche friction coefficients: influence of physical properties of snow. *Journal of Glaciology*, 59(216):771–782.

Newmark, N. (1965). Ground-motion amplitude across ridges. *Géotechnique*, 15(2):139–160.

Newmark, N. and Hall, W. (1982). *Effects of earthquakes on dams and embankments*. Monograph, Earthquake Engineering Research Institute, Berkeley, California.

Nishimura, K. and Izumi, K. (1997). Seismic signals induced by snow avalanche flow. *Natural Hazards*, 15(1):89–100.

Pedersen, H., Le Brun, B., Hatzfeld, D., Campillo, M., and Bard, P.-Y. (1994). Ground-motion amplitude across ridges. *Bulletin of the Seismological Society of America*, 84(6):1786–1800.

Pérez-Guillén, C., Sovilla, B., Suriñach, E., Tapia, M., and Köhler, A. (2016). Deducing avalanche size and flow regimes from seismic measurements. *Cold Regions Science and Technology*, 121:25–41.

Pérez-Guillén, C., Tapia, M., Furdada, G., Suriñach, E., McElwaine, J., Steinkogler, W., and Hiller, M. (2014). Evaluation of a snow avalanche possibly triggered by a local earthquake at Vallée de la Sionne, Switzerland. *Cold Regions Science and Technology*, 108:149–162.

Peters, L. E., Anandakrishnan, S., Alley, R. B., and Voigt, D. E. (2012). Seismic attenuation in glacial ice: A proxy for englacial temperature. *Journal of Geophysical Research*, 117(F2):F02008.

Peterson, J. (1993). *Observations and modeling of seismic background noise*. US Geological Survey.

Pilger, C. and Bittner, M. (2009). Infrasound from tropospheric sources: impact on mesopause temperature? *Journal of Atmospheric and Solar- Terrestrial Physics*, 71(8-9):816–822.

Plafker, G., Ericksen, G. E., and Concha, J. F. (1971). Geological aspects of the May 31, 1970, Peru earthquake. *Bulletin of the Seismological Society of America*, 61(3):543–578.

Podolskiy, E. A., Nishimura, K., Abe, O., and Chernous, P. (2010a). Compiling an inventory of earthquake-induced snow avalanches. In *Avalanche Subcommittee of Japanese Society of Snow and Ice Letter 45, 89 (14 September 2010)*, pages 21–27.

Podolskiy, E. A., Nishimura, K., Abe, O., and Chernous, P. A. (2010b). Earthquake-induced snow avalanches: I. Historical case studies. *Journal of Glaciology*, 56(197):431–446.

Podolskiy, E. A., Nishimura, K., Abe, O., and Chernous, P. A. (2010c). Earthquake-induced snow avalanches: II. Experimental study. *Journal of Glaciology*, 56(197):447–458.

Podolsky, E., Chernous, P., Abe, O., Barashev, N., and Nishimura, K. (2008). Experimental study of short-term loading influence on shear strength. In *Proceedings International Snow Science Workshop. Whistler BC, Canada*, pages 21–27.

Rammer, L., Kern, M. A., Gruber, U., and Tiefenbacher, F. (2007). Comparison of avalanche-velocity measurements by means of pulsed Doppler radar, continuous wave radar and optical methods. *Cold Regions Science and Technology*, 50(1-3):35–54.

Reed, J. (1972). Attenuation of blast waves by the atmosphere. *Journal of Geophysical Research Atmospheres*, 77:1616–1622.

Reiweger, I., Mayer, K., Steiner, K., Dual, J., and Schweizer, J. (2015). Measuring and localizing acoustic emission events in snow prior to fracture. *Cold Regions Science and Technology*, 110:160–169.

Reiweger, I. and Schweizer, J. (2010). Failure of a layer of buried surface hoar. *Geophysical Research Letters*, 37(24). L24501.

Reiweger, I., Schweizer, J., Ernst, R., and Dual, J. (2010). Load-controlled test apparatus for snow. *Cold Regions Science and Technology*, 62(2):119–125.

Roten, D., Fäh, D., Olsen, K. B., and Giardini, D. (2008). A comparison of observed and simulated site response in the Rhône valley. *Geophysical Journal International*, 173(3):958–978.

Sabot, F., Naaim, M., Granada, F., Suriñach, E., Planet, P., and Furdada, G. (1998). Study of avalanche dynamics by seismic methods, image-processing techniques and numerical models. *Annals of Glaciology*, 26:319–323.

Sättele, M., Bründl, M., and Straub, D. (2013). Bayesian networks to quantify the reliability of a debris flow alarm system. *Saftey, reliability, risk and life-cycle performance of structures and infrasctructures*, pages 3661–3668.

Sättele, M., Bründl, M., and Straub, D. (2015). Reliability and effectiveness of early warning systems for natural hazards: Concept and application to debris flow warning. *Reliability Engineering & System Safety*, 142:192–202.

Schaer, M. and Issler, D. (2001). Particle densities, velocities and size distribution in large avalanches from impact-sensor measurements. *Annals of Glaciology*, (32):321–339.

Schaerer, P. A. and Salway, A. A. (1980). *Seismic and impact-pressure monitoring of flowing avalanches*, volume 26. National Research Council Canada, Division of Building Research.

Schneider, D., Bartelt, P., Caplan-Auerbach, J., Christen, M., Huggel, C., and McArdell, B. W. (2010). Insights into rock-ice avalanche dynamics by combined analysis of seismic recordings and a numerical avalanche model. *Journal of Geophysical Research*, 115(F4):F04026.

Schweizer, J. (1998). Laboratory experiments on shear failure of snow. *Annals of Glaciology*, 26:97–102.

Schweizer, J. (1999). Review of dry snow slab avalanche release. *Cold Regions Science and Technology*, 30(1):43–57.

Schweizer, J., Jamieson, B., and Schneebeli, M. (2003). Snow avalanche formation. *Reviews of Geophysics*, 41(4):1–25.

Schweizer, J. and Jamieson, J. B. (2001). Snow cover properties for skier triggering of avalanches. *Cold Regions Science and Technology*, 33(2-3):207–221.

Schweizer, J., Kronholm, K., Jamieson, J. B., and Birkeland, K. W. (2008). Review of spatial variability of snowpack properties and its importance for avalanche formation. *Cold Regions Science and Technology*, 51(2):253–272.

Scott, E. D., Hayward, C. T., Kubichek, R. F., Hamann, J. C., Pierre, J. W., Comey, B., and Mendenhall, T. (2007). Single and multiple sensor identification of avalanche-generated infrasound. *Cold Regions Science and Technology*, 47(1-2):159–170.

Sidler, R. (2015). A porosity-based Biot model for acoustic waves in snow. *Journal of Glaciology*, 61(228):789–798.

Simioni, S., Sidler, R., Dual, J., and Schweizer, J. (2015). Field measurements of snowpack response to explosive loading. *Cold Regions Science and Technology*, 120:179–190.

Sommerfeld, R. A. and Gubler, H. (1983). Snow avalanches and acoustic emissions. *Annals of Glaciology*, 4:271–276.

Sovilla, B. (2004). *Field experiments and numerical modelling of mass entrainment and deposition processes in snow avalanches*. PhD thesis, Swiss Federal Institute of Techonology Zurich.

Sovilla, B. and Bartelt, P. (2002). Observations and modelling of snow avalanche entrainment. *Natural Hazards and Earth System Science*, 2(3/4):169–179.

Sovilla, B., Burlando, P., and Bartelt, P. (2006). Field experiments and numerical modeling of mass entrainment in snow avalanches. *Journal of Geophysical Research*, 111(F3):F03007.

Sovilla, B., McElwaine, J., Steinkogler, W., Hiller, M., Dufour, F., Surinach, E., Pérez-Guillén, C., Fischer, J., Thibert, E., and Baroudi, D. (2013). The Full Scale Avalanche Dynamics Test Site Vallée de la Sionne. pages 1350–1357. In Proceedings of the International Snow Science Workshop ISSW, Grenoble, France.

Sovilla, B., McElwaine, J. N., and Louge, M. Y. (2015). The structure of powder snow avalanches. *Comptes Rendus Physique*, 16(1):97–104.

Sovilla, B., McElwaine, J. N., Schaer, M., and Vallet, J. (2010). Variation of deposition depth with slope angle in snow avalanches: Measurements from Vallée de la Sionne. *Journal of Geophysical Research*, 115(F2):F02016.

Sovilla, B., Schaer, M., Kern, M., and Bartelt, P. (2008a). Impact Pressures and flow regimes in dense snow avalanches observed at the Vallée de la Sionne test site. *Journal of Geophysical Research: Earth Surface*, 113(1):1–14.

Sovilla, B., Schaer, M., and Rammer, L. (2008b). Measurements and analysis of full-scale avalanche impact pressure at the Vallée de la Sionne test site. *Cold Regions Science and Technology*, 51(2-3):122–137.

Sovilla, B., Sonatore, I., Bühler, Y., and Margreth, S. (2012). Wet-snow avalanche interaction with a deflecting dam: field observations and numerical simulations in a case study. *Natural Hazards and Earth System Sciences*, 12:1407–1423.

Spillmann, T. (2007). *Borehole Radar Experiments and microseismic monitoring of the unstable Randa rockslide (Switzerland)*. PhD thesis, ETH Zurich.

St Lawrence, W. and Williams, S. (1976). Seismic signals associated with avalanches. *Journal of Glaciology*, 17(77):521–526.

Stein, S. and Wysession, M. (2003). *An Introduction to Seismology, Earthquakes and Earth Structure*. Blackwell Publishing.

Steinkogler, W., Gaume, J., Löwe, H., Sovilla, B., and Lehning, M. (2015). Granulation of snow: From tumbler experiments to discrete element simulations. *Journal of Geophysical Research: Earth Surface*, 120(6):1107–1126.

Steinkogler, W., Sovilla, B., and Lehning, M. (2014). Influence of snow cover properties on avalanche dynamics. *Cold Regions Science and Technology*, 97:121–131.

Suriñach, E., Furdada, G., Sabot, F., Biescas, B., and Vilaplana, J. (2001). On the characterization of seismic signals generated by snow avalanches for monitoring purposes. *Annals of Glaciology*, 32(1):268–274.

Suriñach, E., Sabot, F., Furdada, G., and Vilaplana, J. (2000). Study of seismic signals of artificially released snow avalanches for monitoring purposes. *Physics and Chemistry of the Earth*, 25(9):721–727.

Suriñach, E., Vilajosana, I., Khazaradze, G., Biescas, B., Furdada, G., and Vilaplana, J. (2005). Seismic detection and characterization of landslides and other mass movements. *Natural Hazards and Earth System Science*, 5(6):791–798.

Suriñach, E., Vilajosana, I., Kleemayr, K., and Rammer, L. (2011). Study of the wavefield generated by a gas exploder used for artificial avalanche release. *Cold Regions Science and Technology*, 66(1):17–29.

Thüring, T., Schoch, M., van Herwijnen, A., and Schweizer, J. (2015). Robust snow avalanche detection using supervised machine learning with infrasonic sensor arrays. *Cold Regions Science and Technology*, 111:60–66.

Toksöz, M. N. and Johnston, D. H. (1981). *Seismic wave attenuation*. Number 2. Soc of Exploration Geophysicists.

Trifunac, M. and Brady, A. (1975). A study on the duration of strong earthquake ground motion. *Bulletin of the Seismological Society of America*, 65(3):581–626.

Turnbull, B. and Bartelt, P. (2003). Mass and Momentum Balance Model of a Mixed Flowing/Powder Snow Avalanche. *Surveys in Geophysics*, 24(5/6):465–477.

Udías, A. (1999). *Principles of Seismology*. Cambridge University Press.

Uhira, K., Yamasato, H., and Takeo, M. (1994). Source mechanism of seismic waves excited by pyroclastic flows observed at Unzen volcano, Japan. *Journal of Geophysical Research: Solid Earth*, 99(B9):17757–17773.

Ulivieri, G., Marchetti, E., Ripepe, M., Chiambretti, I., De Rosa, G., and Segor, V. (2011). Monitoring snow avalanches in Northwestern Italian Alps using an infrasound array. *Cold Regions Science and Technology*, 69(2-3):177–183.

Unesco (1981). Avalanche Atlas. Illustrated International Avalanche Classification. Paris: UNESCO.

Van Herwijnen, A. and Jamieson, B. (2005). High-speed photography of fractures in weak snowpack layers. *Cold Regions Science and Technology*, 43(1-2):71–82.

Van Herwijnen, A. and Schweizer, J. (2011a). Monitoring avalanche activity using a seismic sensor. *Cold Regions Science and Technology*, 69(2-3):165–176.

Van Herwijnen, A. and Schweizer, J. (2011b). Seismic sensor array for monitoring an avalanche start zone: design, deployment and preliminary results. *Journal of Glaciology*, 57(202):267–276.

Vázquez, R., Suriñach, E., Capra, L., Arámbula-Mendoza, R., and Reyes-Dávila, G. (2016). Seismic characterisation of lahars at Volcán de Colima, Mexico. *Bulletin of Volcanology*, 78(2):1–14.

Vilajosana, I. (2008). *Seismic detection and characterization of snow avalanches and other mass movements*. PhD thesis, University of Barcelona.

Vilajosana, I., Khazaradze, G., Suriñach, E., Lied, E., and Kristensen, K. (2007a). Snow avalanche speed determination using seismic methods. *Cold Regions Science and Technology*, 49(1):2–10.

Vilajosana, I., Suriñach, E., Abellán, A., Khazaradze, G., García, D., and Llosa, J. (2008). Rockfall induced seismic signals: case study in Montserrat, Catalonia. *Natural Hazards and Earth System Sciences*, 8(4):805–812.

Vilajosana, I., Suriñach, E., Khazaradze, G., and Gauer, P. (2007b). Snow avalanche energy estimation from seismic signal analysis. *Cold Regions Science and Technology*, 50(1-3):72–85.

Vriend, N. M., McElwaine, J. N., Sovilla, B., Keylock, C. J., Ash, M., and Brennan, P. V. (2013). High-resolution radar measurements of snow avalanches. *Geophysical Research Letters*, 40(4):727–731.

Weichert, D., Horner, R. B., and Evans, S. G. (1994). Seismic signatures of landslides: The 1990 Brenda Mine collapse and the 1965 hope rockslides. *Bulletin of the Seismological Society of America*, 84(5):1523–1532.

Wilson, R. C. and Keefer, D. K. (1983). Dynamic analysis of a slope failure from the 6 August 1979 Coyote Lake, California, earthquake. *Bulletin of the Seismological Society of America*, 73(3):863–877.